STAR
1415

The Telecommunications and Data Acquisition Progress Report 42-75

July-September 1983

E.C. Posner
Editor

(NASA-CR-174610) THE TELECOMMUNICATIONS AND DATA ACQUISITION REPORT Progress Report, Jul. - Sep. 1983 (Jet Propulsion Lab.) 151 p HC A08/MF A01 CSCL 17B G3/32

N84-13401 THRU N84-13416 Unclas 42975

November 15, 1983

National Aeronautics and
Space Administration

Jet Propulsion Laboratory
California Institute of Technology
Pasadena, California

The Telecommunications and Data Acquisition Progress Report 42-75

July-September 1983

E.C. Posner
Editor

November 15, 1983

National Aeronautics and
Space Administration

Jet Propulsion Laboratory
California Institute of Technology
Pasadena, California

The research described in this publication was carried out by the Jet Propulsion Laboratory, California Institute of Technology, under contract with the National Aeronautics and Space Administration.

Preface

This quarterly publication provides archival reports on developments in programs managed by JPL's Office of Telecommunications and Data Acquisition (TDA). In space communications, radio navigation, radio science, and ground-based radio astronomy, it reports on activities of the Deep Space Network (DSN) and its associated Ground Communications Facility (GCF) in planning, in supporting research and technology, in implementation, and in operations. Also included is TDA-funded activity at JPL on data and information systems and reimbursable DSN work performed for other space agencies through NASA. The preceding work is all performed for NASA's Office of Space Tracking and Data Systems (OSTDS).

In geodynamics, the publication reports on the application of radio interferometry at microwave frequencies for geodynamic measurements. In the search for extraterrestrial intelligence (SETI), it reports on implementation and operations for searching the microwave spectrum. The latter two programs are performed for NASA's Office of Space Science and Applications (OSSA).

Finally, tasks funded under the JPL Director's Discretionary Fund and the Caltech President's Fund which involve the TDA Office are included.

This and each succeeding issue of the TDA Progress Report will present material in some, but not necessarily all, of the following categories:

OSTDS Tasks:

- DSN Advanced Systems
  - Tracking and Ground-Based Navigation
  - Communications, Spacecraft-Ground
  - Station Control and System Technology
  - Network Data Processing and Productivity
- DSN Systems Implementation
  - Capabilities for New Projects
  - Networks Consolidation Program
  - New Initiatives
  - Network Sustaining
- DSN Operations
  - Network Operations and Operations Support
  - Mission Interface and Support
  - TDA Program Management and Analysis
- GCF Operations and Implementation
- Data and Information Systems

OSSA Tasks:

- Search for Extraterrestrial Intelligence
- Geodynamics
  - Geodetic Instrument Development
  - Geodynamic Science

Discretionary Funded Tasks

Contents

OSTDS TASKS
DSN Advanced Systems
TRACKING AND GROUND-BASED NAVIGATION

Orbit Determination of Highly Elliptical Earth Orbiters Using VLBI and ΔVLBI Measurements 1
R. B. Frauenholz and J. Ellis
NASA Code 310-10-63-59

COMMUNICATIONS, SPACECRAFT — GROUND

The Effects of Reed-Solomon Code Shortening on the Performance of Coded Telemetry Systems 14
L. J. Deutsch
NASA Code 310-20-67-60

Detectors for Optical Communications: A Review 21
J. Katz
NASA Code 310-20-67-59

Superconducting Niobium Thin Film Slow-Wave Structures 39
J. J. Bautista, S. M. Petty, L. H. Allen, M. R. Beasley, and R. H. Hammond
NASA Code 310-20-66-50

VLSI Architectures for Computing Multiplications and Inverses in $GF(2^m)$ 52
C. C. Wang, T. K. Truong, H. M. Shao, L. J. Deutsch, J. K. Omura, and I. S. Reed
NASA Code 310-20-67-64

Deformable Subreflector Computed by Geometric Optics 65
M. S. Katow, I. Khan, and W. F. Williams
NASA Code 310-20-65-62

STATION CONTROL AND SYSTEM TECHNOLOGY

An EPROM-Based Function Generator 79
L. Fowler and J. A. McNeil
NASA Code 310-30-68-16

Polynomial Driven Time Base and PN Generator 84
S. S. Broki
NASA Code 310-30-70-55

DSN Systems Implementation
CAPABILITIES FOR NEW PROJECTS

RF Performance of a Proposed L-Band Antenna System 91
J. R. Withington, H. F. Reilly, Jr., and D. A. Bathker
NASA Code 311-03-50-01-26

Intercontinental Time and Frequency Transfer Using a Global Positioning System Timing Receiver 98
P. A. Clements
NASA Code 312-03-56-56-18

PRECEDING PAGE BLANK NOT FILMED

NETWORK SUSTAINING

NASTRAN Structural Model for the Large 64-Meter Antenna Pedestal, Part II — Improved Model 105
C. T. Chian
NASA Code 311-03-48-00-07

Energy Consumption Analysis of the Venus Deep Space Station (DSS-13) 114
N. V. Hayes
NASA Code 311-03-44-08-07

A Study of the Charged Particle Calibration Requirements for the Deep Space Network 124
S. A. Townes
NASA Code 311-03-41-81-13

GCF Operations and Implementation

GCF CHANGE ORDER ENGINEERING

Design Issues in the GCF Mark IV Development 132
R. A. Crowe
NASA Code 311-06-20-00-71

OSSA TASKS

Geodynamics

GEODETIC INSTRUMENT DEVELOPMENT

Results of the Australian Geodetic VLBI Experiment 140
B. R. Harvey, A. Stolz, D. L. Jauncey, A. Niell,
D. Morabito and R. Preston
NASA Code 692-40-01-01-02

N84 13402

Orbit Determination of Highly Elliptical Earth Orbiters Using VLBI and ΔVLBI Measurements

R. B. Frauenholz
J. Ellis
Navigations Systems Section

This paper shows the feasibility of using Very Long Baseline Interferometric data acquired by the Deep Space Network to navigate highly elliptical Earth orbiting satellites. The mission orbit of the Ion Release Module of the Active Magnetospheric Particle Tracer Explorers is used as a reference for developing strategies and provides the first opportunity for a possible flight demonstration with a spacecraft in a highly elliptical orbit.

The navigation accuracy improvements achievable with VLBI and ΔVLBI data types are determined for comparison with the doppler capability. Preferred VLBI data acquisition strategies are developed to achieve optimum navigation performance and to minimize antenna support requirements. The sensitivity of the VLBI navigation accuracy to the baseline orientation relative to the orbit plane is examined, as are the effects of major error sources such as gravitational harmonics and atmospheric drag.

The results showed that strategies using wideband ΔVLBI measurements taken near periapse performed best, determining the apoapse position to an order of magnitude better than conventional doppler. A similar approach using narrowband ΔVLBI near periapse achieves results comparable to the doppler capability. Overall, VLBI measurements perform as well or better than strategies using conventional doppler, while substantially reducing the required antenna support.

I. Introduction

For many years both Earth-orbiting and interplanetary spacecraft have been successfully navigated using conventional radio metric doppler and range measurements acquired by a worldwide network of ground stations. These techniques have served well but have often required either numerous or long data acquisition passes to achieve the desired navigation accuracies. As the number of missions to be supported increases and navigation accuracies become more demanding, resulting increases in antenna committments often lead to overloading. The recent development and application of Very Long Baseline Interferometry (VLBI) technology have served not only to improve the achievable navigation accuracies for

deep space missions such as Voyager, but also to reduce the antenna support needed for these missions.

Future interplanetary navigation is expected to rely on VLBI for the determination of the geocentric angular position and velocity of deep space probes (Ref. 1). This technique uses two widely separated tracking stations to simultaneously receive a signal broadcast by a beacon onboard the spacecraft. Cross-correlation of the received signals provides a precise measure of the differential time delay for wide bandwidth signals, and the rate of change of time delay for narrow bandwidth signals. By alternately tracking the probe and a nearby extra galactic radio source (EGRS, or quasar) of known location, a doubly-differenced one-way measurement (ΔVLBI) is constructed which is insensitive to major error sources common to each downlink. Differencing the two signals cancels common ground and spacecraft error sources and reduces the effects of transmission media, timing, polar motion, and station location uncertainties. The degree of error reduction depends on the spacecraft-quasar angular separation. In addition to eliminating the need for an uplink, the VLBI technique significantly reduces the antenna support requirements, with a typical measurement requiring from 5 to 10 minutes of acquisition time.

Two basic types of ΔVLBI measurements have been used for deep space navigation. For a spacecraft with a wideband transponder, a differential one-way range (ΔDOR) is acquired with a typical 1σ random measurement error of 15 cm. If only a narrow band spacecraft signal is available then the ΔVLBI technique provides a measure of the instantaneous rate of change of the delay with a typical 1σ accuracy of 0.1 mm/s. Observations from two nearly orthogonal baselines are required to simultaneously resolve the geocentric right ascension and declination.

A restricted bandwidth form of ΔDOR is currently being used for Voyager navigation. With a bandwidth of 14 Mhz, accuracies of 70 nanoradians have been achieved (Ref. 2). Galileo will be the first deep space mission to carry a wideband transponder specifically for ΔDOR acquisition. With the 38 Mhz bandwidth, accuracies of 50 nanoradians are expected (J. B. Thomas, "An Error Analysis for Galileo Angular Position Measurements with the Block I ΔDOR System," JPL Internal Memorandum, EM 335-26, Nov., 1981). The narrowband form has proven to be primarily useful for navigation of planetary orbiters. Covariance studies have shown that for a low altitude circular orbiter such as the Venus Orbiting Imaging Radar mission, narrowband data are necessary to determine the orbit plane orientation (Ref. 3).

There are future plans to demonstrate the use of ΔDOR for geosynchronous orbit determination using data acquired from the Air Force DSCC II satellite. Covariance studies have shown a potential accuracy of 5–10 meters can be achieved for this application (Ref. 4).

For deep space applications, the heliocentric angular position and velocity of the probe are relatively constant over a single overlap period. Because of the large distance between the probe and the stations, we may assume that the topocentric and geocentric directions to the probe are equal; hence a DOR observation will determine the angle between the station baseline and the direction to the probe. For a highly elliptical Earth orbiter, DOR observations that are not near periapse will provide similar angular information. Since the angular change for an Earth orbiter may be considerable over a single overlap period, frequent DOR measurements across the overlap will also provide precise angular rate information.

In this paper we wish to determine the navigation accuracies achievable for a highly elliptical Earth orbiter using ΔDOR, DOR, and NBΔVLBI measurements for direct comparison with the capabilities of conventional two-way doppler and range. We will also define a convenient means of observing the information content of VLBI measurements in terms of orbit geometry. First we will describe the DSN station viewing geometries of the reference orbit for the acquisition of both conventional and VLBI measurements.

II. The Reference Orbit and DSN Viewing Geometries

A. Reference Orbit

Our reference orbit, that of the AMPTE/IRM spacecraft, is 550 km × 17.7 R_e altitude with an inclination of 28.7 deg. The time and altitude history of this orbit, shown in Fig. 1, indicates that the spacecraft spends all but one hour of each orbital period beyond 1 R_e. With a period of 43.8 hrs, a series of unique viewperiods by DSN ground stations are provided during 11-day intervals while the spacecraft completes 6 orbital periods.

B. DSN Viewperiods

The viewperiods of the DSN complexes at Goldstone, Madrid, and Canberra are related to orbit position in Fig. 2. We see that nearly all regions about the orbit are covered by the three complexes, with several tracking passes also including periapse. Similar, but not identical, viewperiod sets are repeated during subsequent 11-day intervals. This viewing geometry provides generous opportunities to acquire conventional radio metric doppler and range measurements at almost any position in the orbit.

To acquire measurements for generating the VLBI and ΔVLBI data types, simultaneous viewing by two of the DSN

complexes is needed. The three DSN complexes form three different baselines to acquire these measurements. While we will not concern ourselves with other orbit geometries in this paper, it is important to note that the number and length of overlaps increase with orbital period and apoapse height, and that the orbital inclination dictates which stations provide the overlaps. Because of the 28.7-deg inclination of our reference orbit, we found overlaps only from the Goldstone-Canberra and the Goldstone-Madrid baselines. There are two possible viewperiod overlaps from each of these baselines during each orbital period. A composite of the visible overlaps during a 7-orbit sequence is shown for each baseline in Fig. 3. There are a total of 9 overlaps available for the Goldstone-Canberra baseline during the initial 11-day cycle; there are 8 for Goldstone-Madrid. These overlaps are sequentially numbered and are shown to walk through the orbit, providing a different geometric view of the orbit with each overlap. An odd-even numbering scheme has been selected to indicate the expected occurrence of two overlaps during each orbital period. When a second overlap is not visible it is identified, for example, as overlap number 13. The 12th overlap for each baseline occurs during the 7th orbit and is included to illustrate the repetition of the viewing geometry following the fundamental 6-orbit cycle. Table 1 lists the individual orbit numbers identified in Fig. 3, and defines the duration and total true anomaly change of each visible overlap

III. Navigation System Error Model

Our reference orbit spends approximately 90% of the 43.8-hr period beyond 5 R_e, as shown in Fig. 1. Such an orbit increases the effects of solar and lunar gravitational perturbations, causing the periapse altitudes over an annual cycle to be as low as 290 km (Ref. 5). This results in measurable atmospheric drag and increases the orbit sensitivity to uncertainties in the Earth's geopotential field and gravitational constant (GM).

The error model used in this navigation study includes the effects of uncertainties in the Earth's geopotential field and GM, the lunar GM and ephemeris, solar pressure and flux, atmospheric drag coefficient, and tropospheric refraction. In addition, the effects of station location and timing uncertainties on the accuracy of the orbit are also modelled. The 1σ uncertainties in each error source are presented in Table 2. These error sources will be treated as considered parameters in a batch filter process in which we will usually estimate only the spacecraft state prior to the data arc.

In this study uncertainties in the Earth's geopotential field are represented by a lumped parameter model, defined by scaling the difference between two independent geopotential models. In our study we use 75% of the difference between APL (Applied Physics Laboratory) and SAO (Smithsonian Astrophysical Observatory) 8 X 8 models to represent the uncertainty in the geopotential field. It will later be shown that this error source dominates the total achievable navigation accuracy when using VLBI for our Earth orbiter application, and that the achievable navigation accuracy may be improved by using a more accurate geopotential model.

IV. Navigation Capability Using Doppler and Range

The navigation capability using conventional two-way doppler and range is established to provide a reference against which the performance of candidate strategies using VLBI and ΔVLBI can be compared. This reference represents an operationally realistic navigation strategy capable of satisfying orbit accuracy for both science and DSN antenna acquisition requirements for an IRM-like orbit. We have conservatively restricted our data acquisition strategies to viewperiods ±90 deg of true anomaly away from periapse (±28 min) to avoid the possible presence of high antenna-relative angular rates.

To develop our reference strategy we first examined the use of doppler alone, initially for a single station at each DSN complex, then for each of the three possible two-complex pairs, and finally for a station from each of the three complexes. These strategies were analyzed using the navigation system error model presented in Table 2. We have considered each error source while estimating only the spacecraft state. In each case the definitive orbit accuracy was based on a single 30-min pass per day for each station for 10 consecutive days. These passes were taken from the center of each available viewperiod (see Fig. 2). Orbit errors were then propagated for an additional 10 days. The largest definitive position uncertainties were found to occur near apoapse. The 3σ RSS apoapse position accuracies achievable by different station combinations are compared to a typical 3σ DSN antenna acquisition requirement in Fig. 4. The best single-station performance is obtained by Goldstone, while the best two-station strategy is provided by the Goldstone-Canberra combination. When data from Madrid are added to those data from the Goldstone-Canberra pair, very little improvement in orbit accuracy is realized. Adding a single range point to each doppler pass also results in only modest improvements. Therefore, we have chosen to adopt the Goldstone-Canberra strategy using doppler alone as our reference capability for conventional radio metric data.

In Fig. 5 we have decomposed the total 1σ RSS position uncertainties for the doppler strategy into the individual contributions due to data noise and considered parameters. Data noise errors are decomposed into radial, cross-track, and along-track components. In the definitive phase, data noise

dominates the total position uncertainty, with maximum RSS totals occurring near apoapse. The radial component was determined most accurately, as expected for a doppler strategy, while the relatively large magnitude of the cross-track component indicates the difficulty of using doppler to determine orbit plane orientation. In the predictive phase, on the other hand, total position uncertainty was dominated by considered parameters. By this time accumulating velocity errors due to gravitational harmonics resulted in orbital period errors which shifted associated position errors to the periapse region.

A breakdown of the total position error into the contributions of data noise and considered parameters is presented in Fig. 6 for both the apoapse and periapse regions of the orbit. Near apoapse both definitive and predictive phases perform similarly, with uncertainties dominated by data noise. The smaller effects of the considered parameters are primarily due to the Earth's geopotential field and gravitational constant, and to a lesser extent to atmospheric drag. Near periapse both the definitive and predictive uncertainties are dominated by errors in the geopotential field. Accuracy improvement near apoapse is best achieved by increasing the amount of data to overcome the effects of the data noise, rather than by estimating one or more of the considered parameters. To improve the accuracy near periapse would require an improved estimate of the geopotential field. Because we are representing this error source as a lumped parameter, we could not isolate the effects of individual harmonics in our estimation process.

V. Navigation Strategies Using VLBI Data

A. VLBI Data Content

In this section our objective is to qualitatively anticipate the characteristics of VLBI data value for a highly elliptical Earth orbiter based on our experience with deep space applications. The covariance analysis used to estimate the navigation performance will examine the sensitivity of VLBI strategies to orbit geometry, data sampling rate, and baseline selection.

Geocentric angular position and velocity are relatively constant for deep space probes across typical VLBI data acquisition viewperiods. As a result, the use of weekly ΔDOR observations is adequate. Velocity and acceleration estimates are obtained by sampling over intervals up to several weeks. The motion of the probe relative to the central body is inferred from a combination of dynamic modelling and angular accelerations. By comparison, the time scale for our highly elliptical orbiter application is considerably compressed. Geocentric angular changes may be very large over a single ΔDOR viewing opportunity. Consequently, data strategies using frequent sampling over a single pass may be quite typical.

The VLBI measurement provides an instantaneous measure of the angle between the baseline and the probe. If the baseline lies entirely in the orbit plane, successive VLBI measurements would provide in-plane angular position and angular rates relative to this baseline. A baseline orthogonal to the plane would yield information about the orbit plane orientation. The time history of the angle between the baseline and the projection of the baseline in the orbit plane, which is displayed in Fig. 7, shows that the Goldstone-Canberra baseline inclination angle varies from 62 to 72 deg, and from 12 to 30 deg for Goldstone-Madrid. Based on these trends, we may expect that data from both baselines will be required to resolve both the position and velocity.

In addition to the average trend of the inclination histories, we are also interested in the variation within each overlap. When the variation is greatest we can expect to observe the greatest change in baseline-relative spacecraft motion since all overlaps will have Earth-rotation effects in common. In Fig. 7 the #8 overlap for the Goldstone-Madrid baseline has an inclination trend which is dramatically different from those of all the other overlaps shown for either baseline. Figure 3 illustrates that this overlap occurs near periapse, and that there are only two such overlaps available during the 11-day cycle, one for each baseline. We will later demonstrate that there is considerably more information content in these two overlaps than in all of the other available overlaps combined.

B. Navigation Strategies Using ΔDOR

Initially the navigation capabilities using ΔDOR strategies are developed and compared with DOR strategies, and then both are compared to our reference doppler capabilities. The use of ΔDOR requires the availability of a nearby quasar, as the improved accuracy of this measurement results from the elimination of station clock synchronization errors and the reduction of sensitivity to media effects by differencing spacecraft and quasar VLBI observables. We have assumed quasar availability and have used the ΔDOR noise and bias values in Table 2 for our studies.

To develop our ΔDOR strategies we separately examined the performance for each baseline using all overlaps visible during the 11-day cycle (Fig. 3). To reflect changes in information content across each overlap in our analysis, a single measurement near the beginning, the middle, and the end of each overlap was selected. We first examined the capability using only the center measurement, then both end points, and finally all three points. From this process it was determined that the Goldstone-Canberra baseline performed somewhat better than Goldstone-Madrid. Figure 8(b) compares the capability of the 1-, 2-, and 3-point strategies for the Goldstone-Canberra baseline, illustrating the 1σ RSS position uncertainty for a 10-day definitive period and a predictive interval of an additional

10 days. The definitive accuracy of the 2-point strategy is an order-of-magnitude better than the single-point case and performed essentially the same as the 3-point strategy. We observe better performance from the multiple-point strategies because these measurements are acquired at different true anomalies, providing in-plane angular position information across the overlap that is not possible using the single measurement. All three ΔDOR strategies demonstrate similar predictive uncertainties due to the dominating influence of gravitational harmonics. One can also see that the capability of the single-point strategy compares favorably with the doppler capability provided for reference in Fig. 8(a). At once we see a means of matching the doppler results, but with significantly fewer measurments. With these results we adopted the 2-point strategy as a ΔDOR reference for comparison with other possibilities.

Our next objective was to understand the sensitivity of the measurements from each overlap as a function of orbit geometry. We earlier alleged, using data in Fig. 7 and Table 2, that large changes in the true anomaly during an overlap reflected large changes in baseline-relative spacecraft dynamics, and that we might expect to benefit from such geometry. In fact, we have already witnessed this effect in arriving at our 2-point reference strategy. Not surprisingly, Table 2 identifies the largest changes in true anomaly as occuring near periapse. To gain a measure of the data strength of the single periapse overlap contained in our Goldstone-Canberra baseline, we removed it from our data set. The capabilities of the 2-point strategy with and without the data from the single periapse overlap are compared in Fig. 8(c). Here, the definitive orbit accuracy degrades an order-of-magnitude when the periapse data is omitted, and tends to perform similar to our doppler strategy. However, both strategies yield similar maximum predictive accuracies due to the dominant effects of uncertainties in the Earth's geopotential field.

With the influence of the periapse data established, we next evaluated the performance using only the periapse data. The use of 3 points spanning the periapse overlap from either baseline represented an extremely underdetermined system. It is operationally feasible to collect data for a single ΔDOR measurement once every 10 min, including acquiring a nearby quasar. Even with this increased sampling rate a single baseline still performed poorly. However, as we see in Fig. 8(d), when we combine 3 points from each baseline, the results are comparable to our original 2-point strategy when all 9 overlaps from the Goldstone-Canberra baseline were used. One can see that the position uncertainties obtained by the two strategies follow each other reasonably well except near periapse #4. Here our two-baseline periapse strategy performs better because it contains the powerful Goldstone-Madrid periapse data that are naturally missing from the Goldstone-Canberra 2-point strategy. In Fig. 8(e) we see that our ΔDOR periapse strategy determines the 1σ apoapse position to about 285 m, compared to 3800 m for our doppler strategy.

We have decomposed the total 1σ RSS position uncertainty for our ΔDOR periapse strategy into radial, cross-track, and along-track components in Fig. 9. In addition, Fig. 10 shows a similar decomposition of the data noise contribution. Comparison of Figs. 9 and 10 indicates our ΔDOR strategy is dominated by the effects of considered parameters. Also, when one compares the data noise contribution in Fig. 10 to those for doppler in Fig. 5, it is clear that the information content of the ΔDOR measurements allows for two orders of magnitude reduction in data noise.

From the data in Fig. 9 it is evident that the cross-track position component is the best-determined. The rather broad sinusoidal signature peaks near each apoapse and predicts about as well as it is determined. Approximately 90% of the signature amplitude is due to uncertainties in the Earth's geopotential field. We expected the cross-track component to be determined fairly well since our Goldstone-Canberra baseline provided strong out-of-plane information.

The along-track component shown in Fig. 9 exhibits maximum amplitude near periapse, primarily due to uncertainties in the Earth's geopotential field. This trend continues during the predictive phase as well, although atmospheric drag effects grow from a negligible contribution at the beginning of this period to a sizable 40% at the end. By this time atmospheric drag has induced an orbital period uncertainty of about 5 min. We attempted to estimate drag coefficient but found that there was insufficient information content in our ΔDOR measurements to confidently estimate this parameter.

During the definitive time period the radial component exhibits a sinusoidal behavior with maximum and minimum points occurring near alternating periapse epochs. Both extremes are dominated by contributions of the Earth's geopotential field. The predictive position uncertainty peaks near periapse and is also dominated by the effects of the Earth's geopotential field. Like the along-track component, the radial component has a negligible drag contribution at the beginning of the predictive period that grows to about 40% by the end.

The following were accomplished using ΔDOR measurements acquired at periapse by two orthogonal baselines:

(1) The in-plane angular position was defined well by the Goldstone-Madrid baseline;

(2) The orbit orientation was defined well by the Goldstone-Canberra baseline;

(3) Some angular rate information was provided by each baseline because of the large true anomaly changes which occurred during each overlap; and

(4) The sensitivity to gravity harmonics was reduced by the combination of two baselines.

C. Strategies Using DOR

Differenced one-way range (DOR) is acquired in a manner similar to that of ΔDOR, except that quasar acquisition is not necessary. However, the ability to remove errors common to each downlink through double-differencing in also eliminated, and therefore increases the effective measurement noise and bias (see Table 2). With these larger measurement uncertainties we evaluated the performance of the DOR strategy using the same two-baseline periapse data acquisition scenario previously developed for ΔDOR. We observed very little difference in overall performance between DOR and ΔDOR due to the dominant influence of uncertainties in the Earth's geopotential field. These results were obtained using an error magnitude equal to 75% of the lumped parameter difference in two independent geopotential models. Improvement in the geopotential model would directly improve the performance of both the ΔDOR and DOR strategies. We have evaluated the performance of the two strategies, assuming a much smaller error magnitude of 5%, and the results are compared in Fig. 8(f). Both strategies provided substantially improved performance during the definitive phase, but the greatest improvement is realized during the predictive phase. Now the difference in the ΔDOR and DOR performance is due specifically to the differences in the data noise and bias values used for the two strategies.

The capability of the doppler strategy using the JPL geopotential model was compared to our reference case and found to be similar since data noise is the primary source of position uncertainty.

D. Strategies Using Narrowband ΔVLBI

A brief evaluation of the capabilities of narrowband ΔVLBI showed that the performance of this measurement type is very similar to that of doppler. Like the other VLBI strategies we have evaluated, NBΔVLBI performance was dominated by uncertainties in the geopotential model. This conclusion is based on the results of a strategy using the same two-baseline periapse scenario we used for ΔDOR. Although this strategy performs no better than doppler, it is possible to achieve this capability with only 3 measurements from each of two periapse overlaps, compared to a much larger antenna commitment required for the doppler strategy.

VI. Conclusions

The results of our covariance analysis demonstrate that for an IRM-type Earth orbiter, an order-of-magnitude improvement in definitive position accuracies can be achieved using VLBI data in place of doppler with a significant reduction in antenna support requirements. There is a 10:1 reduction in the number of data acquisition passes and a 100:1 reduction in the total number of measurements.

By evaluating the sensitivity of VLBI measurements in terms of orbit geometry we found that data acquired near periapse performed best due to the large true anomaly changes across the overlap. The use of two orthogonal baselines defined both the in-plane angular position and the orbit plane orientation.

We showed that ΔDOR and DOR strategies performed similarly due to the dominant influence of uncertainties in the Earth's geopotential field. Even when the navigation performance was evaluated for an improved geopotential model, it was found that the difference in ΔDOR and DOR capabilities was not significant. As a result it would be feasible to use DOR strategies in place of ΔDOR and avoid the requirement for a nearby quasar. The use of NBΔVLBI does not show the same potential as ΔDOR and DOR, although it can match doppler performance with much less antenna support.

Based on the results of this study the use of VLBI and ΔVLBI measurements for navigating a highly elliptical Earth orbiter like the AMPTE/IRM appears very promising. The AMPTE mission will be launched in August 1984 and at that time it may be possible to conduct in-flight demonstrations and compare the results with those presented here.

Acknowledgement

The authors wish to express appreciation to M. C. Hanna, J. A. Kechichian and C. S. Christensen for their contributions to this work.

References

1. Melbourne, W. G., and Curkendall, D. W., "Radio Metric Direction Finding: A New Approach to Deep Space Navigation," AAS/AIAA Astrodynamics Specialist Conference, Jackson Hole, WY, September 1977 (unnumbered paper).

2. Border, J. S., Donivan, F. F., Finley, S. G., Hildebrand, C. E., Moultrie, T. and Skjerve, L. J., "Determining Spacecraft Angular Position with ΔVLBI: The Voyager Demonstration," AIAA Paper No. 82-1471, AIAA/AAS Astrodynamics Conference, San Diego, CA, August 1982.

3. Curkendall, D. W., "Radio Metric Technology for Deep Space Navigation: A Development Overview," AIAA Paper No. 78-1395, AIAA/AAS Astrodynamics Conference, Palo Alto, CA, August 1978.

4. Yunck, T. P. and Wu, S. C., "Orbit Determination of Geosynchronous Satellites by VLBI and ΔVLBI," AIAA Paper No. 82-1446, AIAA/AAS Astrodynamics Conference, San Diego, CA, August 1982.

5. Frauenholz, R. B., "Tracking and Orbit Determination Strategies for the AMPTE Mission Set," AIAA Paper No. 82-0206, AIAA 20th Aerospace Sciences Meeting, Orlando, FL, January 1982.

Table 1. DSN station viewperiod overlaps (reference epoch: 8/13/84, 07:33:10 GMT)

Overlap number	Goldstone-Canberra Baseline			Goldstone-Madrid Baseline		
	Orbit number	Duration (hh:mm)	True anomaly change, deg	Orbit number	Duration (hh:mm)	True anomaly change, deg
1	1	03:41	4.06	1	03:08	5.21
2	1	*	*	1	01:04	2.25
3	2	03:42	3.89	2	02:46	3.39
4	3	02:04	112.11	2	*	*
5	3	03:40	4.06	3	02:27	2.63
6	4	03:31	11.69	3	*	*
7	4	03:37	4.75	4	02:09	2.27
8	5	03:39	6.24	4,5	04:54	274.86
9	5	03:29	6.55	5	01:46	2.04
10	6	03:41	4.64	6	03:10	8.58
11	6	*	*	6	01:11	1.72
12	7	03:41	4.02	7	02:46	4.26
13	7	*	*	7	*	*

*Not visible

Table 2. Navigation system error model

Error source	One-Sigma uncertainty
Earth geopotential field	75% of SAO-APL 8 x 8 model difference to consider; 100% to estimate
Earth *GM*	$GM \times 10^{-6}$
Lunar *GM*	$GM \times 10^{-6}$
Lunar ephemeris	100 m each axis
Drag coefficient	50% of nominal to consider 100% of nominal to estimate
Solar pressure	10% of nominal reflectivity
Solar flux	30% of nominal
Tropospheric refraction	10% of nominal
Station timing error	1 ms
Station location	
For doppler/range:	
Local X and Y	5 m
Local Z	15 m
For VLBI data types	0.8 m interstation baseline
Two-way doppler noise	2 cm/sec
Range (continuous wave)	
Noise	1000 m (deweighted)
Bias	15 m
ΔDOR	
Noise	0.15 m
Bias	0.20 m
DOR	
Noise	0.3 m
Bias	3.1 m
NBΔVLBI noise	0.1 mm/sec

ORIGINAL PAGE IS
OF POOR QUALITY

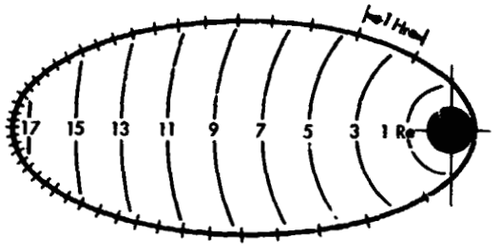

Fig. 1. Time and altitude history of the reference orbit

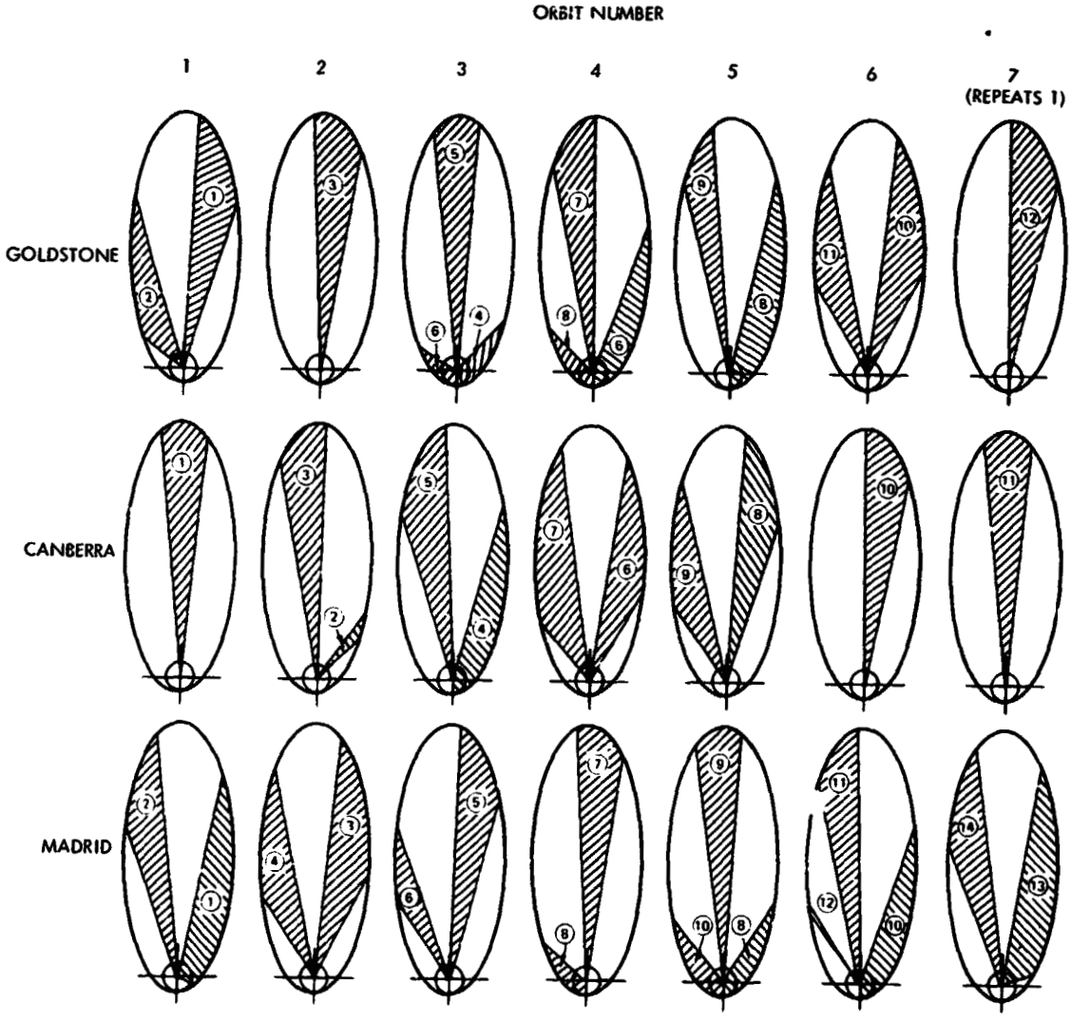

Fig. 2. DSN viewperiods of the reference orbit (minimum elevation is 10 deg)

ORIGINAL PAGE IS
OF POOR QUALITY

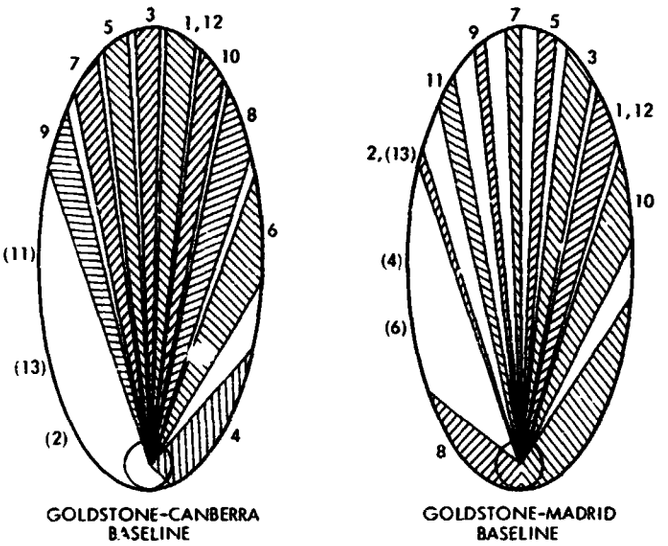

Fig. 3. Composite of DSN viewperiod overlaps for 7-orbit sequence

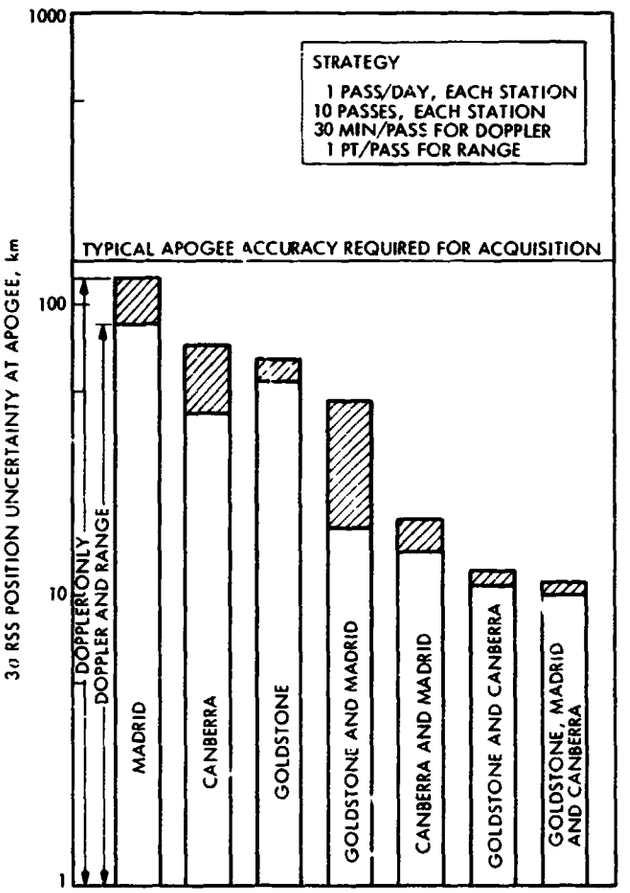

Fig. 4. Accuracy in apoapse position using two-way doppler and range

ORIGINAL PAGE IS
OF POOR QUALITY

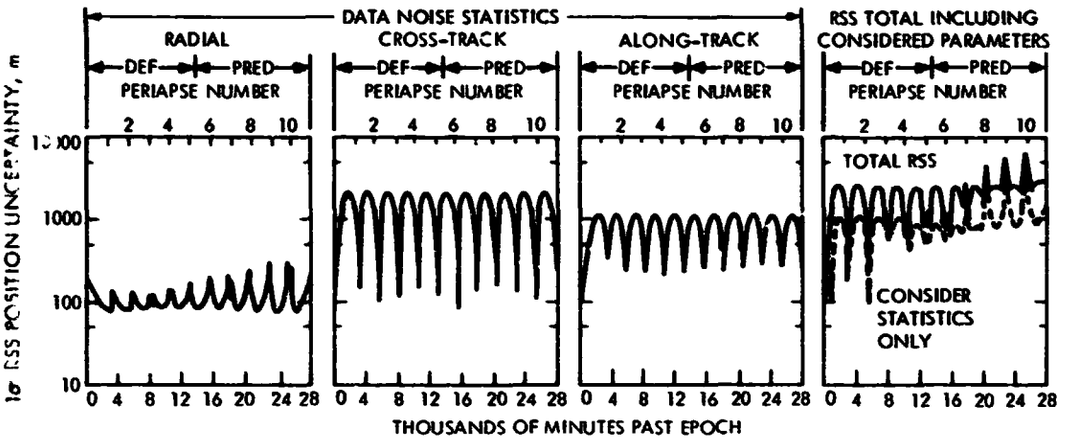

Fig. 5. Position accuracy using doppler from Goldstone and Canberra

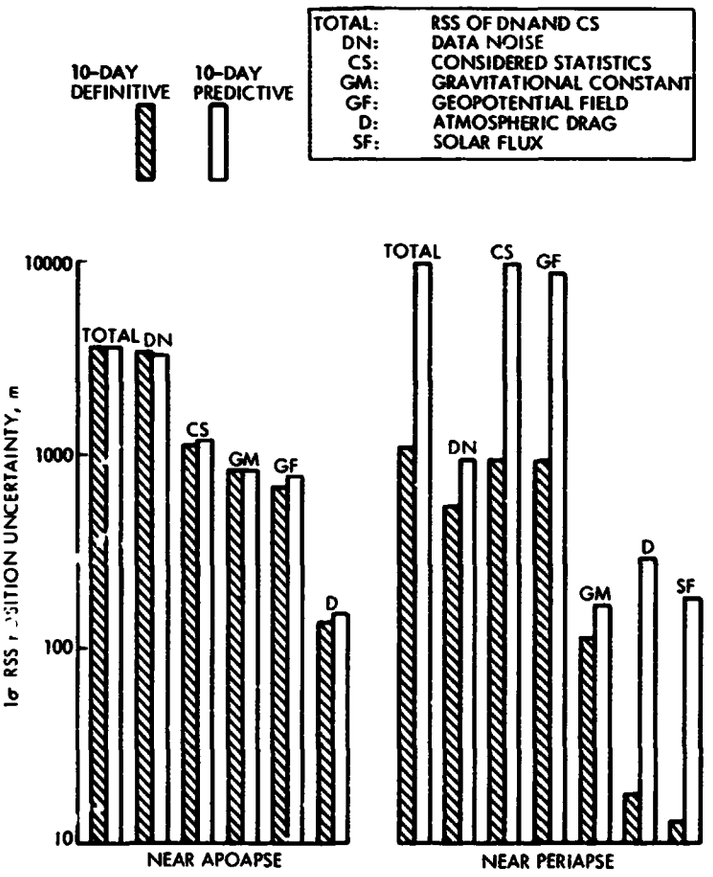

Fig. 6. Comparison of definitive and predictive position accuracies near apoapse and periapse using doppler from Goldstone and Canberra

ORIGINAL PAGE IS
OF POOR QUALITY

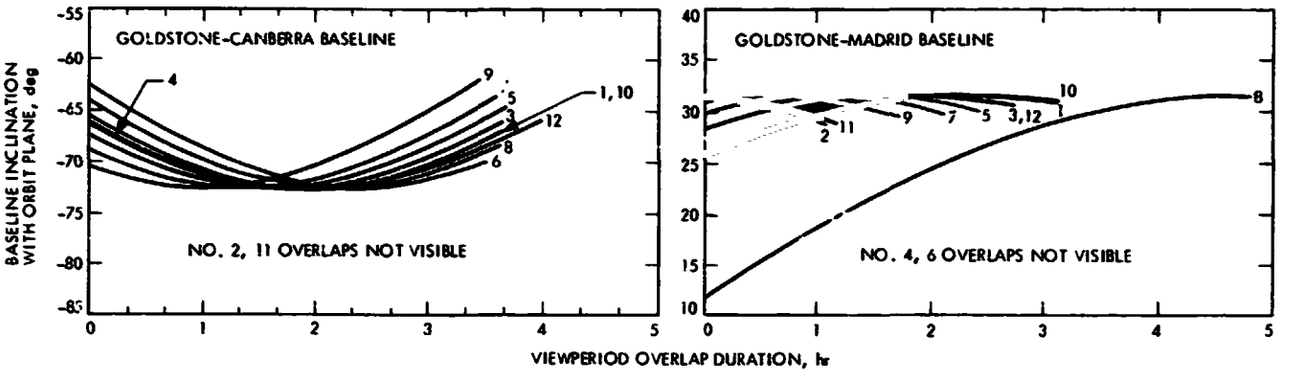
GOLDSTONE-CANBERRA BASELINE
GOLDSTONE-MADRID BASELINE
BASELINE INCLINATION WITH ORBIT PLANE, deg
NO. 2, 11 OVERLAPS NOT VISIBLE
NO. 4, 6 OVERLAPS NOT VISIBLE
VIEWPERIOD OVERLAP DURATION, hr

Fig. 7. Baseline inclination with reference orbit plane

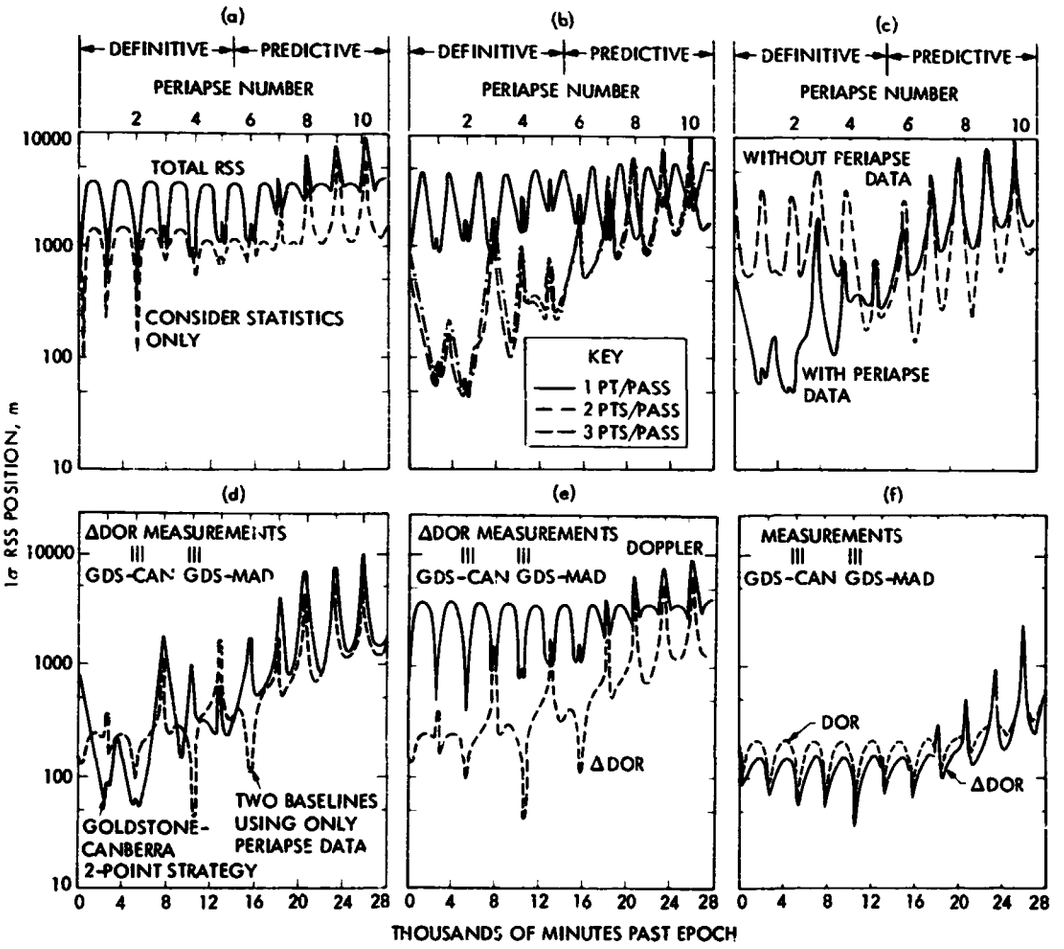

Fig. 8. ΔDOR capability using Goldstone-Canberra baseline: (a) Reference position accuracy using doppler (see Fig. 5); (b) ΔDOR accuracy using 9 overlap passes (see Fig. 3); (c) ΔDOR 2-point strategy with and without periapse data; (d) Two periapse baselines versus 2-point strategy; (e) ΔDOR periapse strategy versus doppler; (f) ΔDOR versus DOR for 5% geopotential model

ORIGINAL PAGE IS
OF POOR QUALITY

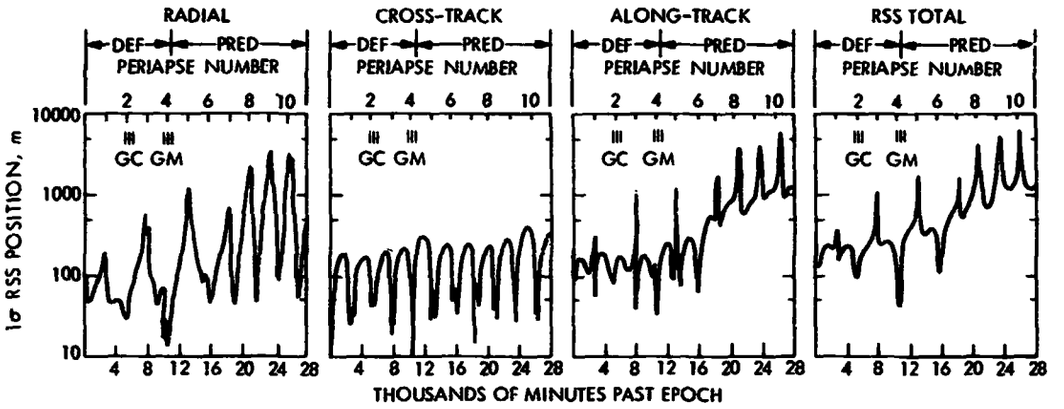

Fig. 9. Radial, cross-track, and along-track components of the ΔDOR periapse strategy

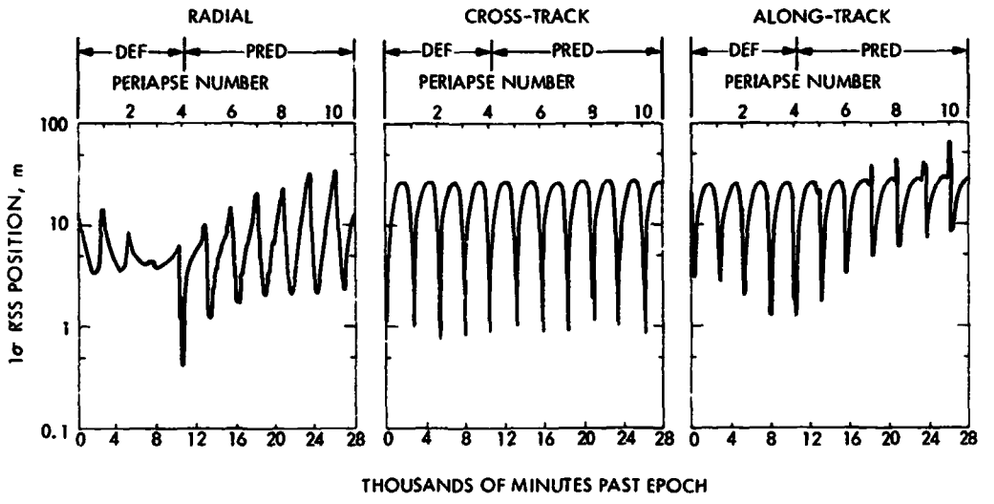

Fig. 10. Components of data noise for the ΔDOR two-baseline periapse strategy

D2

N84 13403

The Effects of Reed-Solomon Code Shortening on the Performance of Coded Telemetry Systems

L. J. Deutsch
Communications Systems Research Section

In the proposed NASA/ESA telemetry/coding standard, a (255, 223) Reed-Solomon code is concatenated with an inner (7, 1/2) convolutional code. Under some circumstances, it would be desirable to use a shorter outer code word length. For example, the format of the data coming from science instruments on board a spacecraft may lend itself naturally to a word length of 200 symbols rather than 223. To accommodate such code word lengths, the Reed-Solomon code can be shortened to an (N, N-32) code where N can be any integer between 33 and 255. Shortening the code, nowever, changes its performance. On one hand, the amount of redundancy per information symbol increases. This would, by itself, imply that performance would improve. However, because of this increased redundancy, the amount of energy per information symbol is decreased by code shortening. The overall effect is to degrade the performance of the code. This report develops the theory of Reed-Solomon code shortening in general and quantifies the degradation due to shortening in the context of concatenated coding. It is shown that in the NASA/ESA concatenated system, significant degradations (greater than 0.1 dB at a bit error rate of 10^{-6}) occur only when $N < 180$.

I. Introduction

All planned NASA and European Space Agency (ESA) deep space missions are expected to have the capability of using a concatenated Reed-Solomon/convolutional coding scheme for downlink telemetry. In fact, this coding system is a proposed NASA/ESA standard (Ref. 1). The inner code is a (7, 1/2) convolutional code. This is the same code that is currently used by tne Voyager spacecraft. The outer code is a (255, 223) Reed-Solomon code. The proposed standard code is slightly different than that used by Voyager in that a different representation is used to represent the eight-bit Reed-Solomon symbols. The two Reed-Solomon codes, however, share the same code length parameters and hence have identical performances. Many studies have been performed to determine the performance of this concatenated coding system under various conditions (Refs. 1,2,3, and 4).

Since the Reed-Solomon code words consist of 223 eight bit information symbols, 1,784 bits are required from the spacecraft's data system to encode each code word. Some of these bits will typically be frame headers that contain identification, timing, and synchronization information. The remainder of the bits are data from various scientific instruments. There could conceivably be cases in which the spacecraft instruments produce data in a form that is more amenable to being packed into a smaller number of bits. In fact, it is even possible to imagine scenarios for which the number of bits that form such

an information packet might vary with time. Under such conditions, it is desirable for the Reed-Solomon encoder to be able to process fewer than 1,784 bits at a time.

Fortunately, this is possible by adapting the (255, 223) code for use as a (N, N-32) code for $N < 255$. One way of accomplishing this is illustrated in Fig. 1. Suppose that $M = N$-32 information symbols are generated by the spacecraft data system and that $M < 223$. To these symbols, the Reed-Solomon processor appends $223 - M$ additional symbols, all of which happen to be zeroes. Since there are now 223 symbols, encoding can take place. A code word consisting of 255 symbols is generated. Since all Reed-Solomon codes that are planned for use in space missions are systematic, the information symbols are themselves a portion of the code word – in this case they are the first 223 symbols The zeroes that were added for the purposes of encoding are now stripped away and the rest of the code word is sent to the convolutional encoder. After Viterbi decoding on the ground, the zeroes are once again added to the code word. This allows it to be decoded. Following Reed-Solomon decoding, the zeroes are finally stripped away to reveal the "original" information sequence.

The above process is an example of Reed-Solomon code shortening. The effect is to use a (255, 223) encoder and decoder, to implement an (N, N-32) code. In general, the fixed sequence that is added to the input information sequence can be of any form. It is called the "fill sequence." If, as in the above example, it is the all zero sequence, then the process is sometimes referred to as "virtual zero fill." The fill sequence can be merged with the information sequence in any way – not just at the end as in the example. It is crucial, however, that the fill sequence be added in the same way at the decoding end of the system.

There are two phenomena that occur in Reed-Solomon code shortening that affect the overall performance of the system. The first is that the code rate is changed with shortening. The code rate of the original Reed-Solomon code is 223/255. The code rate of a length N shortened RS code is $(N - 32)/N$. Since

$$(N - 32)/N < 223/255$$

for all $N < 255$, shortening reduces the code rate. If all other aspects could be held constant, this might imply improved performance. However, a second effect of code shortening is to reduce the energy that is expended for each Reed-Solomon code word in the transmitter. This tends to degrade the overall performance. In fact, the second effect is greater than the first. Reed-Solomon code shortening does degrade the performance of the concatenated coding system.

In the following sections of this report, a theory of Reed-Solomon code shortening is developed. The performance of a concatenated (7, 1/2) convolutional/(N – 32, N) Reed-Solomon system is also calculated. It is shown that the degradation is actually quite small. Only if the Reed-Solomon code word length is shortened to $N = 180$ symbols or less will there be a 0.1 dB loss at a concatenated decoded bit error rate of 10^{-6}.

II. The Theory of Reed-Solomon Code Shortening

Throughout the remainder of this report, it is assumed that the coding system is the proposed standard concatenated system shown in Fig. 2.

Suppose that the energy in each channel symbol (the digital entities that are output from the convolutional decoder) is E_s. Then the symbol energy to noise spectral density ratio is E_s/N_0. Since the rate of the convolutional inner code is 1/2, the signal to noise ratio for the bits that are input to the convolutional encoder is given by

$$\frac{E_V}{N_0} = 2\frac{E_s}{N_0}$$

Now suppose that the (255, 223) Reed-Solomon code is shortened to length N ($32 < N < 255$). This means that the Reed-Solomon encoder assumes that the $N - 32$ input information Reed-Solomon (RS) symbols are merged with a fill sequence of length $255 - N$ RS symbols to form an input sequence of length 223 RS symbols. The encoder can then generate the 32 parity check symbols that are appended to the input sequence to form a length N code word. The rate of the shortened code is

$$R_N = \frac{N-32}{N}$$

This implies that the information bit (bits input to RS encoder) signal to noise ratio is

$$\frac{E_b}{N_0} = \frac{N}{N-32}\frac{E_V}{N_0} = \frac{2N}{N-32}\frac{E_s}{N_0} \qquad (1)$$

The performance of the Viterbi decoded inner code can be expressed in terms of E_V/N_0. Let

$$p = f\left(\frac{E_V}{N_0}\right) \qquad (2)$$

and

$$\pi = g\left(\frac{E_V}{N_0}\right) \tag{3}$$

represent the Viterbi-decoded bit error rate and the error rate for sets of eight consecutive bits respectively. The quantity π is also the input RS symbol error rate for the Reed-Solomon decoder. If the Reed-Solomon code is infinitely interleaved, then the overall bit error rate of the concatenated code is

$$p_{bit} = \frac{p}{\pi} \sum_{j=17}^{N} \left(\frac{j}{N}\right)\binom{N}{j}\pi^j (1-\pi)^{N-j} \tag{4}$$

This theory can be applied to any concatenated coding system where the outer code is a shortened (255, 223) Reed-Solomon code. This is done by appropriately defining p and π to be the bit error rate and the error rate for sets of eight bits respectively for the inner code. One special case is when the inner code is non-existent. In this case, the coding system consists only of the Reed-Solomon code. The bit error rate, p, of the "inner code" is just the bit error rate of uncoded transmission.

If the channel is memoryless, then

$$\pi = 1 - (1-p)^8$$

III. Numerical Results

The theory developed in Section II was used to evaluate the performance of concatenated coding with Reed-Solomon code shortening. The values of p and π that define the performance of the (7, 1/2) Viterbi-decoded convolutional code came from software simulations that were reported in Ref. 3. These functions are shown graphically in Fig. 3.

The Reed-Solomon decoded bit error probability was then computed as a function of E_b/N_0 [Eqs. (1) - (4)]. Fig. 4 shows the results of these calculations for several values of the shortened code length N. The full code case (N = 255) is included for comparison. It should be noted that these results assume that there are no degradations from the analogue parts of the telemetry receiving system and that both convolutional and Reed-Solomon code synchronization are maintained perfectly. Also, infinite interleaving of Reed-Solomon symbols is assumed. It is true, however, in the full code length case, that the difference in performance between an interleaving depth of five and one of infinity is negligible.

The loss due to the code shortening is the additional E_b/N_0 that must be added to the signal to make the shortened code's performance equal to that of the full length code. For a fixed overall bit error rate, this degradation is just the horizontal distance between the corresponding curves on the graph measured at that error rate. Graphs of this loss for overall bit error rates of 10^{-4}, 10^{-5}, and 10^{-6} are shown in Fig. 5.

IV. Conclusions

The results of the computations performed in Section III show that the degradation due to Reed-Solomon code shortening in the concatenated coding system is small for moderate amounts of shortening. Even at a bit error rate of 10^{-6}, a code word length of less than 180 must be used before a loss of 0.1 dB exists. In fact, the loss due to shortening does not vary much with the bit error rate (at least for probabilities less than 10^{-4}). This is because the Reed-Solomon performance curve is almost a perfect exponential function in this region.

It is not known at this time how degradations in the receiver, subcarrier tracking loop, and symbol synchronizer may effect these results. It is also not known how node synchronization losses in Viterbi decoder (Ref. 5) or frame synchronization losses in the Reed-Solomon decoder (Ref. 6) will affect the performance of shortened codes. However, it seems that a small amount of shortening can be accommodated with only a negligible loss in overall system performance.

References

1. Layland, J. W., "Information Systems: Performance of Short Constraint Length Convolutional Codes and a Heuristic Code-Construction Algorithm," *Space Program Summary 37-64*, Vol. II, Jet Propulsion Laboratory, Pasadena, Calif., August, 1970.

2. Odenwalder, J. P., "Concatenated Reed-Solomon/Viterbi Channel Coding for Advanced Planetary Missions: Analysis, Simulations, and Tests," submitted to the Jet Propulsion Laboratory by Linkabit Corporation., San Diego, Calif., Contract No. 953866, December, 1974.

3. Miller, R. L., Deutsch, L. J., and Butman, S. A., *On the Error Statistics of Viterbi Decoding and the Performance of Concatenated Codes*, Publication 81-9, Jet Propulsion Laboratory, Pasadena, Calif., September, 1981.

4. Butman, S. A., Deutsch, L. J., Miller, R. L., "New Results on Antenna Arraying: Part One," *TDA Progress Report 42-62*, Jet Propulsion Laboratory, Pasadena, Calif., January and February, 1981.

5. Deutsch, L. J., and Miller, R. L., "Viterbi Decoder Node Synchronization Losses in the Reed-Solomon/Viterbi Concatenated Channel," *TDA Progress Report 42-71*, Jet Propulsion Laboratory, Pasadena, Calif., July-September, 1982.

6. Swanson, L., *A Comparison of Frame Synchronization Methods*, Publication 82-100, Jet Propulsion Laboratory, Pasadena, Calif., December, 1982.

ORIGINAL PAGE IS
OF POOR QUALITY

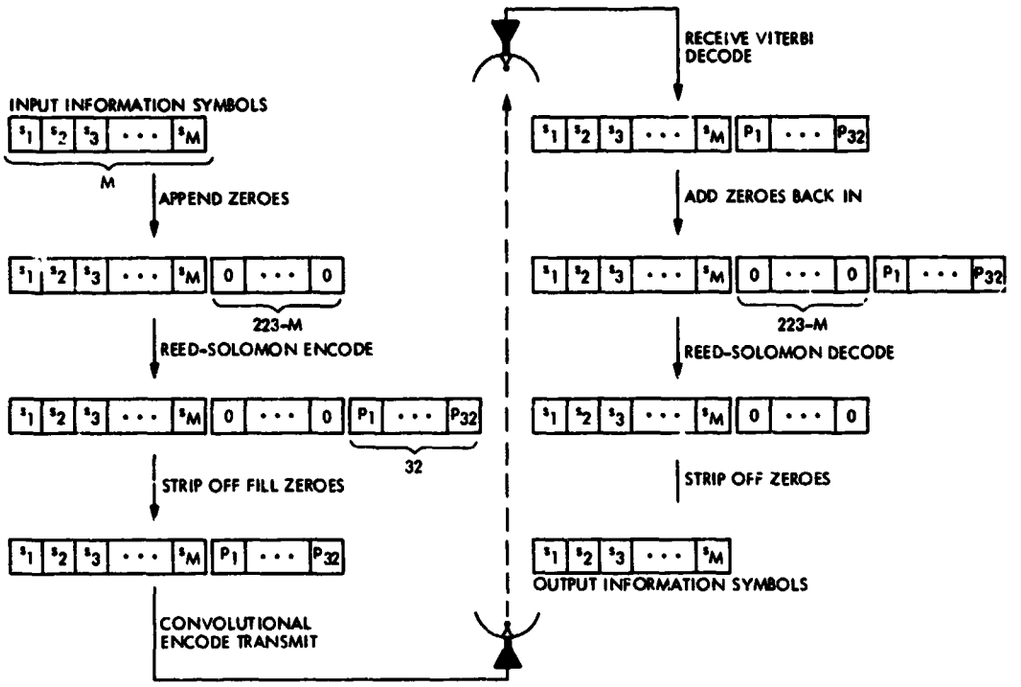

Fig. 1. An example of concatenated coding with Reed-Solomon code shortening

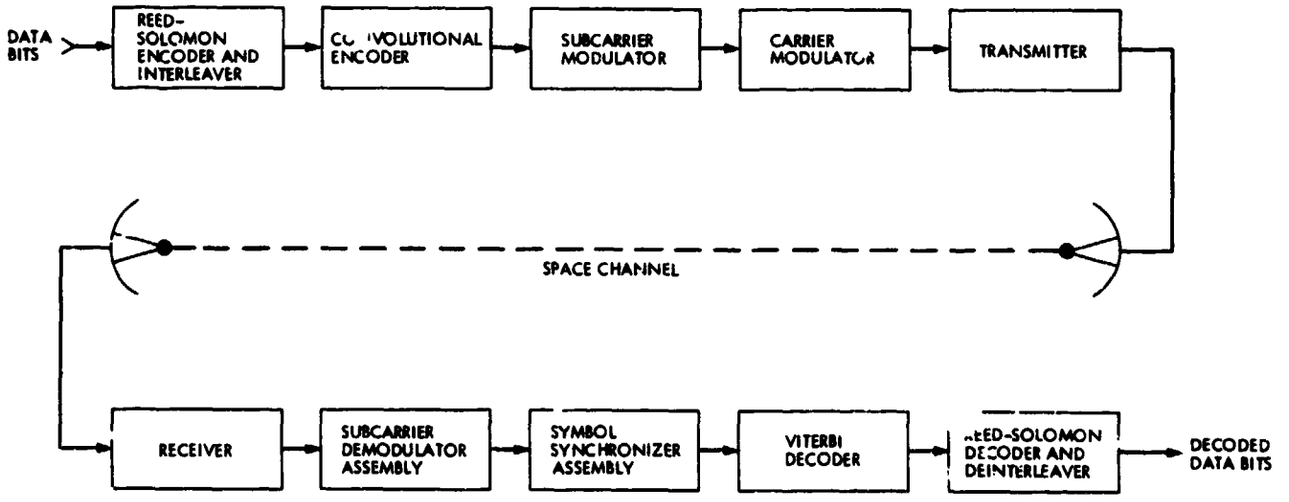

Fig. 2. Concatenated coding system block diagram

ORIGINAL PAGE IS
OF POOR QUALITY

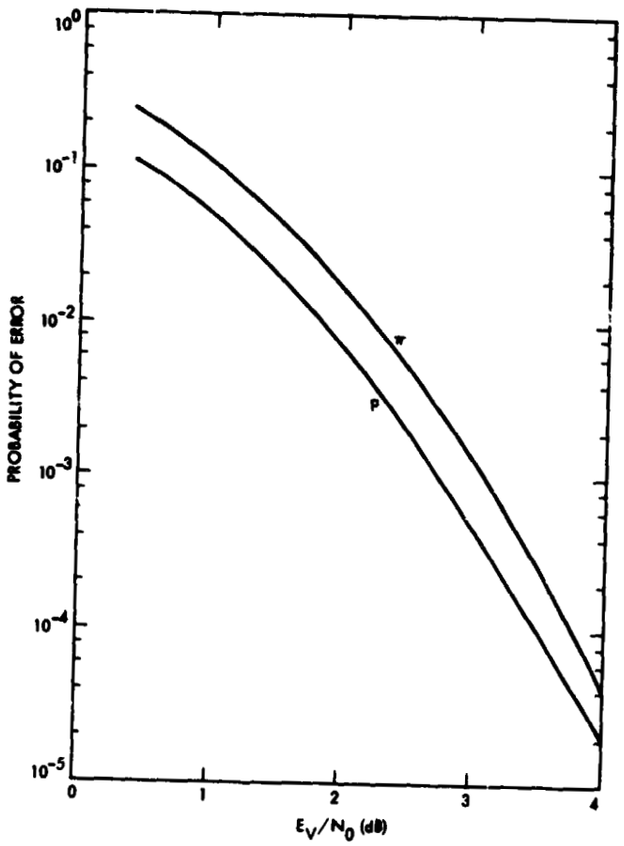

Fig. 3. Bit (p) and symbol (π) error rate performance of (7, 1/2) Viterbi decoder

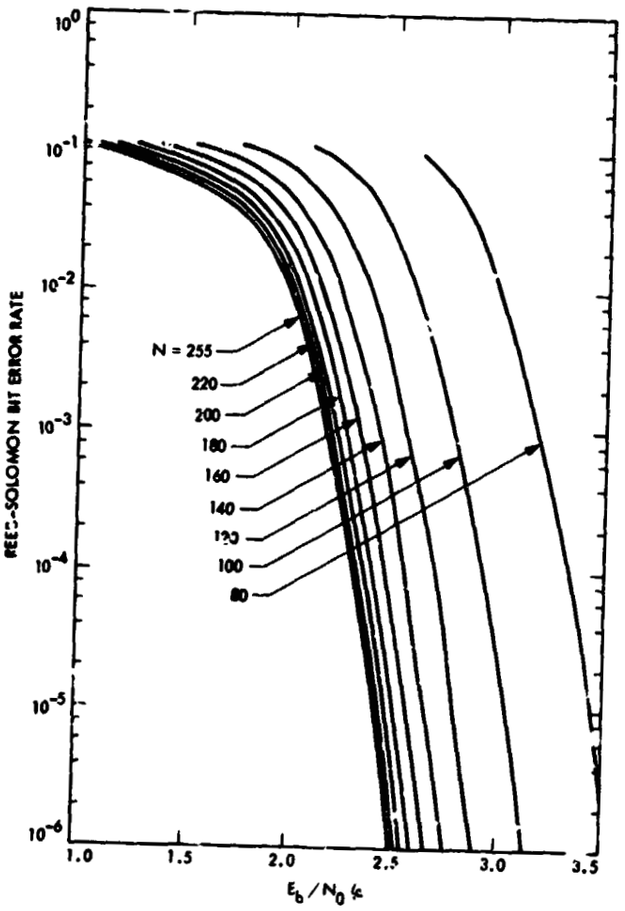

Fig. 4. Reed-Solomon bit error rate performance as a function of shortened code word length N

ORIGINAL PAGE IS
OF POOR QUALITY

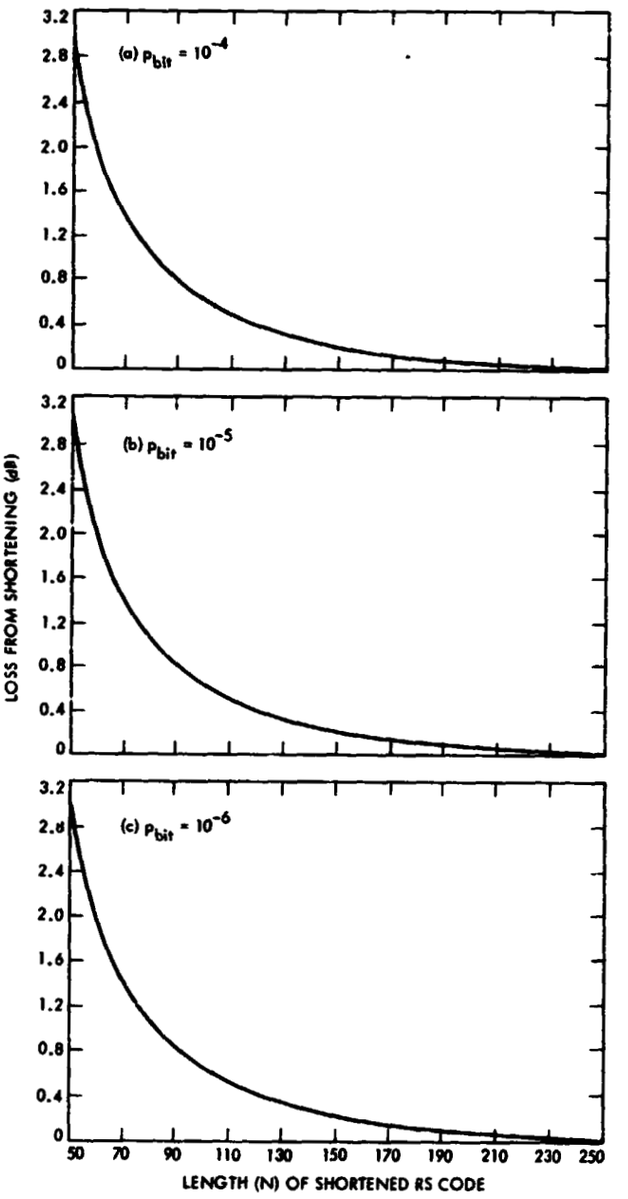

Fig. 5. Loss due to Reed-Solomon code word shortening

N84 13404

Detectors for Optical Communications: A Review

J. Katz
Communications Systems Research Section

The subject of detectors for optical communications in the visible and near-infrared regions of the spectrum is reviewed. The three generic types of detectors described are photomultipliers, photodiodes and avalanche photodiodes. Although the discussion is from the perspective of space-based applications, most of the information (excluding, perhaps, the material on photomultipliers) is applicable to other optical communications systems (e.g., fiber optics).

I. Introduction

The purpose of this paper is to describe three basic types of photodetectors which may be useful for the different channels of optical communications in the visible-near infrared region of the electromagnetic spectrum ($0.4\,\mu m \lesssim \lambda \lesssim 1.7\,\mu m$): Photomultiplier tube (PMT), photodiode (PD), and the avalanche photodiode (APD). These channels include both guided transmission (through optical fibers) and unguided transmission (e.g. among any combinations of spacecraft/satellites/airplanes/ground stations). The basic physical principle in all these detectors is the conversion of incoming photons directly into charge carriers. The detectors differ in the subsequent processing of the photo-generated carriers: In PMTs electrons are emitted into a vacuum tube which operates as an electron multiplier; in photodiodes the carriers (both electrons and holes) are swept out of the device into the subsequent amplifier circuit; and in APDs, generated carriers first undergo a random multiplication process within the device itself. Other detector types – both electronic and thermal – are not discussed here because of their speed and/or sensitivity limitations. The particular type of detector to be used depends on overall system considerations. PMTs, which are unique in their capability to detect individual photons, are the preferred choice in extremely low signal and low background noise channels. PDs can be used in heterodyne systems (where a local oscillator helps to overcome thermal noise) and in high background noise environments. Finally, APDs give better performance than PDs in systems which are thermal noise limited, and thus are used extensively in high-speed long-range optical fiber links.

In the following sections each of the three generic detector types will be described. Points to be discussed include the basic physical mechanism of operation, materials considerations and operational characteristics in terms of responsivity, noise, speed and limitations for space applications. Finally the last subsection will briefly review the subject of detector arrays which may be useful in acquisition/tracking/pointing subsystems of the communications link.

II. Photomultiplier Tubes (PMTs)

A. Principles of Operation

PMTs are the most sensitive detectors. In free space optical communications they should be used only under conditions

where they can produce a usable output to a single photon detection event. Only characteristics which are relevant to this operational mode will be discussed here. The generic structure of the PMT is shown in Fig. 1(a). It is basically an evacuated glass tube containing a photo-sensitive surface (photocathode), electron multiplier consisting of a chain of dynodes, and an output terminal (anode). Resistor bias network establishes positive potentials between each successive element of the PMT [Fig. 1(b)].

There are many types of PMTs. They differ by their size (PMTs with diameters ranging from roughly 1 to 50 cm are commercially available), structural arrangement and details of the photocathode and dynode chain, and materials of which they are fabricated. Special PMTs employ a magnetic field in addition to the electric field in order to reduce the temporal dispersion of the electrons, thus obtaining faster response. (These cross-field PMTs have lower gains than their all-electrostatic field counterparts.)

The photo-detection process in the PMT can be basically described as follows: a photon impinges upon the photocathode, and there is a certain probability (called "quantum efficiency") that a (primary) electron will be emitted. This electron (for larger light intensities several primary electrons can be emitted almost simultaneously) is focused and accelerated on the first dynode by the electric field established by the bias network. When it reaches the first dynode it has an energy of 200-500 eV, and it produces low-energy secondary electrons. (The characteristics of this process depend on the dynode material and on the primary energy.) These electrons are again focused and accelerated to the second dynode, where more electrons are emitted in a secondary emission process. This process is repeated at each dynode (there can be from several up to about 15 dynodes in a PMT), and as a result there is a large average number of electrons at the anode for each photoelectron emitted by the photocathode. It should be noted that there are some newer versions of PMTs where the electron multiplier is not a dynode chain but a microchannel plate (MCP). The inner walls of the channels of the MCP are coated with a material with a high secondary emission coefficient. The gain is thus distributed along the channels, and is usually smaller than that achievable with regular PMTs.

B. Basic Parameters

1. **Quantum efficiency**. Quantum efficiency (η) is a property of the photocathode of the PMT and is defined as the ratio of the number of photoelectrons emitted from the photocathode to the number of photons impinging upon it. The most popular class of photocathode materials is the multi-alkalis (Na-K-Sb-Cs) which has good response from the UV to near IR [Fig. 2(a)], with $\eta \simeq 20\%$ at $\lambda = 0.53\ \mu m$. The long wavelength response can be extended to 0.9 μm by special processing. GaAs activated in cesium is used in applications which require a higher sensitivity in the near IR. For this material $\eta \simeq 20\%$ at $\lambda = 0.8\ \mu m$ and $\eta \cong 25\%$ at $\lambda = 0.53\ \mu m$ in commercially available PMTs [Fig. 2(b)]. There are no photocathodes with good quantum efficiency for $\lambda > 1\ \mu m$. The only material is Ag-O-Cs, which has $\eta < 0.1\%$ at the Nd:YAG laser wavelength ($\lambda = 1.06\ \mu m$).

2. **Gain**. Gain (G) is the ratio of the number of electrons leaving the PMT anode to the number of photoelectrons emitted by the photocathode. Because of the statistical nature of the secondary emission process at each dynode, G is a random process. The probability density function of G has been calculated and found to be different from the Gaussian distribution, so it cannot be fully characterized only by its first two moments. Since in our application we want to be able to detect single photoelectron events, the magnitude of the average gain, $\bar{G}$, needed is determined by the condition that the peak current by a single electron response is larger than the RMS input current noise to the next stage of detection (e.g., pre-amplifier). This condition can be expressed as

$$\frac{q\bar{G}}{2t_r} \gg \sqrt{\frac{4KT_eB}{R}} \tag{1}$$

The term on the lefthand side of Eq. (1) is the approximate peak of the single photoelectron current pulse (t_r is the rise time of the PMT and q is the electron charge), and the term on the right hand side is the thermal (Johnson) noise current of the system to which the PMT is connected (K is Boltzman constant, B is the bandwidth, R is the input resistance and T_e is the equivalent noise temperature of the amplifier). For $B \simeq 1/t_r$, $R = 50\Omega$, and $T_e = 900$ K (corresponding to a typical commercial amplifier with a Noise Figure of 4.8 dB), Eq. (1) results in

$$\bar{G} \gg \frac{12500}{\sqrt{B\,[\mathrm{GHz}]}} \tag{2}$$

As an example, for $B = 140$ MHz (corresponding to $t_r \simeq 2.5$ ns), a PMT with $G \gg 3 \cdot 10^4$ is needed. This requirement can be easily met in commercially available PMTs which possess average gains of up to 10^6 to 10^7. For a given PMT, the average gain can be modified by varying the voltage V applied to it, approximately according to the following expression

$$\bar{G} = aV^b \tag{3}$$

where a and b are constants.

3. **Time response.** The time response of the PMT is characterized mainly by two parameters; both are affected by the dynode structure and the voltage applied to the PMT:

(1) Transit time is the delay between emission of a photoelectron from the photocathode and the instant when the anode output pulse reaches its peak amplitude. Typical transit times in regular PMTs are 10 to 100 ns (~1 ns for MCP-PMTs).

(2) Rise Time (t_r) is the time it takes the anode signal amplitude to rise from 10% to 90% of its peak value. Typical rise times are 2 to 20 ns for regular PMTs, and cross-field PMTs are up to an order of magnitude faster.

4. **Noise.** The relevant noise parameter in photon counting is the anode dark current, or, more specifically, the rate of dark counts. Since by using the high gain of the PMT we can virtually overcome effects of thermal noise in the system, the dark current is the only relevant system-generated noise (there are, of course, other noise sources, such as background radiation or the statistical nature of the signal radiation). The dark current increases with increasing PMT voltage.

Sources of dark current are:

(1) Thermionic emission of electrons from the photocathode: Since the rate of this process is proportional to $T^2\ e^{-E_W/KT}$ (where E_W is the work function of the photocathode material, and T is the absolute temperature), a modest amount of cooling of the PMT (to ~ -30°C) can virtually eliminate this mechanism.

(2) Unavoidable imperfections of the PMT: These include, for example, ionization of residual gases in the tube, field emission (mainly at high voltage levels), ohmic leakage and scintillation in the glass envelope or faceplate of the tube.

(3) Dark counts caused by Cherenkov radiation due to cosmic rays passing through the PMT faceplate (that part of the tube envelope facing the photocathode): This radiation is the ultimate lower limit of the dark current because cosmic rays can not be blocked. The flux of high energy cosmic rays is about $2 \cdot 10^{-2}$ cm^{-2}-sec^{-1} at sea level and about 1 cm^{-2}-sec^{-1} above earth atmosphere (exact values depend upon orientation of the PMT and other effects which are beyond the scope of this document). Each high energy particle can emit many photons (up to ~100) when passing through the PMT faceplate. Because of these large noise pulse levels, they can be effectively discriminated against the usually lower signal pulses.

C. Reliability

One of the major issues in using PMTs in space applications is their reliability. This issue is important when comparing PMTs to solid-state detectors, described later in this section, which have very long lifetimes. More and more data, albeit not under outer space conditions, are being accumulated mainly from particle physics experiments which use thousands of PMTs. Values of MTTFs (mean time to failure) are more than 2×10^7 hours for catastrophic failures (e.g., cracks in the glass envelope, short or open circuit of the electrodes) and $4 \cdot 10^6$ hours for partial failures (e.g., increased values of dark current, reduced photocathode quantum efficiency, gain drifts). These are long lifetimes even without taking into account the fact that, at least reliability-wise, a PMT can be considered as a system and not as a component. Of course, more testing needs to be done in order to evaluate PMT reliability in the space environment. It should be noted, however, that many space missions have included PMTs on board.

III. Photodiodes (PDs)

A. Principles of Operation

In contrast to PMTs, PDs are unity gain devices, i.e., there is no internal gain mechanisms in the device, so a subsequent electronic amplification of the resulting signal is always needed. The dominant detection process in PDs in our wavelengths region of interest is intrinsic absorption, schematically depicted in Fig. 3. Since this process involves a transition of an electron from the valence band to an unoccupied state in the conduction band of a semiconductor, the minimum photon energy required is Eg, the bandgap energy of the semiconductor, or

$$h\ \nu \gtrsim Eg \tag{4}$$

where h is Planck constant and ν is the frequency of the light radiation. Using $\nu = c/\lambda$ (c is the light velocity in vacuum), we obtain the cutoff wavelength λ_0, which is the longest wavelength that can be detected by intrinsic absorption (other absorption mechanisms are also possible but are of less relevance to our application):

$$\lambda_0\ [\mu m] = \frac{1.24}{Eg[eV]} \tag{5}$$

For $\lambda < \lambda_0$, the absorption coefficient α increases with decreasing wavelengths. The details of the $\alpha(\lambda)$ curve depend on the band structure of the specific semiconductor (including doping effects), on the temperature and on the electric field in the semiconductor (Franz-Keldysh effect). The lower limit on the wavelengths that can practically be detected is reached

when α is so large that most of the incoming photons are absorbed close to the surface, where several phenomena tend to reduce the efficiency of the detection process.

In order for the generated carriers (Fig. 3) to contribute to current in the external circuit, they have to be separated (otherwise they recombine). The usual method of obtaining this goal is to construct the detector as a pn diode. Thus carriers which are generated either in the depletion region, or roughly within one diffusion length from it will contribute to the photogenerated current. The pn diode is operated in a reverse bias, which improves the diode performance in terms of linearity, speed of response and quantum efficiency.

For high speed applications, two generic diode structures are used: PIN diode (Fig. 4) and Schottky diode (Fig. 5). In the PIN PD (Fig. 4) the region where most of the light is absorbed (I, or intrinsic, region) is designed to have low doping level, thus resulting in a fairly uniform electrical field in that region. The diode bias voltage is chosen such that the peak field (i.e., at the junction itself) is lower than the value needed for avalanche multiplication, and the field magnitude at the other edge of the intrinsic region is sufficiently large to maintain saturation drift velocity of the carriers. This assures the minimum possible transit time (see Section III.B) and thus helps to optimize the PD temporal response. The Schottky PD (Fig. 5) has a simpler structure: In its most basic structure it consists of a semiconductor on which a thin film ($\lesssim 500$ Å) of metal is deposited. Schottky PDs usually have lower quantum efficiency than PIN PDs, but they have faster response and extended response towards the short wavelengths region.

B. Basic Parameters

1. **Quantum efficiency**. Quantum efficiency (η) is defined as the ratio of the number of charge carriers contributing to the current (i_{ph}) and the number of photons impinging upon the diode surface per second.

$$\eta = \frac{i_{ph}/q}{P/h\nu} = \frac{hc}{q\lambda}\frac{i_{ph}}{P} \tag{6}$$

where P is the optical power. An ideal photodiode has $\eta = 1$ (or 100%), and practical PDs approach this ideal value. A related parameter is the *responsivity*, $\mathscr{R}$, of the photodiode, which has units of Ampere/Watt. The relation between η and $\mathscr{R}$ is

$$\eta = \frac{1.24\,\mathscr{R}\ [\text{A/W}]}{\lambda\ [\mu\text{m}]} \tag{7}$$

η (and $\mathscr{R}$) depends upon the diode material, structure, wavelength and temperature. Among the things done in order to optimize the structure of the PD are tailoring the depletion region to overlap as much as possible with the region where most of the light is absorbed (subject to speed constraints) and employing antireflection coating on the photosensitive surface of the PD (see Fig. 4).

2. **Speed of response**. Speed of response is determined by the combination of the following time constants:

(1) Carrier drift time in the depletion region, which is proportional to the width of the region and inversely proportional to the carrier velocity.

(2) Diffusion time constant of minority carriers which are generated within approximately one diffusion length from the depletion region.

(3) *RC* time constant associated with the diode shunt capacitance and series resistance (including contributions from the diode itself, and from the diode housing, wires and other parasitics). This time constant can be minimized by reducing the diode area and fabricating it on semi-insulating substrates (in GaAs).

A general rule of thumb is to minimize the diffusion time constant and to design the transit time to be approximately equal to the *RC* time constant. Usually there is a tradeoff between speed of response and the quantum efficiency. Both PIN and Schottky diodes with frequency response exceeding 20 GHz (and rise-times of 35 ps) have been demonstrated in the laboratory and some are commercially available. Recently a GaAs Schottky PD with a 3 dB bandwidth of 100 GHz has been demonstrated.

3. **Noise in PDs**. A typical detector circuit is shown in Fig. 6a, and the equivalent circuit, including all the noise sources, is shown in Fig. 6b. The signal source is given by

$$i_s = \frac{\eta q \lambda}{hc} P_s \tag{8}$$

where P_s is the optical power impinging upon the diode. The noise sources, are:

(1) The diode equivalent circuit contains three white spectrum shot-noise current sources which originate from carriers generated by signal photons $\left(\overline{i_s^2}\right)^{1/2}$, background photons $\left(\overline{i_b^2}\right)^{1/2}$, and dark current $\left(\overline{i_d^2}\right)^{1/2}$ (which is caused by generation recombination process in the depletion region, minority carrier diffusion and surface leakage). These three current sources are given by

$$\overline{i_s^2} = 2\frac{q^2\eta}{h\nu} P_s B \qquad [A^2] \tag{9a}$$

ORIGINAL PAGE IS
OF POOR QUALITY

$$\overline{i_b^2} = 2\frac{q^2\eta}{h\nu} P_b B \qquad [A^2] \qquad (9b)$$

$$\overline{i_d^2} = 2 q i_d B \qquad [A^2] \qquad (9c)$$

where P_b is the background optical power.

(2) The bias and load resistances have a white spectrum thermal (Johnson) noise current source given by

$$\overline{i_{th}^2} = \frac{4KTB}{R_e} \qquad (10)$$

with R_e as the parallel combination of R_B and R_L.

(3) Since PDs are virtually always followed by an amplifier, its noise has to be taken into account. There are two main types of front-end amplifiers.

The first type is the transimpedance amplifier, shown on Fig. 7(a), where the thermal noise contribution is mainly determined by the feedback resistance R_f. The second type is the high impedance amplifier, whose first stage, which determines the overall behavior of the amplifier, is made of either a field-effect transistor (FET) (Fig. 7(b)) or a bipolar junction transistor (BJT). In the case of an FET, $\left(\overline{i_a^2}\right)^{1/2}$ [Fig. 6(b)] can be neglected. The voltage noise source is given approximately by

$$\overline{v_a^2} \simeq \frac{2.8KTB}{g_m} \qquad [V^2] \qquad (11)$$

where g_m is the FET transconductance. This noise source can be transformed into an equivalent noise source which appears in parallel to the PD noise sources and replaces all the other noise sources $\left(\text{i.e., } \overline{i_{th}^2}, \overline{v_a^2}\right)$:

$$\overline{i_{th}'^2} = \frac{4KTB}{R_e} + \frac{2.8KTB}{g_m} \times \left[\frac{1}{R_e^2} + \frac{[2\pi(C_d + C_L)]^2 B^2}{3}\right] \qquad [A^2] \qquad (12)$$

where C_d and L_L are the diode and the load capacitances, respectively. From Eq. (12) we see that low capacitances are important not only for high frequency but also for low noise performance.

For the BJT front-end amplifier we have

$$\overline{i_a^2} = \frac{2KTB}{r_e} \qquad (13)$$

$$\overline{v_a^2} = \frac{2KTB}{\beta} r_e \qquad (14)$$

where r_e is the AC input resistance of the BJT and ($r_e \simeq KT/qI_B$) and β is its current gain. As in the case with a FET, the amplifier noise dominates for large values of R_e. For the BJT high-impedance front-end amplifier there is an optimum bias point which yields the following value of the BJT thermal noise:

$$\overline{i_{th,\min}^2} = 4KTB \cdot \frac{2\pi(C_d + C_L)B}{\sqrt{3\beta}} \qquad (15)$$

By comparing Eqs. (12) and (15) we see that BJTs are better than FETs in high frequency operation (B^2 vs. B^3 dependence). The reason is that the transconductance of the FET is basically fixed, while that of the BJT can be increased by varying the bias point.

The signal to noise ratio at the PD-amplifier combination is found by combining Eqs. (8), (9) and (12) or (15)

$$\frac{S}{N} = \left(\frac{\eta q \lambda}{hc}\right)^2 \frac{P_s^2}{\left[2q(i_s + i_b + i_d) + \frac{4KT_e}{R_e}\right]B} \qquad (16)$$

where T_e is an equivalent noise temperature which depends on the circuit bandwidth, and whose value can be found from Eq. (12) or (15).

As an example, consider a PD/FET combination with the following parameters: T = 300 K, λ = 0.85 μm, P_s = 0.1 μW, i_d = nA, i_b = 0, B = 100 MHz, $(C_d + C_L)$ = 1 pF, R_e = 10 KΩ, g_m = 10 mS and η = 0.8. These parameters are achievable with a careful design (including hybrid or monolithic integration of the PD and the FET). Under these conditions the major noise mechanism is still the thermal noise of R_e. The resulting signal to noise ratio is $S/N \simeq 4.1$. The S/N can be improved by increasing R_e. Postamplification equalization is usually employed with these high-impedance (integrating) amplifiers.

An important parameter characterizing the overall sensitivity of the PD (and any detector) is the Noise Equivalent

Power (*NEP*) (or its inverse, *Detectivity*, $D \equiv 1/NEP$) which is the optical signal power for which $S/N = 1$. Dimensions of the *NEP* are Watt/$\sqrt{\text{Hz}}$. In many cases the Detectivity is normalized to the area of the detector and is denoted by D^*:

$$D^* \equiv D\sqrt{\text{Area}} \quad [\sqrt{\text{Hz}}\text{-cm/W}] \tag{17}$$

For optical communications, D^* is usually not a relevant parameter since the light distribution on the PD is not uniform. In addition, contribution from peripheral leakage currents in small-area PD does not scale as the area. Typical *NEP* of commercially available Si PDs (at their peak wavelength) is 10^{-14} to 10^{-13} W/$\sqrt{\text{Hz}}$ (corresponding D^* are approximately $0.5\text{-}5 \cdot 10^{12}$ cm-$\sqrt{\text{Hz}}$/W).

C. Materials Considerations

1. **Silicon**. Silicon (Si) is by far the preferred material because it is technologically the most mature. With an indirect bandgap of 1.1 eV it can be used for the wavelength region $0.4\ \mu\text{m} \lesssim \lambda \lesssim 1.1\ \mu\text{m}$, although special structures have to be used in order to extend the efficient range of operation beyond 1 μm. Quantum efficiencies at the peak wavelengths (0.8 to 0.9 μm) can exceed 80%. Quantum efficiencies of ~60% are available at the Nd:YAG laser wavelength (1.06 μm) and its second harmonic (0.53 μm). Dark currents are as low as 0.1 nA in commercially available Si PDs.

2. **Germanium**. Germanium (Ge) which can cover the $0.8\ \mu\text{m} \lesssim \lambda \lesssim 1.7\ \mu\text{m}$ region has the disadvantage of very high dark currents due to its smaller bandgap and higher surface recombination. Dark currents are typically 3 orders of magnitudes more than in Si. Quantum efficiencies are comparable to Si.

3. **GaAs**. GaAs basically covers approximately the same wavelengths region as Si ($0.4\ \mu\text{m} \lesssim \lambda \lesssim 0.9\ \mu\text{m}$), and thus it is used less extensively. The advantage of GaAs is that semi-insulating substrates are available, and thus devices with very low capacitance can be fabricated on the structures. Very fast Schottky PDs made in this fashion have been recently demonstrated. Other advantages of GaAs are its higher radiation resistance (20 to 30 times more than silicon) and its ability to operate at higher temperatures (because its bandgap is larger than in silicon) – both properties which are especially important in space application.

4. **Ternary and Quarternary Components/Hetrojunctions**. Different combinations of materials from the GaAlAs, InGaAsP and GaAlAsSb systems can be utilized to make PDs which can span at least the $0.6\ \mu\text{m} \lesssim \lambda \lesssim 1.7\ \mu\text{m}$ region. Once these materials and their fabrication processes become more technologically mature, PDs will have excellent performance characteristics. By including heterostructures in these materials, one could separately tailor the quantum efficiency of the PD, its spectral response and the speed of response. Thus $\eta \gtrsim 0.95$ is achievable even at high speed operation and at selected regions of the spectrum. Today performance of these PDs is better than Ge, but somewhat worse than Si, in particular in terms of higher dark currents.

IV. Avalanche Photo-Diodes (APDs)

A. Principles of Operation

The Avalanche Photo-Diode (APD) is a photodiode which contains an additional region where the photogenerated carriers are multiplied via the avalanche process. In this multiplication region the electric field is very high (several times 10^5 V/cm). Carriers are accelerated by the field, and upon acquiring enough kinetic energy (approximately 1.5 E_g) they can create new carrier-pairs by impact ionization. As this process repeats itself, more carriers are generated, which is an effective amplification process, as depicted schematically in Fig. 8.

A structure of a common version of an APD (Reach-Through APD) and the electric field distribution across it are shown in Fig. 9. The incoming light is absorbed mostly in the low doped (π) region. in a similar way to the drift region in a PIN diode. Holes are swept out the p-contact, and electrons enter the high field region near the np junction where the multiplication process takes place. As we will now see, it is important which type of carrier (electrons or holes) enters the multiplication region. The basic reason is electrons and holes have different ionization coefficients in a given material.

The ionization coefficient, denoted by α_n (for electrons) or α_p (for holes) is defined as the number of ionizing collisions per unit length for each carrier. Both α_p and α_n are strong functions of the electric field $\mathscr{E}$, and they are expressed by the empirical formula

$$\alpha_n = A_n e^{-(B_n/\mathscr{E})^u} \tag{18a}$$

$$\alpha_p = A_p e^{-(B_p/\mathscr{E})^u} \tag{18b}$$

where A_n, A_p, B_n, B_p, and u are material parameters. The ratio between the ionization coefficients

$$k \equiv \frac{\alpha_p}{\alpha_n} \tag{19}$$

ORIGINAL PAGE IS
OF POOR QUALITY

(which by itself depends on the electric field) is a key parameter of the APD. $k = 0$ (or $1/k = 0$) means that only electrons (or only holes) can create secondary pairs via impact ionization. In this case, and assuming constant electric field in the multiplication region, the gain M is given by

$$M_{p,n} = e^{\alpha_{p,n} W} \tag{20a}$$

where W is the width of the multiplication region. The other extreme case is when $\alpha_p = \alpha_n$. Now the multiplication process is influenced by feedback mechanisms, and the resulting expression for the gain is

$$M_{p,n} = \frac{1}{1 - \alpha_{p,n} W} \tag{20b}$$

For general values of k we obtain

$$M_n = \frac{\left(1 - \frac{1}{k}\right) e^{\alpha_p W \left(1 - \frac{1}{k}\right)}}{1 - \frac{1}{k} e^{\alpha_p W \left(1 - \frac{1}{k}\right)}} \tag{21a}$$

and

$$M_n = \frac{(1-k)\, e^{\alpha_n W (1-k)}}{1 - k\, e^{\alpha_n W (1-k)}} \tag{21b}$$

When we can not assume a constant electric field in the multiplication region, the expressions are more complicated. In order to avoid numerical calculations, we define effective values so that

$$\int_{x_1}^{x_2} \alpha_{p,n}\, dx \equiv \overline{\alpha_{p,n}} \cdot \overline{W_a} \tag{22a}$$

$$\overline{k_1} \equiv \overline{\alpha_p} / \overline{\alpha_n} \tag{22b}$$

and

$$\overline{W_a} \equiv x_2 - x_1 \tag{22c}$$

where $\{x_1, x_2\}$ is the interval which contributes significantly to the multiplication process (i.e., the high-field region).

Inspection of Eqs. (21) shows that in order for the gain to be less sensitive to minor field variations, those carriers which have a higher ionization coefficient should be injected into the multiplication region. As we will see later, the k-parameter is very important in determining the noise characteristics of the APD. It should be noted that $\alpha_{p,n}$ represents average parameter values of the impact ionization process, and thus the gain mechanism of the APD is a random process. In Fig. 10 we see an example of the probability density function for the number of electrons leaving the multiplication region. It is interesting to note that even for high multiplication values, M, the most probable event is less than the average value.

B. Basic Parameters

1. Gain. Gain, or multiplication factor, M, of the APD is basically defined as the ratio of the actual current of the APD to the current that would have flown if no impact-ionization processes took place. The gain varies with the applied reverse voltage V_D on the APD approximately according to the empirical formula

$$M = \frac{1}{1 - \left(\frac{V_D}{V_B}\right)^u} \tag{23}$$

where V_B is the breakdown voltage of the diode and u is an empirical constant. As we will see later, the actual value of M is chosen to optimize the signal to noise ratio of the APD. These values are of the order of 100. In addition, there is a limit to the maximum gain that can be obtained from an APD in a regular bias circuit. Since

$$V_D = V_{KK} - I_D R_B \tag{24}$$

where V_{KK} is the voltage of the bias network, I_D is the APD current and R_B is the bias resistor, and

$$I_D = M(i_{ph} + i_d) \tag{25}$$

where i_{ph} and i_d are the photo-generated and the dark currents, respectively (before multiplication), then by setting V_{KK} to its maximum allowable value $V_{KK} = V_B$, using Eqs. (14) and (25) in Eq. (23) we obtain the maximum multiplication:

$$M_{\max} = \left[\frac{V_B}{(i_{ph} + i_d) R_B u}\right]^{1/2} \tag{26}$$

From Eq. (26) we can see the importance of reducing the dark current of the APD. In addition, we see the saturation effects caused by the signal that can introduce distortions which are

ORIGINAL PAGE IS
OF POOR QUALITY

of great concern in analog applications. Typical operating gains of APDs are 100 to 500.

2. **Time response.** There are two basic limitations on the time response of APDs. At high multiplication factors, the time constant associated with the avalanche process is the dominant one. Because of the feedback effects (which are due to non-zero k values), this time constant is proportional to M. Thus at the high gain region the gain-bandwidth product is constant, given by

$$M_{p,n}(0)\,B \simeq \frac{1}{2\pi\chi\,\tau_a\,k,(1/k)} \tag{27}$$

where $M_{p,n}(0)$ is the DC value of the multiplication, τ_a is the effective transition time of carriers in the multiplication region, and χ is a slowly varying function of $k(1/k)$ (e.g., $\chi(1) = 1/3, \chi(10^{-3}) = 2$).

At low multiplication factors,

$$M(0) \ll \frac{W_d}{3\,k\,\chi\,W_a} \tag{28}$$

(where W_d is the width of the drift region), the dominant constraint is the drift time, similar to the PIN PD. Thus in this region the bandwidth is constant, and the gain-bandwidth product increases linearly with M:

$$M(0)\,B \simeq M(0) \cdot \frac{v_n}{2\,W_d} \tag{29}$$

where v_n is the drift saturation velocity of the electrons. The overall behavior of the gain-bandwidth product is shown in Fig. 11 for typical APD parameters: $(\tau_a\ \chi\ k) = 5 \cdot 10^{-13}$ s, $W_d = 50\ \mu$m and $v_n = 10^7$ cm/s. Since the gain of the PMT is usually determined from noise considerations, the bandwidth is determined by it too. Typical rise times are 0.1 to 1 ns, and typical gain-bandwidth products are 100 to 200 GHz.

3. **Noise.** The random nature of the gain process in the APD and in particular the feedback effects resulting from non-zero k values (i.e., both carrier types can initiate impact-ionization) cause an additional noise mechanism, called "Excess Noise," which increases at a faster rate than the rate at which the signal is amplified with increasing values of gain M. The excess noise prevents us from operating the APD at very high M values and thus virtually overcoming the effects of thermal noise, as is the case of PMTs.

Using basically similar analysis to that done for the PD, the expression for the signal to noise ratio of the APD is given by

$$\frac{S}{N} = \left(\frac{\eta q \lambda}{hc}\right)^2 \times \frac{(M P_s)^2}{\left\{2q\,(i_s + i_b + i_d - i_{ds})\,M^2\,F + \left[2q\,i_{ds} + \dfrac{4\,K\,T_e}{R_e}\right]\right\} B} \tag{30}$$

where i_{ds} is that component of the dark current that does not flow through the avalanche region and thus does not get multiplied (e.g., surface leakage current) and F is the excess noise factor of the APD which denotes the additional noise above that which is due to amplified shot-noise alone. (The other terms in Eq. (30) are explained in conjunction with Eq. (16).) F is a function of both k and M.

The excess noise factor for pure electron injection into the multiplication region is given by:

$$F_n = M_n - (1 - k)\frac{(M_n - 1)^2}{M_n} \xrightarrow[M_n \gg 1]{} kM_n \tag{31a}$$

and similarly for holes

$$F_p = M_p - \left(1 - \frac{1}{k}\right)\frac{(M_p - 1)^2}{M_p} \xrightarrow[M_p \gg 1]{} \frac{1}{k}\,M_p \tag{31b}$$

For $k = 1$, $F_n = F_p = M$, and for $k, (1/k) = 0$, $F_n = F_p = 2$. Generally, for a given operating region, F is sometimes approximated by

$$F = M^x \tag{32}$$

where x is a non-ideality factor.

From Eq. (30) we see that an ideal APD (i.e., $k(1/k) = 0$) can operate, in principle, like a PMT: By increasing M we can eliminate effects of thermal noise. However, in real APDs, the shot-noise is amplified more than the signal, so the optimum operating point M_{opt} is not at $M \to \infty$ but when the two noise terms in the denominator of Eq. (30) are equal. For a signal limited shot-noise, and assuming $F = kM$, we obtain

$$M_{opt} = \left[\frac{2\,k\,T_e}{q} \cdot \frac{h\,c}{\eta\,\lambda\,k} \cdot \frac{1}{R_e\,P_s}\right]^{1/3} \tag{33}$$

M_{opt} depends on the excess noise, load resistor and signal levels. In many applications we cannot neglect the dark and background currents. In this case the expressions become more complicated, though the calculations are straightforward. Figure 12 shows a graph of an *NEP* of an APD vs *M*. The optimum operating point is clearly seen. For lower values of *M* the thermal noise dominates, and for higher values of *M* the excess noise dominates. Typical values of *NEP* for Si APDs are of the order of 10^{-14} W/$\sqrt{\text{Hz}}$ in the near infrared region. Typical values of total dark current are 0.1 to 1 μA, which is mainly due to surface currents.

C. Materials Considerations

Wavelengths of operation, quantum efficiencies and dark currents for different materials are basically the same for PDs and APDs. For a brief review on these aspects the reader is referred to Section III.C. The material parameter that is unique to the APD operation is $k \equiv \alpha_p/\alpha_n$. Table 1 lists this factor for various materials. We see that for all the materials considered to be used in optical communications $0.01 \lesssim k \lesssim 100$. For $\lambda \lesssim 1.1$ μm silicon is the best material for APDs also from the excess noise factor aspect. The basic problem in APD technology today is that good materials which can be used for $\lambda \gtrsim 1.1$ μm (i.e., where Si can no longer be used) have $k(1/k)$ factors which are too close to 1, which implies large excess noise factors. Some novel structures have been devised to overcome this limitation by using heterostructure devices where the dynamics of electrons and holes can be separately controlled, thus yielding effective *k*-values which are much larger than the bulk values. In certain atomic systems (e.g., GaAlSb) one could also possibly utilize certain details of the band structure in order to enhance the *k*-factor.

D. The APD as a Solid State PMT

Under certain conditions, APDs can be operated in a "geiger-tube" mode so that they can respond to single electron events and thus can be used as photon counters. In order to operate in this mode, the APD must be cooled to liquid nitrogen temperatures in order to reduce the dark current (to approximately 100 electrons/s or less). The diode is biased at a voltage level above the avalanche breakdown voltage (which is lower than the dielectric breakdown voltage of the APD) by an amount of up to several tens of volts. A single carrier, which is either photo or thermally generated, has a high probability of causing sustained avalanche. At this point the diode voltage drops to the avalanche breakdown voltage, thus producing a voltage pulse whose magnitude is the difference between the bias and the avalanche voltages. This pulse can be easily detected without any further amplification. Then the avalanche has to be quenched and the device is ready for a new detection event. Since quantum efficiencies of solid-state detectors are higher than those of PMTs, and since for relatively high over-bias the probability that a single carrier will generate sustained avalanche is high (up to 50%), APDs operating in this mode may be an attractive alternative to PMTs, especially with the added bonus of their improved size, ruggedness and reliability.

V. Detector Arrays

In order to perform beam pointing, acquisition and tracking optically, it is necessary to use an optical detector that provides some position information from the received light signal. This information can be derived from single detectors ("position sensors"), small arrays, (e.g., quadrant detectors) or large arrays (e.g., CCD arrays) which are usually used for imaging but can also be used to perform functions such as one-step acquisition.

A. Position Sensors

Position sensors are usually PIN PDs with relatively large areas (~1 cm^2). Photogenerated current is collected from four electrodes, which are placed in pairs across opposite edges of the detector area. The position of the received light spot on the detector can be determined from the relative magnitudes of the currents at the individual electrodes. The absolute position accuracy in this device is very coarse (±10% approx.) but it can detect very minute changes in the position (on the order of

$$\Delta x[\text{Å}] \simeq \sqrt{\Delta f[\text{Hz}]/P_s[\mu\text{W}]}$$

where Δf is the system bandwidth).

B. Small Arrays

Solid state quadrant detectors are available in PDs and APDs. The common application of this segmented detector is to detect position deviations from the optical axis of a system, and thus they are best suited to perform tracking functions. Changes of the order of

$$\Delta x[\text{Å}] \simeq \sqrt{\Delta f[\text{Hz}] \times \text{spot area } [\text{cm}^2]/P_s[\text{W}]}$$

can be detected with quadrant detectors.

MCP-PMTs (see Section II.A) can utilize the fact that spatial information is preserved in the MCP amplification. PMTs with several anodes are available (from 4 X 4 to approximately 20 X 20 anode arrays). Several hundreds of photoelectrons are needed in order to achieve optimum performance in

terms of spatial resolution. For the 4 X 4 anode arrays $\Delta x \sim$ 0.2 mm which is about 1% of the photocathode area.

C. Large Arrays

Large arrays are usually used for imaging, similar to TV tubes. The most common type are CCD arrays, which are arrays of PDs which contain, on the same chip, a mechanism for charge read-out, similar to a "bucket-brigade" operation. A detailed description of CCD arrays is beyond the scope of this paper. These devices are made of silicon, so the quantum efficiency is comparable to Si PDs. There are additional noise mechanisms associated with the read-out process. Under optimized conditions (cooling to 77 K and readout at an optimum rate) RMS noise levels corresponding to 10 electrons per CCD cell can be achieved. Array sizes up to 800 X 800 cells are available.

Acknowledgment

The following figures were reprinted or adapted by permission:

Figs. 1(a), 2(a): Engstrom, R. W., "RCA Photomultiplier Handbook," RCA Corp., Lancaster, Penn. (1980);

Figs. 1(b), 2(b), 9: Various (uncopyrighted) RCA data sheets;

Figs. 4(a), 5(a), 6, 7(a), 8, 11, 12: Muller, J., "Photodiodes for Optical Communications," in *Advances in Electronics and Electron Physics, 55*, Marton and Marton, Editors, Academic Press, New York (1981);

Fig. 10: McIntyre, R. J., "The Distribution of Gains in Uniformly Multiplying Avalanche Photodiodes: Theory," IEEE Trans. Electron. Dev. *ED-19*, pp. 702-713 (1972).

Bibliography

General

Yariv, A., "Introduction to Optical Electronics," 2nd Edition, Holt, Rinehart and Winston, New York (1976) (Chapters 10, 11).

Photomultipliers

Boutot, J. P., Nussli, J., and Vallat, D., "Recent Trends in Photomultipliers for Nuclear Physics" in *Advances in Electronics and Electron Physics*, Vol. 60, P. W. Hawkes, Editor, Academic Press, New York (1983).

Engstrom, R. W., "Photomultiplier Handbook," RCA Corp., Lancaster, Penn. (1980).

Reisse, D., Creecy, R., and Poultny, S. K., "Single Photon Detection and Sub-Nanosecond Timing Resolution with the RCA C31034 Photomultiplier," Rev. Sci. Instru. *44*, pp. 1666-1668 (1973).

Shockley, W., and Pierce, J. R., "A Theory of Noise for Electron Multipliers," Proc. IRE, *26*, pp. 321-333 (1938).

Tan, H. H., "A Statistical Model of the Photomultiplier Gain Process with Applications to Optical ... se Detection," *TDA Progress Report 42-68*, pp. 55-67, Jet Propulsion Laborat... asadena, Calif. (1982).

Young, A. T., "Photomultipliers: Their Cause and Cure," Chapter 1 in *Methods of Experimental Physics*, Vol. 12, Part A, N. Carleton, Editor, Academic Pre... New York (1974).

Photodiodes and Avalanche Photodiodes — General

Capasso, F., Tsang, W. T., and Williams, G. F., "Staircase Solid-State Photomultipliers and Avalanche Photodiodes with Enhanced Ionization Rates Ratio," IEEE Trans. Electron. Dev. *ED-30*, pp. 381-390 (1983), and references therein.

Melchior, H., "Detectors for Lightwave Communication," in *Physics Today*, Nov. 1977, pp. 32-39.

Müller, J., "Photodiode for Optical Communications," in *Advances in Electronics and Electron Physics, 55*, Marton and Marton, Editors, Academic Press, New York (1981).

Stillman, G. E., and Wolfe, C. M., "Semiconductors and Semimetals," *12*, Academic Press, New York (1977).

Sze, S. M., *Physics of Semiconductor Devices*, 2nd Ed., Wiley Interscience, New York (1981) (Chapter 13).

Wang, S. Y., and Bloom, D. M., "100 GHz Bandwidth Planar GaAs Schottky Photodiode," Electron Lett., *19*, pp. 554-555 (1983).

Webb, P. P., McIntyre, R. J., and Conradi, J., "Properties of Avalanche Photodiodes," RCA Rev., *35*, pp. 235-278 (1974)

Avalanche Photodiodes Statistics

Ingerson, T. E., Kearney, R. J., and Coulter, R. L., "Photon Counting with Photodiodes," Appl. Opt. *22*, pp. 2013-2018 (1983), and references therein.

McIntyre, R. J., "Multiplication Noise in Uniform Avalanche Diodes," IEEE Trans. Electron. Dev., *ED-13*, pp. 164-168 (1966).

McIntyre, R. J., "The Distribution of Gains in Uniformly Multiplying Avalanche Photodiodes: Theory," IEEE Trans. Electron Dev., *ED-19*, pp. 703-713 (1972).

Personick, S. D., "New Results on Avalanche Multiplication Statistics with Applications to Optical Detection," Bell Sys. Tech. J., *50*, pp. 167-189 (1971).

Personick, S. D., "Statistics of a General Class of Avalanched Detectors with Applications to Optical Communication," Bell Sys. Tech. J., *50*, pp. 3075-3095 (1971).

ORIGINAL PAGE IS
OF POOR QUALITY

Table 1. Ionization coefficient parameters of several semiconductors

Material	Parameters of Eq. (18)					k =	
	A_n	A_p	B_n	B_p			
	cm^{-1}	cm^{-1}	V/cm	V/cm		Low	n
	$\times 10^6$	$\times 10^6$	$\times 10^6$	$\times 10^6$	u	field	ield
Si	3.8	2.25	1.75	3.26	1	0.02	0.1
Ge	15.5	1	1.5	1.28	1	10	2
GaAs	12	360	2.3	2.9	1	3	5
GaSb	3.2	300	0.36	0.55	1	0.5	>1
InP	2000	30	1.5	2.5	1	0.2	0.4
InAs						10	20
GaAlSb	0.104	0.19	0.41	0.41	2	2	2
$Ga_xIn_{1-x}As$							
$x = 0.14$	1000	130	3.6	2.7	1	2	
$x = 0.2$						50	
$x = 0.47$						0.2	
GaAsSb	0.15	0.11	0.64	0.72	1	0.4	0.7
InGaAsP						0.3	>1

ORIGINAL PAGE IS
OF POOR QUALITY

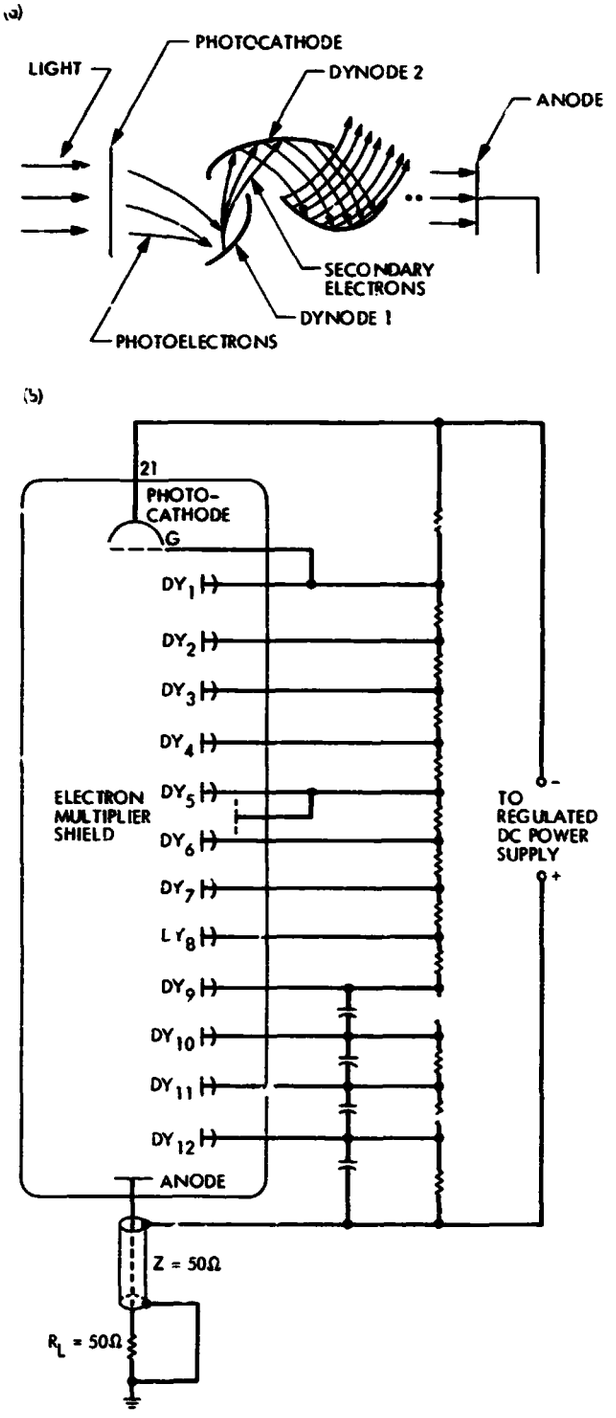

Fig. 1. Photomultiplier tube: (a) schematic structure; (b) including bias circuit

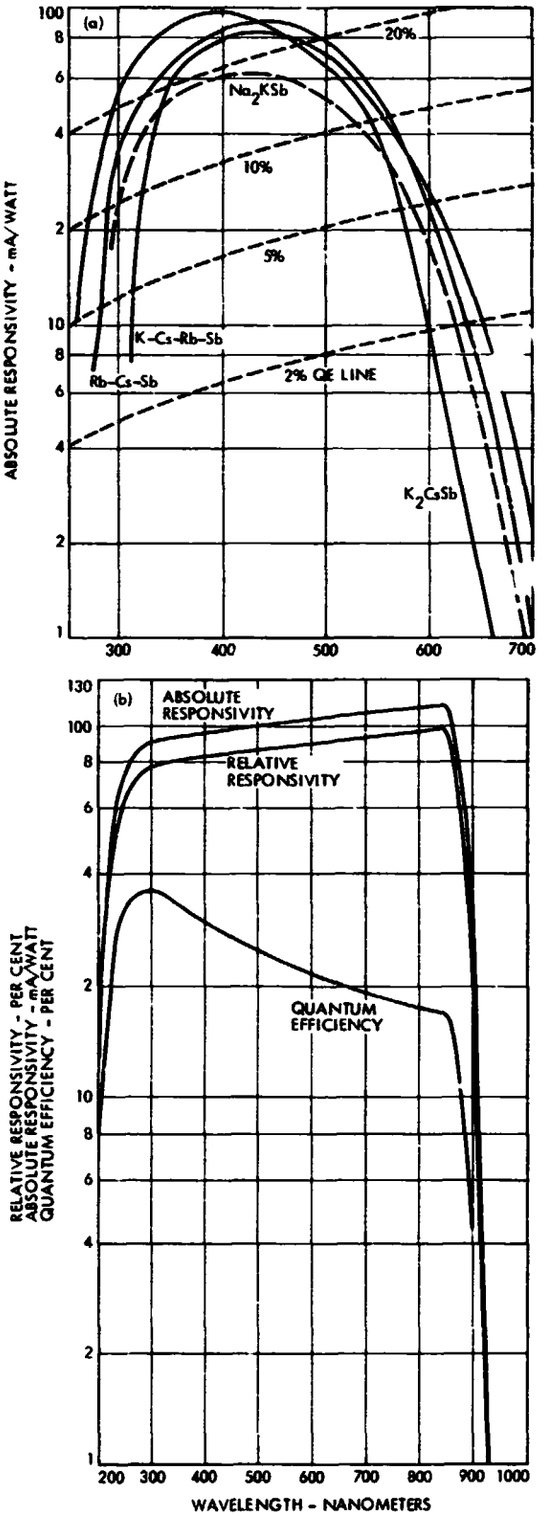

Fig. 2. Spectral response of PMT photocathodes: (a) multi-alkali photocathode; (b) GaAs (Cs) photocathode

ORIGINAL PAGE IS
OF POOR QUALITY

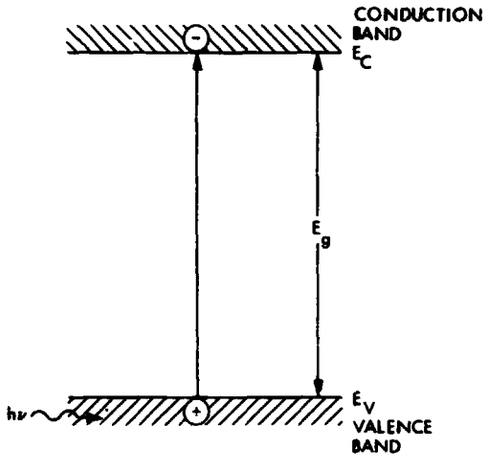

Fig. 3. Schematic band diagram of an intrinsic absorption process

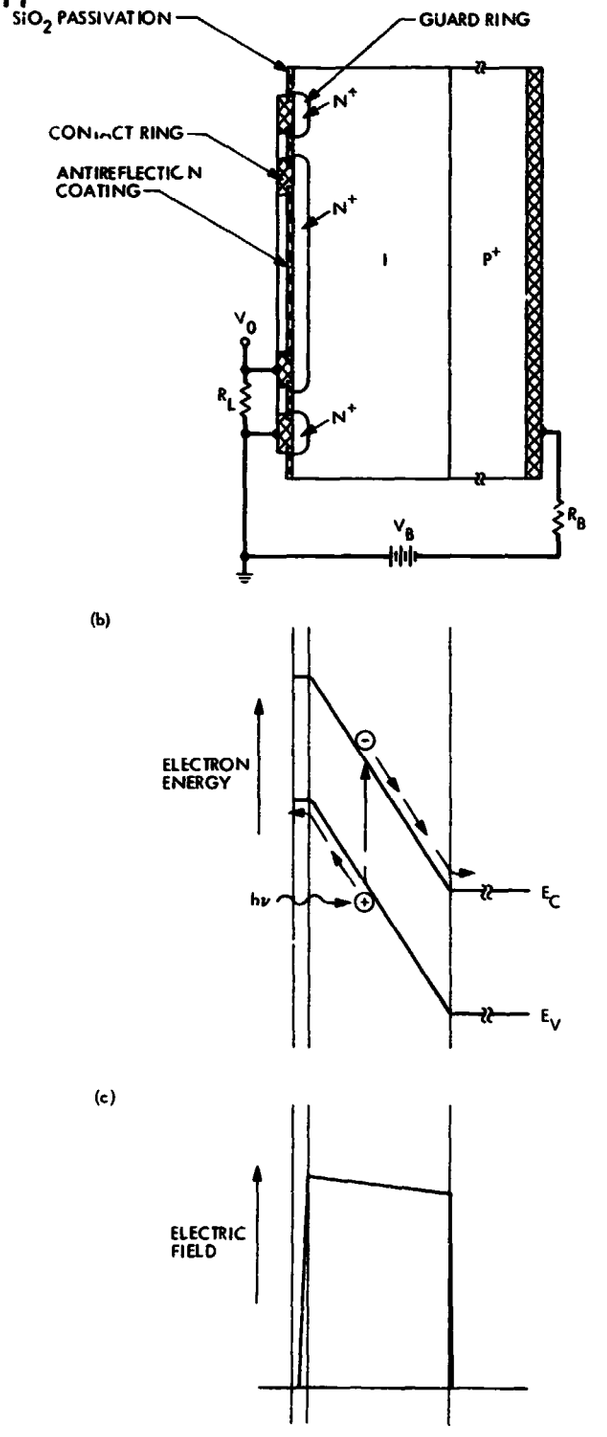

Fig. 4. PIN PD: (a) schematic structure of a Si device (the guard-ring shunts surface leakage currents from the load resistor); (b) band diagram; (c) electric field distribution (*I* region in this case is a lightly doped p-region, usually denoted π)

ORIGINAL PAGE IS
OF POOR QUALITY

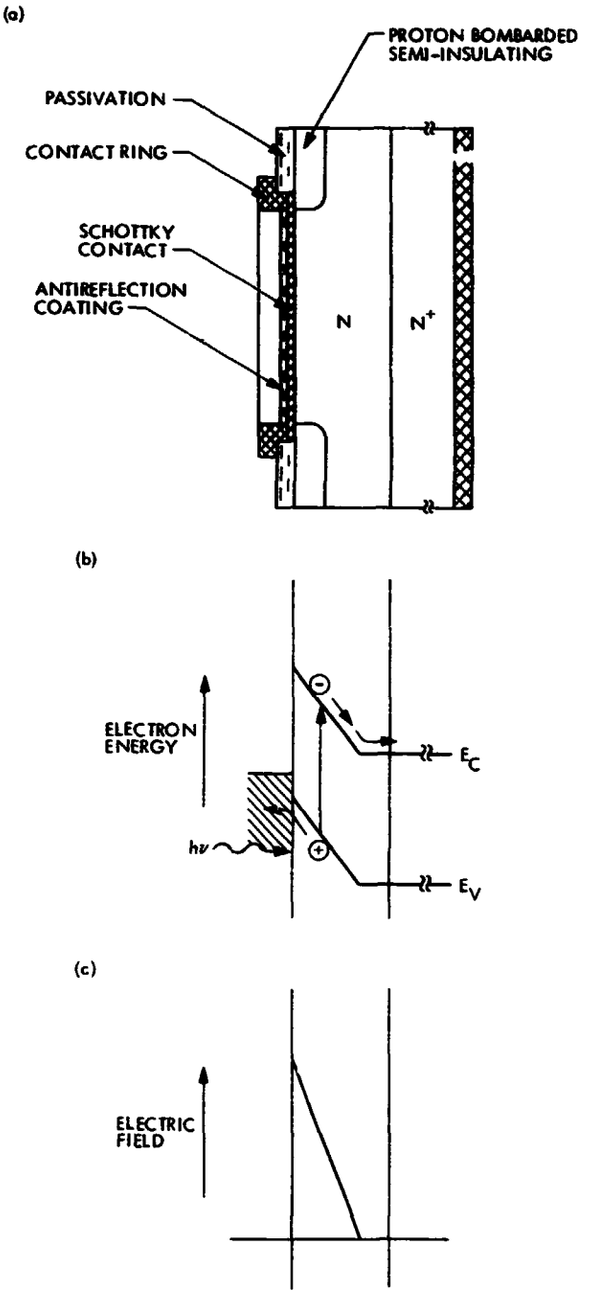

Fig. 5. Schottky PD: (a) schematic structure; (b) band diagram; (c) electric field distribution (details at nn^+ junction are neglected)

ORIGINAL PAGE IS
OF POOR QUALITY

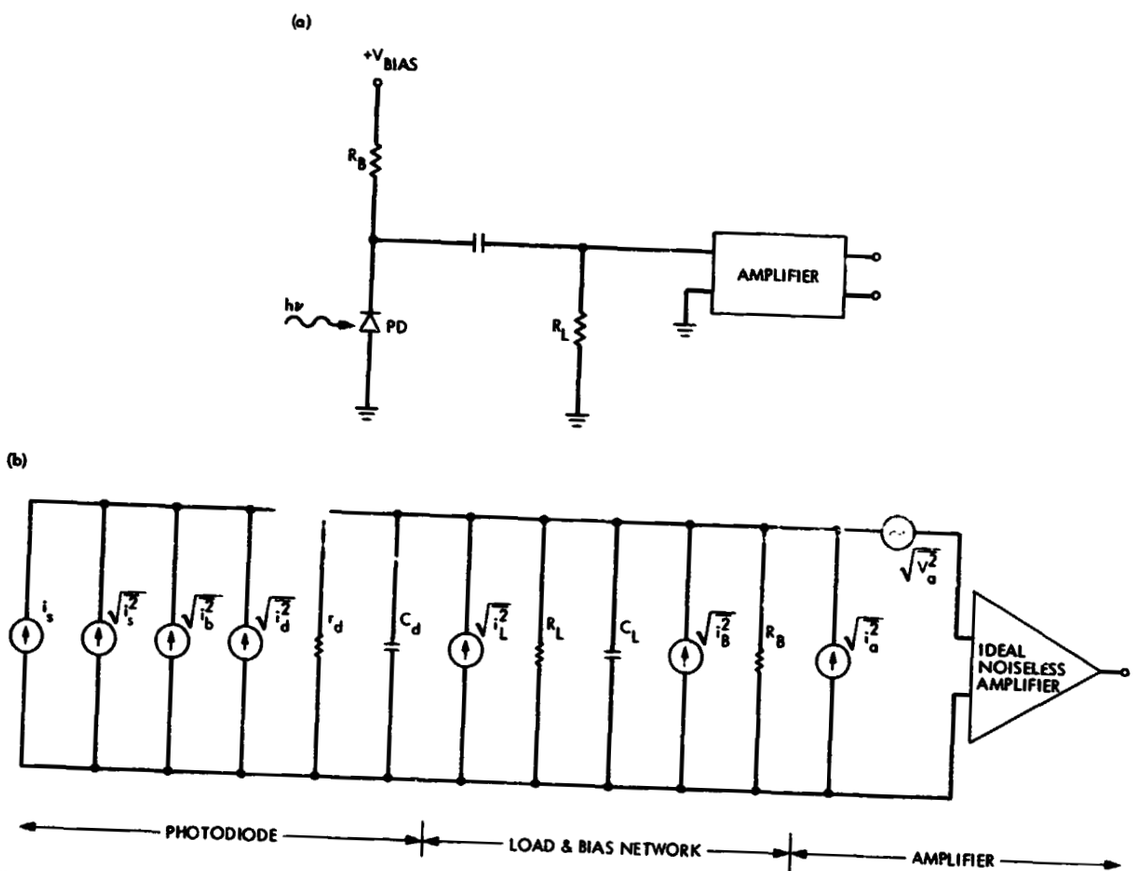

Fig. 6. Basic photodiode optical receiver: (a) detector circuit using a PD; (b) equivalent circuit (including noise sources) of the circuit in Fig. 6(a) (r_d is the PD dynamic resistance; the other parameters are explained in the text)

ORIGINAL PAGE IS
OF POOR QUALITY

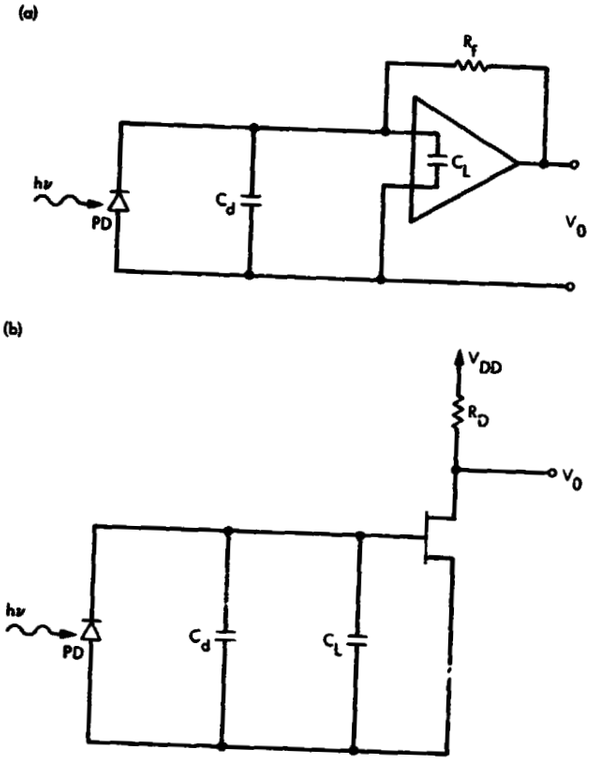

Fig. 7. Generic types of front-end detector circuits: (a) trans-impedance amplifier; (b) high impedance FET front end amplifier

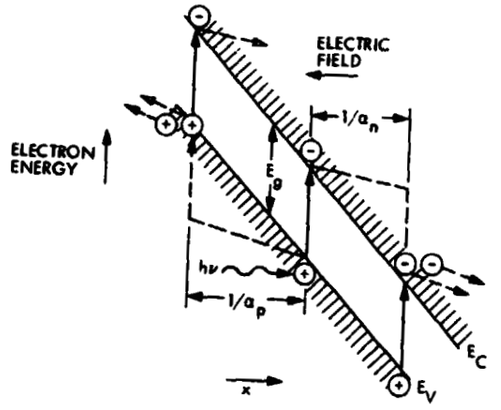

Fig. 8. Schematic depiction of the avalanche gain (impact ionization) process

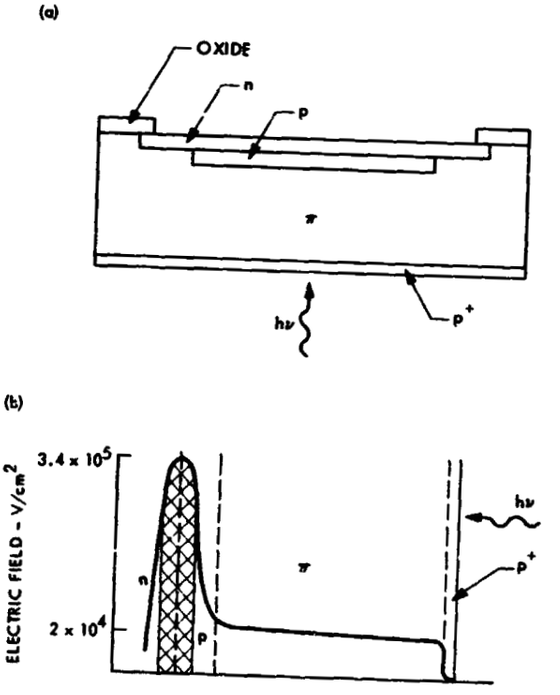

Fig. 9. Avalanche photodiode: (a) structure of a reach-through APD; (b) electric field distribution in the APD (the cross-hatched area is the multiplication region)

ORIGINAL PAGE IS
OF POOR QUALITY

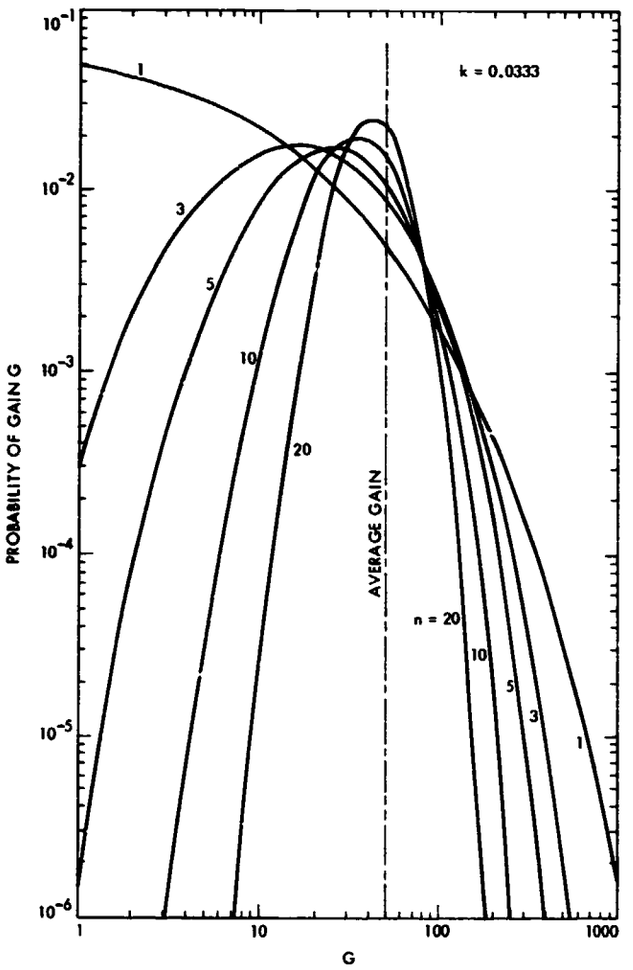

Fig. 10. Probability distribution of gain process of an APD with an average gain of 50. *n* is the number of carriers injected initially to the multiplication region

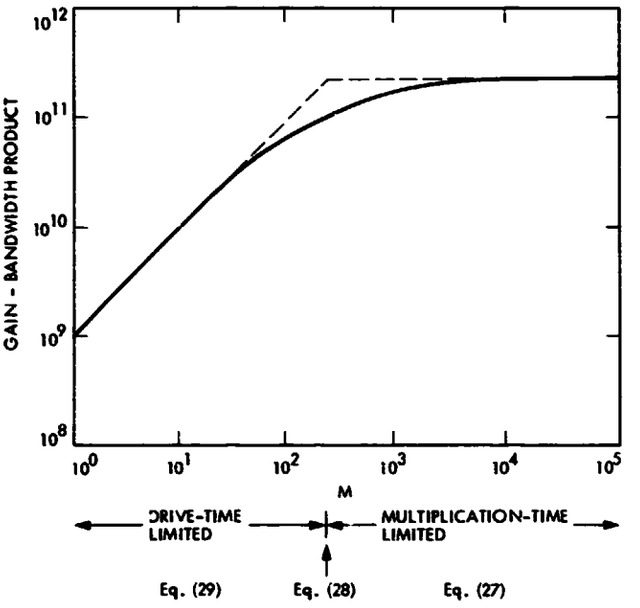

Fig. 11. Gain bandwidth product of an APD

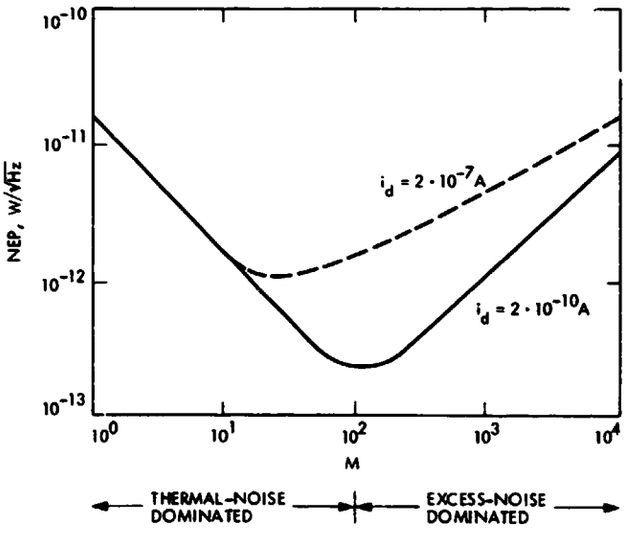

Fig. 12. *NEP* of APD versus gain *M* (k = 0.1, λ = 0.85 μm, *B* = MHz, R_e/T_e = 10.7 Ω/K, i_d/I_{ds} = 2;

N84 13405

Superconducting Niobium Thin Film Slow-Wave Structures

J. J. Bautista and S. M. Petty
Radio Frequency and Microwave Subsystem Section
L. H. Allen, M. R. Beasley and R. H. Hammond
Stanford University

A superconducting comb structure as a slow-wave element in a traveling-wave maser will significantly improve maser noise temperature and gain by reducing the insertion loss. This article presents the results of the insertion loss measurements of superconducting niobium slow-wave structures subjected to maser operating conditions at X-Band frequencies.

I. Introduction

In a traveling wave maser the principle function of a slow-wave structure is to increase the interaction time of the received signal with the maser material in order to maximize the gain per unit length. The increased gain per unit length will, unfortunately, be accompanied by a proportional increase in ohmic losses per unit length (Refs. 1, 2). The proportionality constant is determined by the material's microwave properties and its temperature.

At low temperatures and high frequencies it is well known that the microwave surface resistance for normal metals is severely limited by the so called "anomalous skin effect" (Ref. 3). For sufficiently high temperatures (depending on the material) and at microwave frequencies the conduction electron mean free path is short compared to the spatial variation of the electromagnetic field. For this classical limit the field is regarded as constant and Ohm's law is applied to derive the skin depth which is found to be inversely proportional to the square root of the electrical conductivity. However, at low temperatures the mean free path exceeds both the spatial variation of the field and the classical skin depth. In this limit the surface resistance becomes independent of the conductivity and temperature, since the only electrons that can contribute to the conductivity are those that remain within the skin depth between collisions (Ref. 4). In fact, the limiting surface resistance of a normal metal like copper at low temperatures (below 50 K) is approximately one-fourth to one-fifth the room temperature value (Ref. 5).

Although the microwave surface resistance of a superconductor is not zero below the critical temperature (T_c), it can be several orders of magnitude less than the best normal conductor. In fact, for $T < 0.5T_c$ the surface resistance can be approximated by the following expression (Ref. 6)

$$R_s \sim f^2/T \exp(-\Delta/kT) \qquad (1)$$

where f = frequency, T = temperature, k = Boltzman constant and 2Δ = superconducting energy gap.

This finite surface resistance can be understood by recalling that electrons in the superconducting state are bound into

electron pairs by an interaction involving the lattice vibrations of the metal. The binding energy (2Δ) is $2\Delta(0)$ at $T = 0$ K and approaches zero as T approaches T_c. At $T = 0$ K all of the electrons are bound pairs. However, for finite temperatures the thermal energy present will excite and break some of the electron pairs. In this case the number of electrons excited across the gap is proportional to the Fermi-Dirac distribution function which for $T < T_c$ can be approximated by

$$\exp - (\Delta/kT) \qquad (2)$$

Thus, photons (having a frequency $f < 2\Delta/h$) interacting with these electrons will result in the absorption of energy. Power dissipation occurs when these electrons relax to a lower energy (Ref. 7).

II. Slow-Wave Structure Preparation

The sapphire substrates (length = 3.7 in., width = 0.22 in. and thickness = 0.030 in.) were supplied by INSACO (Quaker Town, Penn.) with one side epi-finished and the c-axis parallel to the longest dimension. Before the deposition the substrates were carefully cleaned with H_2SO_4 and rinsed with deionized water and acetone.

The niobium thin films studied were deposited utilizing two different techniques – magnetron sputtering (Ref. 8) and e-beam evaporation (Ref. 9). The sputtering was performed with the substrate held at room temperature while the evaporation was done with the substrate held at approximately 700°C. Both processes yielded film thicknesses (estimated from the deposition rates) of approximately 1 μm.

The slow-wave pattern which consists of adjacently coupled, half-wavelength resonators (Ref. 10) was produced using conventional photolithographic techniques. A positive photoresist (Shipley 1470) was used to develop the pattern and the excess niobium was removed using a plasma assisted etching technique (Ref. 11).

Pictured in Figs. 1 and 2 are the best samples obtained from the two deposition techniques. Visual inspection of the samples indicates that the better set was produced with the e-beam evaporation technique. The sputtered samples appear blistered and not to have adhered as well to the substrate as the e-beam samples. Unfortunately, this is a consequence of the cooler substrate temperature.

III. Insertion Loss Measurements

A. Microwave Circuit Structure

The microwave circuit of interest (slow-wave structure) is basically a set of 44 unbalanced, stripline resonators, approximately one-half wavelength long at X-band which are adjacently coupled to one another. The niobium thin film resonators are sandwiched between two dielectric substrates – a 40 mil thick ruby bar on one side and 30 mil sapphire and 68 mil alumina bar on the other. The ground planes are defined by the inner copper channel walls of the assembly pictured in Fig. 3. It should be noted that the cross-sectional dimensions of the copper are chosen so that the TE_{20} mode of the pump frequencies (19 and 24 GHz) is supported. In addition, the resonator strip and dielectric dimensions are chosen so that the characteristic impedance of the resonators is approximately 50 ohms. Coupling into and out of the slow-wave structure is achieved with identical coaxial to stripline (copper) transitions whose center conductor is out of the plane of the slow-wave structure but parallel to first element and spaced a distance equal to spacing between adjacent elements. (For a more detailed description of this structure please see Ref. 10.)

B. Cryogenic Apparatus

A sketch of the cryogenic apparatus utilized for the insertion loss measurements is shown in Fig. 4. It consists of two comb structures connected in series for increased measurement sensitivity. The measurements obtained at low temperatures were performed with the apparatus immersed in liquid helium maintained at 4.5 K.

The applied dc magnetic field was supplied by an external electromagnet. The magnet and cryogenic apparatus were positioned such that the direction of magnetic field could be rotated through 180° with respect to a normal through the film-substrate interface.

C. Measurement Setup

A swept measurement technique was utilized for performing the insertion loss measurements. To minimize heat leaks from room temperature to the helium bath stainless steel coaxial lines were used for the signal input and output. Figure 5 contains a block diagram showing the measurement set up.

IV. Results

Prior to commencing the low temperature measurements the insertion loss for the two combs was observed using 5 mW of signal power as the samples cooled. It is interesting to note that the insertion loss of the niobium combs in the normal state was observed to change from 70 dB at 300 K to approximately 8 dB at 10 K (see Fig. 6) while comparable copper combs are known to change only from 10 dB to 4 dB over the same temperature range (R. B. Quinn, private communication).

This significant difference in temperature behavior can be understood by noting that at 8.0 GHz the classical to anomalous "transition" of the surface resistance of copper occurs near 50 K while for Nb this occurs at approximately 13 K (Ref. 12).

A. Signal and Pump Power Level Effects

The microwave performance of a superconductor can be seriously degraded when driven into the normal state. There are two possible mechanisms which can cause this. In one case the peak rf magnetic field can exceed the thermodynamic critical field H_c (H_c = 1900 gauss at T = 0 K for niobium). Inadequate heat dissipation can account for the other mechanism resulting in thermal runaway.

For the second case the rf ohmic losses are not readily dissipated because of a low thermal conductivity and/or poor thermal heat sinking. The resulting increase in temperature rapidly drives the superconductor above its critical temperature T_c (T_c = 9.2 K for niobium). This will occur before the peak rf field exceeds B_c (Ref. 6, 7, 13).

For maser or low power applications heat dissipation is the more important concern. This problem was clearly evidenced when the sputtered niobium combs were first tested in vacuum with the copper ground planes thermally anchored to 4.5 K. For these tests, only modest levels of signal and pump power (approximately 50 mW) were required to significantly degrade the insertion loss.

This problem was alleviated when the combs were measured while immersed in liquid helium. In fact, the insertion loss was found to be nearly independent of signal power up to 800 mW and pump power up to 250 mW (see Fig. 7).

B. Magnetic Field Effects

In order to demonstrate feasibility for use in an X-band maser these structures must remain superconducting in the presence of a dc magnetic field up to 5.5 kgauss. For this part of the study the insertion loss was measured at the passband as a function of the applied dc magnetic field from 0 to 10 kgauss for two orientations (parallel and perpendicular) to the direction of the microwave surface currents.

Figure 8 contains a sample of the measured results obtained for the evaporated combs with the magnetic field in the perpendicular direction. Similar results were obtained for the sputtered combs. The results demonstrated that the field readily penetrates both types of films for this orientation.

Figure 9 contains a sample of results obtained for the evaporated combs with the field in the parallel direction. Similar results were obtained for the sputtered combs. For this orientation it was noted that the measured insertion loss is apparently independent of the magnetic field up to a particular field value. For the sputtered comb this field value was near 5.0 kgauss while for the evaporated film this value was approximately 3.0 kgauss.

Since the insertion loss was found to be sensitive to the magnitude and direction of the magnetic field, the perpendicular position was found (within ±0.5°) by maximizing the loss while rotating the field. The parallel position was then defined by a 90° rotation relative to the perpendicular position.

It should be mentioned before proceeding that these measurements were performed with 5 mW or less of signal power. Furthermore, the samples were tested for hysteretic effects, but none were found within the limits of these measurements.

V. Results and Discussion

A. Insertion Loss

The theoretical insertion loss in dB of a microwave (Tchebyscheff) filter at midband is given by the following expression (Ref. 14)

$$L_0\,(\text{dB}) = 4.343\,\frac{f_0}{\Delta f}\,\frac{1}{Q_u}\sum_{k=1}^{n} g_k \qquad (3)$$

where f_0 is the filter center frequency, Δf is the equal ripple band width, Q_u is the unloaded resonator Q, and g_k are the low-pass prototype filter element values. Now, for a microstrip structure the total loss is the sum of the dielectric, ohmic and radiative losses. That is (Ref. 15, 16),

$$Q_u^{-1} = Q^{-1}\,(\text{dielectric}) + Q^{-1}\,(\text{ohmic}) + Q^{-1}\,(\text{radiative}) \qquad (4)$$

A few simplifying approximations are necessary in order to compare the measured with the expected insertion loss results. Since the reported Q values of sapphire vary from 10^5 to 10^9 (Ref. 17) and since Q (radiative) is essentially infinite for resonators enclosed in a waveguide below cut off, then it is reasonable to assume that $Q_u \simeq Q$ (ohmic). Furthermore, for the special case of a 50 Ω halfwave length resonator open at both ends (Ref. 18)

$$Q_u \simeq 800\,(h/\lambda)\,R_s^{-1} \qquad (5)$$

where h = dielectric thickness, λ = free space wavelength and R_s = the surface resistance of the conducting strip.

In Eq. (3) the g_k's depend on the in-band ripple. Based on the observed return loss and the inband response (see Fig. 10) the summation of the g_k's for $n = 44$ is approximately 100 and $f_0/\Delta f = 6.5$. In addition, in Eq. (5) $h = 0.040$ in. and $\lambda = 1.5$ in. Substituting these values into Eq. (3) yields that

$$L_0\,(\text{dB}) \simeq 145\,R_s, \text{dB} \tag{6}$$

Table 1 contains a comparison of the measured insertion loss values and the expected values using the above approximations. With the exception of the last row, the data are within at least an order of magnitude of the expected values.

Although the agreement (as should have been expected) is poor, it is still instructive to examine the reason for the large discrepancy between the values in the last row which differ by nearly two orders of magnitude. Equation (5) assumes that the strip and ground plane have the same value for the surface resistance. Furthermore, it is generally assumed for microstrip structures that most of the ohmic loss occurs at the strip conductor and not the ground plane (Ref. 15). In this experiment the ground plane is constructed of copper so that the loss is thus dominated by the ground plane when the strip becomes superconducting.

B. Magnetic Field Effects

Although it would have been desirable to use a superconducting ground plane, the most important question to answer for maser applications is whether the slow-wave structure will retain its low loss property at the operating magnetic field values. This question can be answered without the need of a superconducting ground plane.

In order to clearly demonstrate this Figs. 11 and 12 show the normalized insertion loss as a function of applied magnetic field for both evaporated and sputtered films, respectively. Here the normalized insertion loss is defined as the ratio of the insertion loss in the superconducting state to the insertion loss in the normal state.

To first order for a quasi-TEM mode it can be assumed that the microwave currents are primarily along the direction of the half-wavelength resonator (Ref. 19). Figures 11 and 12 thus display the normalized insertion loss for the field perpendicular and parallel to both the microwave surface currents and the film substrate interface.

With the field in the perpendicular direction both the sputtered and evaporated samples show an almost linear dependence on the magnitude of the applied magnetic field until the sample reaches the normal state for a critical magnetic field (H_{c2}). Here the critical magnetic field value for the evaporated samples is 5.0 kgauss while for the sputtered samples it is 9.0 kgauss.

For the case where the magnetic field is parallel to the microwave currents the normalized insertion loss is independent of the field up to a certain value. This field value occurs at 3.0 kgauss for evaporated samples while for the sputtered samples it occurs at 5.0 kgauss. As the field is increased further to a higher critical field (H_{c3}) both samples will eventually reach the normal state. These field values are beyond the limits of the magnet used, thus are not included in Figs. 11 and 12.

The observed field dependence of the normalized insertion loss can be qualitatively understood by recalling some of the properties of a type-II superconductor. For a type-II superconductor like Nb the Meissner state (the exclusion of flux from the interior of the superconductor) exists for field values below the first critical field value H_{c1}. Above H_{c1} and below H_{c2} the mixed state is present. In this field range magnetic flux penetrates the sample in the form of quantized flux lines and the superconductor exhibits a two dimensional structure that consists of normal regions through which flux penetrates surrounded by superconducting regions (Refs. 20, 21).

It is the interaction of the microwave current with the flux lines through the Lorentz force that results in power dissipation. That is, the force per unit length of flux line is given by

$$\vec{f}_L = \vec{j} \times \vec{\Phi}_0 \tag{7}$$

where $\vec{j}$ is the microwave current density and $\Phi_0 = hc/2e = 2.07 \times 10^{-7}$ gauss-cm^2 is a quantum of flux. At microwave frequencies the oscillatory motion of the flux lines occurs through a medium that is regarded as viscous resulting in power loss (Ref. 22). Thus, when the current and field are perpendicular and $H > H_{c1}$ the loss is expected to increase linearly with the field up to H_{c2}. Now, for the case where the field and current are parallel Eq. (7) is zero and the loss is expected to be independent of flux-flow losses as H_{c2} is approached (Ref. 22).

Above H_{c2} for the parallel direction the sample is in the sheath state where the outside surface remains superconducting and the inner portion is in the normal state (Refs. 20, 21). The thickness of the sheath is of the order of the coherence length ($\xi \sim 400$ Å) which is comparable to λ_L (the London penetration depth). As the field is increased the sheath thickness decreases resulting in an increased loss up until H_{c3} is reached where the sample becomes normal (Ref. 23).

The observed quantitative difference in H_{c2} and H_{c3} for the sputtered and evaporated samples is related to the manner in which they were prepared. The parameter that determines H_{c2} and H_{c3} is the coherence length ξ which is the range of coherence of the superconducting phase. The critical fields are given by the following expressions (Ref. 22):

$$H_{c2}(T) = \frac{1}{2\pi} \Phi_0/\xi^2(T)$$

and

$$H_{c3}(T) = 1.695\, H_{c2}(T) \tag{9}$$

where

$$\frac{1}{\xi} = \frac{1}{\xi_0} + \frac{1}{\alpha \ell} \tag{10}$$

and where ξ_0 = intrinsic coherence length at $T = 0$ K, ℓ = the electron mean free path and α is an adjustable parameter. Since it is known that annealing thin film Nb samples increases the electron mean free path, it is expected that the evaporated samples will have a longer mean free path. Thus Eqs. (8), (9) and (10) imply that the critical fields are expected to be lower for the evaporated films which was verified by the measurements.

VI. Remarks and Conclusion

It has been demonstrated that thin film, type-II superconducting materials are feasible for use as slow-wave comb structures in a ruby maser. Although it does not appear that Nb is useful at X-band frequencies, the results do indicate that Nb can be used at S-band frequencies where the applied magnetic fields are less than 3.0 kgauss.

For frequencies at X-band and higher Nb_3Sn should be a suitable candidate. Its surface resistance at X-band and helium temperatures has displayed values less than 1/30 of the values for the Nb samples tested. Furthermore, Nb_3Sn has an H_{c2} of approximately 200 kgauss (nearly 100 times the value for Nb).

Although there are other possible slow-wave structures that could have been tested, these results and previous measurements (Ref. 22) dictate that the structures must be thin along the direction of the field and the microwave currents must also be parallel to this direction. For example, the microwave Pb meander line evaluated by Gandolfo *et al.* (Ref. 23) would have the thin dimension parallel to the field. However, portions of the line would have segments where the microwave currents are perpendicular to the field. Kim (Ref. 22) has observed that the surface resistance (for films having this orientation) is intermediate between the values for the perpendicular and parallel direction. Thus a half-wave comb structure is clearly the optimal slow-wave circuit for these applications.

The noise temperature of a traveling wave maser having a high gain ($G \gg 1$) is given by (Refs. 1, 24, 25)

$$T_m = T_0 \frac{\rho + \beta}{1 - \beta} \tag{11}$$

and the net gain by

$$G(\text{dB}) = \text{Electronic Gain (dB)} - \text{Forward Loss (dB)} \tag{12}$$

where ρ = (Inversion Ratio)$^{-1}$, β = Forward Loss (dB)/Electronic Gain (dB) and T_0 = Bath Temperature. For comparison Table 2 contains the expected T_m and G(dB) for several different metals utilizing the same slow-wave structure pattern (Ref. 10). The values assumed for the Inversion Ratio and the Electronic Gain are typical and nearly ideal values measured for the Block II-A X-band traveling wave masers (D. L. Trowbridge, private communication). It should be mentioned that the best estimate of the isolator contribution to the Forward Loss is from 1 to 2 dB. However, this loss can in principle be further reduced (Ref. 26).

In conclusion, it is noted that Nb_3Sn structures could in principle reduce the noise temperature of existing Block II-A masers by approximately 50% and increase the net gain by 20%. Evidently, the net gain could be further improved by increasing the slowing without significantly increasing the noise temperature. An alternate and possibly more desirable approach would be to widen the bandwidth while keeping the gain and noise temperature constant. Furthermore, Nb_3Sn would be of greater benefit at higher frequencies where dissipative loss is often a more serious problem.

References

1. Siegman, A. E., *Microwave Solid State Masers* (McGraw-Hill Book Company, New York, 1964).
2. Ishii, T. K., *Maser and Laser Engineering* (Robert E. Krieger Publishing Company, New York, 1980).
3. Pippard, A. B., Proc. Roy. Soc. *A191*, 385 (1947).
4. Reuter, G. E. H., and Sondheimer, E. H., Proc. Roy. Soc. *A195*, 336 (1948).
5. Bernard, J., El Minyawi, N. H., and Viet, N. T., Revue de Physique Appliquée *13*, 483 (1978).
6. Septier, A., and Viet, N. T., J. of Phy. E. Sci. Inst. *10*, 1193 (1977).
7. Turneaure, J. P., Proc. 8th Int. Conf. on High Energy Accelerators *51* (Geneva, Switzerland, 1971).
8. Barbee, T. W., and Keith, D. L., "Synthesis of Metastable Materials," Conf. Proc. of the Metal. Soc. of AIME, Pittsburg, 1980.
9. Hammond, R. H., IEEE Trans. Magn. *MAG-11*, 201 (1975).
10. Clauss, R. C., Quinn, R. B., Petty, S. M., and Trowbridge, D. L., "Maser Amplifier Slow-Wave Structure," JPL Case No. 15211 (NASA NPO-15, 211-1).
11. Melliar-Smith, C. M., and Mogab, C. J., in *Thin Film Processes*, Vossen, J. L. and Kern, W., ed. (Academic Press, New York, 1978).
12. Ratcke, J. E., *The Transient Analysis of Coaxial Cables at Low Temperatures Considering Anomalous and Classical Skin Effects with the Inclusion of Electron Relaxation Phenomena*, Ph.D. Thesis, University of Kansas (1969).
13. Kuntze, M., Proc. 9th Inst. Conf. on High Energy Accelerators, 115 (Stanford, 1974).
14. Matthaei, G. L., Young L. and Jones, E. M. T., *Microwave Filters, Impedance-Matching Networks, and Coupling Structures* (Artech House Books, Dedham, Mass., 1980).
15. Pucel, R. A., Masse, D. J., and Hartwig, C. P., IEEE Trans. on Theory and Techniques *MTT-16*, 342 (1968).
16. Denlinger, E. J., IEEE Trans. on Theory and Techniques *MTT-17*, 235 (1969).
17. Braginsky, V. B. and Panov, V. I., IEEE Trans. on Mag. *MAG-15*, 30 (1979).
18. Davidheiser, R. A., AIP Conf. Proc. *44*, Future Trends in Superconducting Electronics, AIP, 219 (1978).
19. Denlinger, E. J., IEEE Trans. on Microwave Theory and Techniques *MTT-19*, 30 (1971).
20. Berlincourt, T. G., in *Superconductivity in Science and Technology*, Cohen, M. H., ed (University of Chicago Press, Chicago, 1968).
21. Rose Innes, A. C., and Rhoderick, E. H., *Introduction to Superconductivity* (Pergamon Press, London, 1969).
22. Kim, S. H., *Microwave Surface Impedance of Superconductors*, Ph.D. Thesis, Wayne State University (1975).

23. Gandolfo, D. A., Boornard, A., and Morris, L. C., J. of App. Phys. *39*, 2657 (1968).

24. Higa, W. H., IEEE Trans. on Microwave Theory and Techniques *MTT-12*, 2 (1964).

25. Clauss, R. C., JPL Space Programs Summary 37-45, *Vol. III*, 40 (April, 1967).

26. Clauss, R. C., "Resonant Isolator for Maser Amplifier," JPL Case No. 15201 (NASA NPO-15201).

ORIGINAL PAGE IS
OF POOR QUALITY

Table 1. Insertion loss at mid-band for X-band comb

Slow-wave structure	Temp, K	R_s, Ω	Calculated I.L.[a], dB	Measured I.L.[a], dB
Cu	300	2.2×10^{-2}	3.2	5.0
Cu	4.5	4.0×10^{-3}	0.6	2.0
Nb-sputtered	300	–	–	35.0
Nb-evaporated normal state	300	–	–	30.0
Nb-sputtered	4.5	–	–	5.0
Nb-evaporated s.c. state	4.5	1.0×10^{-3}	1.5	3.0
Nb-sputtered	4.5	–	–	1.0
Nb-evaporated	4.5	2.0×10^{-4}	0.03	1.2
Nb_3Sn-evaporated	4.3	3.3×10^{-5}	0.005	–

[a]I.L. - Insertion loss

Table 2. T_0 = 4.5 K

Slow-wave structure	T_m	G(dB)	β	ρ
Cu	2.9[c]	44	10/54	1/3.0
Nb[a]	2.0	50	4.0/54	1/3.0
Nb[b]	1.5	54	0.12/54	1/3.0
Nb_3Sn[b]	1.5	54	0.03/54	1/3.0

[a]Superconducting resonators with Cu ground plane
[b]Superconducting resonators with superconducting ground plane
[c]Typical measured value is 3.5 K

ORIGINAL PAGE IS
OF POOR QUALITY

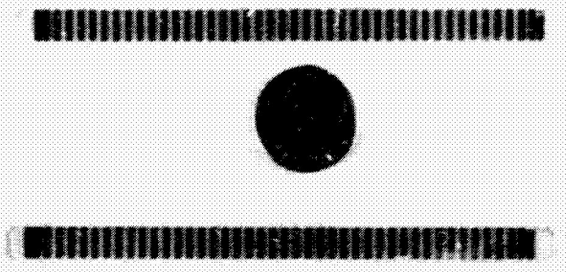

Fig. 1. Sputtered niobium, X-band slow-wave structures

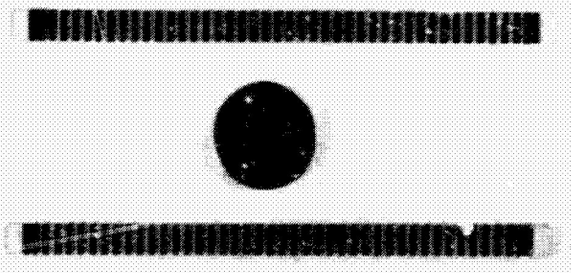

Fig. 2. Electron beam evaporated X-band slow-wave structures

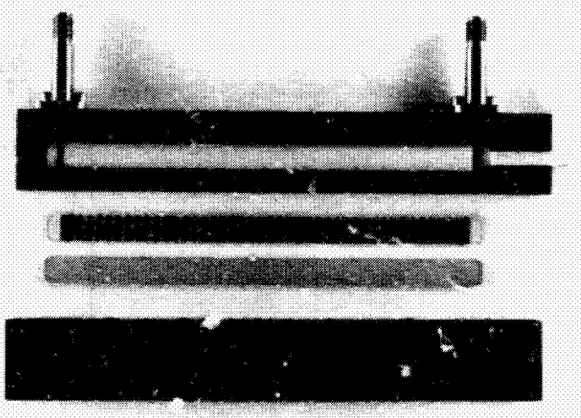

Fig. 3. Disassembled microwave circuit structure

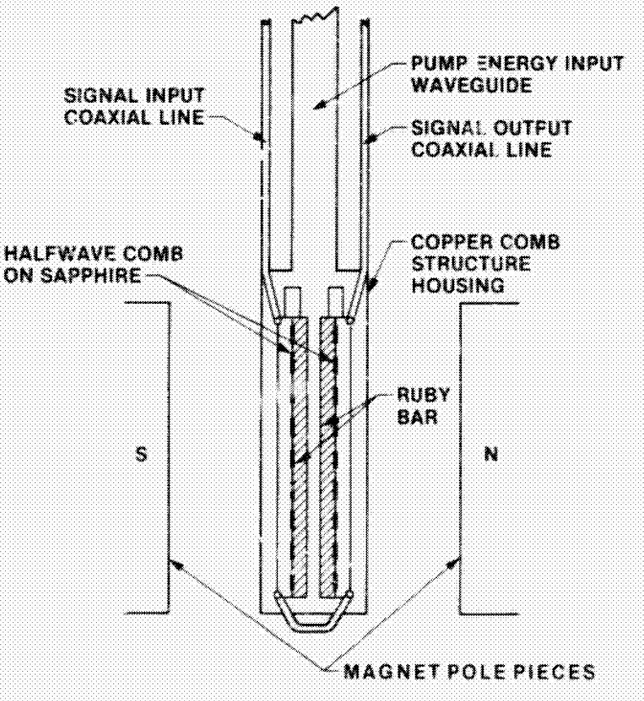

Fig. 4. Sketch of the cryogenic apparatus

ORIGINAL PAGE IS
OF POOR QUALITY

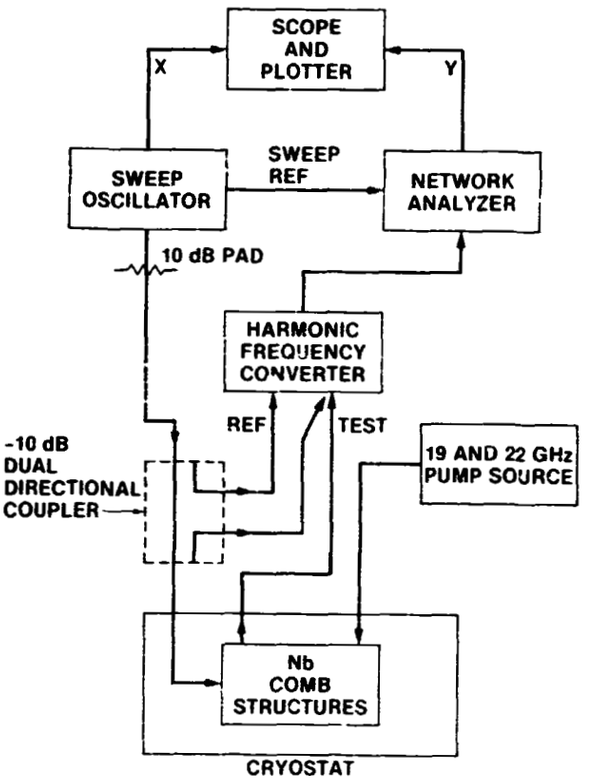

Fig. 5. Block diagram of the sweep measurement set-up

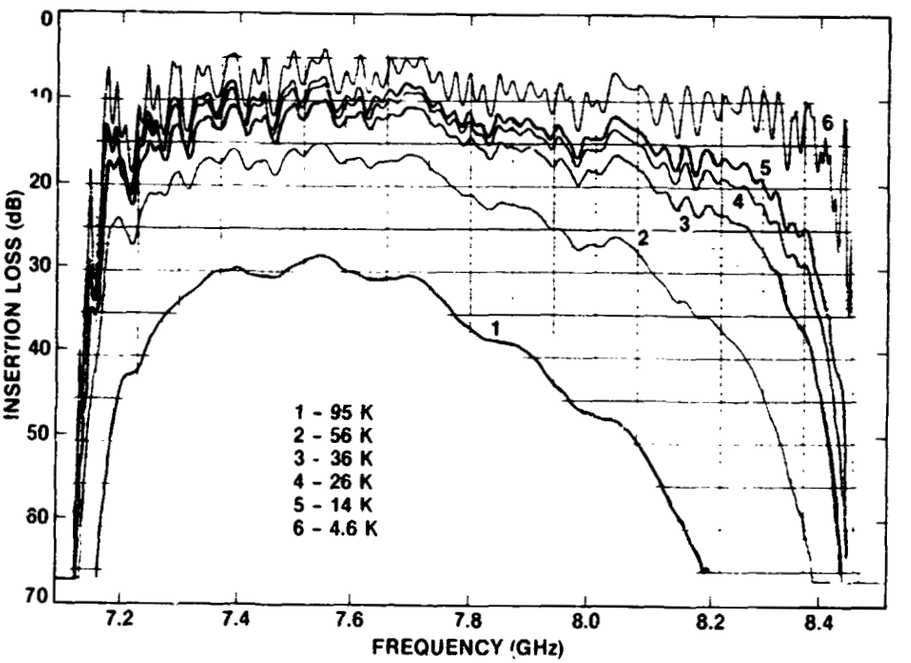

Fig. 6. Insertion loss of evaporated Nb combs at several temperatures

ORIGINAL PAGE IS
OF POOR QUALITY

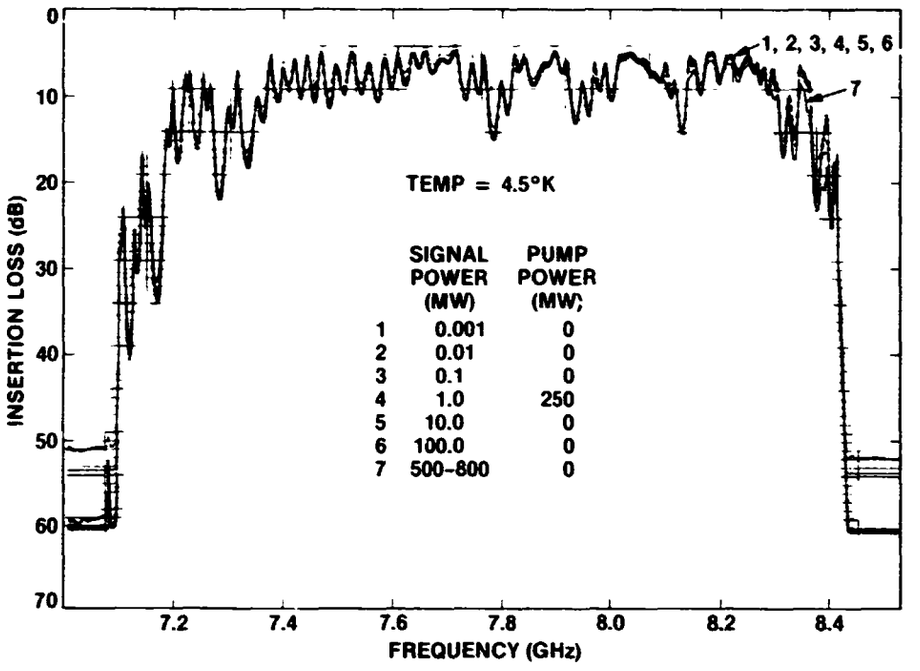

Fig. 7. The insertion loss at various values of signal and pump power for the sputtered Nb combs

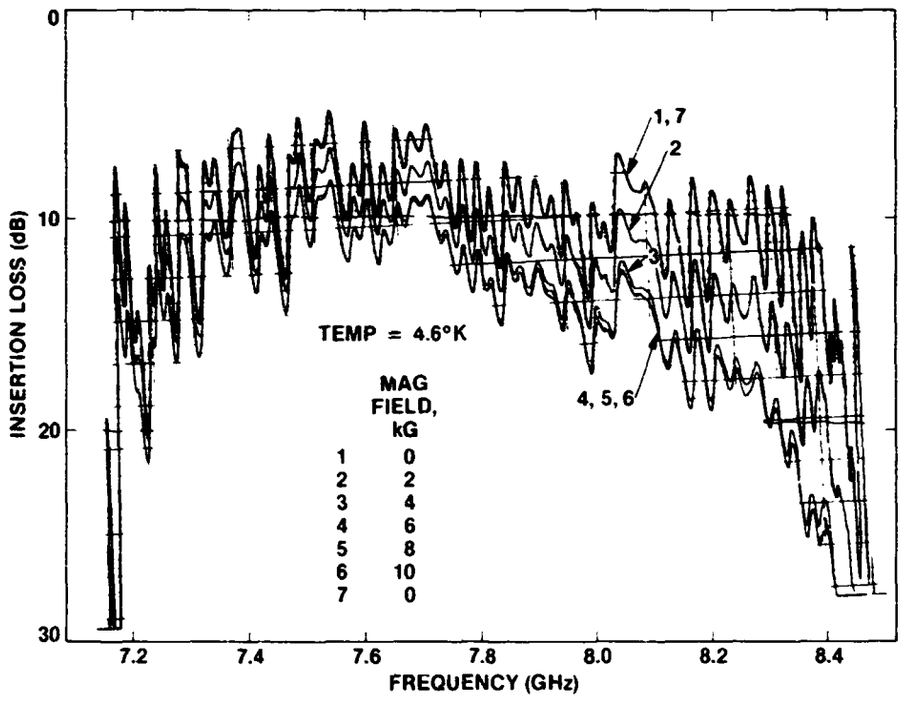

Fig. 8. Uncorrected insertion loss for several values of applied magnetic field perpendicular to the evaporated structures

ORIGINAL PAGE IS
OF POOR QUALITY

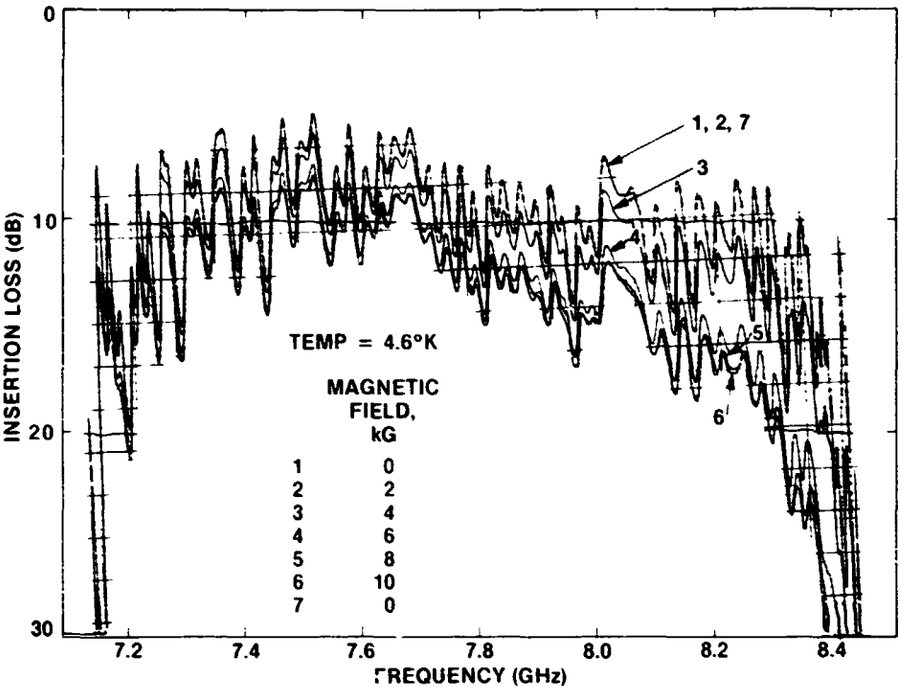

Fig. 9. Uncorrected insertion loss for several values of applied magnetic field parallel to the evaporated structures

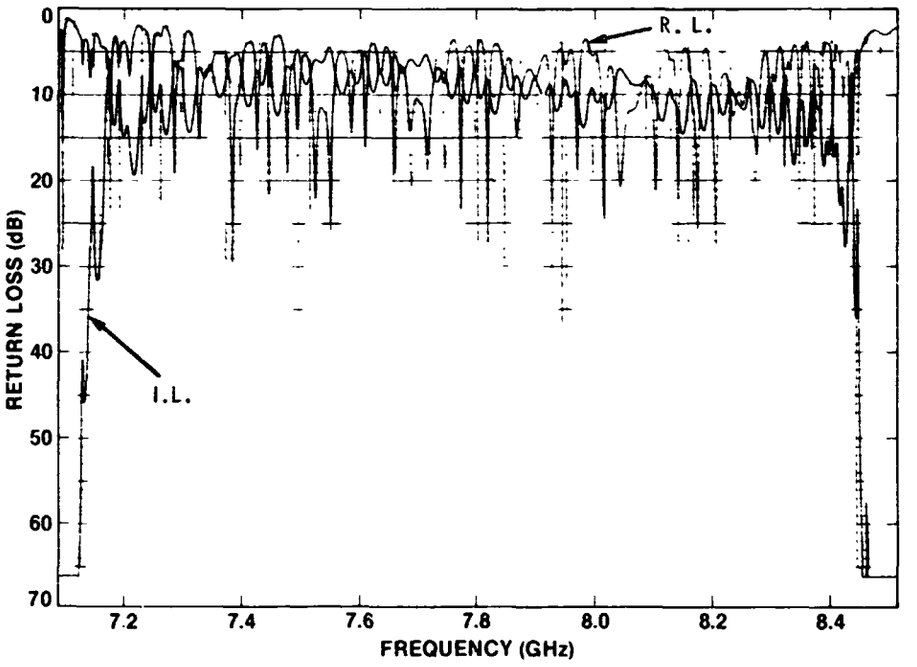

Fig. 10. The uncorrected return loss and insertion loss of the evaporated combs at 4.6 K

ORIGINAL PAGE IS
OF POOR QUALITY

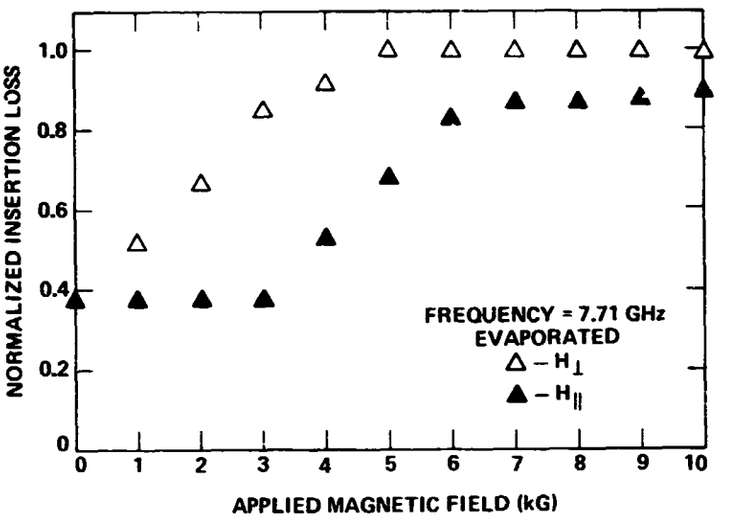

Fig. 11. The normalized insertion loss of the evaporated combs as a function of applied magnetic field

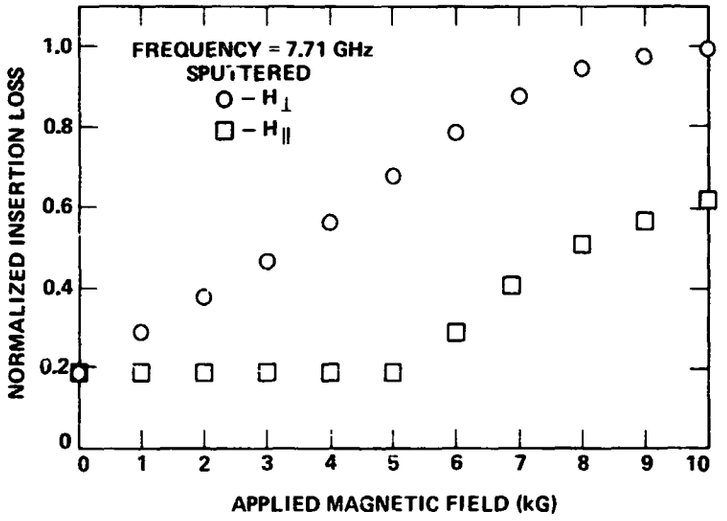

Fig. 12. The normalized insertion loss of the sputtered combs as a function of applied magnetic field

N84 13406

VLSI Architectures for Computing Multiplications and Inverses in $GF(2^m)$

C. C. Wang, T. K. Truong, H. M. Shao and L. J. Deutsch
Communications Systems Research Section

J. K. Omura
University of California, Los Angeles

I. S. Reed
University of Southern California

Finite field arithmetic logic is central in the implementation of Reed-Solomon coders and in some cryptographic algorithms. There is a need for good multiplication and inversion algorithms that can be easily realized on VLSI chips. Massey and Omura recently developed a new multiplication algorithm for Galois fields based on a normal basis representation. In this paper, a pipeline structure is developed to realize the Massey-Omura multiplier in the finite field $GF(2^m)$. With the simple squaring property of the normal-basis representation used together with this multiplier, a pipeline architecture is also developed for computing inverse elements in $GF(2^m)$. The designs developed for the Massey-Omura multiplier and the computation of inverse elements are regular, simple, expandable and, therefore, naturally suitable for VLSI implementation.

I. Introduction

Recently, Massey and Omura (Ref. 1) invented a multiplier which obtains the product of two elements in the finite field $GF(2^m)$. In their invention, they utilize a normal basis of form $\{\alpha, \alpha^2, \alpha^4, \cdots, \alpha^{2^{m-1}}\}$ to represent elements of the field where α is the root of an irreducible polynomial of degree m over $GF(2)$. In this basis each element in the field $GF(2^m)$ can be represented by m binary digits.

In the normal-basis representation the squaring of an element in $GF(2^m)$ is readily shown to be a simple cyclic shift of its binary digits. Multiplication in the normal basis representations requires for any one product digit the same logic circuitry as it does for any other product digit. Adjacent product-digit circuits differ only in their inputs which are cyclically shifted versions of one another. In this paper, a pipeline architecture suitable for VLSI design is developed for a Massey-Omura multiplier on $GF(2^m)$.

The conventional method for finding an inverse element in a finite field uses either table look-up or Euclid's algorithms. These methods are not easily realized in a VLSI circuit. However, using a Massey-Omura multiplier, a recursive, pipeline, inversion circuit is developed. This structure consists of four

ORIGINAL PAGE IS
OF POOR QUALITY

sets of shift registers, one parallel-type Massey-Omura multiplier and two control signals. Such a design is regular, simple and expandable and, hence, naturally suitable for VLSI implementation.

II. Squaring and Multiplying in a Normal Basis Representation

In this section, the work originally described by Massey and Omura (Ref. 1) is reviewed. It is well known that there always exists a normal basis in the finite field $GF(2^m)$ (Ref. 2) for all positive integers, m. That is, one can find a field element α such that $N = \{\alpha, \alpha^2, \alpha^4, \cdots, \alpha^{2^{(m-1)}}\}$ is a basis set of $GF(2^m)$. Thus every field element $\beta \in GF(2^m)$ can be uniquely expressed as

$$\beta = b_0\alpha + b_1\alpha^2 + b_2\alpha^4 + \cdots + b_{m-1}\alpha^{2^{(m-1)}} \tag{1}$$

where $b_0, b_1, b_2, \cdots, b_{m-1}$ are binary digits and addition is mod-2 addition.

Three useful properties of a finite field $GF(2^m)$ are stated here without proof (for proofs see, for example, Ref. 2). These properties are:

(1) Squaring in $GF(2^m)$ is a linear operation. That is, given any two elements α and β in $GF(2^m)$,

$$(\alpha + \beta)^2 = \alpha^2 + \beta^2 \tag{2}$$

(2) For any element α of $GF(2^m)$,

$$\alpha^{2^m} = \alpha \tag{3}$$

(3) If α is a root of any irreducible polynomial $P(x)$ of degree m over $GF(2)$, the powers, $\alpha, \alpha^2, \alpha^4, \cdots, \alpha^{2^{(m-1)}}$, are in $GF(2^m)$ and constitute a complete set of roots of $P(x)$.

With regard to property (3), Peterson and Weldon (Ref. 3) list a set of irreducible polynomials of degree $m \leq 34$ over $GF(2)$ for which the roots $\{\alpha, \alpha^2, \alpha^4, \cdots, \alpha^{2^{(m-1)}}\}$ are linearly independent. These linear independent roots clearly form a normal basis of $GF(2^m)$.

Suppose that $\{\alpha, \alpha^2, \alpha^4 \cdots, \alpha^{2^{(m-1)}}\}$ is a normal basis of $GF(2^m)$. By (2) and (3) the square of (1) is

$$\begin{aligned}\beta^2 &= b_0\alpha^2 + b_1\alpha^4 + b_2\alpha^8 + \cdots + b_{m-2}\alpha^{2^{(m-1)}} + b_{m-1}\alpha^{2^m} \\ &= b_{m-1}\alpha + b_0\alpha^2 + b_1\alpha^4 + \cdots b_{m-2}\alpha^{2^{(m-1)}}\end{aligned} \tag{4}$$

Thus, if β is represented as a vector of components of the normal basis elements of $GF(2^m)$ in the form $\beta = [b_0, b_1, b_2, \cdots, b_{m-1}]$, then $\beta^2 = [b_{m-1}, b_0, b_1, \cdots, b_{m-2}]$. In the normal basis representation β^2 is a cyclic shift of β. Hence squaring in $GF(2^m)$ can be realized physically by logic circuitry which accomplishes cyclic shifts in a binary register. Such squaring circuitry is illustrated in block form in Fig. 1.

By (2) and (3) it is readily seen that $1 = \alpha + \alpha^2 + \alpha^4 + \cdots + \alpha^{2^{(m-1)}}$ for any element α in $GF(2^m)$. This implies that the normal basis representation of 1 is $(1, 1, 1, \cdots, 1)$.

Let $\beta = [b_0, b_1, \cdots, b_{m-1}]$ and $\gamma = [c_0, c_1, \cdots, c_{m-1}]$ be two elements of $GF(2^m)$ in a normal basis representation. Then the last term d_{m-1} of the product,

$$\delta = \beta \cdot \gamma = [d_0, d_1, \cdots, d_{m-1}], \tag{5}$$

is some binary function of the components of β and γ, i.e.,

$$d_{m-1} = f(b_0, b_1, \cdots, b_{m-1}; c_0, c_1, \cdots, c_{m-1}) \tag{6}$$

Since squaring means a cyclic shift of an element in a normal basis representation, one has

$$\left.\begin{aligned}\delta^2 &= \beta^2 \cdot \gamma^2 \\ &= [b_{m-1}, b_0, b_1, \cdots, b_{m-2}] \\ &\quad \cdot [c_{m-1}, c_0, c_1, \cdots, c_{m-2}] \\ &= [d_{m-1}, d_0, d_1, \cdots, d_{m-2}]\end{aligned}\right\} \tag{7}$$

Hence the last component d_{m-2} of δ^2 is obtained by the same function f in (6) operation on the components of β^2 and γ^2. That is, $d_{m-2} = f(b_{m-1}, b_0, b_1, \cdots, b_{m-2}; c_{m-1}, c_0, c_1, \cdots, c_{m-2})$. By squaring δ repeatedly, it is evident that

$$\left.\begin{aligned}d_{m-1} &= f(b_0, b_1, \cdots, b_{m-1}; c_0, c_1, \cdots, c_{m-1}) \\ d_{m-2} &= f(b_{m-1}, b_0, b_1, \cdots, b_{m-2}; \\ &\qquad c_{m-1}, c_0, c_1, \cdots, c_{m-2}) \\ &\vdots \\ d_0 &= f(b_1, b_2, \cdots, b_{m-1}, b_0; \\ &\qquad c_1, c_2, \cdots, c_{m-1}, c_0)\end{aligned}\right\} \tag{8}$$

ORIGINAL PAGE IS
OF POOR QUALITY

The equations in (8) define the Massey-Omura multiplier. In the normal basis representation this multiplier has the property that the same logic function f which is used to find the last component of d_{m-1} of the product δ can be used to find sequentially the remaining components d_{m-2}, d_{m-3}, $\cdots$, d_0 of the product. This feature of the product operation requires only one logic function f of the $2m$ components of β and γ to sequentially compute the m components of the product.

Figure 2 illustrates the logic diagram of the above-described sequential-type Massey-Omura multiplier on $GF(2^m)$. Alternately, for parallel operation this feature permits the use of m identical logic functions, f, for calculating simultaneously all components of the product. In the latter case, the inputs to the m logic functions f are connected directly to the components of β and γ. The only difference in the connections to the components of β or γ to a function f is that they are cyclically shifted versions of one another. Figure 3 shows the structure of the parallel-type Massey-Omura multiplier for the simple case of $m = 4$. The extension of this type of structure to a general case of $GF(2^m)$ is straightforward.

III. A Pipeline Structure for Implementing Massey-Omura Multiplier

A detailed design of a Massey-Omura multiplier is now developed for the finite field $GF(2^4)$. As illustrated in Figs. 2 and 3, the design of either the sequential-type or parallel-type Massey-Omura multiplier must focus on the product function f.

The design of f begins with the selection of an irreducible polynomial $P(x) = x^4 + x^3 + 1$ of degree $m = 4$ over $GF(2)$. This particular polynomial function has linearly independent roots, namely, α, α^2, α^4 and α^8. Hence, the set of roots $\{\alpha, \alpha^2, \alpha^4, \alpha^8\}$ constitutes a normal basis of $GF(2^4)$. Any two elements β and γ in $GF(2^4)$ can be expressed as

$$\begin{aligned} \beta &= b_0\alpha + b_1\alpha^2 + b_2\alpha^4 + b_3\alpha^8 \\ \gamma &= c_0\alpha + c_1\alpha^2 + c_2\alpha^4 + c_3\alpha^8 \end{aligned} \tag{9}$$

By (9) the product of β and γ is

$$\left.\begin{aligned} \delta = \beta\cdot\gamma &= (b_0\alpha + b_1\alpha^2 + b_2\alpha^4 + b_3\alpha^8) \\ &\quad\cdot(c_0\alpha + c_1\alpha^2 + c_2\alpha^4 + c_3\alpha^8) \\ &= d_0\alpha + d_1\alpha^2 + d_2\alpha^4 + d_3\alpha^8 \end{aligned}\right\} \tag{10}$$

By (10) and the fact that $\alpha^4 = \alpha^3 + 1$, one obtains

$$\left.\begin{aligned} d_3 &= b_2c_2 + b_3c_2 + b_2c_3 + b_3c_1 + b_1c_3 \\ &\quad + b_3c_0 + b_0c_3 + b_1c_0 + b_0c_1 \\ d_2 &= b_1c_1 + b_2c_1 + b_1c_2 + b_2c_0 + b_0c_2 \\ &\quad + b_2c_3 + b_3c_2 + b_0c_3 + b_3c_0 \\ d_1 &= b_0c_0 + b_1c_0 + b_0c_1 + b_1c_3 + b_3c_1 \\ &\quad + b_1c_2 + b_2c_1 + b_3c_2 + b_2c_3 \\ d_0 &= b_2c_3 + b_0c_3 + b_3c_0 + b_0c_2 + b_2c_0 \\ &\quad + b_0c_1 + b_1c_0 + b_2c_1 + b_1c_2 \end{aligned}\right\} \tag{11}$$

Comparing (11) with (8), the function f is given by

$$\begin{aligned} f(b_0, b_1, b_2, b_3; c_0, c_1, c_2, c_3) &= b_2c_2 + b_3c_2 + b_2c_3 + b_3c_1 + b_1c_3 \\ &\quad + b_3c_0 + b_0c_3 + b_1c_0 + b_0c_1 \end{aligned} \tag{12}$$

Since the mod-2 sum in (12) can be implemented by the "exclusive or" operation (XOR), the structure of the product function f can be represented by the logic circuit in Fig. 4. This circuit consists of two portions; the left half is an AND plane which computes each term of (12), while the right half is XOR plane which computes the mod-2 sum. The inputs to the AND plane are the complements of the components of β and γ. This is due to the fact that the AND operation in the AND plane is obtained by the NOR operation on the complements of the two digits being ANDed, i.e., $xy = \overline{(\bar{x} + \bar{y})}$ where $\bar{x}$ is the complement of $\bar{x}$.

A pipeline structure of a Massey-Omura multiplier for $GF(2^4)$ is shown in Fig. 5. This structure has a sequential type of operation. For each of the two inputs, corresponding to β and γ, to the f function, an inverter, two sets of shift registers, B and R, and 11 gate transistors are utilized. Note that registers B and R have an identical circuit structure.

In Fig. 5 during the first three clock cycles, when signal $LD = 0$, the complements of b_3, b_2, b_1 and c_3, c_2, c_1 are fed

ORIGINAL PAGE IS
OF POOR QUALITY

sequentially into three buffer flip-flops B_k for (k = 1, 2, 3). At the fourth clock cycle, when Ld = 1, the values of $\bar{b}_3$, $\bar{b}_2$, $\bar{b}_1$ and $\bar{c}_3$, $\bar{c}_2$, $\bar{c}_1$, previously stored in buffer registers B_k and $\bar{b}_0$ and $\bar{c}_0$ are shifted into the second set of registers R_k for (k = 1, 2, 3, 4). Then the R-registers are cyclically shifted Such a cyclic-shift operation is needed to sequentially yield the product components d_3, d_2, d_1 and d_0 of δ. While the R-registers are cyclically shifting the components of β (or γ), the components of another element in $GF(2^4)$ following β (or γ) can be fed into the buffer B-registers. Therefore, the structure in Fig. 5 provides a pipeline operation in which no time is lost except for an initial fixed time delay. The VLSI layout of a Massey-Omura multiplier for $GF(2^4)$ is shown in Fig. 6.

Figure 7 illustrates a system structure of a pipelined Massey-Omura multiplier for $GF(2^m)$. For this general case over $GF(2^m)$, the buffer and the cyclic shift mechanism in Fig. 7 have m - 1 and m stages, respectively. Each stage consists of a shift register and a gate transistor. The product function f is a mod-2 sum of AND products of the components of the two inputs being multiplied. Such a circuit for function f consists of an AND programmed logic array (PLA) (Ref. 4) followed by an XOR sequential-PLA. In the XOR sequential-PLA there are several levels of XORs. At each level, the inputs, pair-by-pair, are fed sequentially one-by-one into an XOR as shown in Fig. 4.

Let $n(j)$ be the number of XOR circuits at the j-th level of the XOR sequential-PLA. Then $n(j + 1) = [n(j)/2]$ where $[x]$ is the smallest integer greater than x and where initially, $n(0)$ = total number of terms to be XORed in product function f. At the last level, there is only one XOR circuit and the output is the value of f. In general, if k denotes the number of levels required in the XOR sequential-PLA, $k = [\log_2 n(0)]$.

It should be noted that as m gets large, the number of mod-2 sums in the function f becomes large. In this case, more XORs and as a consequence more levels in the XOR sequential-PLA are required. To maximize the pipeline operation speed, shift registers are required between the XOR levels in order to store the XOR outputs of the intermediate levels.

Another approach to the realization of product function f is to use a standard AND-OR PLA (Ref. 4). This is possible since $x + y = \bar{x}y \vee x\bar{y}$ where $\vee$ denotes inclusive OR. In general, although the design of f by the use of such a PLA is tedious, the product function f can be accomplished in less than one clock cycle. One trade-off for such a design is the large chip area required. The required area for such a PLA increases dramatically with m. Hence, a design utilizing a standard AND-OR PLA to realize f is practical only for small m.

IV. A Pipeline Structure for Computing an Inverse Element in the Finite Field ($GF(2^m)$)

For any α in the finite field $GF(2^m)$, $\alpha^{2^m} = \alpha$. Hence the inverse of α is $\alpha^{-1} = \alpha^{2^m-2}$. Let $2^m - 2$ be decomposed as $2 + 2^2 + 2^3 + \cdots + 2^{m-1}$, then α^{-1} can be expressed as

$$\alpha^{-1} = (\alpha^2) \cdot (\alpha^{2^2}) \cdot (\alpha^{2^3}) \cdot \cdots \cdot (\alpha^{2^{m-1}}) \qquad (13)$$

As discussed in Section II, if α is represented in a normal basis, squaring can be realized by a cyclic shift operation. α^{2^j} is the j-th cyclical shift (CS) of α. Thus, the inverse element α^{-1} can be obtained by using successive cyclic-shift operations and a Massey-Omura multiplier. The algorithm for α^{-1} is the following:

(1) Obtain the cyclic shift of α, i.e., $\alpha^2 = CS(\alpha)$ where CS denotes the cylic shift function. Let $B = CS(\alpha)$ and C = 1. Let k = 0.

(2) Multiply B and C to obtain the product, $D = B \cdot C$. Set $k = k + 1$.

(3) If k = m - 1, $\alpha^{-1} = D$. Stop. If $k < m - 1$, let $B = CS(B)$ and $C = D$.

(4) Go back to (2).

Figure 8 shows a flow chart diagram of this procedure.

This recursive algorithm for computing an inverse element in $GF(2^4)$ can be realized using the circuit shown in Fig. 9. In this circuit the parallel-type Massey-Omura multiplier shown in Fig. 3 with the circuit for the product function f shown in Fig. 4 is utilized.

To illustrate, let Ld_1 and Ld_2 be two control signals with period of four clock signals as shown in Fig. 9. Also let the normal basis representation of α be (a_0, a_1, a_2, a_3). At the end of the third clock pulse, the values $\bar{a}_1$, $\bar{a}_2$, $\bar{a}_3$ are stored in the input buffer flip-flops B_1, B_2, B_3, respectively. During the four clock cycle, $\bar{a}_3$, $\bar{a}_0$, $\bar{a}_1$ and $\bar{a}_2$ are simultaneously shifted to R_1, R_2, R_3 and R_4, respectively. With the appropriate connections among the input buffer flip-flops B_k and flip-flops R_k, the cyclic shift of $\bar{\alpha} = (\bar{a}_0, \bar{a}_1, \bar{a}_2, \bar{a}_3)$, i.e., $\bar{\alpha}^2 = (\bar{a}_3, \bar{a}_0, a_1, a_2)$ is obtained in R. At the fourth clock pulse R_5, R_6, R_7, R_8 are also fed the value "0". These four complementary values of "1" introduce the element 1 in $GF(2^4)$.

As it was discussed in Section II, a parallel-type $GF(2^4)$ Massey-Omura multiplier simultaneously yields four product components d_0, d_1, d_2, d_3. Therefore, during the next three clocks three successive multiplications, i.e., $\beta_1 = 1 \cdot \alpha^2$, $\beta_2 = \beta_1 \cdot \alpha^4$ and $\beta_3 = \beta_2 \cdot \alpha^8$ are performed for the inversion. When the third multiplication is completed, Ld_2 = 1. Thus

the output product digits, which together represent the inverse element α^{-1}, are fed into the output buffer flip-flops B_k. Finally these are sequentially shifted from the inversion circuit.

The above technique for computing the inverse of an element in $GF(2^4)$ takes four clock cycles. During these four clock cycles, the circuit in Fig. 9 allows the bits of the next element (following α) to be fed into it and the bits of the previous element to be shifted out of it, simultaneously. This type of circuit provides a full pipeline capability. A VLSI layout of the pipeline inversion circuitry for $GF(2^4)$ is presented in Fig. 10. Figure 11 shows the system structure of an inversion circuit for the general finite field $FG(2^m)$.

References

1. Massey, J. L., and Omura, J. K., Patent Application of *Computational Method and Apparatus for Finite Field Arithmetic*, submitted in 1981.
2. MacWilliams, F. J., and Sloane, N. J. A., *The Theory of Error-Correcting Codes*, North-Holland Publishing, New York, 1977.
3. Peterson, W. W., and Weldon, E. J., Jr., *Error-Correcting Codes*, MIT Press, Cambridge, 1972.
4. Mead, C., and Conway, L., *Introduction to VLSI Systems*, Addison-Wesley, Reading, 1980.

ORIGINAL PAGE IS
OF POOR QUALITY

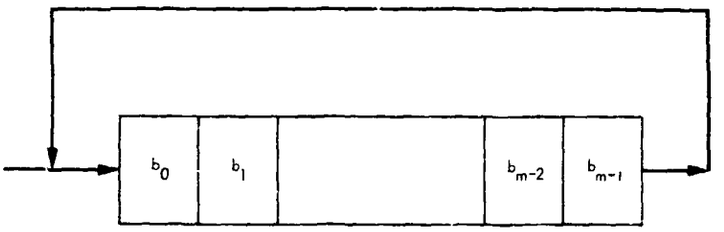

Fig. 1. The squaring operation for a normal-basis representation over $GF(2^m)$

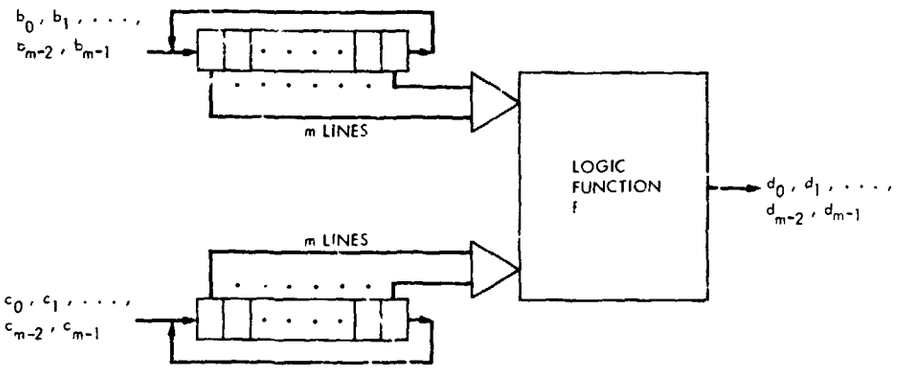

Fig. 2. System-logic diagram of a sequential-type Massey-Omura multiplier over $GF(2^m)$

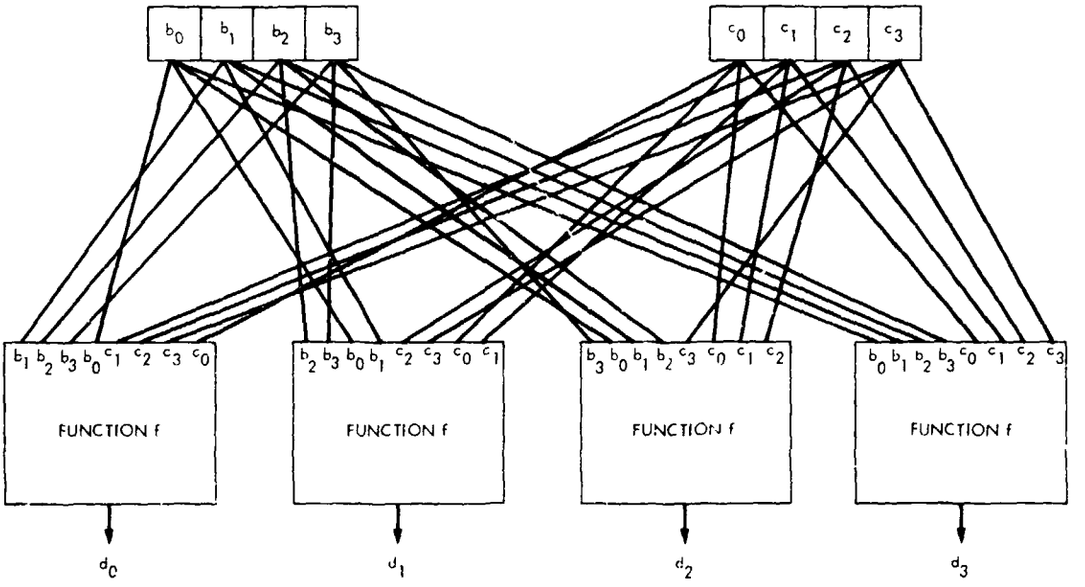

Fig. 3. Architecture of parallel-type Massey-Omura multiplier over $GF(2^4)$

ORIGINAL PAGE IS
OF POOR QUALITY

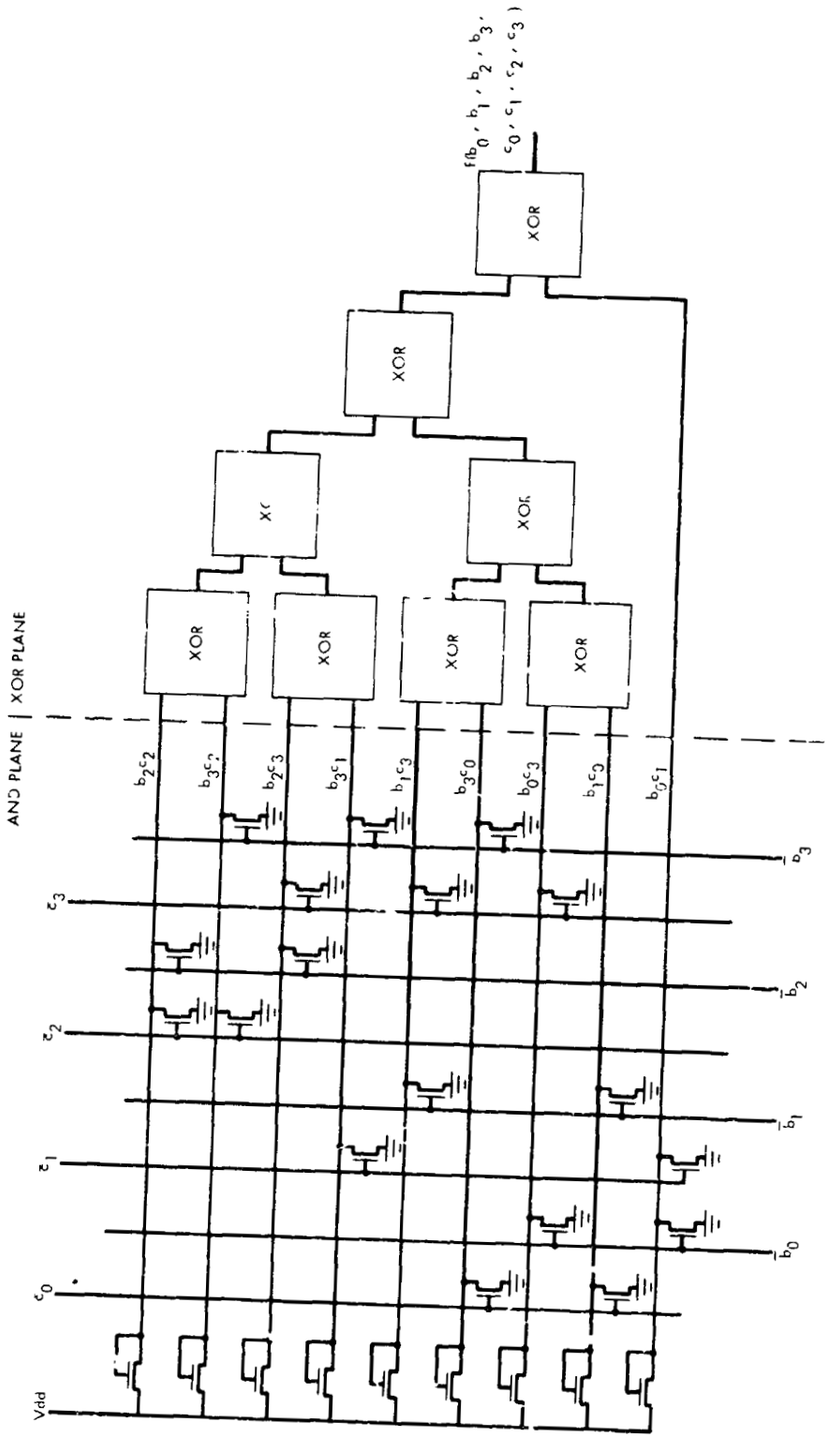

Fig. 4. Circuit diagram of product function f on GF(2⁴)

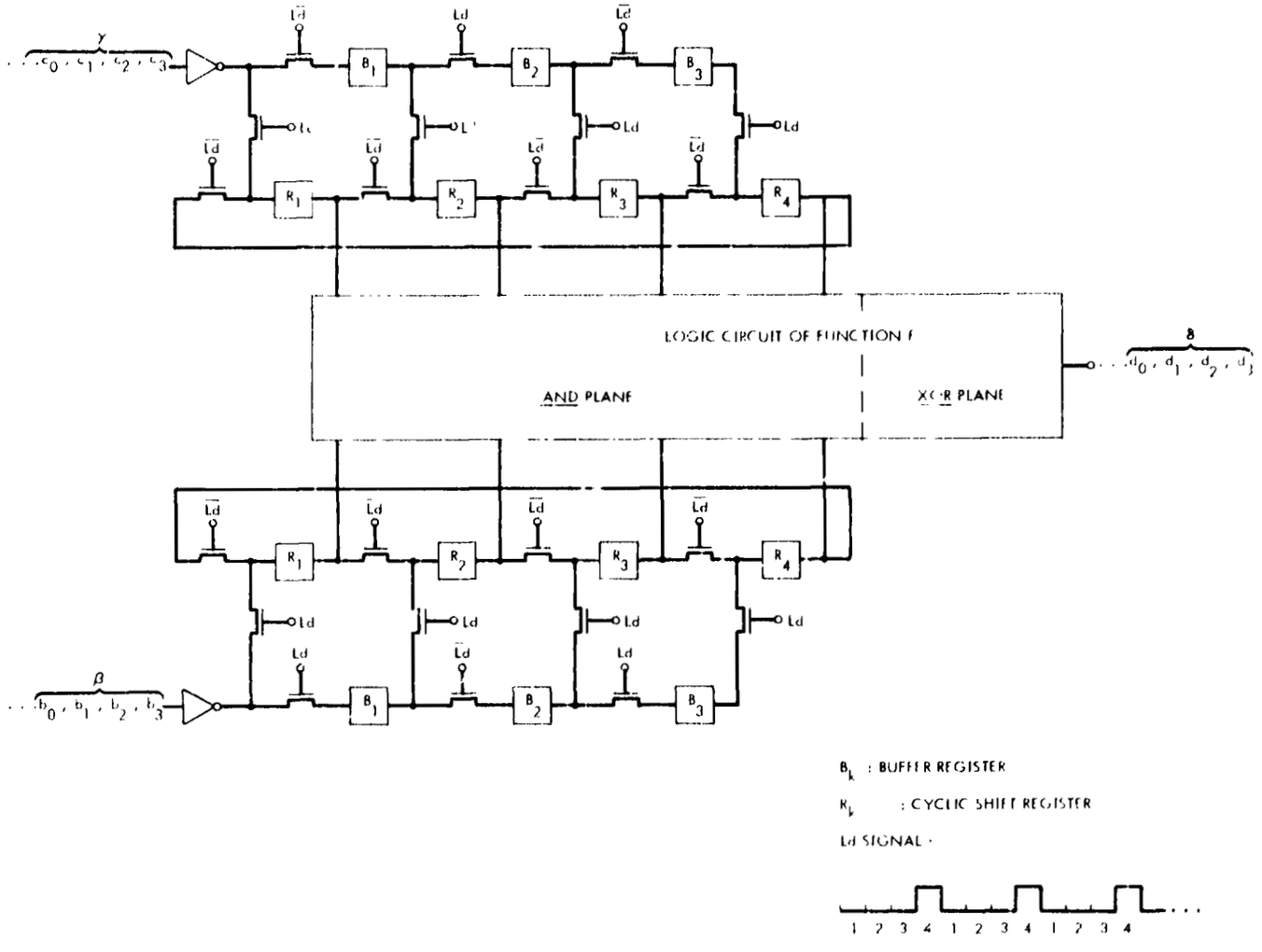

Fig. 5. A pipeline Massey-Omura multiplier for $GF(2^4)$

ORIGINAL PAGE IS
OF POOR QUALITY

ORIGINAL PAGE IS
OF POOR QUALITY

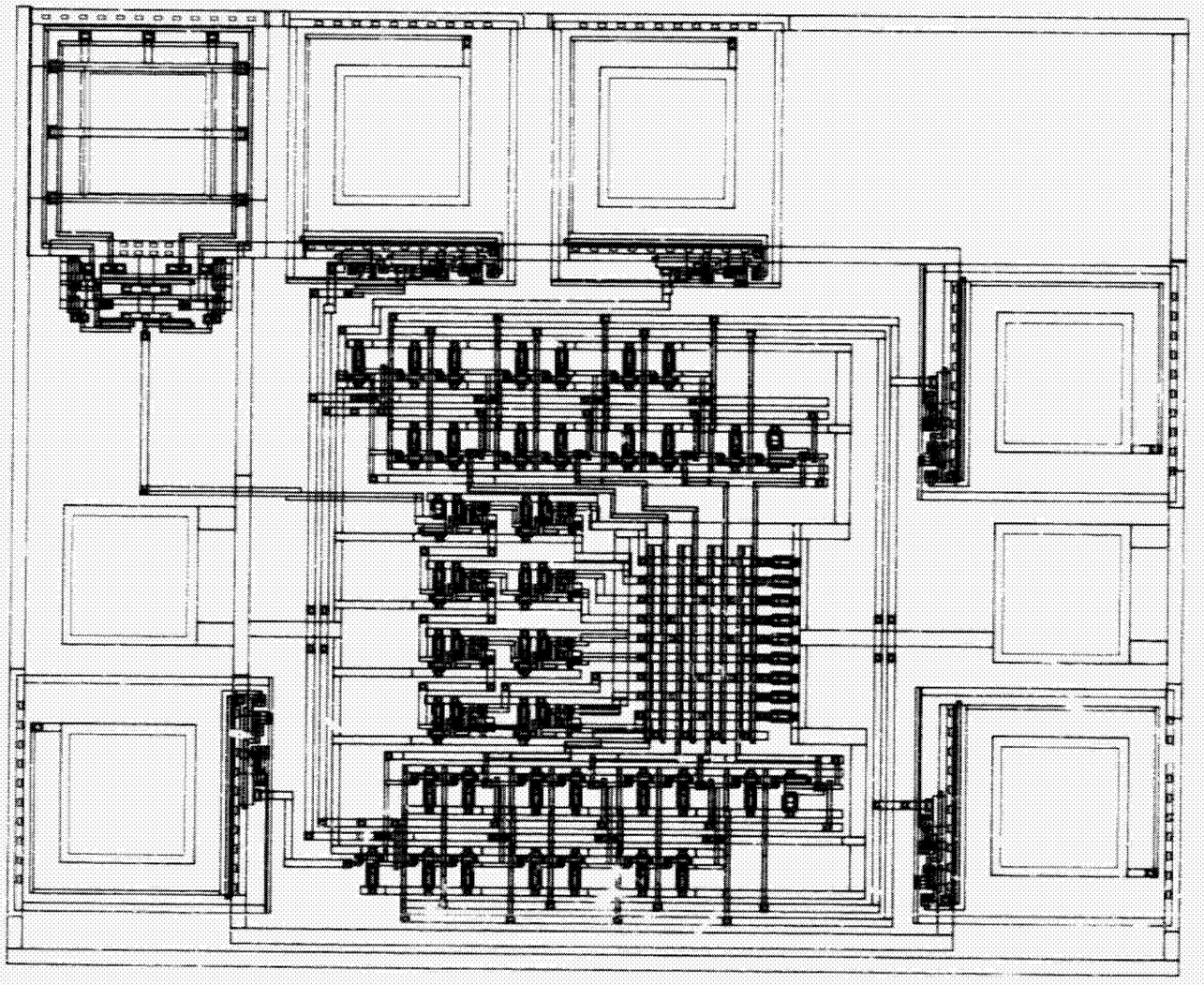

Fig. 6. Laycut of a Massey-Omura multiplier for $GF(2^4)$

ORIGINAL PAGE IS
OF POOR QUALITY

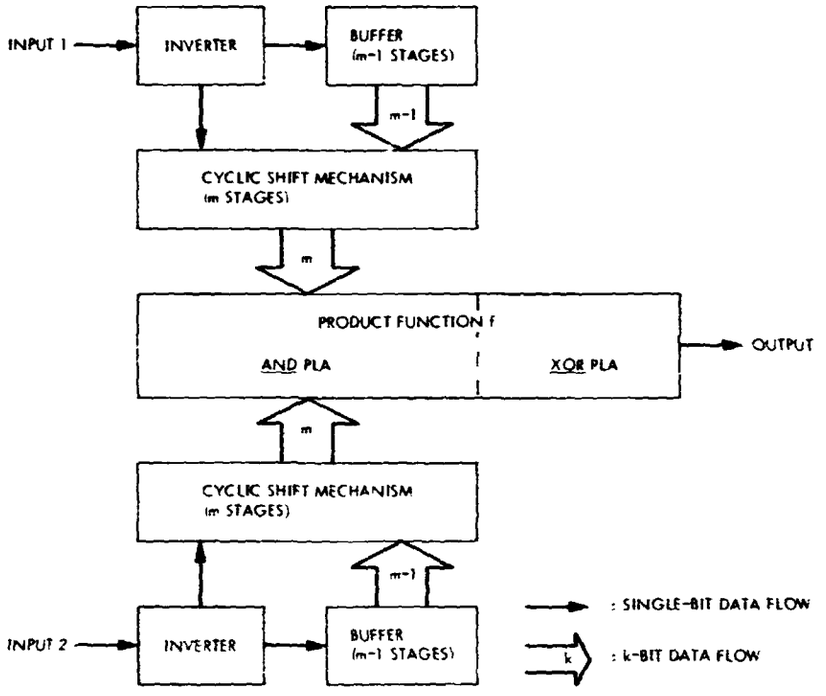

Fig. 7. System structure of a pipeline Massey-Omura multiplier for GF(2^m)

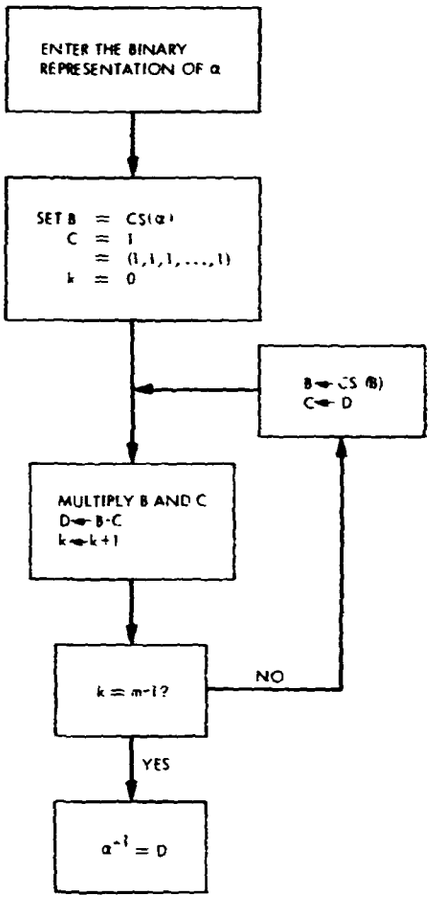

Fig. 8. Flow chart diagram of computing the inverse

ORIGINAL PAGE IS
OF POOR QUALITY

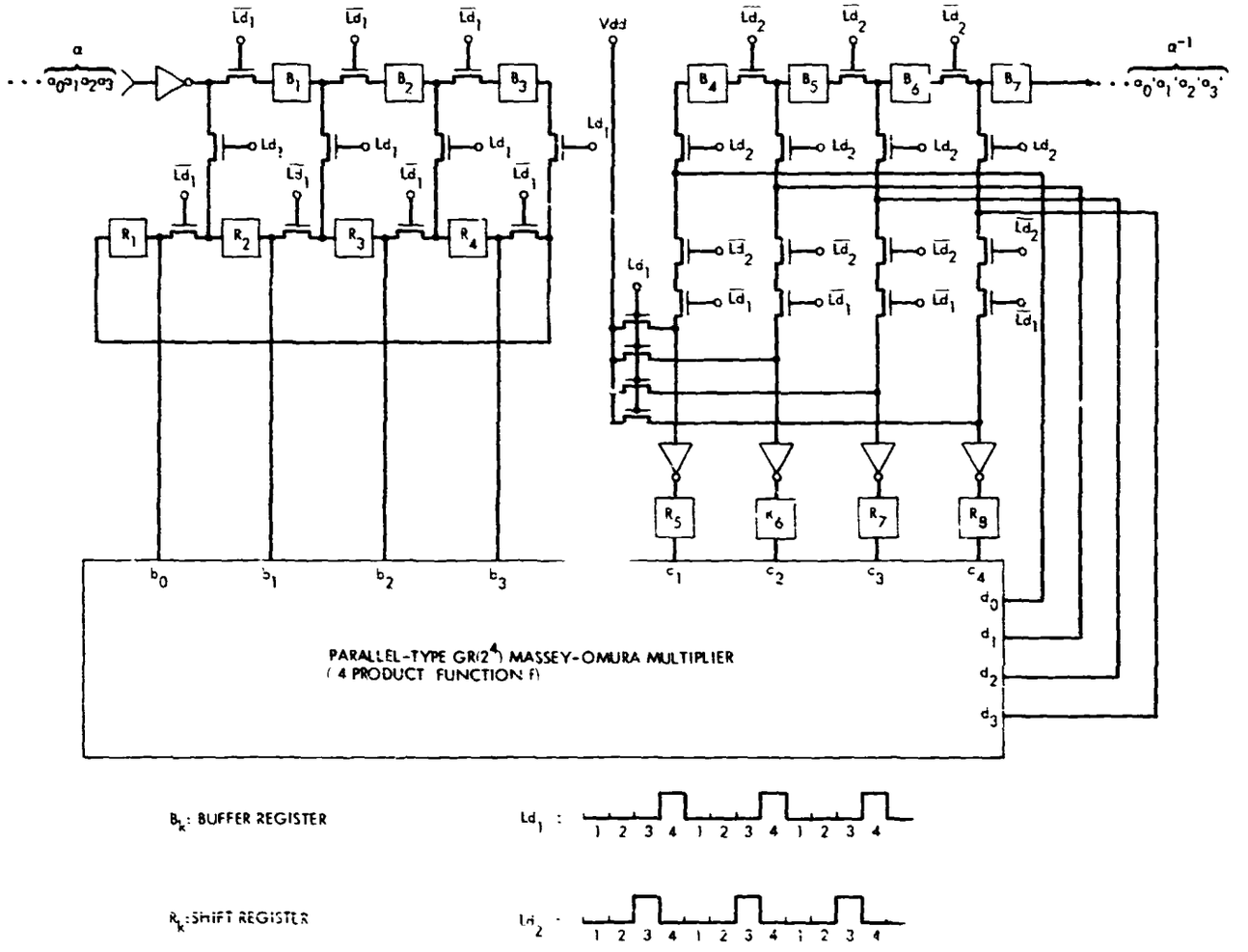
PARALLEL-TYPE GF(2^4) MASSEY-OMURA MULTIPLIER
(4 PRODUCT FUNCTION F)
B_k: BUFFER REGISTER
R_k: SHIFT REGISTER
Ld1 : 1 2 3 4 1 2 3 4 1 2 3 4
Ld2 : 1 2 3 4 1 2 3 4 1 2 3 4

Fig. 9. Pipeline structure of computing the inverse element in GF(2⁴)

ORIGINAL PAGE IS
OF POOR QUALITY

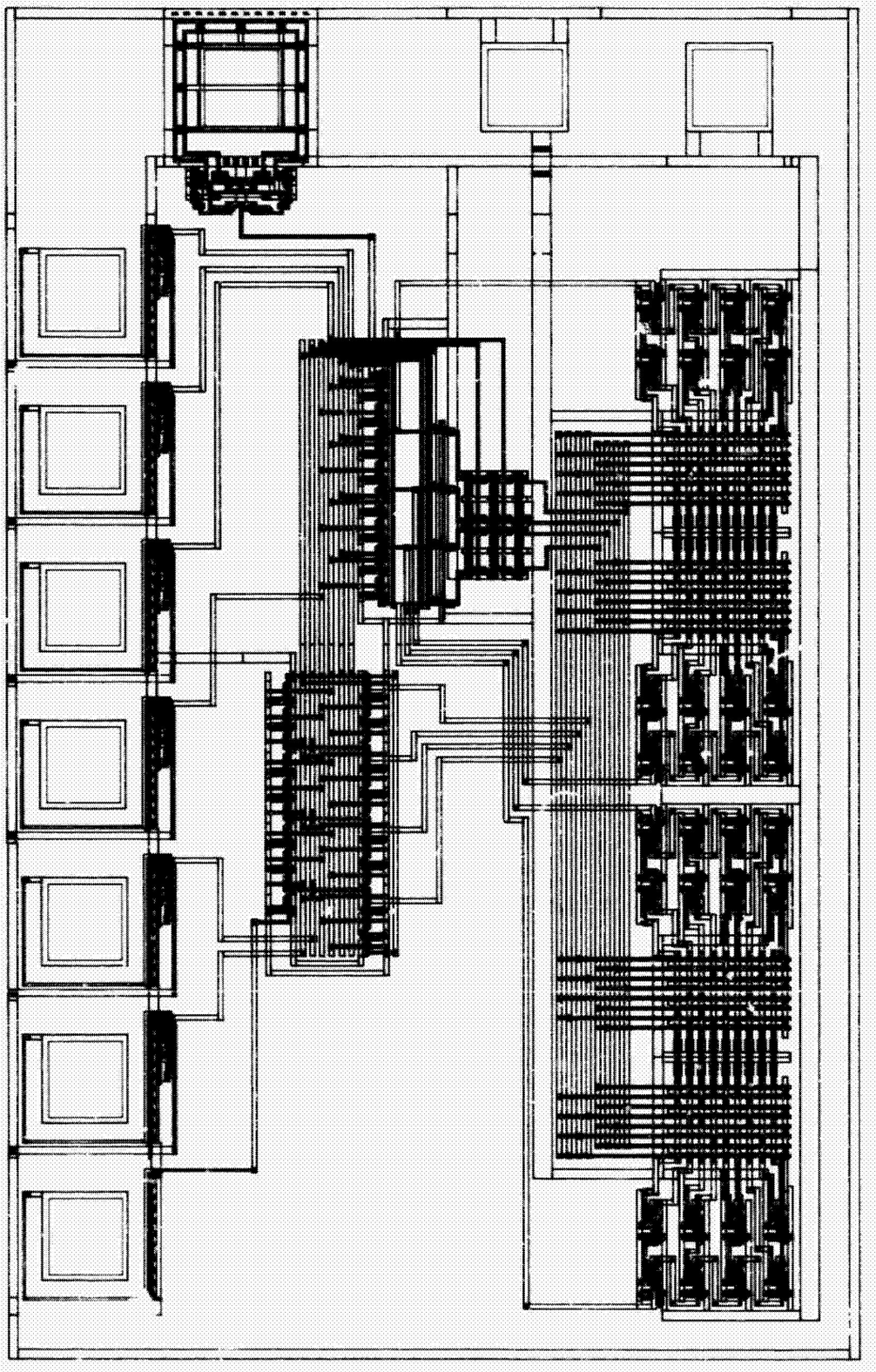

Fig. 10. Layout of the inversion circuit for $GF(2^4)$

ORIGINAL PAGE IS
OF POOR QUALITY

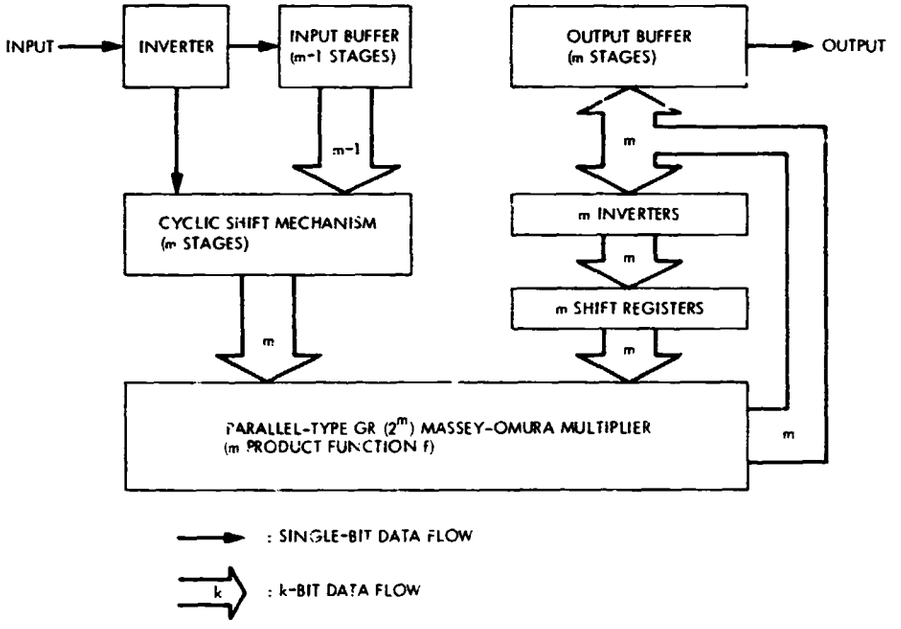

Fig. 11. System structure of a pipeline inversion circuitry for $GF(2^m)$

N84 13407

Deformable Subreflector Computed by Geometric Optics

M. S. Katow and I. Khan
Ground Antenna and Facilities Engineering Section

W. F. Williams
Radio Frequency and Microwave Subsystems Section

Using a Cassegrainian geometry, the 64-meter antenna with its distorted paraboloidal reflecting surface can be forced to produce a uniform phase wavefront by a pathlength-compensating subreflector. First, the computed distortion vectors at the joints or nodes of the main reflector structure supporting the surface panels are best fitted to a paraboloid. Second, the resulting residual distortion errors are used to determine a compensating subreflector surface by ray tracing using geometric optics principles. This computationally corrected subreflector surface is defined by the normal directions and distances to the surface of the original symmetric hyperboloid for the purpose of evaluation. Finally, contour maps of distortions of the paraboloid reflector and the compensating subreflector are presented. A field-measured check of the subreflector in focused position as computed by the described methodology is also presented for the antenna position at horizon look with the geometry at 45 degrees elevation.

I. Introduction

In the Cassegrainian radiofrequency (RF) antenna, the spherical wavefront emanating from the RF feed reverses direction at the hyperboloid focus, then it is reflected by the paraboloid reflector into a flat, uniform-phase wavefront to space. Since the diameter of the paraboloid is generally about ten times larger than the hyperboloid (and therefore more massive), its surface errors can introduce much larger distortions to the reflecting RF rays and hence introduce larger pathlength differences to the desired planar wavefront. The subreflector surface errors are usually minor or negligible in comparison.

Using a geometric-optics based ray-tracing technique in a subreflector-forming (SUBFORMING) computer program, the RF pathlength error introduced by the paraboloid's distortion may theoretically be compensated for at the subreflector's surface for each defined ray.

The 64-meter antenna reflector structure (at DSS 14), with structural brace modification included, has been modeled using NASTRAN computer analysis to compute distortions caused by environmental loads, e.g., gravity loading due to elevation angle motion. The distortions of the structural joints of the forty-eight main radial ribs (Ref. 1) were computed for the gravity loading at the antenna's horizon position

(elevation angle = 0) with the surface panels previously set to the design paraboloid at a 45-deg elevation angle. A paraboloid was best fitted to these distortions using the RMS program (Ref. 2) and the resulting antenna variables were used in the SUBFORMING program and evaluated by the NORM program.

II. Analysis Steps

The input data required by the geometric optics-based program SUBFORMING (see Appendix A) are delineated in Fig. 1. The main reflector structure's computed distortions in Cartesian coordinates ΔX, ΔY, and ΔZ are added vectorially to the undeformed coordinates of the reflector structure to define the distorted shape. A new best-fit paraboloid is then determined for this distorted shape using the RMS program (Ref. 2), which defines a new coordinate system for the new paraboloid (which has been rotated and translated relative to the original). The rotation-translation of the best-fit paraboloid is indicated in Fig. 1 by *ZETA* (rotation) and *HZ*, *HY* (translations).

The RF feed phase center is defined in Fig. 1 by PDSC. The RF feed phase center and the focus of the best-fit paraboloid have deflected from gravity loading, assuming that the hyperboloid system is focused axially and laterally. The hyperboloid focal length *FCO* has changed to *FC* due to the deflections of the RF feed and the change in focal length of the paraboloid.

The original nodes of the paraboloid (before the distortions ΔX, ΔY, and ΔZ) were located on radial lines equally spaced at 7.5 deg (ψ) around the central axis and in approximately equal intervals (9 points) along the radials. However, with distortions and surface-slope changes resulting from gravity loading, a ray parallel to the axis of the best-fit paraboloid will not necessarily stay in the plane defined by the ray and the hyperboloid's axis as the ray reflects from the distorted surface of the paraboloid. When this reflected ray impinges on a symmetric hyperboloidal subreflector and is again reflected, it will miss the RF feed phase center. Therefore, a compensating reflecting surface on the subreflector will be required to maintain focus.

The SUBFORMING program computes points P on the compensating subreflector, thus maintaining the equal path-length requirements for all rays, as described in Appendix A. In a spherical coordinate system as delineated in Fig. 2, the program outputs the radius R and the angles θ and ϕ to locate points P and the vector normal to the surface of the compensating subreflector at points P.

One assumption was made at this time: the normal to the compensating subreflector lies in the ϕ-plane, although SUBFORMING may not generate this answer for distorted paraboloids. This reduces the solution of the normal corrections with respect to the design hyperboloid parameters to a two-dimensional problem. The normal corrections computed for each ϕ value could then be used to plot the surface contours with minor errors.

Referring to Fig. 3, the equation of the normal correction, *PS*, can be developed from the data described in Fig. 2 (see Appendix B). The normal's intercept point, S, on the hyperboloid is computed and the normal length *PS* (required correction) is then computed.

The above described steps were incorporated in the computer program NORM with an added provision to translate points P parallel to the symmetric axis *0Q* of Fig. 3 to simulate the focusing motion along the symmetric axis of the hyperboloid.

The computed normal corrections may be contour plotted using JPL's plotting subroutines where the intersection points of the normals and the hyperboloid are not required to be uniformly spaced.

III. Solution Verification

One check of the methodology was made by considering the 64-meter antenna reflector data with no distortions as inputs to the SUBFORMING program using the design values (Fig. 3) for the 45-deg elevation as follows:

Paraboloid focal length:		26.0933 m (1027.294 in.)
Hyperboloid parameters:	a =	4.5219 m (178.029 in.)
	b =	5.1560 m (202.992 in.)
	c =	6.8580 m (270.000 in.)

The answers from the SUBFORMING program were input to the NORM program; the largest normal corrections were found to be 0.0015 mm (0.00006 in.). In other words, the SUBFORMING program's output of points P was verified to be accurate enough for the design hyperboloid.

A. Check On Antenna Horizon Position

In antenna operation, the reflective surfaces are "rigged" or set at 45 deg elevation angle. As the antenna rotates to the horizon position, the main paraboloidal reflector not only distorts, but also changes in focal length as described by the best-fit paraboloid. The prime focus translation requires focusing motion of the design hyperboloidal subreflector as well as

shape changes to maximize performance. By use of the SUBFORMING program, the original design hyperboloid can be proven to be in perfect focusing position for the shorter focal length best-fit paraboloid of the horizon position, if the distance a of Fig. 3 is correct.

The computed parameters after the best-fit of a paraboloid to the distortions at horizon position are shown in Fig. 4 with the contour map of the normal errors pictured in Fig. 5 (generated by the RMS program).

First, it was necessary to locate the position a of the design hyperboloid at focused position. This was accomplished by reducing the distortion of the best-fit paraboloid to zero. Second, the curve of the subreflector generated by the SUBFORMING program was matched exactly to the original design hyperboloid by translating the generated subreflector until the normal corrections were reduced to very small values. This was accomplished by iteration of X_1 of Fig. 3 in the NORM program, and by changing the value of a.

Finally, by using distances a and x_1 (computed above), the horizon position distortions were added to the SUBFORMING program and the deformed shapes of the compensating subreflector (as described by normal corrections to the design hyperboloid) were then contour plotted in Fig. 6. As expected, the normal corrections on the hyperboloid are the exact picture of the paraboloid's distortion as given by Fig. 5.

B. Field Verification

A comparison of the focused position of the 64-meter antenna hyperboloid computed in this article and field data is made. Figure 7 illustrates the computed hyperboloid focus travel from the 45-deg setting position to the horizon position, which is 2.11 cm (0.83 in.).

Figure 8 (Ref. 3) presents the field data where a rather large extrapolation is required to determine that the subreflector indicated movement is (2.54 cm -0.58 cm) or 1.96 cm (0.77 in.). Since the field-indicated position of the subreflector is obtained from a revolution counter on the jackscrew drive of the subreflector's supporting system, the deflections of the jackscrew mechanism and the supports of the subreflector are lost. If some of the above noted lost deflection is added to the measured travel of 1.96 cm (0.77 in.), the field data will compare closely to the computed 2.11-cm (0.83-in.) travel.

It should be noted that there has been a lack of consistency of the indicated subreflector position between different RF feeds; this inconsistency has not been resolved to date. A possible reason involves the RF beamshaping peripheral flange, fitted around the hyperboloidal portion of the subreflector. This flange is effective in reducing feed spillover power beyond the paraboloid edge, and is optimum for S-band. The 30.48-cm (12-in.) radial distance of the flange (about 2λ at S-band) is not optimum at other (particularly higher) frequencies. We believe that these field-measured subreflector positions for the antenna maximum gain are influenced by phase best fitting, of the feed wavefront ripples near the paraboloid rim.

IV. Summary

(1) The duplication of the distortions of the main paraboloidal reflector and the compensating subreflector by contour maps indicated accurate solutions by the SUBFORMING program. For improving the performance of a Cassegrain antenna, the subreflector surface can be altered mechanically as the antenna rotates from its "rigged" or setting elevation position.

(2) The mathematical methods used in the SUBFORMING program were checked for accuracy by: (a) generating a perfect hyperboloidal subreflector for a perfect paraboloidal main reflector, and (b) determining the new focus of the original design hyperboloid for a paraboloid with a changed focal length that checks the field measured value for the 64-meter antenna.

(3) Deforming the subreflector of the 64-meter antenna to match the bumps over the elevation bearing will be difficult to implement because: (1) the sharp curvature changes will require stretching, and (2) additional stiffness is required of the subreflector to satisfy operational specifications in a high-wind environment.

References

1. Tracking and Data Acquisition, Technical Staff. *The NASA/JPL 64-Meter-Diameter Antenna at Goldstone, California: Project Report*. Technical Memorandum 33-671, Jet Propulsion Laboratory, Pasadena, Calif., July 15, 1974.

2. Katow, M. S., and L. W. Schmele, "Antenna Structures: Evaluation Techniques of Reflector Distortions," in *Supporting Research and Advanced Development, Space Programs Summary 37-40*, Vol. IV, pp. 176-184. Jet Propulsion Laboratory, Pasadena, Calif., Aug. 31, 1965.

3. Freiley, A. J., "Radio Frequency Performance of DSS14 64-m Antenna at X-Band Using a Dual Hybrid Mode Feed," *DSN Progress Report 42-53*, July and August, 1979, Jet Propulsion Laboratory, Pasadena, Calif.

ORIGINAL PAGE IS
OF POOR QUALITY

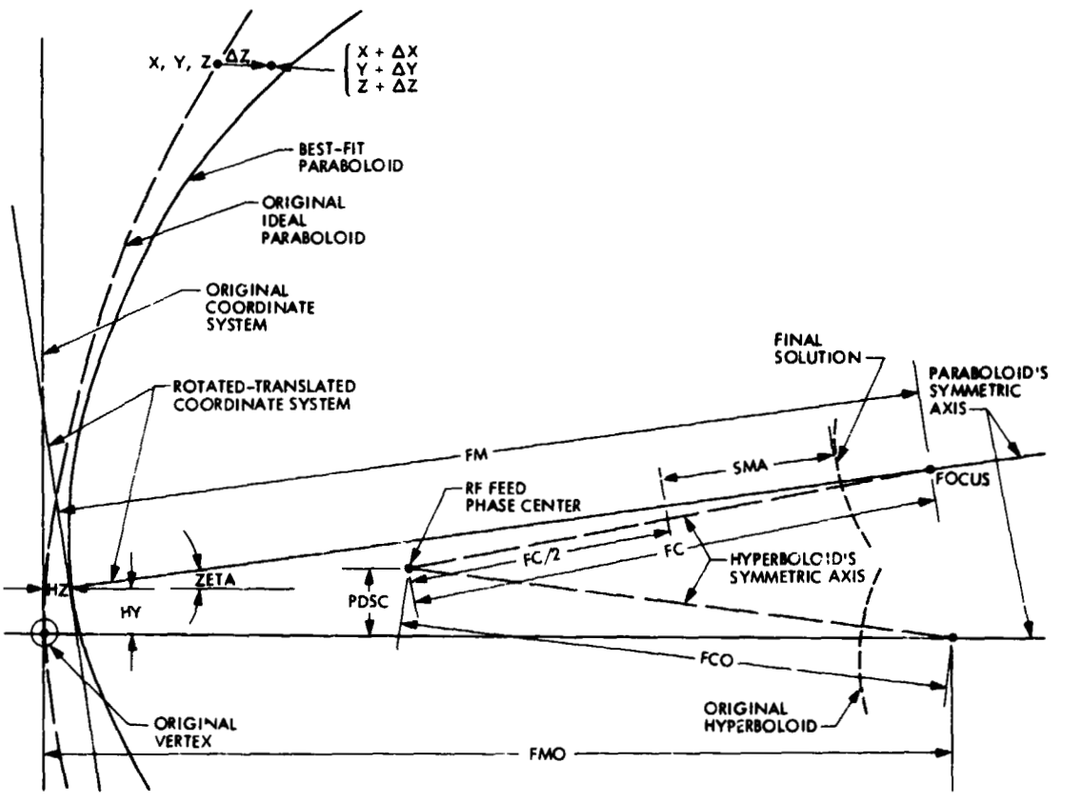

Fig. 1. Best-fit paraboloid's coordinate system

ORIGINAL PAGE IS
OF POOR QUALITY

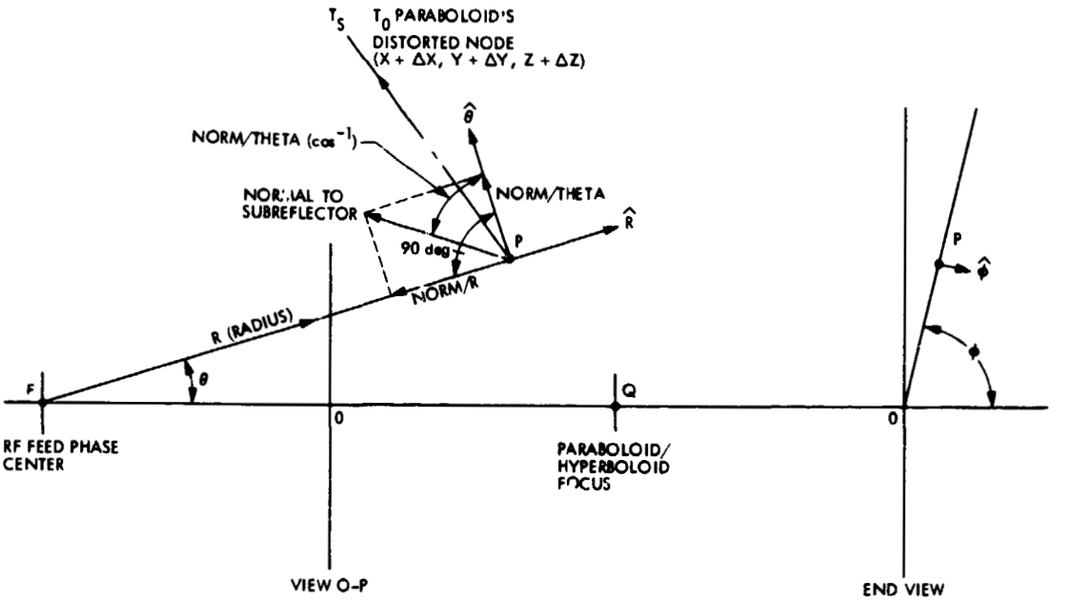

Fig. 2. RF rays coordinate system at feed phase center

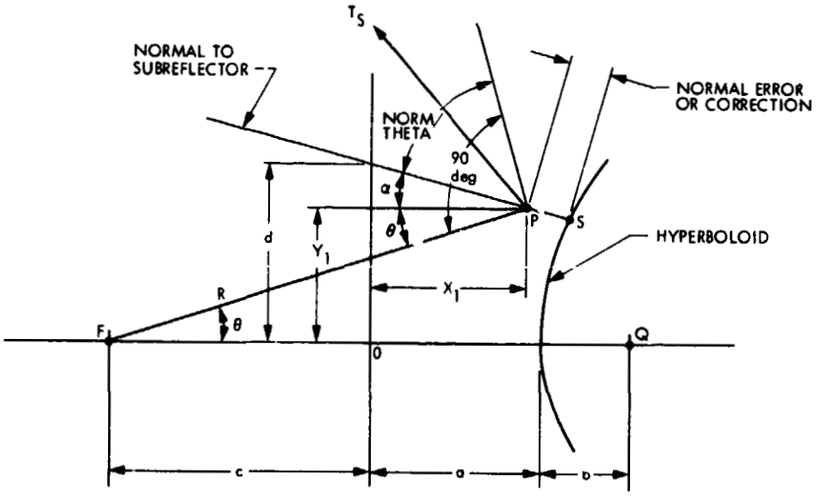

Fig. 3. Normal error or correction in ϕ-plane

ORIGINAL PAGE IS
OF POOR QUALITY

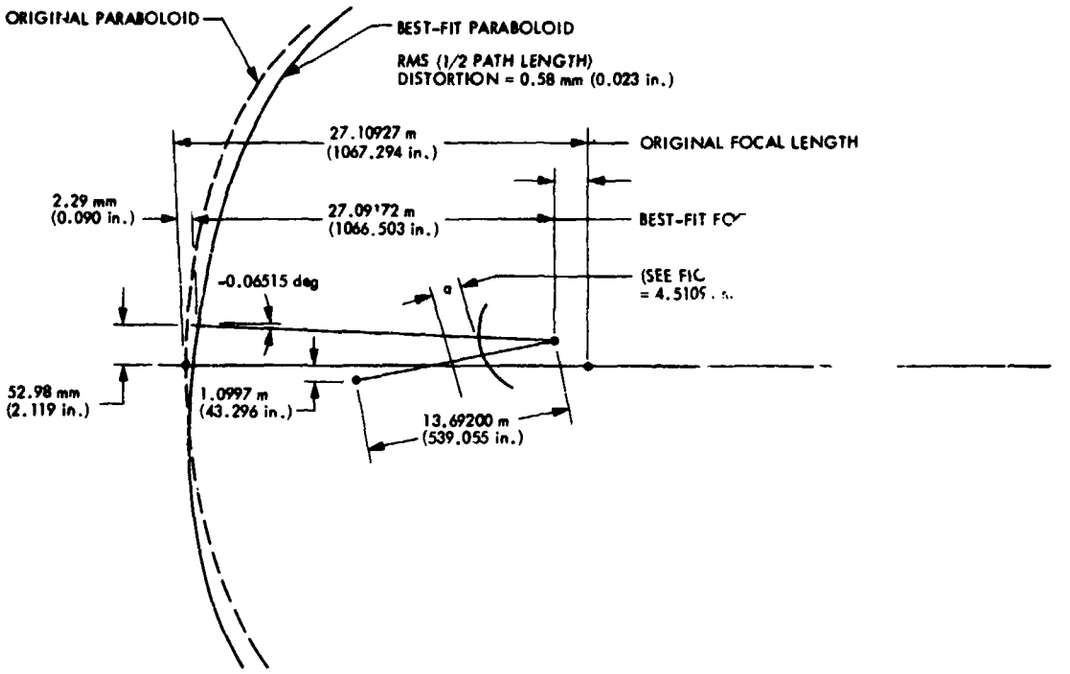

Fig. 4. Horizon position best-fit parameters (surface panels set at 45 deg)

ORIGINAL PAGE IS
OF POOR QUALITY

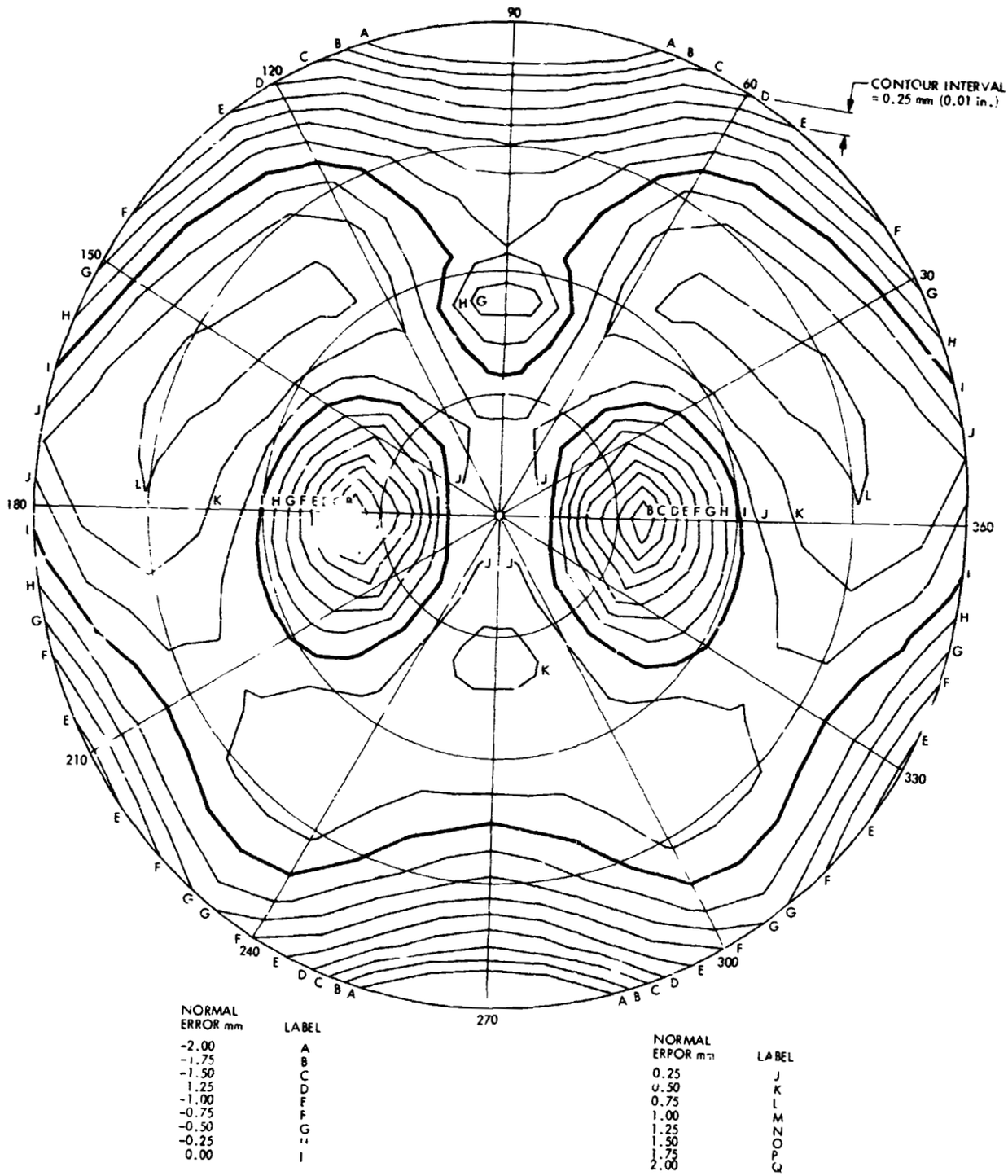

Fig. 5. 64-meter parabolic distortion contour map-after best-fit at horizon position (surface panels set at 45 deg)

ORIGINAL PAGE IS
OF POOR QUALITY

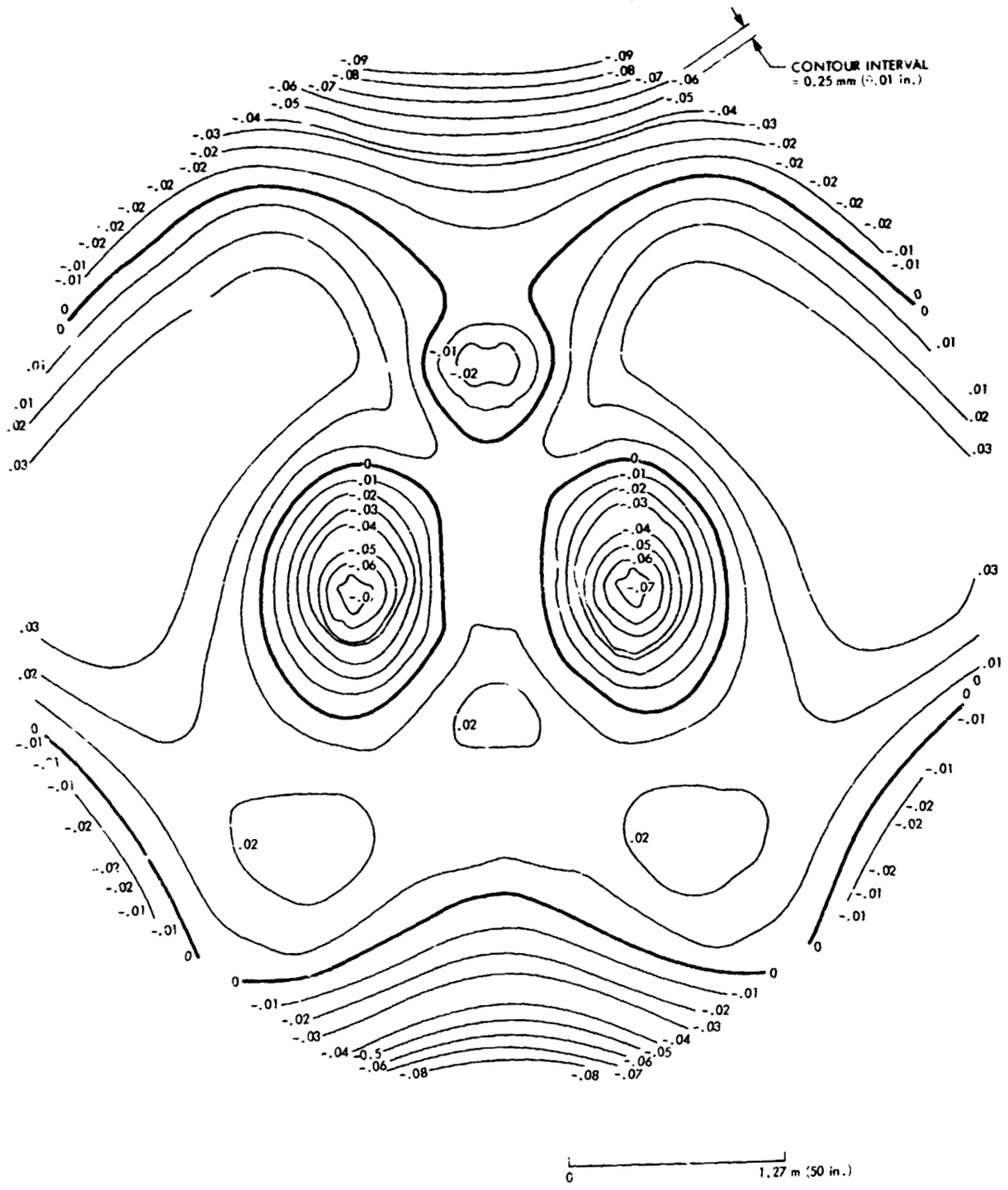

Fig. 6. Deformed compensating subreflector contour map (horizon position, setting at 45 deg)

ORIGINAL PAGE IS
OF POOR QUALITY

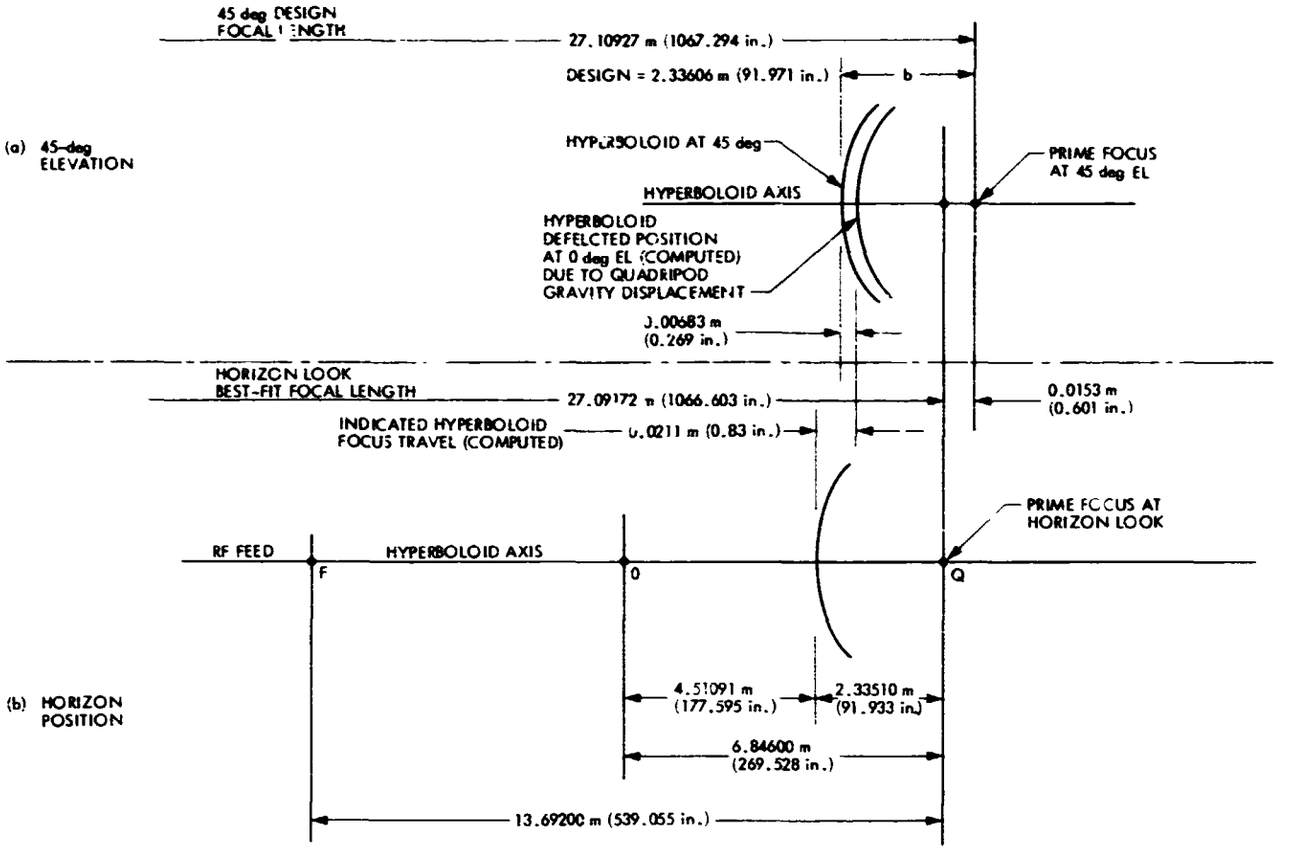

Fig. 7. Computed focus travel of the hyperboloid from 45-deg elevation to horizon position

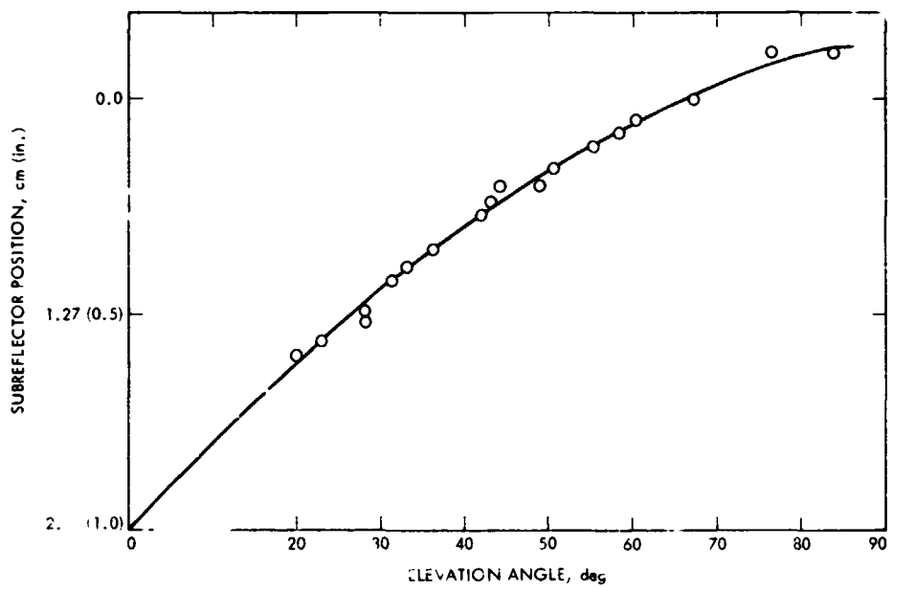

Fig. 8. Indicated subreflector position vs. elevation angle (field readings)

Appendix A

The Subforming Program

I. Theory of Operation

A computer program has been developed, using geometric optics, for synthesizing the needed deformation of a subreflector to compensate for a deformed main reflector, maintaining R^{-} path lengths and hence eliminating phase loss. This synthesis depends upon three factors to be determined about each main reflector point. These are: (a) the point, X, Y, and Z, (b) partial derivatives at each point, $\partial/\partial Z$, $\partial/\partial\rho$ and $\partial/\partial\psi$ (choosing a cylindrical system) and, (c) a chosen pathlength that must be held constant. The technique for doing this is as follows: at a main reflector point, (deformed), determine the slopes of the surface, $\partial/\partial\rho$, $\partial/\partial Z$ and $\partial/\partial\psi$ (in cylindrical coordinates), and from this determine the components of the normals, n_z, n_ρ, n_ψ. The direction of the incoming rays is known, assumed in the $-Z$ direction, and hence the reflected ray direction can be determined. The direction cosines for the reflected ray are then calculated. This reflected ray must intersect the unknown (to be calculated) deformed subreflector and be reflected to the RF feed point, or focus. Total distances for all rays must be equal and constant. This pathlength is somewhat arbitrary. The length used in the SUBFORMING program is the distance from the paraboloid aperture along the axes to the paraboloid vertex, back to the original hyperboloid vertex and back to the feed focus (or phase center). The ray direction and this pathlength requirement represent sufficient information to determine the subreflector points, (X_S, Y_S, Z_S). The reflected ray will also determine the components of the normal and the slopes, $\partial Z_S/\partial X_S$ and $\partial Z_S/\partial Y_S$. This same data is used to calculate the points in the spherical coordinate system as is generally desired. (Ref. 4)

Performing these operations upon a paraboloid that is deformed in some closed-form analog manner is fairly straightforward, e.g.,

$$\Delta Z = A\,\rho\cos N\psi$$

Partial derivities can be evaluated at as many points as desired; normals and direction cosines and hence ray directions are determined and a matching subreflector point is obtained corresponding to the main reflector data point. However, with a real system (the 64-meter, DSS 14 antenna), deformation data is presented in a regular fashion as digital error points along approximately equal radial distances from the antenna vertex and at approximately equal angles around the azimuth direction ψ. No data regarding slopes are available and so a method should be found to determine these required functions. The 432 distinct points are available (from DSS 14 data) and the appropriate slopes are found for each point. The approach chosen is to place a best-fit polynomial surface through nine points, eight of them surrounding the central point, as indicated in Fig. A-1. In this two-dimensional figure, the dimension Z is not indicated, only the cylindrical coordinates ρ and ψ. The best-fit surface is theoretically determined using available JPL computer subroutines. A separate surface is obtained for each deformed point of the paraboloid since the local surface determination will be at its best for the one central point. Exceptions are for the last points (farthest) out on the antenna periphery (rim) and the innermost points near the vertex. In these cases, slopes are determined using the surface that is generated about the next adjacent point on the radial.

The best-fit surface generated for each deformed point will be represented by a quadratic equation $Z = g(\rho, \psi)$ with six constants determined by the subroutine. Partial derivatives are then determined and evaluated. Normals and direction cosines are calculated. The subreflector point (X_S, Y_S, Z_S) is determined as a point on the ray path which, with reflection, will fulfill the chosen equal pathlength requirement. The direction of the ray reflection is used to calculate subreflector slopes and normals. Spherical and/or cylindrical coordinates are obtainable directly from the Cartesian solution.

Use of the computer program is described in the following paragraphs. Input parameters are as shown in Fig. 1.

II. Program Structure

Distortion data are input as error positions, ΔX, ΔY, and ΔZ, from the main reflector coordinates, X, Y, and Z. These distortion points must be presented in a sequence that: (1) proceeds from an inner hub position, (2) proceeds out along an approximate radial line to a final position on this radial, (3) proceeds to a next-adjacent radial starting at the hub, and again proceeds out this radial, and (4) continues around the reflector surface until completed. Angular positions between radials should be approximately equal as should the radial spacing between listed radial points, for improved program accuracy. The program is set to accept up to 15 points on any radial position and 60 radial lines, i.e., 6 deg apart, for a total of 900 distortion points. These distortion points will generally be defined relative to an "ideal" paraboloidal reflector with a coordinate system, which has its origin at

the vertex and its Z-axis through a focal point. A best-fit paraboloid is recognized as a better fit to the distorted system. In this case, it is desirable to define a new coordinate system according to this best-fit paraboloid vertex and focal length. This coordinate system is input to the program.

The solution is a set of output points P defining a subreflector contour. Each point matches, on a one-to-one basis, a point on the distorted paraboloid. The slope of and the normal to the surface are determined for each point. The data appear on three files when the program is executed. The first file contains the input data concerning the main reflector, the second file contains subreflector data in spherical coordinates, and the third file contains the same data in Cartesian coordinates. These files can then be recorded in a data file, punched or placed on temporary files, and printed.

III. Inputs

1. Title = your choice
2. *FMO* = focal length of original "ideal" paraboloid
3. *FCO* = focal length of original hyperboloid
4. *FM* = focal length of chosen "best-fit" paraboloid, can be the original focal length, *FMO*.
5. *D* = diameter of main reflector
6. *FC* = focal length of chosen subreflector, i.e., distance from feed focus to the focal point at *FM*, could be *FCO*
7. *SMA* = the dimension "a" of a hyperboloid, taken from the chosen vertex of the subreflector to the origin of *FC*/2
8. *PDSC* = feed displacement relative to the "ideal" paraboloid reflector axis in Y direction only
9. *HZ* = best-fit vertex translation in Z direction, taken from original coordinate system origin (may be 0.0)
10. *HY* = as *HZ*, but in Y idirection
11. *ZETA* = best-fit axis rotation relative to original axis, in Y-Z plane only (may be 0.0)
12. *JMAX* = Number of data points on one radial; must be equal for all radials
13. *KMAX* = Number of radial lines
14. $X(J,K)$, $Y(J,K)$, $Z(J,K)$ = Coordinates of point (J, K) on the original "ideal" reflector.
15. $DX(J,K)$, $DY(J,K)$, $DZ(J,K)$ = Distortion magnitude in the X, Y, and Z directions to the final reflector

IV. Output

The printed output consists of the listed input main reflector (deformed) data in the new coordinate system and the solution for the subreflector in spherical coordinates in this same coordinate system.

ORIGINAL PAGE IS
OF POOR QUALITY

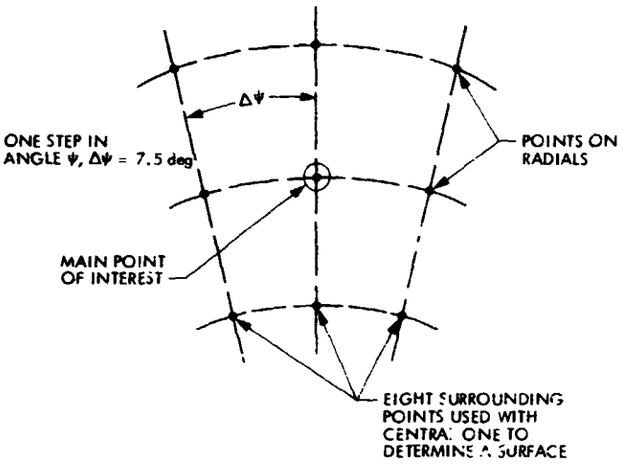

Fig. A-1. Nine points best-fit polynomial surface

ORIGINAL PAGE IS
OF POOR QUALITY

Appendix B

NORM Program

Referring to Fig. 3, the equation for the normal *PS* was developed, and after its intercept to the hyperboloid (two dimensional analysis in plane ϕ, see Fig. 2) was calculated, its length between the point *P* and *S* was computed. The equation of the normal is

$$Y = mX + d \tag{B-1}$$

where

$X_1 = R \cos\theta - 270$

$Y_1 = R \sin\theta$

$\alpha = -90 + \cos^{-1}(\text{norm/theta}) + \theta$

$m = \tan\alpha$

$d = Y_1 - X_1 \tan\alpha$

Substituting above values in Eq. (B-1),

$$X = (TA)Y - C1 \tag{B-2}$$

where

$$TA = 1/\tan\alpha$$

or

$$\frac{Y_1}{\tan\alpha} - X_1 = C_1$$

The hyperbola equation is

$$\frac{x^2}{a^2} - \frac{Y^2}{b^2} = 1 \tag{B-3}$$

Substituting equation (B-2) into (B-3) for *X* and solving the resulting equation by the binomial equation, the intercepts on hyperbola become

$$Y_H = \frac{-CB \pm \sqrt{CB^2 - 4 \cdot CA \cdot CC}}{2 \cdot CA}$$

$$X_H = \sqrt{\frac{a^2 b^2 + a^2 Y_H^2}{b^2}}$$

where

$$CA = TA^2 - \frac{a^2}{b^2}$$

$CB = -2TAC1$

$CC = C1^2 - a^2$

N84 13408

An EPROM-Based Function Generator

L. Fowler and J. A. McNeil
Radio Frequency and Microwave Subsystems Section

A circuit is described to produce arbitrary time-dependent voltage functions derived from digital information stored in EPROMs. While this circuit is designed to be used as a modulator of the microwave pump source for a solid state low noise maser, it can be readily adapted for other applications

I. Introduction

Although there are many published descriptions of circuits to generate specific (sinusoidal, logarithmic, etc.) or arbitrary waveforms using electrically programmable read-only memory (EPROM) and digital-to-analog converter (DAC) devices, this report presents an implementation that is somewhat unique in that (1) it can be controlled and monitored externally by a computer through parallel ports, and (2) it can be programmed to hold a particular output, or to sweep over any portion of the output function without sweeping the entire range. These special features make this circuit particularly useful as a voltage source for the frequency modulation of an IMPATT oscillator, which is used as a microwave pump for the solid state masers used in the DSN as very low noise amplifiers. Since the waveform is determined by the operating characteristics of an individual maser, the use of an EPROM allows the waveform to be readily modified. The discussion of this particular application will be the subject, however, of another TDA report. In this report we describe the circuit and its operation.

II. Circuit Design and Description

The circuit described here provides a periodic voltage of amplitude from 0 to 10 volts, with 12-bit resolution, utilizing readily available components. In addition to the two requirements described above, this circuit is designed to provide an output symmetrical about one-half the total period.

Figure 1 shows a block diagram of the circuit. The symmetrical output is achieved by controlling a 12 bit up/down counter to count up continuously from a low value (low limit) to a high value (high limit) and then reversing direction (i.e., count down) until the low limit is reached again. This linear digital sweep produced by the counter is used as the address for the EPROM, whose output is then tied to the DAC where the output voltage is produced. (The output can be held constant by setting the high limit and the low limit equal to each other.)

Figure 2 shows the schematic for the clock oscillator, the low and high limit comparators and logic providing the up/down control, and the command decoder providing the external control. A brief description of each section is presented here.

A. Clock

The clock signal is generated by a (74C14) Schmitt trigger oscillator and is buffered by another Schmitt trigger. This signal is steered by the counter control logic to provide the count up and count down clocks for the binary counter. The clock frequency used in this application is 2 MHz, which at 32 point/period provides an output frequency of 60 kHz (2000 kHz/32).

B. Counter Control Logic

High and low limits supplied by the data bus are stored by hex latches (74C174) when enabled by the command decoder,

and compared to the EPROM address as provided on the counter bus. Cascaded 12-bit magnitude comparators (74C85) provide low/high limit signals to the up/down counter controller circuit, which when enabled on the positive clock transition drive the bidirectional binary counter. The logic insures that the counters start at known value and begin sweeping in the proper direction.

C. Command Decoder Circuit

Commands provided on the control bus are decoded by Intel (8205) 3 bit to 8 line decoders to provide four commands. U24 provides a card type select decoder, U23 a unit select, and U22 provides a command select. As implemented here, the command syntax is as follows.

bit	7	6	5	4	3	2	1	0	
	0	0	1	0	0	0	x	x	
	x	x	x	.	.	.	.	.	card type, 0 - 7
				x	x	x	.	.	unit number, 0 - 7
							0	0	run
							0	1	load low limit. hold
							1	0	load high limit, hold
							1	1	load low and high limit, hold

This syntax was chosen so that the command byte can be generated in software by ORing with masks.

Figure 3 shows the schematics for the binary counters, the EPROMs, the DAC, and output stages, which we describe here briefly.

D. Binary Counter

The binary up/down counter consists of three 4-bit presettable up/down counters (74C193) cascaded with the clear inputs disabled. A load high and low command causes the twelve bits on the data bus to be loaded simultaneously into the high and low comparators and the binary counters. The quality signals from both comparators prevent the clock signal from appearing at the count up or down clocks. Thus the address on the EPROM is a fixed value, and the output of the DAC will be held at the corresponding fixed voltage. In this manner the function can be swept through point by point by the external computer. If, however, the load high and low command is followed by a load low (or high) command. the binary counter and the low (or high) comparator are loaded with new data to be found on the data bus. Only one of the low (or high) comparators now shows equality, and the steering logic will cause the counters to ramp up (or down) starting at the low (or high) address entered. (There is nothing to prevent low value to exceed the high value. The counter will increase from the low value entered, wrap around the zero, and continue to increase *until the high value is reached, then reverse its direction.)* Since the EPROMs used here are Intel 2716 (2048 x 8), only the eleven counter bits 0 to 10 are used to provide the addressing. However, all twelve bits are used by the control logic.

E. EPROM

Two EPROMs are addressed in parallel to provide 16-bits of output data. Since the DAC chosen is a 12-bit converter, four of the data lines of the second EPROM are not used.

F. DAC and Output Stage

The DAC used here is the Analog Devices HDD1206SM, which has an integral sample and hold circuit to minimize the effects of switching transients, and is sufficiently fast to provide satisfactory operation at 2 MHz. Uniform switching transients are observed, and are measured to be less than 3×2^{-12} of the output with settling times less than 100 ns. Two op amps provide level shifting and buffering at the output, and two potentiometers allow for adjustments of offset and gain for 0 to 10 volt output.

III. Comments

The clock frequency is determined by the choice of R1 and C1. The command of the circuit at the bus can be modified at U22-U24. Alternately, the circuit can be hardware controlled by connecting the lines at U22, pins 1, 2, and 3 to a rotary switch. Straightforward modifications to the steering logic providing the load counter, count up clock, and count down clock will allow this circuit to sawtooth in either direction. In order to use 2732 EPROMs, the bit 11 output from the binary counter would be used to address the EPROMs. The overall performance of this function generator is dominated by that of the DAC. Adaptation of this circuit to more demanding specifications may dictate the use of a higher performance DAC. U21 is used here only as an active pull up for U6, U11, U14, U23, and U24, and four of the hex inverters in U30 are unused. The capacitors C5 through C26 denote by-pass capacitors for each IC.

ORIGINAL PAGE IS
OF POOR QUALITY

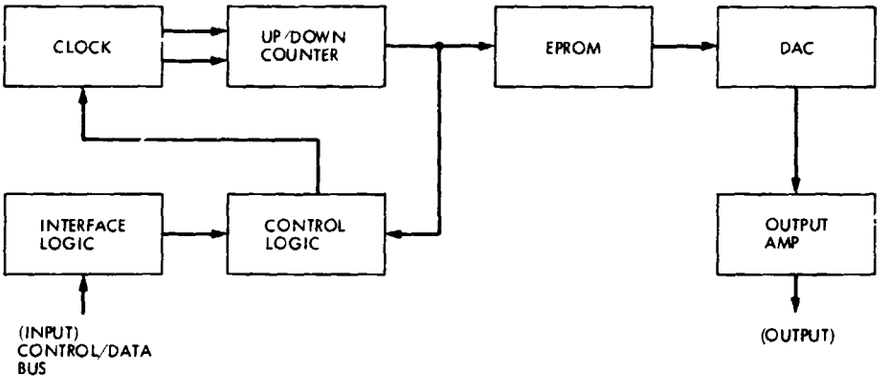

Fig. 1. The block dia- control logic, which is derived from a command on the bus, causing the up/down veep between two limits, also derived from the bus. The counter provides the EPROM, the output of which is converted to the desired analog signal by the ut stage provides scaling and buffering.

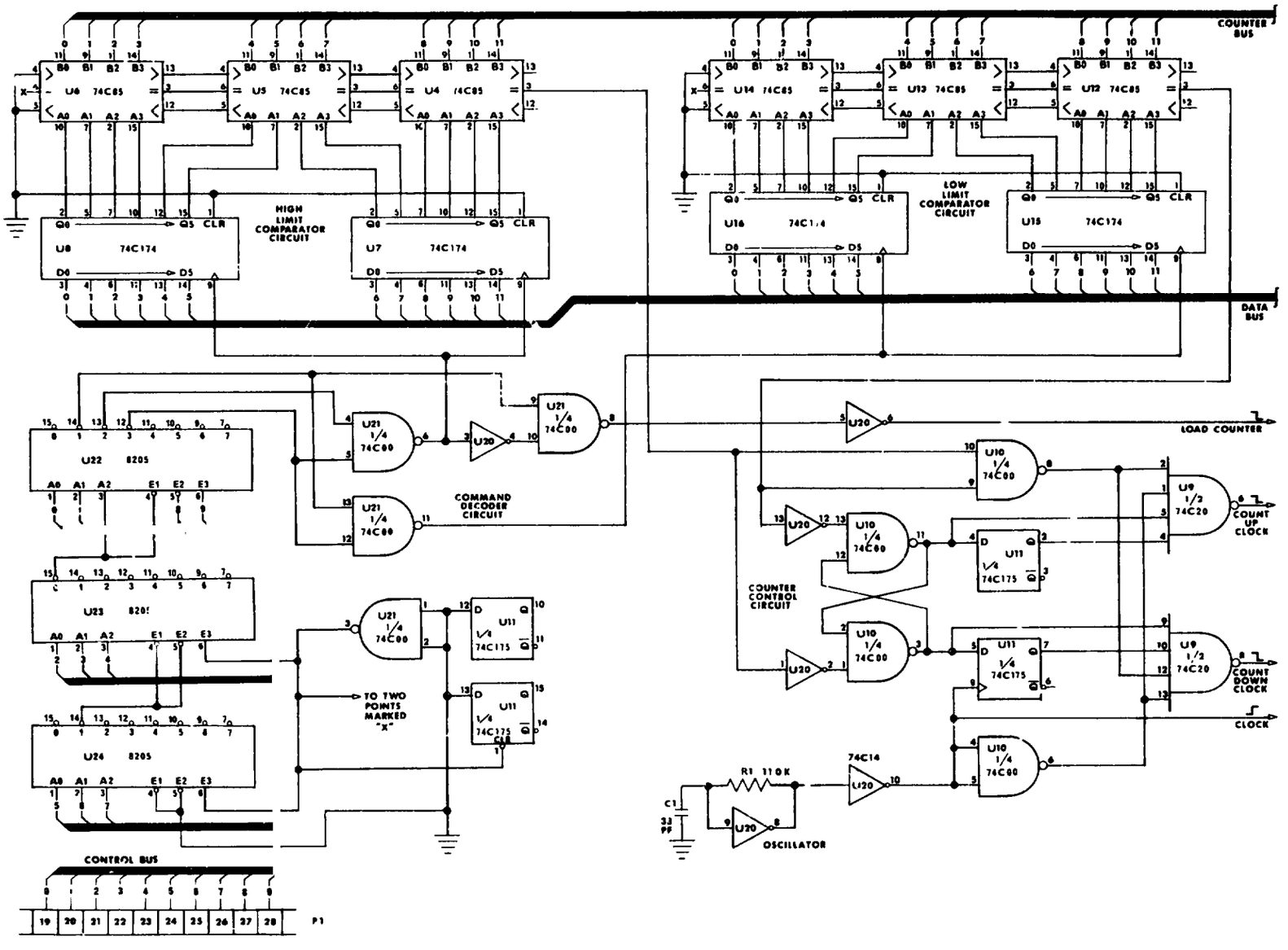

Fig. 2. Schematic of the command decoder and steering logic providing a linear up/down binary sweep, and thus an output waveform with even symmetry about half its period.

ORIGINAL PAGE IS
OF POOR QUALITY

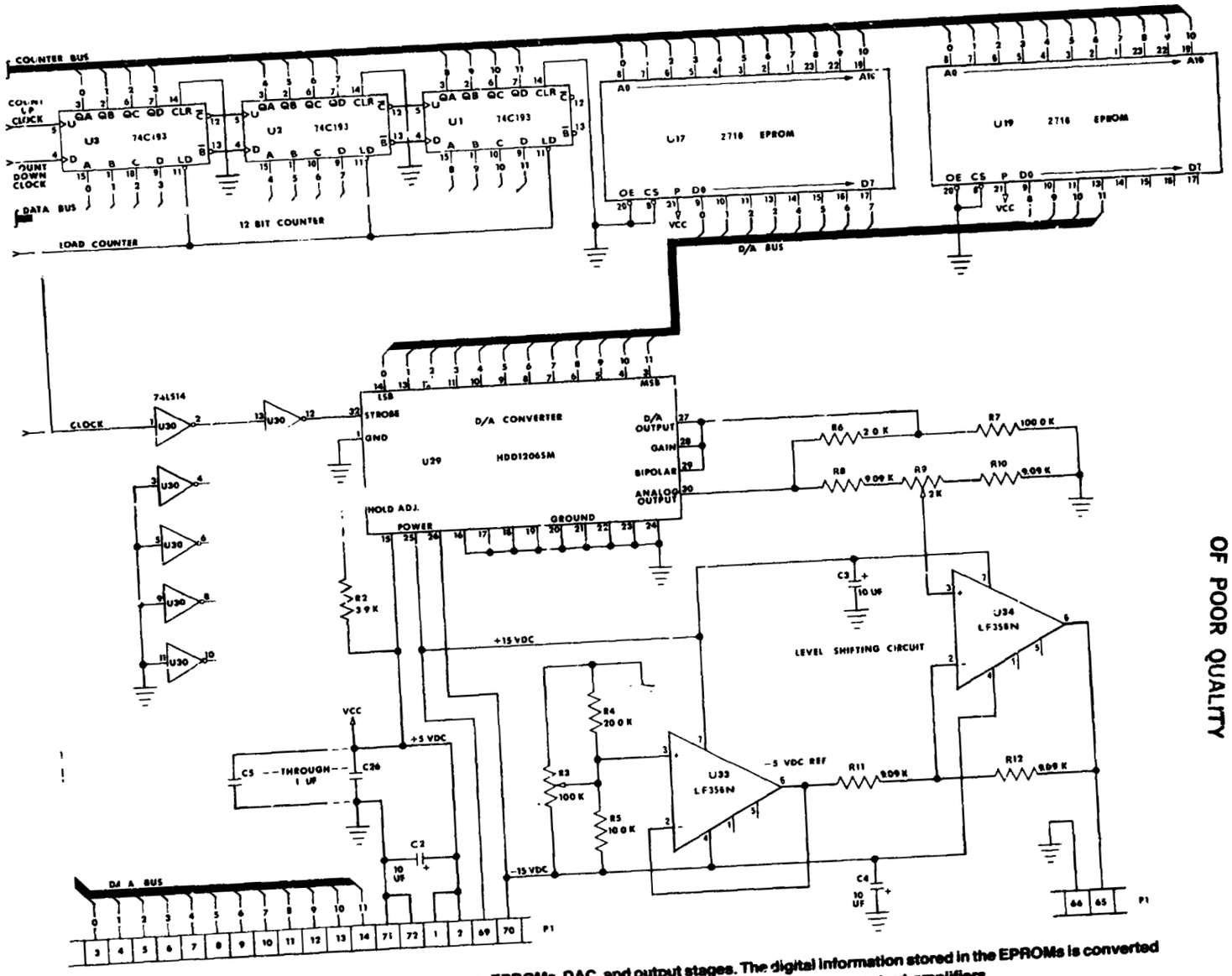

Fig. 3. Schematic of the binary counters, EPROMs, DAC, and output stages. The digital information stored in the EPROMs is converted to an analog signal by the DAC, and is scaled and buffered by the output amplifiers.

ORIGINAL PAGE IS
OF POOR QUALITY

N84 13409

Polynomial Driven Time Base and PN Generator

S. S. Brokl
Communications Systems Research Section

In support of the planetary radar upgrade new hardware has been designed to increase resolution and take advantage of new technology. Included in this article is a description of the Polynomial Driven Time Base and PN Generator which is used for range gate coding in the planetary radar system.

I. Introduction

Digital data acquisition systems designed to receive data from artificial satellites and planetary objects encounter effects caused by the relative motion of these objects. The effects manifest themselves as a Doppler shift in the carrier frequency and a slight stretching or compressing of the information signal. The Doppler frequency shift is usually removed by heterodyning the incoming signal with a programmed local oscillator that removes the Doppler shift to the extent that it can be computed in advance of the observation. In many experiments, it is also desirable or essential to remove the effects of the time compression or expansion so that the signal samples remain in phase with the information baud rate. In the case of radar or pulsar astronomy, it is essential to perform this operation, since the non-deterministic signals are averaged over extended periods of time to reveal the statistical details of the signal. This article discusses the design and details of the operation of a new polynomial driven time base generator and PN generator. The PN generator is used in radar applications to form the original signal that is transmitted and to decode the received reflected signal. This particular design provides a timing precision of 20 ns over a period of one second. The time base system is designed to be updated at one second intervals from data computed from Chebyshev polynomials. During a given second, the time base is drifted linearly. Figure 1 is a block diagram of the planetary radar acquisition system that is currently being implemented. It shows how the Polynomial Driven Time Base and PN Generator fits into the system.

The Polynomial Driven Time Base and PN Generator (PDPG) is controlled by a VAX 11/780 computer via a Unibus DR11C interface. The PN generator runs at a 10 MHz chip rate derived from a 50 MHz clock and synchronized from a precision 1 second pulse (1PPS). PN coding is used as a form of pulse compression to give the best signal to noise ratio possible for planetary radar experiments.

Figure 2 is the block diagram of the Polynomial Driven Time Base and PN Generator. The PDPG consists of the following; a computer interface (via DEC DR11C Unibus interface), a precision programmed baud rate generator, a shift register with feedback, and a word detector with precision counter. The PDPG's primary function will be as the Radar Coder The PN codes that were chosen are maximal length codes that yield an optimum correlation function with mini-

mum side lobes and give the lowest signal to clutter ratio. The coding allows precision range determination modulo for the duration of the code.

II. Computer Interface

The main interface to the VAX 11/780 computer for the Radar Coders is a Unibus DR11C (Ref. 1). The DR11C requires three address locations for operation on the Unibus. Address XXX0 is DRCSR (DR11C Control and Status Register). The second address location can be used as a read/write port and is being used for write only. The third address location is for read only and is being used for the purpose of reading back the coder internal registers.

Figures 3 and 4 are the formats and functions of the Coder Internal Control and Status Register (ICSR) and functional hold registers. The DR11C CSR bits CSR1 and CSR0 are used to control the mode of operation in read/write to DR11C addresses. With both CSR1 and CSR0 equal to zero, addresses 2 and 3 write or read from the ICSR in the coder. With CSR1 = 0 and CSR0 = 1, addresses 2 and 3 write and read from the registers pointed to by the ICSR. The register pointer within the ICSR can be set to auto increment on read or write.

The ICSR is common to all four coders. When writing or reading, all four coder ICSR registers respond. The interrupt mask bits 9, 10, 11, 12 are unique to each coder and use open collector output drivers to eliminate interference. The "Clear Interrupt" is decoded to clear only the interrupt pointed to by the coder select bits 6, 7. Interrupt A (INTA) on the DR11C is used by Request A (REQA) from the Coders. Because an interrupt could occur prior to enabling the interrupts, all interrupts should be cleared initially before enabling the interrupts on the DR11C interface (INT ENB A). The Word Counter is disabled after an interrupt and will not run until the next 1PPS. The interrupt should be cleared before the next 1PPS time.

As can be seen in Fig. 4, the coder has a number of internal registers for controlling the baud rate generator, setting the maximal length PN code and controlling the word detect. The Word Counter keeps the time delay in clock pulses from the one second pulse until word detect. The word counter output is read on registers 6 and 7 which are read only types.

III. Precision Programmed Baud Rate Generator

The Baud Rate Generator is used to set precisely the shift rate (chip rate) of the PN code generator which follows. At the heart of this generator is a divide by 4, 5, 6 counter which generates a normal 10 MHz clock, plus or minus one clock per generator rate. The Pre-Range (PRN) and Pre-Range Complement (PRNC) registers hold values which, in conjunction with an adder and feedback register, act as a Number Controlled Oscillator that controls the number of deletions or additions per second of pulses obtained by the divide 4, 5, 6 counter. By picking the correct values for PRN and PRNC, a precise number of clocks can be generated during a one second interval. This slewed clock is used for tracking time shifts in the returned signal caused by the relative motion between the object and the earth observer. The PRN register holds the value of the increment and the PRNC register holds the 2's complement of the increment plus the clock frequency. The Number Controlled Oscillator works by initially loading the PRNC value at the 1PPS time and adding the PRNC to zero which is contained in the feedback register. At the first clock after the 1PPS time, the PRN value is presented to the adder and the value in the adder is loaded into the feedback register. From this point on, PRN plus the last value in the feedback register is continuously added with each clock pulse until A is greater than B in the comparator. The B side of the comparator is set with switches to a value equal to the clock frequency, i.e. 10 million. At that point PRNC is again presented to the adder and the cycle repeats continuously until the 1PPS time. At the 1PPS time the feedback register is again zeroed and a new value from PRNC and PRN is loaded.

The Word Counter is read to determine the phase of the PN Code Generator. A new value for PRN and PRNC can then be calculated and loaded at the next 1PPS time to correct the phase.

The divide by N and divide by M counters set the baud rate for the PN Generator. The SMPL signal is used by the Demodulators for over-sampling the incoming signals. The output of the divide by M counter is the shift clock to the PN generator. The values of N and M are program-selectable with the SPL and SPLB register.

IV. Pseudorandom Code Generator

The PN generator consists of a feedback shift register, a word comparator, and a phase counter. The basic PN generator is made from the shift register and parity feedback network. The feedback taps are selected by Programmable Read-Only Memory (PROM). Maximal length codes up to length 2^{24} can be selected by addressing the PROMs.

The word detector and counter are used to determine the precise time elapsed from the detection of an all 1's state within the coder following the 1PPS signal. The word length PROM stores the all 1's state and the shifted sequence just prior to

the all 1's for a maximal length code. Since the radar echoes are returning from planetary distances (i.e., Venus, Mars, etc.) with round trip light times of 8 minutes or more, it is important to know which echo is being received at any instant in time. Without precise timing, range information contained in the returned signal could not be extracted. The word counter holds the number of 50 MHz clocks which occurred between the 1PPS and the word detect. The word detect stops the counter and generates an interrupt so the value can be read by the computer.

V. Conclusion

The PDPG operates with two input clocks 10 MHz and 50 MHz and a 1PPS input signal, all coherent. Additionally it is programmable via a Unibus DR11C interface from a VAX 11/780 computer. The PDPG can operate with maximal length PN codes of 2 through 2^{24}. The time phase can be tracked to plus or minus 20 ns over the entire code length. Four PDPG modules are being built for the planetary radar system upgrade.

Acknowledgments

The author wishes to thank George Morris for system architecture; Tak Wong for original coder design; Juan Sanchez for detailed drawings; and Keyvan Farazian for PN code simulations.

References

1. *DR11C General Device Interface User's Manual* Digital Equipment Corp., Maynard, Mass., 1978.

ORIGINAL PAGE IS
OF POOR QUALITY

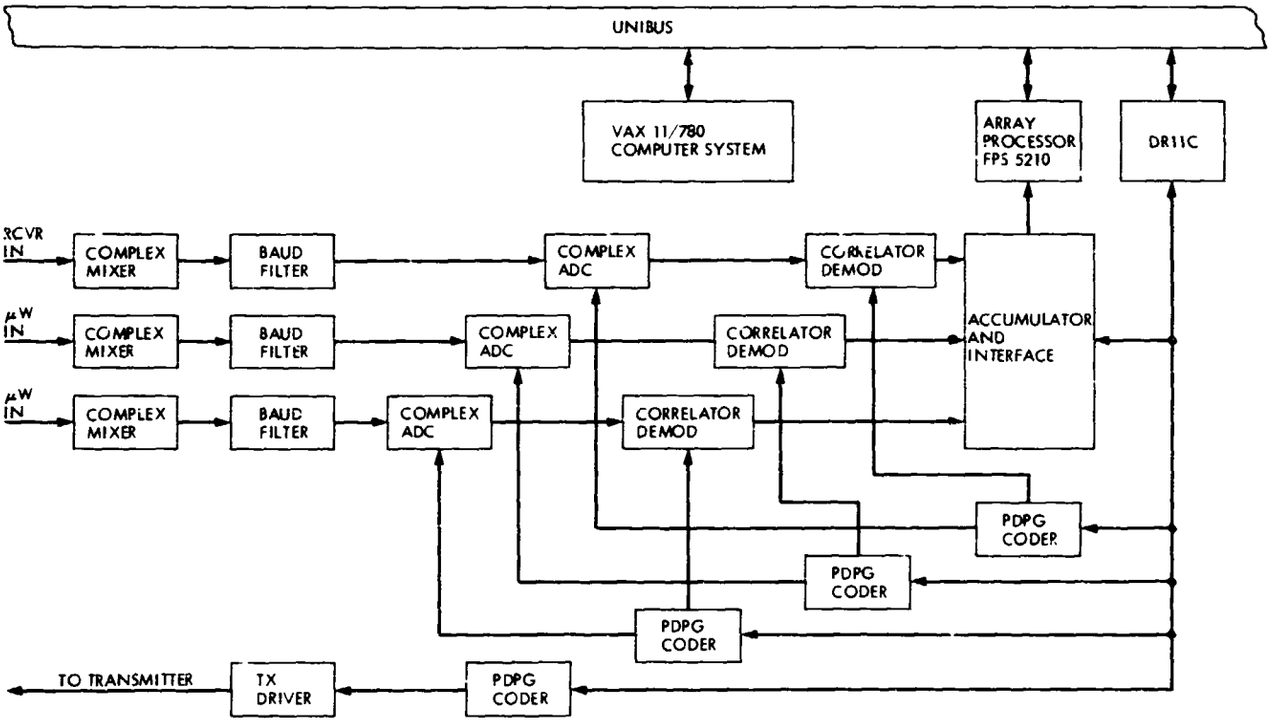

Fig. 1. High resolution radar system

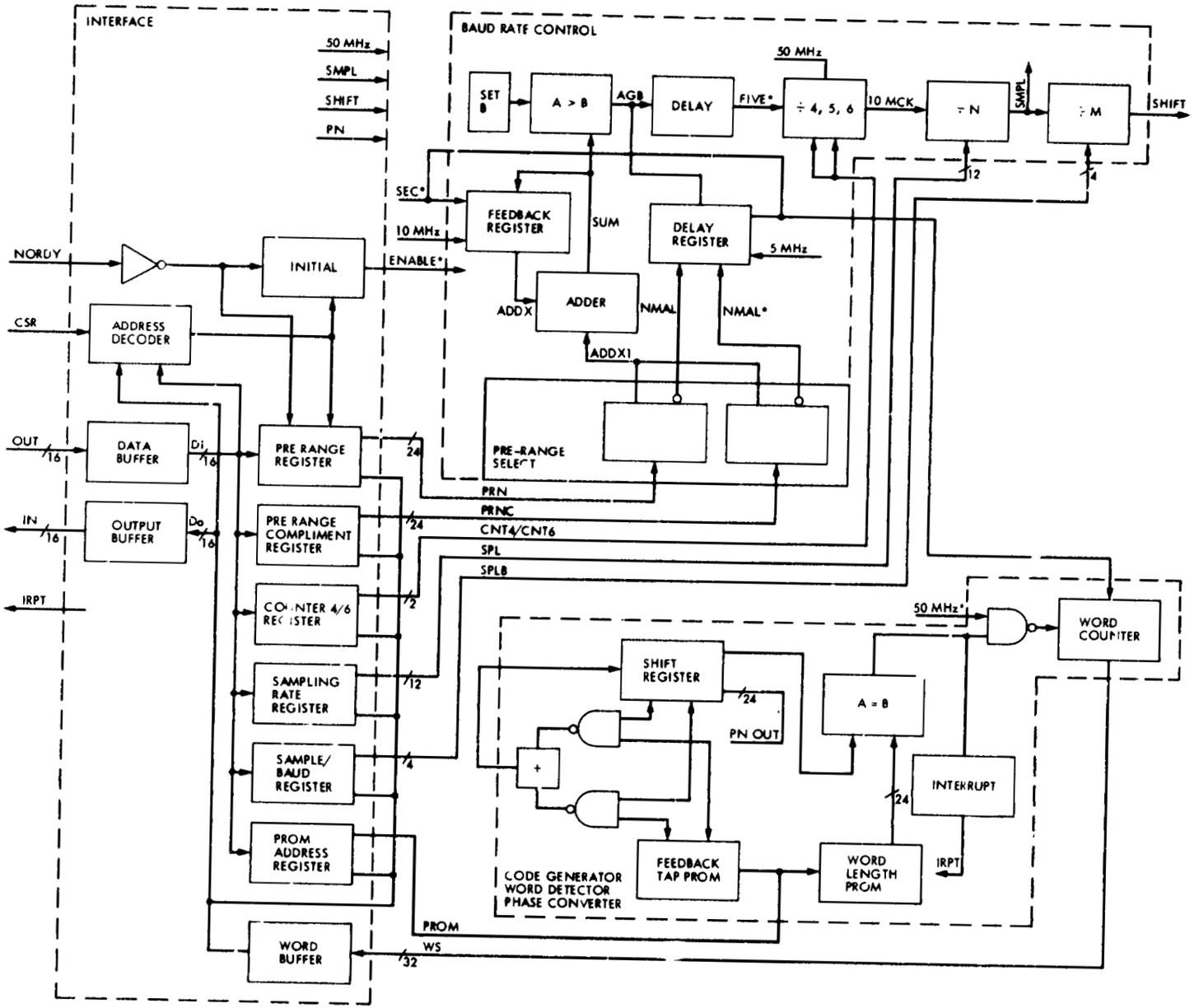

Fig. 2. Block diagram of the Polynomial Driven Time Base and PN Generator (PDPG)

ORIGINAL PAGE IS
OF POOR QUALITY

ORIGINAL PAGE IS
OF POOR QUALITY

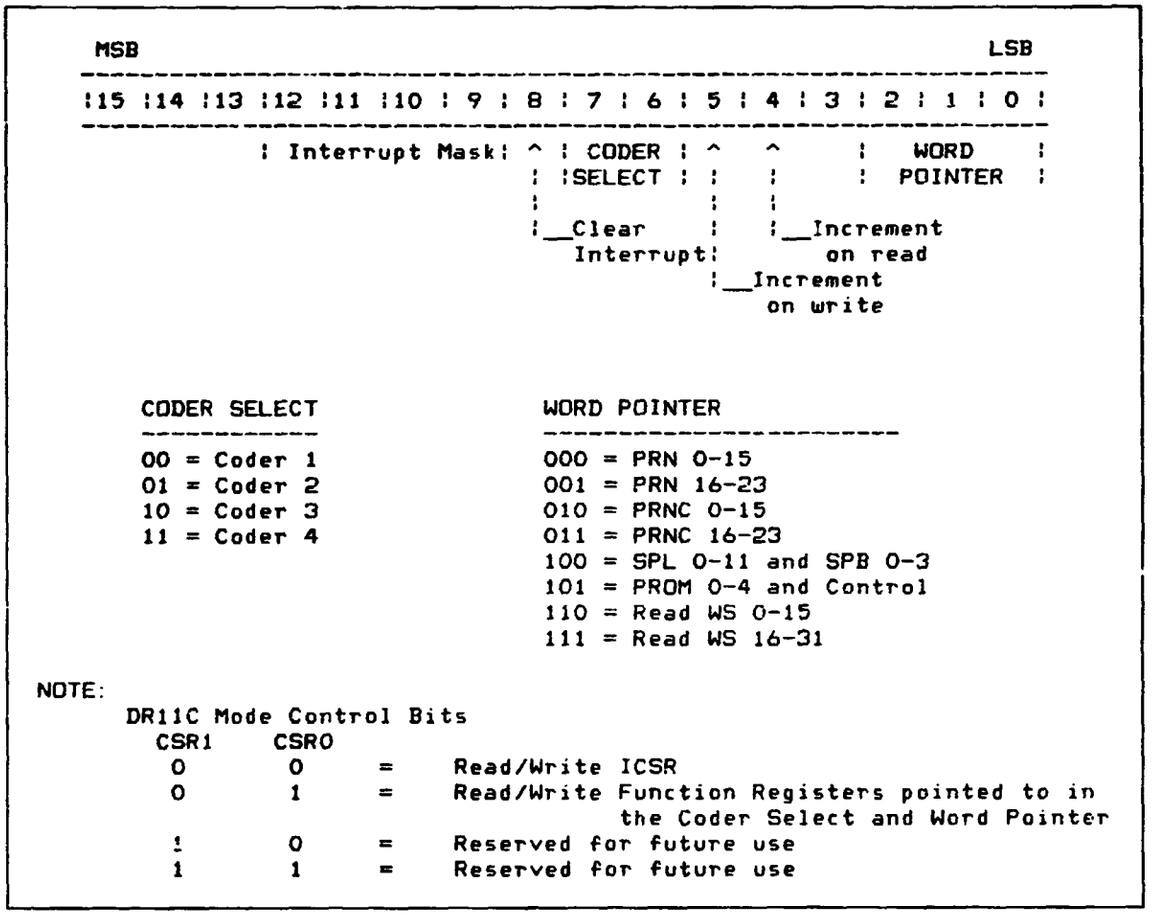
MSB
LSB
15 14 13 12 11 10 9 8 7 6 5 4 3 2 1 0
Interrupt Mask
CODER SELECT
WORD POINTER
Clear Interrupt
Increment on read
Increment on write
CODER SELECT
00 = Coder 1
01 = Coder 2
10 = Coder 3
11 = Coder 4
WORD POINTER
000 = PRN 0-15
001 = PRN 16-23
010 = PRNC 0-15
011 = PRNC 16-23
100 = SPL 0-11 and SPB 0-3
101 = PROM 0-4 and Control
110 = Read WS 0-15
111 = Read WS 16-31
NOTE:
DR11C Mode Control Bits
CSR1 CSR0
0 0 = Read/Write ICSR
0 1 = Read/Write Function Registers pointed to in the Coder Select and Word Pointer
1 0 = Reserved for future use
1 1 = Reserved for future use

Fig. 3. Coder Internal Control and Status Register (ICSR)

ORIGINAL PAGE IS
OF POOR QUALITY

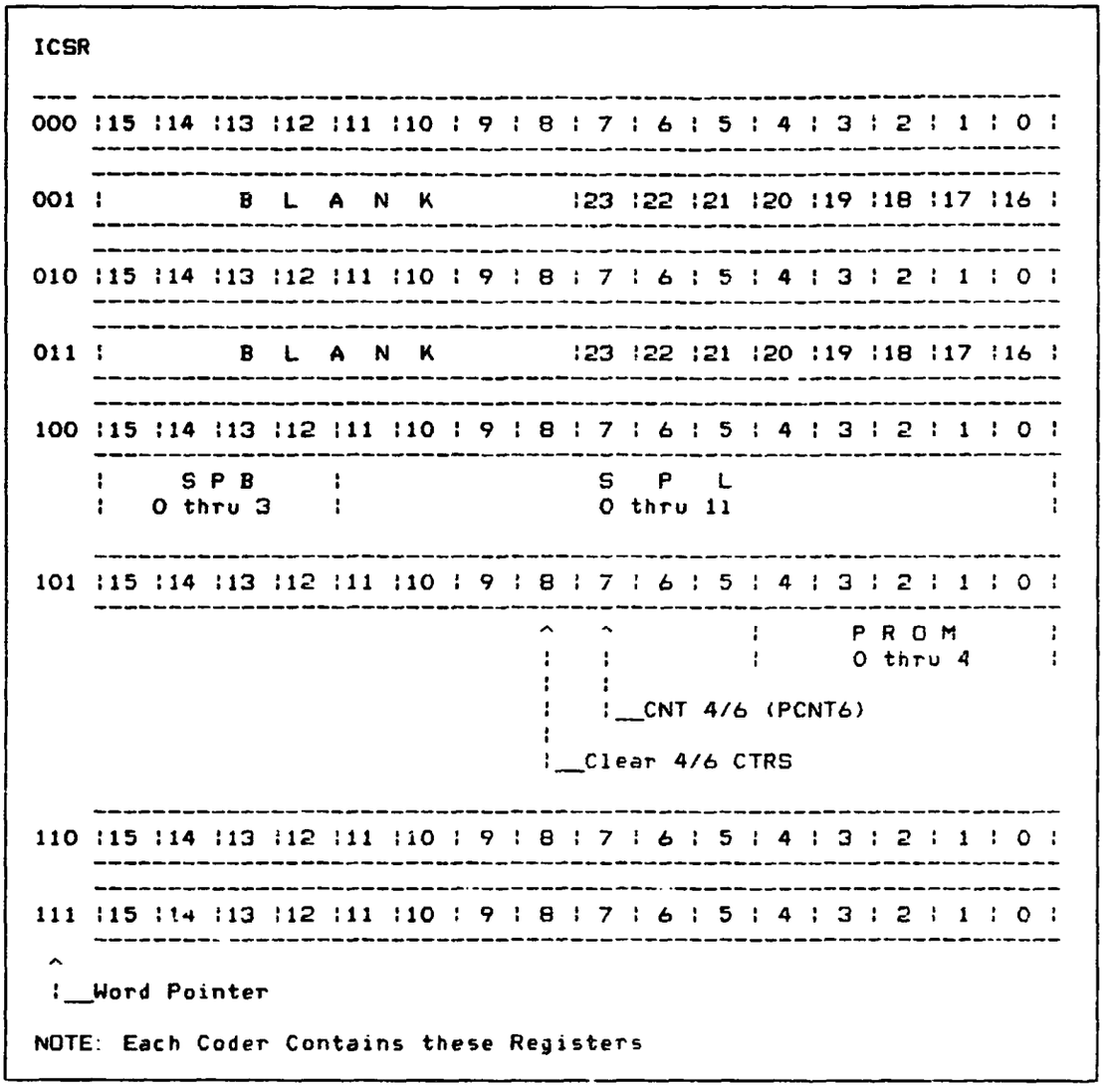

Fig. 4. Function register formats

N84 13410

RF Performance of a Proposed L-Band Antenna System

J. R. Withington, H. F. Reilly Jr., and D. A. Bathker
Radio Frequency and Microwave Subsystems Section

Scale model work to determine efficiencies and bandwidth were made on a smooth wall dual mode feedhorn to study the feasibility of its use at L-Band for the Venus Balloon Project. Measured feedhorn patterns were made and scattered from a symmetrical subreflector. A perturbation technique was then used to predict efficiencies due to scanning effects. A correction for the asymmetrical subreflector was also made. Tables of results and patterns are included.

A series of antenna range experiments and computer predictions were performed to estimate efficiency and bandwidth performance of a proposed L-band (nominally 1668 MHz) feed for the DSN 64 meter antennas. In order to provide for a maximum of future users, it was desired to know overall antenna performance over the widest possible frequency band, limited primarily by a constraint to use simple smooth-walled dual mode (TE_{11} + TM_{11}) feedhorns. This constraint arose in order to take advantage of existing S-band feedhorns (3 units), which are modifiable to the L-band missions, and because of the short project time available for implementation at all three 64 meter stations. It had long been suspected that such smooth walled horns of requisite dimensions provided only about 5 percent bandwidth (at roughly -0.5 dB performance degradation). Therefore, some care in evaluating expected performance and in selecting the center frequency of operation was indicated and accomplished. This article details the work, gives final performance estimates, and provides archival data.

An X-band horn model having the approximate correct scale factor was available and radiation patterns were obtained, taped and filed for the next evaluation step. Using a symmetric equivalent computer model of the 64 meter asymmetric (Tricone) subreflector, we were able to efficiently scatter the ten experimental horn pattern sets from this analytic subreflector and then evaluate those patterns for spillover, illumination efficiency and other factors.

Two additional losses were also considered. First, the gain is affected by slight higher order mode generation by the asymmetrical subreflector. Past experience has shown this to be less than 0.05 dB. And secondly, a computed scanning loss of less than 0.05 dB occurs due to the unfortunate but necessary placement of the L-band feedhorn slightly off the focal "ring" of the 64 meter antenna.

The results of the first step in this procedure are given in Table 1. Table 1 contains those factors of interest to the feed designers and contains useful information to determine a judgement on bandwidth, as various factors deteriorate in different ways. (Table 2 provides final predicted *system* efficiencies.) In Table 1 it can be seen that maximum gain is achieved with an antenna having a main reflector edge angle of about 55°. When designing a Cassegrain antenna for an optimum G/T ratio experience has shown that the best illumination angle is somewhat less than the main reflector edge angle; in effect a low noise design requires some main reflector peripheral "shielding." For the 64 m antenna with an edge angle of 61.4°, this

angle is about 55° at mid-band making the L-band feed very close to the optimum. Here we sacrifice about 7 percent gain (0.77 → 0.71) to achieve low spillover, but obtain a better final G/T ratio. Table 1 also shows the feed cross polarization behavior in the diagonal (45°) plane, as yet another bandwidth indicator. From Table 1 we select 8650 MHz as the best band center and this performance is scaled to 1690 (not 1668) MHz. This was to extend the radio science upper band to 1740 MHz to accommodate their bandwidth requirements. Effectively then, the horn performance available at 8537 MHz will scale to 1668 MHz. Resulting bandwidth, for high performance use (-0.3 dB gain reduction from center frequency) is 1640-1740 MHz; a 6% band. Within this band, no problems are anticipated.

Figure 2, parts a and b, shows the 64 m subreflector (symmetric equivalent) scattering patterns at 1661 MHz (from the available horn pattern at the 8500 MHz frequency). From these amplitude and phase patterns one can observe the E- and H-plane beamwidth equality across the aperture (±61.4°), the very low rear spillover (±61.4 to ±90°) and quite acceptable forward spillover (±90 to ±180°). Figures 1 and 3 show the scattered patterns at 1563 and 1758 MHz (from 8000 and 9000 MHz available horn patterns). At the lower frequency, the rather extreme spillovers are obvious and at the upper frequency, the lack of beamwidth equality with higher than desired forward spillover can be seen. It is instructive to observe all 3 scattered patterns with reference to Table 1 efficiency listings.

Table 2 builds upon Table 1, by including quadripod blocking and feed dissipation loss factors, taken as constant over such a bandwidth. Also shown in Table 2 are the spillovers and zenith noise due to rear spillover. Over the bandwidth studied, rear spillover noise is not a problem, but forward spillover is one of the primary bandwidth determinants, with illumination and cross polarization playing a further role.

In Table 2, we can estimate the L-band system overall efficiency as close to 60 percent at 1668 MHz with, as mentioned, a -0.3 dB bandwidth of 1640-1740 MHz. Operation beyond this band is possible but with reduced performance both in the efficiency and overall reflector system radiation pattern dimensions.

Finally, Fig. 4 is included, again for archival reasons, to enable possible future expansion of this system for other frequencies in the 1400-1800 MHz region. For example, it may be possible to add an aperture extension to obtain good performance at the hydrogen line (~ 1420 MHz). However associated feed parts (not addressed in this analysis such as the circular polarizer and waveguide transitions) would also most likely require modifications to reach that band.

Acknowledgments

The authors acknowledge Dr. Mike Klein for his sustained interest and advice with regard to selecting center frequency and bandwidth for a maximum number of users, and to Y. Rahmat-Samii who did the analysis of the displaced feedhorn beam scan loss.

ORIGINAL PAGE IS
OF POOR QUALITY

Table 1. Symmetric equivalent subreflector scattering-efficiency analysis

X-band horn freq., MHz	L-band operational freq., MHz[a]	Reflector Aperture angle (deg) for maximum efficiency, Θ	Available maximum efficiency, %	Reflector available efficiencies at Θ = 61.4°					Feed cross polarization, dB from peak (Reference)	Note
				Spillover	Illumination	Phase	Central blocking	Total		
8,000	1563	–	–	–	–	–	–	–	–	See Fig. 1
8,100	1583	54.3	61	0.778	0.85	0.87	0.94	0.54	−17	
8,200	1602	54.8	66	0.829	0.85	0.90	0.94	0.60	−20	
8,300	1622	54.9	68	0.849	0.85	0.91	0.94	0.62	−21	
8,400	1641	55.3	73	0.889	0.85	0.94	0.95	0.67	−26	
8,500	1661	55.3	77	0.913	0.84	0.96	0.94	0.69	−32	See Fig. 2
8,600	1680	55.4	77	0.933	0.84	0.97	0.94	0.71	−33	
8,700	1700	55.2	77	0.941	0.82	0.98	0.94	0.71	−28	
8,800	1719	55.0	76	0.942	0.81	0.97	0.94	0.70	−24	
8,900	1739	54.3	73	0.931	0.80	0.96	0.93	0.66	−21	
9,000	1758	53.8	71	0.918	0.79	0.95	0.93	0.63	−19	See Fig. 3

[a]Recommended scale factor

Table 2. L-Band system overall efficiency and spillover noise

L-band operational Freq., MHz	Overall efficiency, %[a]	Forward spillover, %	Zenith rear spillover, %	Zenith spillover noise, K
1583	45	21.7	0.5	1.2
1602	51	16.6	0.5	1.2
1622	52	14.7	0.4	1.0
1641	57	10.6	0.5	1.2
1661	58	8.3	0.4	1.0
1680	60	6.4	0.3	0.7
1700	60	5.5	0.4	1.0
1719	59	5.5	0.3	0.7
1739	56	6.6	0.3	0.7
1758	53	7.9	0.3	0.7

[a]Total from Table 1, times 0.88 quadripod blocking, times 0.98 feed dissipation factors times 0.98 mode and scan factor.

ORIGINAL PAGE IS
OF POOR QUALITY

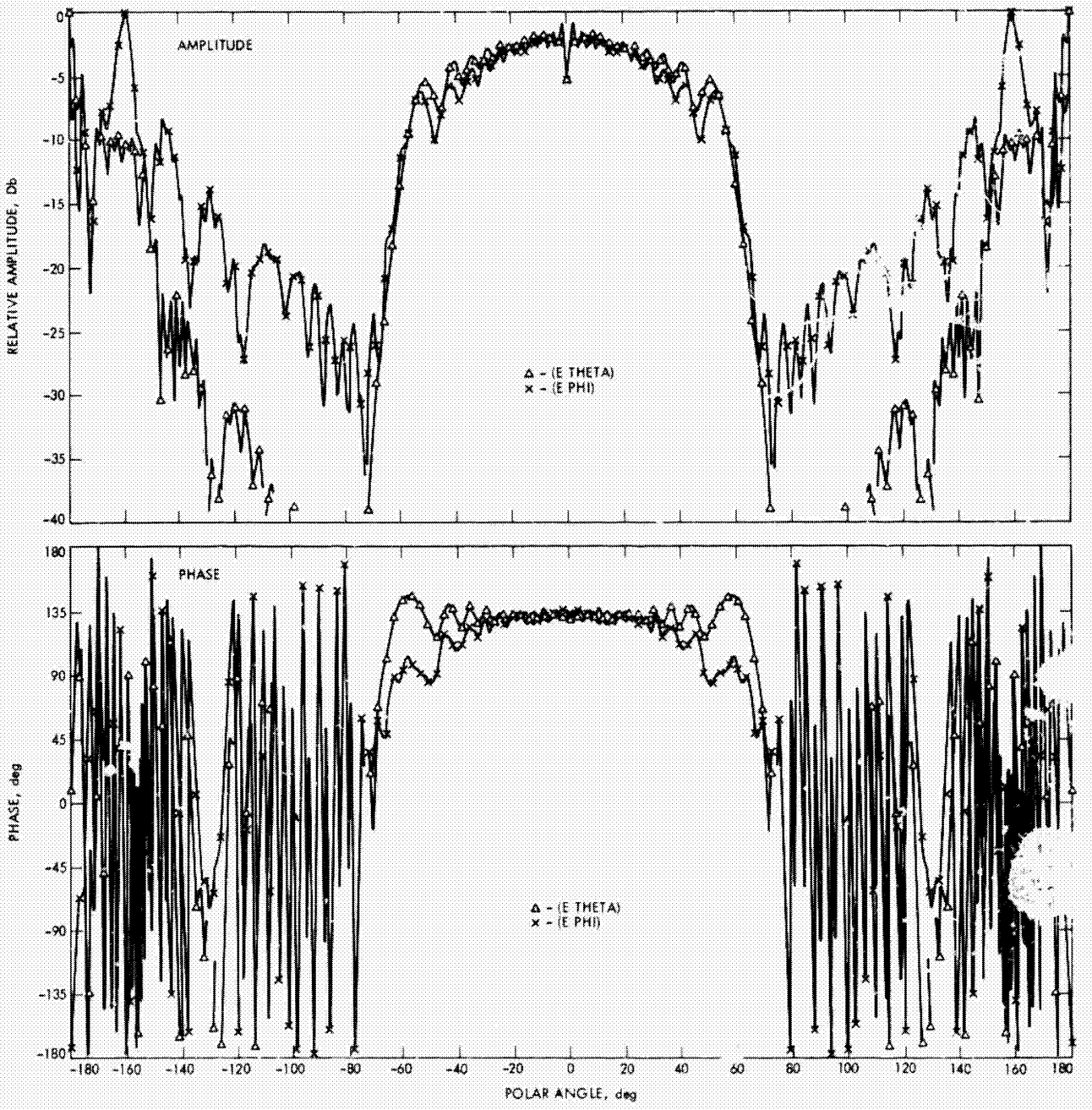

Fig. 1. L-band scattered patterns from an equivalent 64-m symmetrical subreflector, frequency = 1.563 GHz

ORIGINAL PAGE IS
OF POOR QUALITY

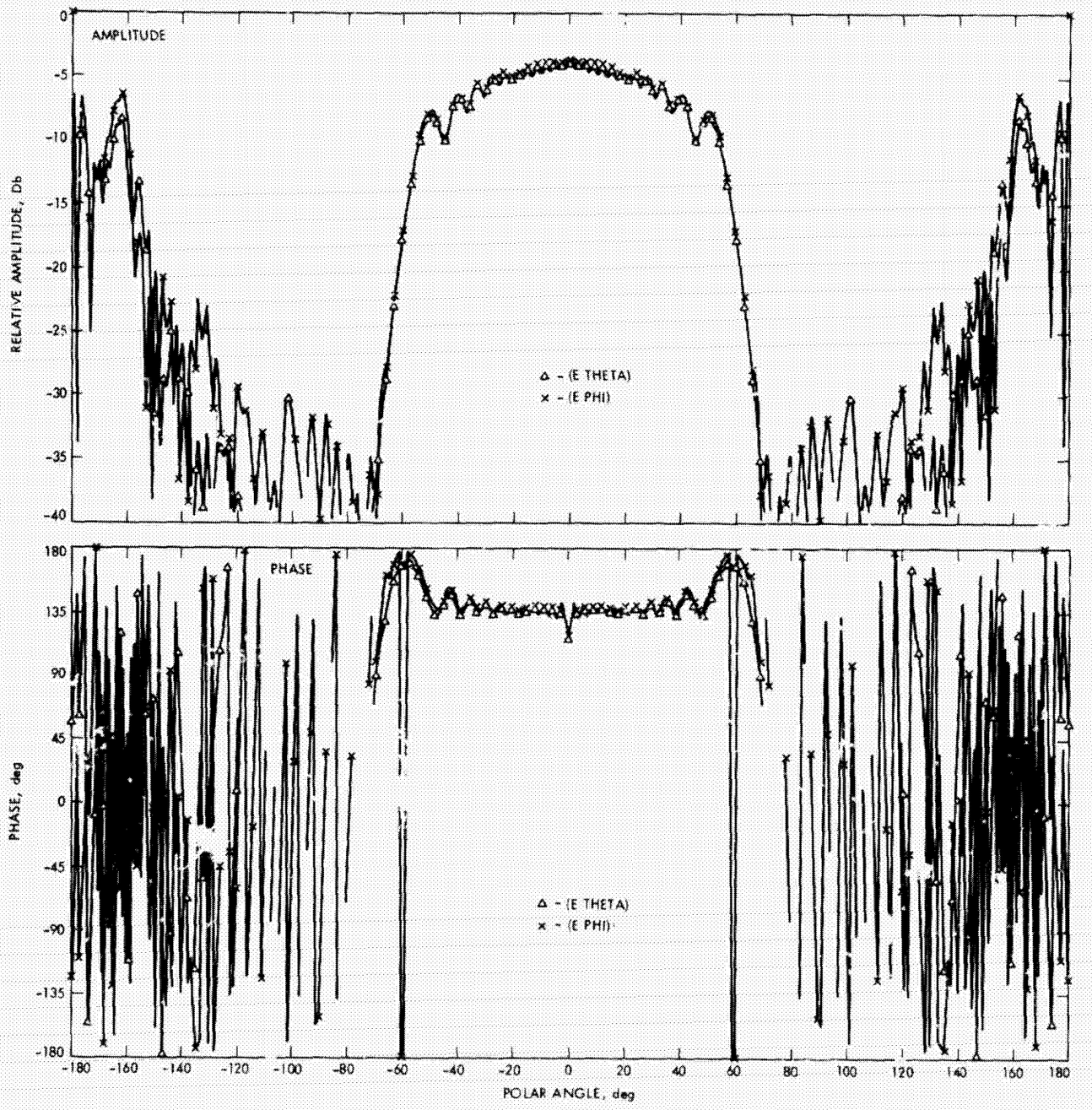

Fig. 2. L-band scattered patterns from an equivalent 64-m symmetrical subreflector, frequency = 1.661 GHz

ORIGINAL PAGE IS
OF POOR QUALITY

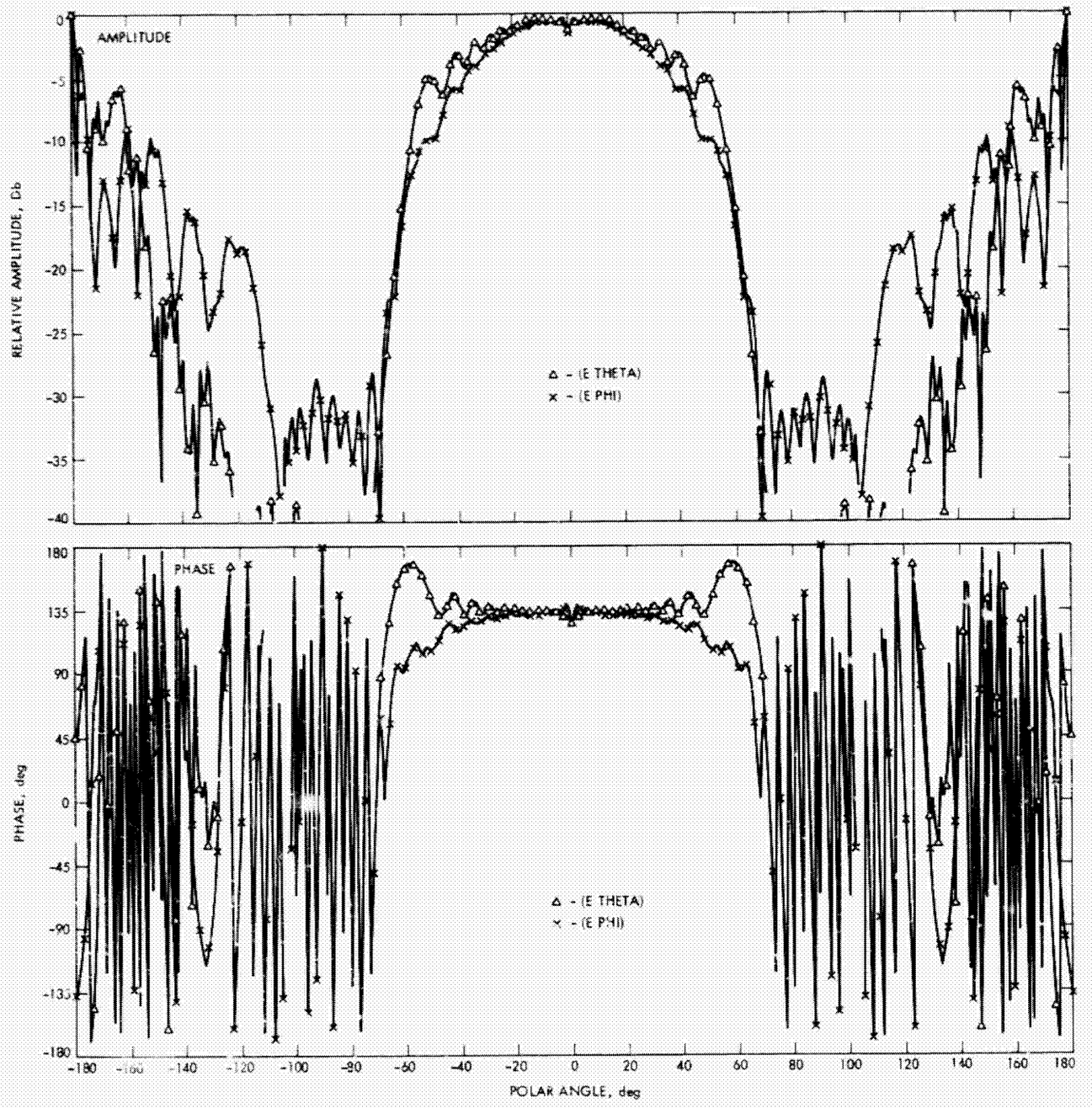

Fig. 3. L-band scattered patterns from an equivalent 64-m symmetrical subreflector, frequency = 1.4 GHz

ORIGINAL PAGE IS
OF POOR QUALITY

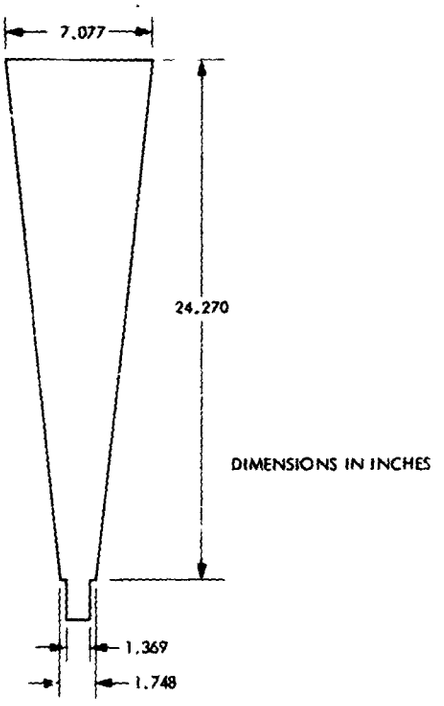

Fig. 4. X-band model horn evaluated for L-band application

D10

N84 13411

Intercontinental Time and Frequency Transfer Using a Global Positioning System Timing Receiver

P. A. Clements
Communications Systems Research Section

The DSN has a requirement to maintain knowledge of the frequency offset between DSN stations with 3×10^{-13} and time offset within 10 microseconds. It is further anticipated that in the 1987–1990 era the requirement for knowledge of time offset between DSN stations will be less than 10 nanoseconds.

JPL is using the Global Positioning System (GPS) Space Vehicles, as a development project, to transfer time and frequency over intercontinental distances between stations of the DSN and between the DSN and other agencies. JPL has installed GPS timing receivers at its tracking station near Barstow, California, and at its tracking station near Madrid, Spain.

The details of the experiment and the data are reported. There is a discussion of the ultimate capabilities of these techniques for meeting the functional requirements of the DSN.

I. Introduction

The DSN has a requirement to maintain knowledge of frequency offset between complexes of 3×10^{-13} ($\Delta f/f$), and a knowledge of time offset to within 10 microseconds. It is further anticipated that in the 1987–1990 era the requirement for knowledge of time offset between DSN complexes will be less than 10 nanoseconds (ns). Clearly, new measurement techniques will be needed to meet these requirements.

Among the new measurement techniques being investigated by JPL, to meet these requirements, is the use of Global Positioning System (GPS) timing receivers. The GPS timing receivers presently being used by JPL were developed and built by the National Bureau of Standards (NBS). Part of this development was funded by JPL.

II. Description of the Receivers

The NBS receiver is described in the 1982 proceedings of the Precise Time and Time Interval Applications and Planning Meeting (Ref. 1). It uses one frequency containing the CA code which is transmitted by each space vehicle. The receiver locks on the space vehicle's signal; therefore, it needs only a small omnidirectional antenna rather than a steerable dish. The receiver is controlled by an internal microprocessor that automatically handles schedules, length of reception time, and other tasks. Once the receiver is set up, normal operation only

requires occasional human intervention. For instance, the reception time is decremented 4 minutes every day which of course is a little different than a sidereal day. This is done to make it a bit more convenient by having to deal only with whole minutes. It is necessary to adjust the schedule every few weeks to keep the viewing angles correct.

III. Configuration of the System

At present JPL has two GPS timing receivers, one of which is located at the Goldstone Tracking Station Complex (GTS) near Barstow, California. This receiver gets its 1-second timing pulse from a cesium clock, Goldstone clock 5, GTS(C15), which is located about 20 km from a hydrogen maser clock Goldstone Station Reference GTS(SR), which is at another station (DSS 14) in the same complex. The hydrogen maser clock is the same one used in Very Long Baseline Interferometry (VLBI) which measures, among other things, the time offset between the DSN complexes. A clock trip using a portable cesium clock is made once a week between GTS(C15) and GTS(SR). These clock trips are done in conjunction with the regularly scheduled weekly VLBI measurements.

The second GPS timing receiver is located at DSS 61/63. The Madrid receiver gets its timing pulse from a hydrogen maser clock which is that station's reference clock MAD(SR). MAD(SR) is another hydrogen maser clock used in the VLBI measurements and is at the other end of the weekly VLBI measurement between California and Spain.

Two other receivers involved in this test were located at NBS in Boulder, Colorado, and at the United States Naval Observatory (USNO) in Washington, DC. The NBS receiver is identical to those used at JPL. It gets its timing pulse from the NBS clock 9 which is one of the clocks in the NBS ensemble. A daily offset of clock 9 to UTC(NBS) is available at the month's end and the receiver is accessible by telephone through a modem. The USNO GPS timing receiver is a Stanford Telecommunications receiver of similar functional design to the NBS receiver. Its schedule is decremented 4 minutes per day[1]. The receiver gets its timing pulse from UTC(USNO, MC). There are corrections available to UTC(USNO).

IV. Procedures for Gathering and Processing the Data

The receivers will store internally one to two weeks of data depending on how much data is acquired during each day. The data from the receivers are acquired by telephone usually once a week. In the use of the NBS type receiver, the receivers themselves are accessed. In the case of the USNO receiver, the data are acquired from a public database service provided by USNO. In both cases the data are transmitted at a 300-baud rate and are received and printed out on a terminal. The data are then entered by hand into a Hewlett Packard 9845 calculator at JPL.

All of the data were taken during a mutual view of the GPS space vehicle by pairs of timing receivers. This method promises the best results and is the simplest with respect to processing the data. As more space vehicles are added to the GPS constellation, there will be additional opportunities for mutual view around the world.

The receivers are programmed to take data for 10 minutes (600 seconds). These data are then reduced in the receiver to a single data point which represents the time offset between the local clock and the GPS clock. The difference between the two values of local clock and GPS time is then calculated. This is done for each space vehicle that is available for mutual view each day. These values are then averaged to produce a single value for the day. If data points are missing, then a linear interpolation is made on the original measurement.

V. Results

The first measurement in late 1982 was clock 5 at GTS and NBS clock 9. The distance between these two stations is approximately 1200 km and regular clock trips were made between GTS and NBS so the measurements could be verified. The data axis of all of the figures is labeled in Modified Julian Day (MJD). An MJD of 5225 represents September 13, 1982, on the conventional calendar.

Figure 1 shows the results of the UTC(NBS) - GTS (clock 5) with the results of the cesium portable clock trips shown. Because of different antennas being used at NBS a receiver calibration was not available; therefore the first clock trip was used as a calibration. The second trip disagreed by 36 ns and the third by 5 ns.

This receiver is now probably a de facto permanent installation at GTS and will probably eventually eliminate or at least curtail the need for most future clock trips between NBS and GTS.

A second GPS timing receiver was installed at the DSN station in Spain (DSS 63). A schedule of mutual observation (observed at the same time) of two space vehicles (SV5 and SV8) was started. These are the only two space vehicles that are mutually observable from both compiexes. The space vehi-

[1] Prior to the first of 1983 and during the tests reported here, the USNO receiver schedule has been decremented 27 minutes one week and 28 minutes the alternate week. This allowed an approximation to a sidereal day. This was changed to a 4 min/day decrement starting about the first of 1983.

cle observation schedule was made to have the same angle of observation from both stations. Some slight adjustments were made to equalize the angles from 41 degrees to 45 degrees above the horizon. The space vehicles are over Greenland at observation time and seen within a few degrees of each other in the sky at each station.

A clock offset measurement is made every day from each space vehicle and the mean is used as the value of the clock offset. The same procedure for getting a value of clock offset is used between GTS(C15) and MAD(SR) and between UTC(NBS) and GTS(C15) with the exception that only two space vehicles are available between GTS and MAD. A plot of the clock offset values is seen in Fig. 2. Figure 3 is the same graph with a frequency offset removed.

The frequency offset between the GTS(C15) and MAD(SR) was calculated using 10 days of data. The calculations assumed statistical independence between the measurements using the two space vehicles. A typical frequency offset measurement was 9.5×10^{-13} ($\Delta f/f$) with a (confidence) standard deviation of the mean of 2.8×10^{-14} ($\Delta f/f$). This is within the requirements to have knowledge of frequency offset to within the 3×10^{-13} ($\Delta f/f$) DSN specification.

VI. Confirmation by Independent GPS Measurements

Unlike the clock offset measurements between GTS and NBS, the measurements from California to Spain cannot be confirmed by frequent clock trips. One attempt at confirmation was a daily indirect time difference measurement made through the U.S. Naval Observatory (USNO). This was accomplished in two steps: First, there was a daily mutual view schedule maintained by NBS, USNO and Goldstone. Second, USNO and Madrid maintain a mutual view schedule, which results in daily time offset measurement between their clocks. These direct and indirect time offset measurements between Goldstone and Madrid are nearly statistically independent.

Figure 4 shows the differences in the measurement of the time offset between Goldstone and Madrid by two different paths. There was a mean offset of 140 ns. An explanation of this could be an error in the coordinates of the receiver. There is some reason to believe this is true at Goldstone and there have been no checks made at Spain. The new firmware to be installed in 1983 into the NBS receivers will contain a navigation program. Then it will be possible to verify the antenna location within a few meters.

A good candidate for the cause of the daily variation is the different scheduling methods used by JPL and NBS and that used by USNO. This problem should clear up in data taken in 1983 after USNO started decrementing their schedule by 4 minutes/day. These tests have been continued during 1983 and will be reported in a future article. Some of the daily variations are probably caused by ionospheric changes. There is no attempt to account for this in the NBS and JPL receiver during this time but one would expect this error to be less than is presently seen.

VII. Confirmation Using VLBI Measurements

Approximately once every week a VLBI measurement is made between GTS and MAD and between GTS and the DSN Australian complex. One of the results of the VLBI measurement is the time offset between the involved stations. By using the regular clock trips between GTS(C15) and GST(SR), the GPS and timing receiver results can produce a weekly approximate time offset between GTS(SR) and the MAD(SR) (Fig. 5). These time offset measurements can be compared to the time offset results of the VLBI measurements as seen in Fig. 6.

A linear fit on each of the two sets of data shows an excellent agreement. These measurements will be continued throughout 1983. It is planned to make measurements internal to the stations to find the offset difference between the VLBI and the GPS measurements.

VIII. Conclusions

The conclusions of the experiment are as follows:

(1) The present GPS timing receivers can meet the 1985 requirements specified for the DSN. With better data collection, the addition of software filters in the data processing, and ionosphere correction, there is reason to believe the intercontinental time measurements, with the existing equipment, can approach an accuracy of 10–20 nanoseconds. Certainly, one can expect to further refine the measurement of frequency offset.

(2) The GPS and VLBI measurements of time offset will complement each other for some time to come.

(3) It has been shown that the GPS timing receiver is an operational item of equipment capable of replacing regular clock trips over short distances and shows promise of replacing clock trips over intercontinental distances.

Acknowledgments

The author wishes to thank Mr. David Allan and Mr. Dick Davis of NBS for their technical assistance. Mr. Paul Wheeler and others on the staff of USNO were extremely helpful and generous in scheduling their receiver. Appreciation is given to the staff of the DSN station 61 in Spain, in particular Sr. José Alonso and Sr. Delgado Muñoz for their time and effort beyond their regular duties. The receiver at Goldstone was operated by Mr. Jesse Myers, which is also much appreciated.

References

1. Unprecedented Syntonization and Synchronization Accuracy via Simultaneous Viewing with GPS Receivers; Construction Characteristics of an NBS/GPS Receiver, D. D. Davis, M. Weiss, A. Clements, D. W. Allan, 1981. *Proceedings of the 13th Annual Precise Time and Time Interval Applications and Planning Meeting*, Naval Research Laboratory, Washington, D.C.

ORIGINAL PAGE IS
OF POOR QUALITY

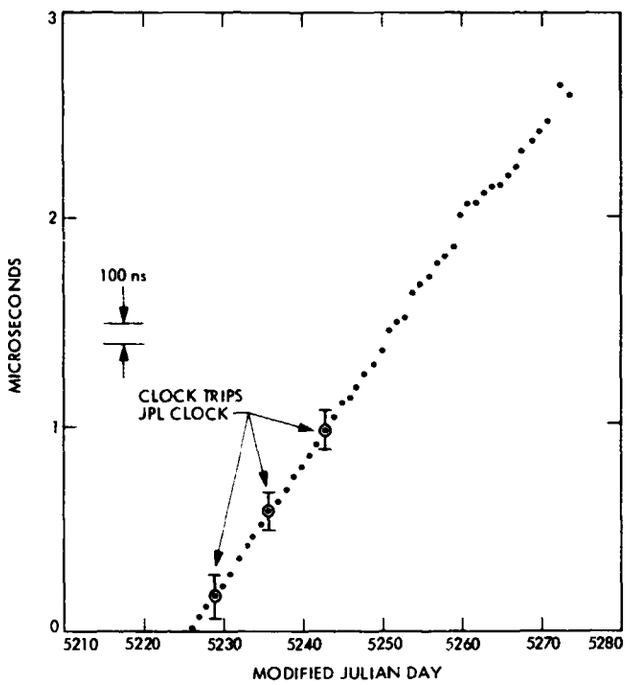

Fig. 1. UTC(NBS)–Goldstone (clock 5)

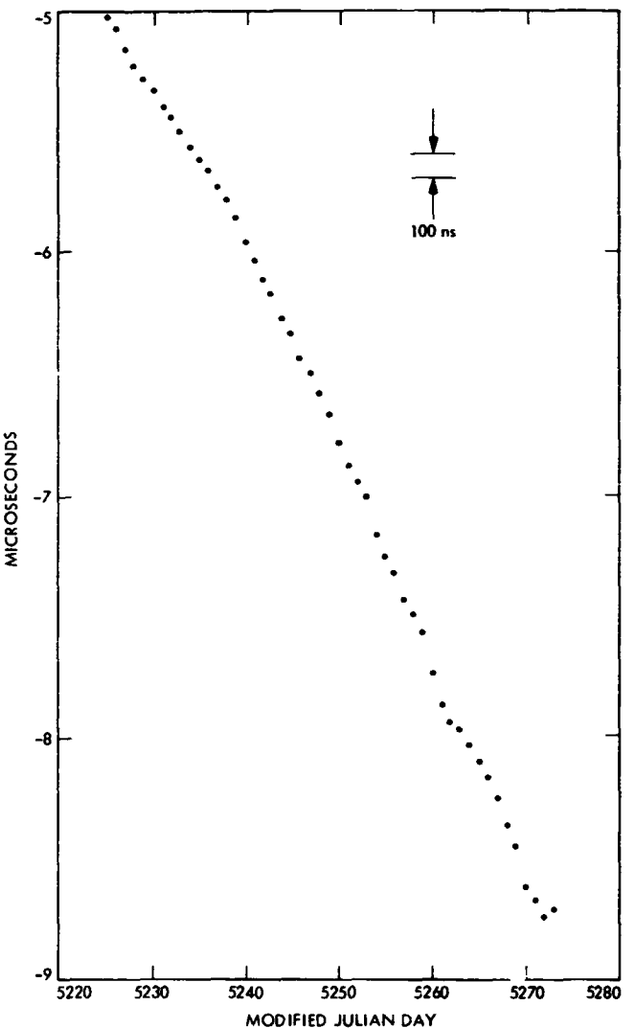

Fig. 2. Goldstone–Madrid as directly measured by CPS timing receivers (Goldstone [clock 5]–Madrid [station reference])

ORIGINAL PAGE IS
OF POOR QUALITY

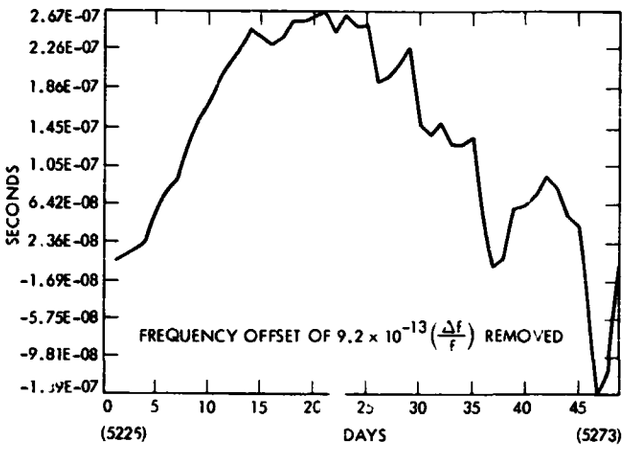

Fig. 3. Goldstone (clock 5)–Madrid (station reference)

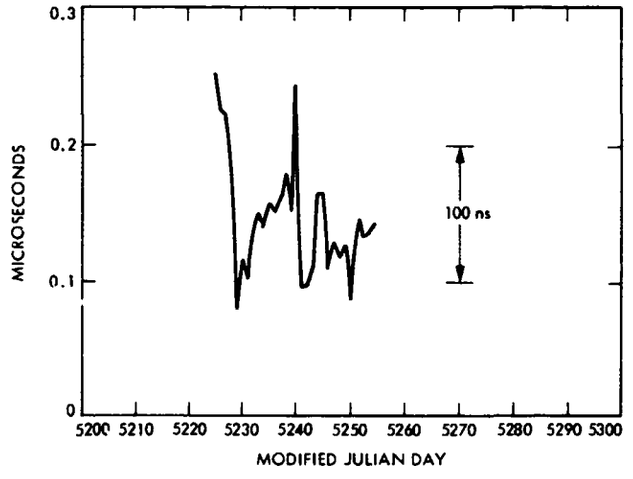

Fig. 4. Difference between Goldstone to Madrid time directly and through USNO

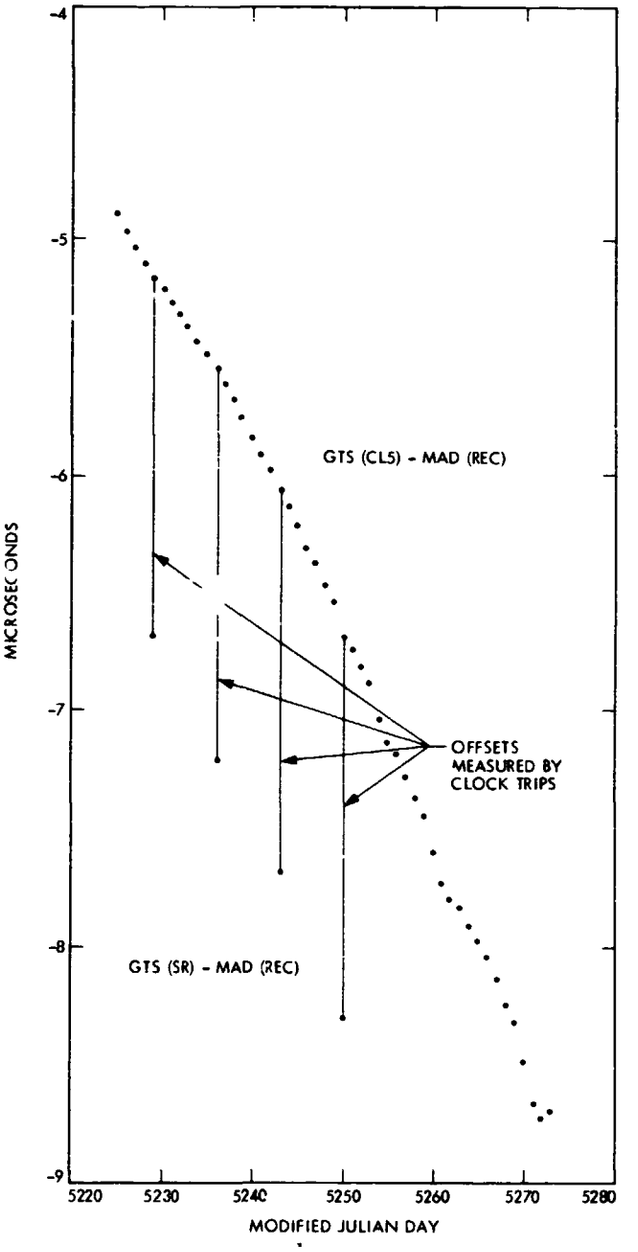

Fig. 5. Goldstone–Madrid directly showing offset to Goldstone (station reference)

ORIGINAL PAGE IS
OF POOR QUALITY

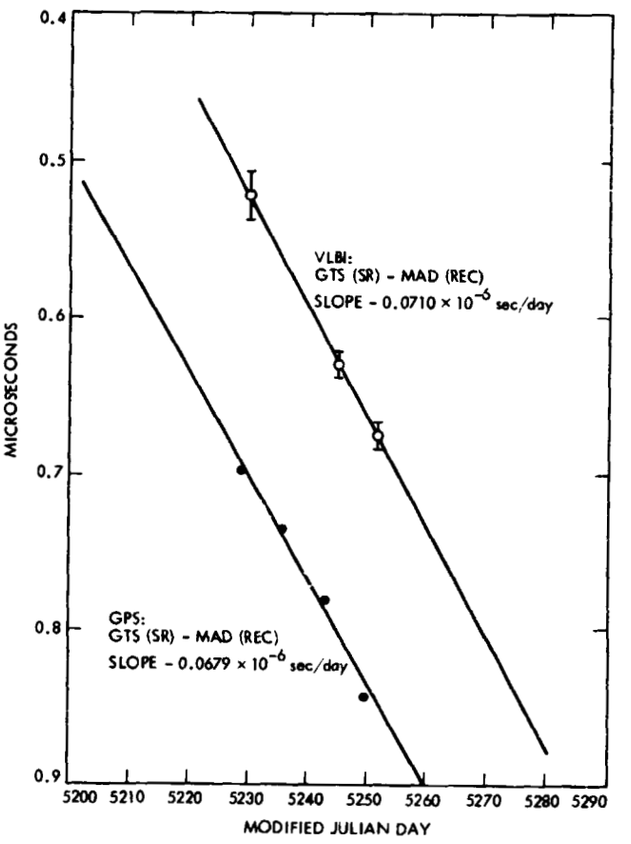

Fig. 6. Comparison of GPS and VLBI clock offset measurements: Goldstone–Madrid

N84 13412

NASTRAN Structural Model for the Large 64-Meter Antenna Pedestal, Part II — Improved Model

C. T. Chian
Ground Antennas and Facilities Engineering Section

Static analysis and a computer structural model for the large 64-m antenna pedestal are developed using the MSC version of the NASTRAN program. This improved pedestal model includes the haunch areas and the actual pressure pattern of the oil under the hydrostatic bearing pad. The results obtained from the new improved model have indicated that the deflections due to pad loads are in good agreement with field measurements. The top surface deflection of the pedestal obtained from the NASTRAN model is used as an input to the oil film computer program to determine the minimum oil film thickness under the pad.

I. Introduction

This article is the second in a series of reports on the static analysis and computer modeling performed for the large 64-m antenna pedestal. The pedestal is under pressure loadings at the three hydrostatic bearing pads. The pedestal computer model previously reported in Ref. 1 has been improved in order to better represent the displacement and force distribution throughout the pedestal, as well as to obtain the state of stress and strain.

The deflections of the pedestal under the pad resulted from the NASTRAN model are used as inputs to the oil film height program[1] to evaluate the corner oil film thickness between the pad and the runner. A minimum hydrostatic bearing oil film of 0.13 mm (0.005 in.) is required to avoid any metal to metal contact between the pad and the runner and to accommodate any runner malfunctioning and placement tolerance.

[1]This is a modified version of the program initially developed by the Franklin Institute, Ref. 3.

II. Description of the Improved Model

The first computer structural model of the pedestal was reported in Ref. 1. The assumptions made in this initial model are that (1) the pedestal is a cylinder of uniform wall thickness, thus ignoring the effect of the haunch; (2) the pedestal loading is uniform with 6.9×10^6 N/m^2 (1000 psi) pressure over the pad length and width; and (3) the modulus of elasticity of the entire pedestal concrete is 2.8×10^{10} N/m^2 (4.0×10^6 psi). By symmetry, the pedestal could be modelled as one 60 degree segment with two boundary conditions. (1) zero slope at the points representing the centerline of the pad, and

(2) zero slope at the points representing midposition between two pads

In the present improved pedestal model, the first two assumptions are modified to include (1) the actual haunch contour in the pedestal to provide additional stiffness on the pedestal wall, and (2) the actual pressure profile of the oil under the pad. The model was developed using the MSC version of the NASTRAN structural program.

The improved pedestal model consists of a wall, haunch, and top slab, as shown in Fig. 1. Figure 2 is a cross-sectional diagram of the pedestal. A cross-sectional diagram of the hydrostatic bearing is shown in Fig. 3. Deflected shapes of the hydrostatic bearing pad and runner surface are illustrated in Fig. 4. Relative deflections within the hydrostatic bearing pad and within the runner surface from centerline to edge of pad are shown as Δ_p and Δ_r, respectively. Design constraints required that the mismatch of deflected surfaces, δ, be within 0.10 mm (0.004 in.). Part of this 0.10 mm (0.004 in.) total mismatch, a maximum mismatch of deflected shapes of 0.08 mm (0.003 in.) was established as the limit for creep during construction, hence before the bearing pads could be moved. The remaining 0.025 mm (0.001 in.) was the design criteria for mismatch of elastic deformations (Ref. 2). If the creep strains are compensated for by releveling of the runner, then the total δ of 0.10 mm (0.004 in.) might be tolerated for the elastic deformations portion alone.

The actual pressure profile of the oil under the hydrostatic bearing pad is illustrated in Fig. 5. For simplicity, the pressure pattern of the oil under the pad is assumed to be symmetric with respect to the pad centerline in the NASTRAN pedestal model. Therefore, $p_1 = p_3$ and $p_4 = p_6$. Pad 3, which experiences the highest load among the three pads, is the one considered in our model. The values of the pad recess pressures are given in Table 1.

Figure 6 shows a typical deflection map of the top pedestal surface under pad load. This deflection map is used as the input to the oil film height model to determine the minimum oil film thickness between the pad and the runner.

III. Comparison with Field Measurements

Field measured load-deformation relationships of the pedestal were obtained and used to calibrate the present NASTRAN pedestal model. The pad load tests can also be used to determine the spatial distribution of deteriorated concrete in the haunch.

The field measurements were conducted by JPL in cooperation with Construction Technology Laboratories (CTL) of Skokie, Illinois. (CTL is a division of the Portland Cement Association.) Figure 7 shows the locations of the gauges for deflection measurements. Instruments were installed to measure vertical deformations over a 1.27 m (50 in.) gauge length on the external surface of the haunch and the wall. Figure 8 is a schematic of the instrumentation used. As shown, small blocks were bonded to the structure at the preselected locations. A direct current differential transformer (DCDT) mounted in a fixture was attached to the upper block. A wire from the spring-loaded plunger of the DCDT was attached to the lower block. The output of the DCDT was continuously recorded during the time required for antenna Pad 3 to be moved across the instrumented location. This time is approximately 3 minutes.

Figures 9 and 10 show the good correlation between the field deflection measurements and the NASTRAN predicted values for two different locations: azimuth 49° and azimuth 96°.

IV. Conclusions

The improved NASTRAN structural model for the large 64-m antenna pedestal shows excellent correlation with the field deflection measurement. This new model incorporates improvements over the previous model of Ref. 1 which includes the actual haunch areas in the pedestal and the actual pressure pattern of the oil under the hydrostatic bearing pad.

The maximum pad out-of-flatness and the minimum oil film thickness are important factors to evaluate the condition of the hydrostatic bearing performance. The new pedestal computer model will be a useful tool in the large antenna bearing rehabilitation and upgrade studies. A series of parametric studies using the improved NASTRAN pedestal model and the oil film thickness program will be performed. For example, the effects of varying moduli of elasticity in different regions of the pedestal concrete, and the effects of increasing pad loads due to 64-m to 70-m extension will be investigated.

Acknowledgment

The author acknowledges the assistance given by F. Lansing, H. Phillips, A. Riewe, R. Oesterle and B. Morgan (both the last two with Construction Technology Laboratories) during the various execution steps of this work.

References

1. Chain, C. T., Katow, M. S., and McGinness, H., "NASTRAN Structural Model for the Large 64-m Antenna Pedestal, Part I," *TDA Progress Report 42-74*, Jet Propulsion Laboratory, Pasadena, CA, August 15, 1983.

2. TDA Technical Staff, "The NASA/JPL 64-Meter-Diameter Antenna at Goldstone, California: Project Report," *JPL Technica. Memorandum 33-671*, Jet Propulsion Laboratory, Pasadena, CA, July 15, 1974.

3. Hinkle, J. G., Castelli, V., Rippel, H. C., and Zimmerman, C. D., "A Computer Proram for Hydrostatic Bearings Including Effects on Non-Uniform Film Thickness and Relative Velocity for Various Methods of Lubricant Supply," The Franklin Institute, *Final Technical Report F-B2099*, Philadelphia, PA, April, 1964.

ORIGINAL PAGE IS
OF POOR QUALITY

Table 1. Pad 3 recess pressures[a]

Recess pressure	p_1	p_2	p_4	p_5
N/m^2	11,383,000	7,757,000	10,859,000	9,480,000
psi	1651	1125	1575	1375

[a]Assume $p_1 = p_3 = \frac{1}{2}(p_1 + p_3)$ and $p_4 = p_6 = \frac{1}{2}(p_4 + p_6)$.

ORIGINAL PAGE IS
OF POOR QUALITY

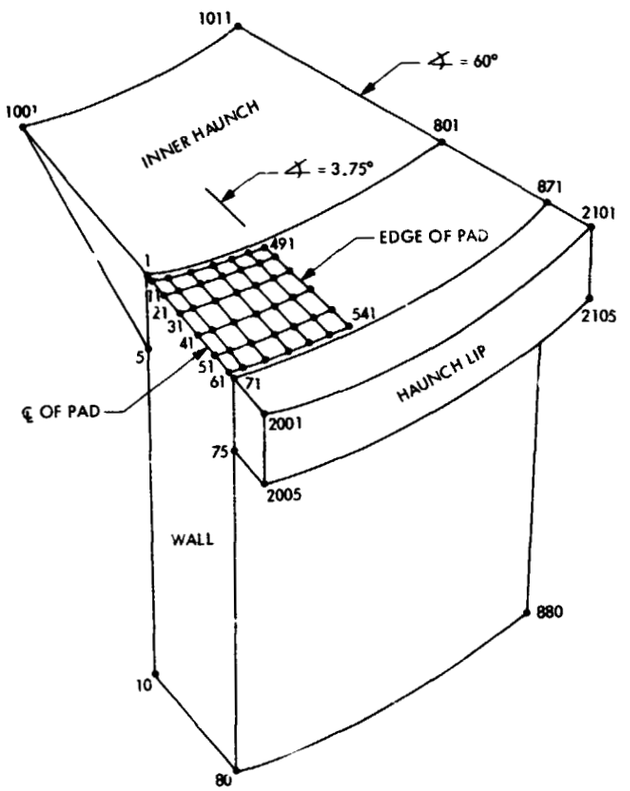

Fig. 1. New NASTRAN pedestal model and nodal points

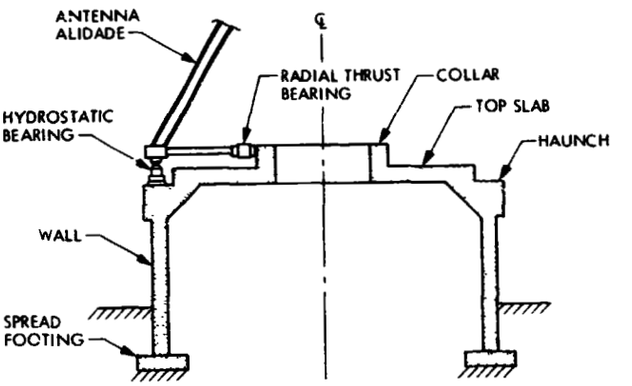

Fig. 2. Cross section of concrete pedestal

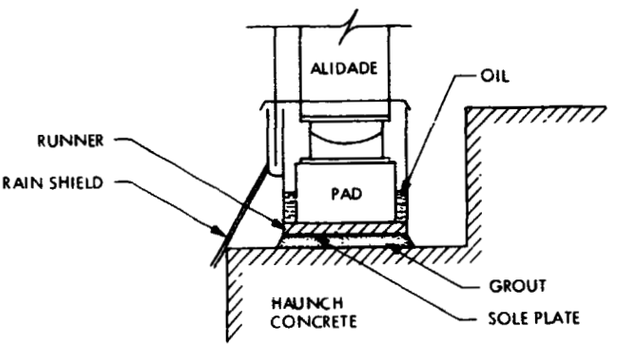

Fig. 3. Cross section of hydrostatic bearing system

ORIGINAL PAGE IS
OF POOR QUALITY

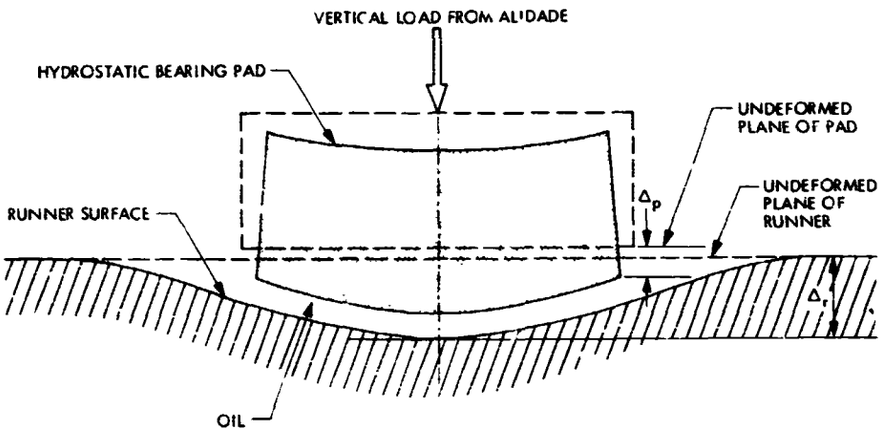

δ = MISMATCH OF DEFLECTED SURFACES

$\delta = \Delta_r - \Delta_p$

Fig. 4. Deflections of hydrostatic bearing pad and runner surface

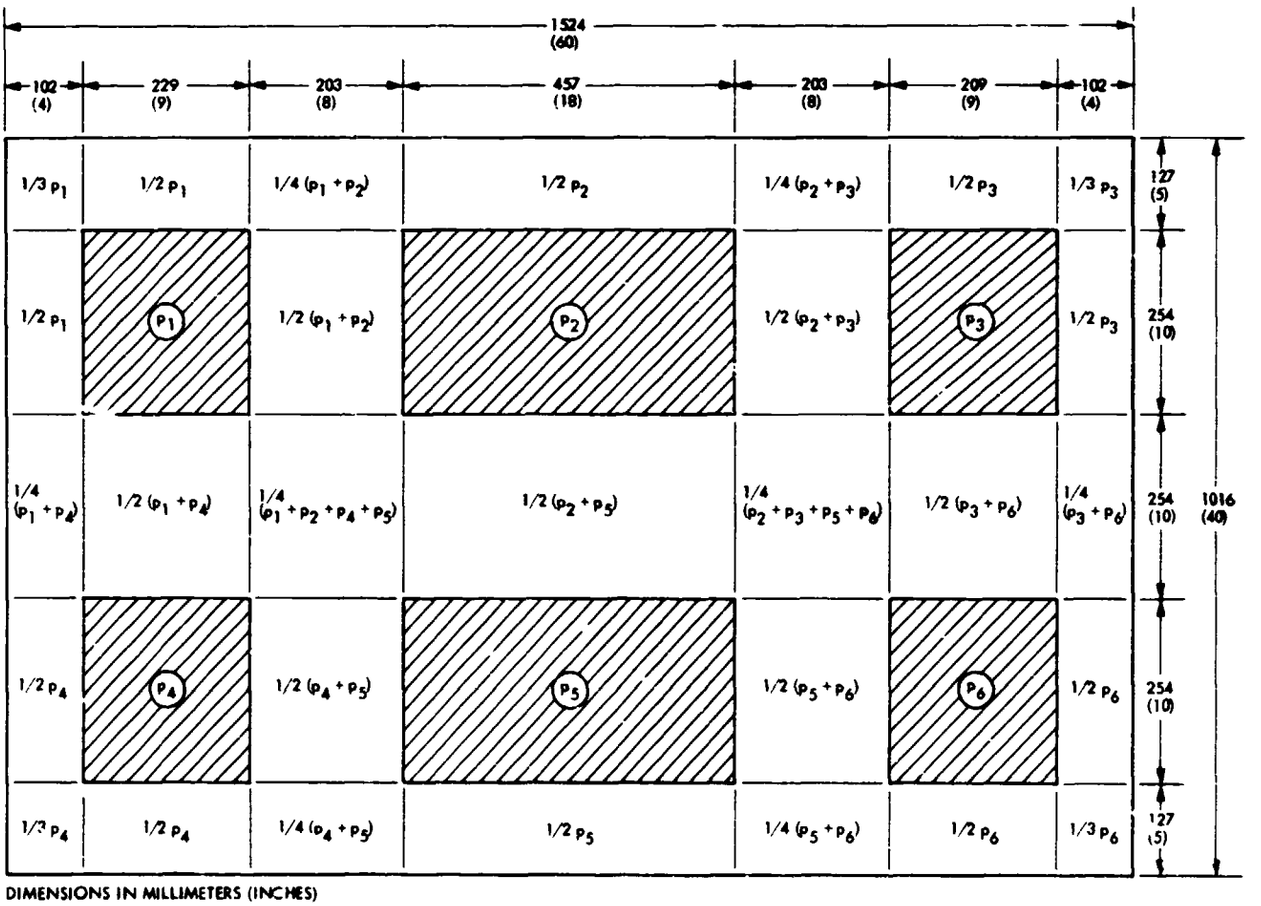

DIMENSIONS IN MILLIMETERS (INCHES)

Fig. 5. Pressure profile of hydrostatic bearing pad

ORIGINAL PAGE IS
OF POOR QUALITY

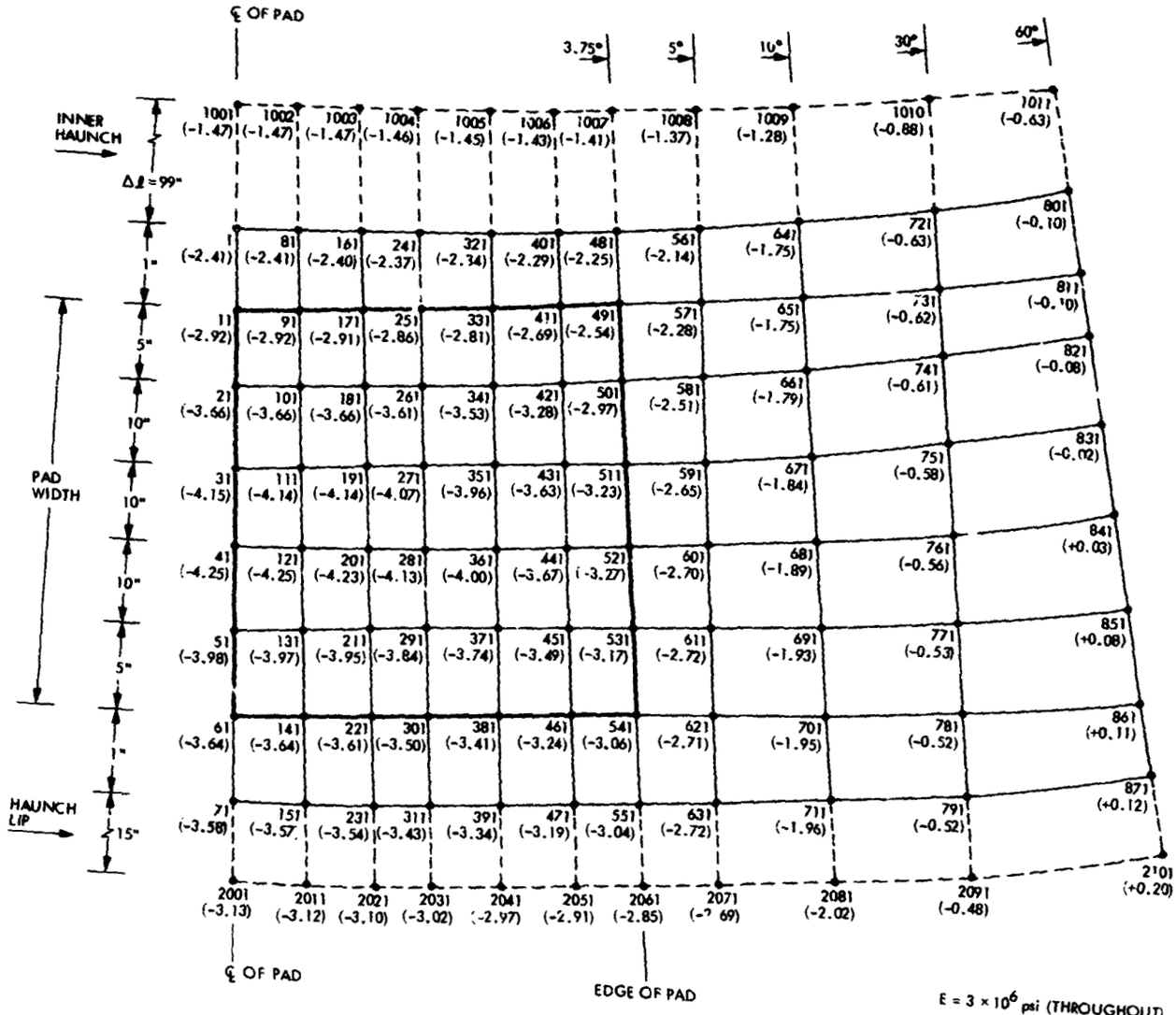

Fig. 6. Deflection map of top pedestal surface

ORIGINAL PAGE IS
OF POOR QUALITY

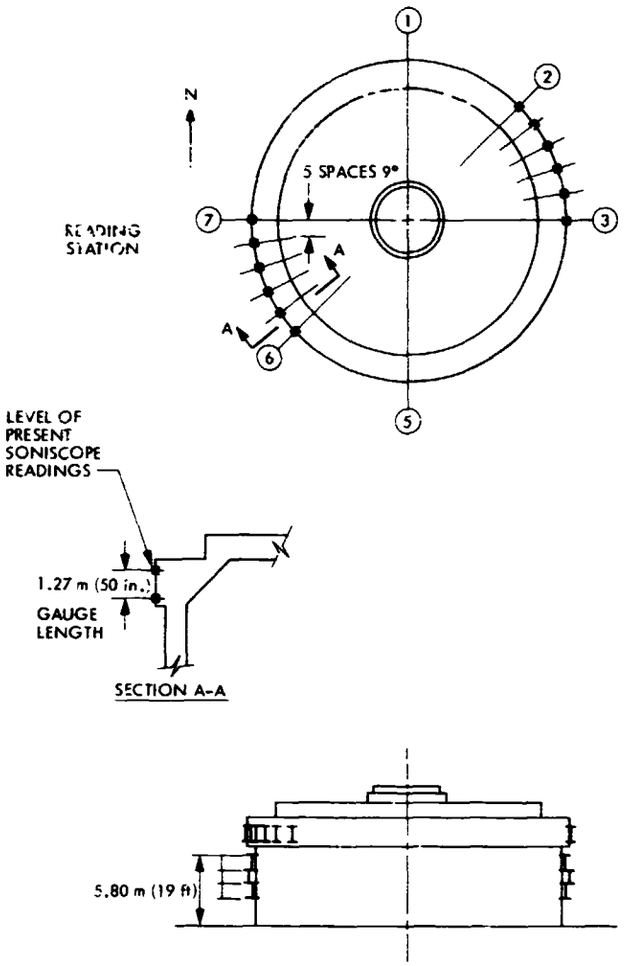

Fig. 7. Location of pad load tests

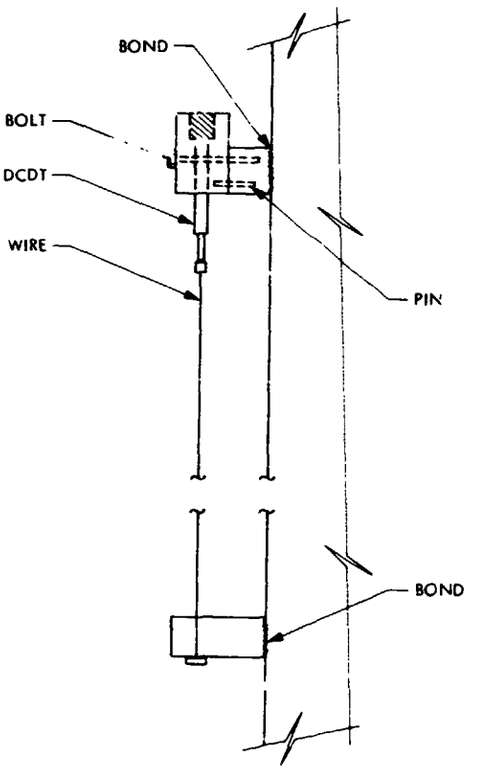

Fig. 8. Load test instrumentation

ORIGINAL PAGE IS
OF POOR QUALITY

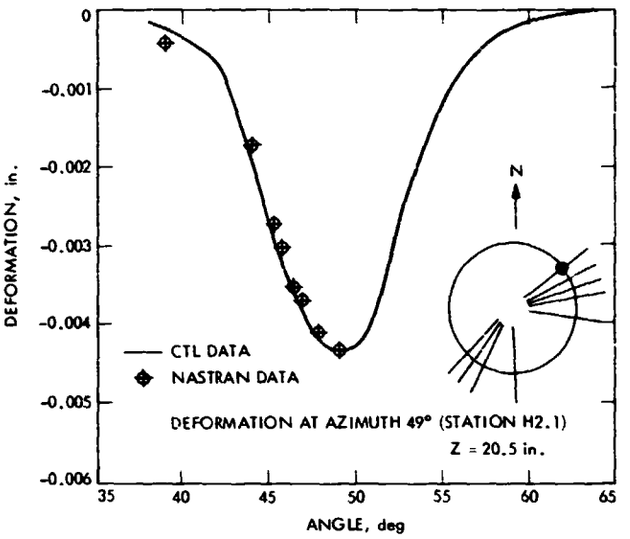

Fig. 9. Comparison of the NASTRAN model results with field test data, azimuth = 49°

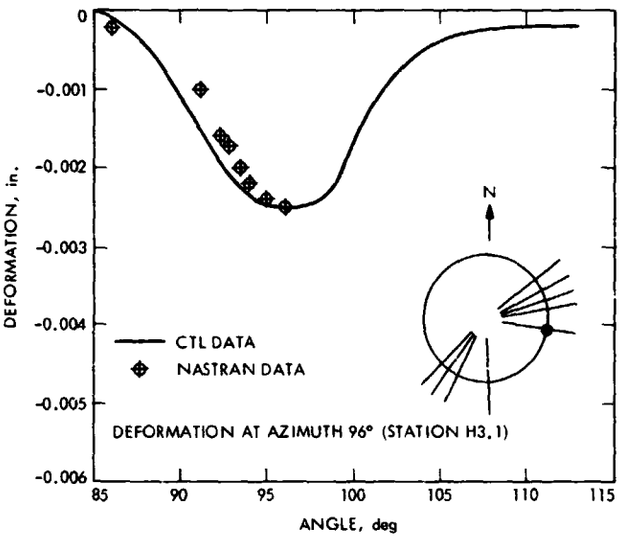

Fig. 10. Comparison of the NASTRAN model results with field test data, azimuth = 96°

D12 N84 13413

Energy Consumption Analysis of the Venus Deep Space Station (DSS-13)

N. V. Hayes
DSN Ground Antennas and Facilities Engineering Section

This report continues the energy consumption analysis and verification study of the tracking stations of the Goldstone Deep Space Communications Complex, and presents an audit of the Venus Deep Space Station (DSS 13). Due to the non-continuous radio-astronomy research and development operations at the station, estimations of energy usage were employed in the energy consumption simulation of both the 9-meter and 26-meter antenna buildings. A 17.9% decrease in station energy consumption was experienced over the 1979-1981 years under study. A comparison of the ECP computer simulations and the station's main watt-hour meter readings showed good agreement.

I. Introduction

In 1973, the Goldstone Deep Space Communications Complex (GDSCC) initiated an energy program in order to reduce its energy consumption following NASA guidelines. The program has the goal of reducing the consumption of purchased energy by 50% at the end of 1985 with the consumption level of 1975 used as a baseline.

In order to simulate the heating and cooling systems of the buildings under study, a computer model, the Energy Consumption Program (ECP), was developed (Ref. 1). Building construction parameters, weather conditions, and mechanical/electrical components usage are needed to calculate the energy consumption requirements of the building, the energy costs, and to suggest modifications of systems and procedures that would result in a reduction of energy usage.

The ECP model simulates the energy profile of a building in four consecutive steps. First, the heat loss or heat gain to the space under observation is computed. Second, the heating or cooling loads imposed on the air handlers are determined. Third, the energy expenditure of the primary equipment or components that comprise the air-conditioning system such as boilers, compressors, heat pumps, etc. is calculated. The simulation yields data that describe daily, monthly, and yearly consumption for the building or buildings under study. Verification of the computer model is achieved through comparison of its results to actual watt-hour meter data.

The GDSCC is composed of four Deep Space Stations. Verification reports for the Echo (DSS 12) and Mars (DSS 14) stations were presented in previous reports (Refs. 2 and 3). The Pioneer Deep Space Station (DSS 11) is presently inactive. The Venus Deep Space Station (DSS 13), converted to a radio astronomy research and development site, is examined in the present report.

II. Energy Consumption Analysis

The Venus station is composed of two RF antennas; one 9-m (30-ft) and the other 26-m (85-ft) in diameter, and four-

teen support, storage, and control buildings. The buildings are listed by their function in Table 1. The energy consumption is itemized by equipment as follows: 1) electrical/electronic equipment, 2) mechanical equipment, 3) heating, ventilation, air-conditioning (HVAC) equipment, 4) accessories, and 5) lights. The electrical equipment category includes digital computers, RF transmitters, RF receivers, electronic racks, and other electrical/electronics equipment not related to HVAC. Mechanical equipment includes those heat-generating machines inside the air conditioned space such as machine shop equipment, air compressors and oil pumps. Auxiliary mechanical and electrical equipment associated with HVAC operation is listed separately under accessories. Accessories are that equipment necessary for the building's operation but which does not affect the space heating and cooling load calculations. All the accessories at Venus station are electrically powered. Air-handler fans, condenser fans (for air-cooled chillers), boiler pumps, and external building lights are electrically-powered accessories. The internal lighting equipment is classified according to type: incandescent or fluorescent.

Collimation towers (G-54, G-57, G-64, G-66) and building G-67 (Distilled Water Building) are not included in the ECP simulation because they are small consumers of energy. Building G-61 (100-kW Transmitter building) and the 9-meter antenna, G-55, are incorporated with Building G-58 (30-ft Hydro-Mech. and Transmitter Building), and the three buildings are treated as a unit. In the three years under study, 1979-1981, the 9-meter antenna experienced a sharp drop in use, and in 1981 it was shut down completely (see Table 2). The 26-meter antenna, G-52, also experienced a sharp drop in use over the years 1979-1981: for this reason the G-58 (9-meter antenna system) and the G-52 (26-meter antenna) ECP simulations are based on 1979 operations, a year of moderate antenna usage.

Table 2 is a record of 9- and 26-meter antenna hours of operation during 1979-1981. The hours of operation are not a direct method through which electrical consumption of the two antennas might be calculated because: (1) both receive and transmit times are included, and (2) the activity at the antenna site is not confined to direct antenna support. The station is a research and development site, in contrast with the Mars and Echo sites, which are primarily devoted to spacecraft tracking operations. Antenna utilization includes, but is not confined to, radar mapping and planetary radio astronomy. Transmitters (Klystron tube type) are inspected at the test bed located in the Transmitter Building (G-53A). Klystrons of up to 400 kW transmitting capability may be tested. The test bed's maximum capability, however, had not been utilized in the three years under study. Averages of test bed loads were used in the simulation.

Records of transmitter use and load per assignment were not consistently kept over the years 1979-1981 for the 26-meter antenna. This antenna was usually in the receive mode. Field estimates show that the 26-m antenna was in the transmit mode 20% of the operation time in 1979, 10% of the operation time in 1980, and very sporadically in 1981. The maximum transmitter output is 100 kW. The Klystron is only 40-60% efficient, and located in the air-conditioned electronics room on the antenna. No extravagant load is placed on the HVAC system, as the transmitter is cooled via water circulation effected by a 18.64 kW (25-hp) pump that is also outside the air-conditioned space. The hot water is cooled by a heat exchanger located outside the Transmitter Building. This cooling system expels 150 kW of heat when the 100 kW transmitter is in operation. For the 26-m antenna, the input parameters to ECP reflect the above considerations.

The 9-m antenna was always in transmit mode. The 9-m antenna (building G-55) consists of the 100 kW Transmitter building, G-61, and the 9-m (30-ft) Hydro-Mech Building, G-58. Adjacent to building G-58 is a 75 kW motor-generator set that supplies power to other parts of DSS 13, and is in continuous use.

III. Results

A month-by-month listing of the simulated energy consumption by each of the above five energy groups is given in Table 3. The station consumes 1418 $MWh_{(e)}$ of electrical energy and about 425 $MWh_{(t)}$ of gas heat on an annual basis. Monthly heating and cooling loads of the major buildings are presented in Tables 4 and 5, and depicted in Figs. 1 and 2. The monthly average and peak heating loads are 28 $MWh_{(t)}$ and 38 $MWh_{(t)}$, respectively. The monthly average and peak cooling loads are 52 $MWh_{(t)}$ and 75 $MWh_{(t)}$, respectively.

A. Electrical Energy Consumption

Figure 3 illustrates the distribution of electrical energy consumption, from Table 3, between electronic equipment, mechanical equipment, HVAC, accessories, and lights. The largest single consumer of energy at the site is the accessories (42% of the total). Electronics and mechanical (non-HVAC) equipment represent about 41% of the total consumption. HVAC equipment represents only about 13% of the total consumption. Figure 4 gives the electrical consumption of the entire Venus station on a monthly basis. The average consumption and peak monthly electrical energy consumption (from Table 3) are 118 and 127 $MWh_{(e)}$, respectively.

Table 6 presents the yearly electrical consumption for site buildings as simulated by ECP. Calculations show that the 26-meter antenna and the 9-meter antenna consumed 29.4%

of total site electrical consumption in 1979, 24% in 1980, and 17.3% in 1981.

Figures 5, 6, 7, and 8 indicate the buildings which are the major energy consumers in four categories: HVAC, electrical equipment, accessories, and lights. The Control Building, G-51, houses data acquisition/reduction equipment and is the largest HVAC consumer. It consumes 28.2% of total site electrical energy (Fig. 9), and 50% of the total station's HVAC expenditure (Fig. 5). The data acquisition and reduction equipment are kept at constant temperature.

The relative distribution of major building electrical consumption is shown also in Fig. 9. Buildings G-51 and G-53B have about the same energy expenditure. G-53B, the 26-m (85-ft) Hydro Mech. building, houses the drive system of the 26-meter antenna. The drive system is not in continuous use, but when it is employed, the electrical expenditure of this building can be significant.

B. Comparison of the ECP Simulations and the Watt-Hour Meter Data

The electrical energy for the station is supplied via DSS 12 by both the local utility, Southern California Edison Company, and by diesel engine generators. The Venus site has three metered substations. Other watt-hour meters have been installed by JPL to monitor buildings or specific equipment as in Fig. 10. All meters are read once a month. A review of the meter records was done for the years 1979-1981. There is generally no one-to-one correlation between meters and buildings. One meter may record the consumption of several buildings, or the consumption of one piece of equipment. The only one-to-one meter-building correlation available is for the Laboratory and Office Building (G-60). Its ECP simulation agreed with the meter readings to 4.6% over the three years under study.

The overall electrical consumption, as recorded at the three Edison substations decreased by 12.8% between 1979 and 1980, and 9.1% between 1980 and 1981. The site had a 17.6% decrease in overall consumption between 1979 and 1981. This is primarily due to decreased antenna operation time.

For the 26-m antenna (G-52) and 9-m antenna (G-58), the simulated electrical consumptions obtained were added to the simulated consumptions for the other major buildings, and the combined result was compared to actual main site meter readings of record for 1979, 1980, and 1981. The simulation totals were found to be in accord with the meter reading totals.

IV. Summary

The ECP program allows a detailed analysis of energy consumption for a complex of buildings, or an individual building. In this study, estimates of antenna time and facilities usage were made because of the intermittent research and development activities at the site. When the ECP-simulations of the other buildings were compared to the main meter readings, total yearly consumption was verified over the three-year study period.

The ECP program allows also a categorization of energy consumption of the Venus station buildings. The computer simulations disclosed that the Control Building (G-51) is the largest consumer in the HVAC category due to its housing of data acquisition/reduction equipment. The simulation also revealed that G-51, the Control Building, and G-53B, the 26-m (85-ft) Hydro-Mech. Building, consumed equal amounts of electrical energy during 1979, a year of moderate antenna usage. This showed the considerable amount of power expended when the 26-m antenna drive system is in operation.

Most buildings at the Venus site are not individually metered. It is suggested that individual meters be installed to facilitate future energy audits. Updated single-line electrical drawings should be made. The meters should be inspected regularly. Also, a system of recording the 26-m antenna operation time, transmit and receive times and RF transmitter load for each assignment would give a better profile of the antenna energy consumption.

Acknowledgments

The author wishes to acknowledge the assistance of P. Stelzmuller and G. Glover in providing building and systems information necessary in the compilation of this report. G. Wischmeyer, K. Gwynn, E. Jackson, and A. Price of GDSCC supplied operational data and HVAC systems information. D. Schonfeld and F. Lansing edited the report.

References

1. Lansing, F. L., et al., "The Updated Algorithm of the Energy Consumption Program (ECP)," *TDA Progress Report 42-49*, Jet Propulsion Laboratory, Pasadena, CA, 1979, 107-115.

2. Guiar, C. N., Schonfeld, D., "Energy Consumption for the Echo Station (DSS-12)," *TDA Progress Report 42-66*, Jet Propulsion Laboratory, Pasadena, CA, September and October 1981, 355-363.

3. Hayes, N. V., "Energy Consumption Analysis for the Mars Deep Space Station," *TDA Progress Report 42-69*, Jet Propulsion Laboratory, Pasadena, CA, March and April, 1982, 200-207.

ORIGINAL PAGE IS
OF POOR QUALITY

Table 1. Venus Station buildings

No.	Description
G-51	Control Building
G-52	26-m (85 ft) Antenna
G-53A	Transmitter Building
G-53B	26-m (85 ft) Hydro-Mech. Building
G-54	Collimation Tower
G-55	9-m (30 ft) Antenna
G-56	Security Building
G-57	Collimation Tower
G-58	9-m (30 ft) Hydro-Mech. and Transmitter Building
G-60	Laboratory and Office Building
G-61	100 kW Transmitter Building
G-62	Fire Line Pump House
G-63	Workshop and Warehouse
G-64	Collimation Tower
G-66	Collimation Tower
G-67	Distilled Water Building

Table 2. Antenna hours of operation – Venus Station

Month	26-m antenna			9-m antenna		
	1979	1980	1981	1979	1980	1981
Jan.	53	161	104	6	3	0
Feb.	157	135	179	12	2	0
Mar.	127	190	71	12	1	0
Apr.	113	142	136	10	0	0
May	206	121	234	19	6	0
Jun.	121	230	90	12	0	0
Jul.	146	201	131	11	0	0
Aug.	169	211	177	12	0	0
Sept.	80	117	162	17	0	0
Oct.	194	168	108	8	0	0
Nov.	143	114	45	10	0	0
Dec.	17	146	276	12	0	0
Total	1526	1936	1713	141	12	0

ORIGINAL PAGE IS
OF POOR QUALITY

Table 3. Simulated energy consumption for the Venus Station, MWh

Month	Electrical accessories	Lights		Electronics equipment	Mechanical equipment	HVAC equipment		Other thermal equipment	Total electrical	Total thermal
		Incandescent	Fluorescent			Thermal	Electrical			
Jan.	48	2	3	31	23	40	10	2	117	42
Feb.	44	2	3	28	21	31	10	2	108	33
Mar.	48	2	3	31	23	33	11	2	118	35
Apr.	47	2	3	22	22	30	12	2	108	32
May	51	2	3	22	23	38	17	2	118	40
Jun.	51	2	3	22	22	32	22	2	122	34
Jul.	52	2	3	22	23	30	25	2	127	32
Aug.	52	2	3	22	23	31	25	2	127	33
Sept.	51	2	3	21	22	33	20	2	119	35
Oct.	49	2	3	21	23	28	15	2	123	30
Nov.	47	2	3	30	22	34	10	2	114	36
Dec.	48	2	3	31	23	41	10	2	117	43
Year Total	5	24	36	313	270	401	187	24	1418	425

Table 4. Major building heating load, $MWH_{(t)}$

Building	Month												Yearly Total
	Jan.	Feb.	March	April	May	June	July	Aug.	Sept.	Oct.	Nov.	Dec.	
G-51	23	18	20	18	26	23	22	22	23	17	20	23	255
G-53B	2	1	1	0	0	0	0	0	0	0	1	2	7
G-56	1	0.4	0.4	0.2	0	0	0	0	0	0	0.5	1	3.5
G-60	10	7	7	6	5	3	3	3	4	5	7	10	70
G-62	1	0	0	0	0	0	0	0	0	0	0	1	2
G-63	1	0.3	0.3	0.2	0	0	0	0	0	0	0.3	1	3.1
Total	38	27	29	24	31	26	25	25	27	22	29	38	341

Table 5. Major building cooling load, $MWh_{(t)}$

Building	Month												Yearly Total
	Jan.	Feb.	March	April	May	June	July	Aug.	Sept.	Oct.	Nov.	Dec.	
G-51	28	27	31	31	38	40	43	42	39	33	29	27	408
G-52	0	1	1	2	3	4	5	5	4	3	1	0	29
G-53A	0	0	0	0	2	4	4	4	3	3	0	0	20
G-53B	2	2	3	3	6	7	8	8	7	3	3	3	55
G-58	0	0	0	0	1	2	2	2	1	0	0	0	8
G-60	6	7	9	9	7	10	12	11	9	10	8	6	104
G-63	0	0	0	0	0	1	1	1	1	1	0	0	5
Total	36	37	44	45	57	68	75	73	64	53	41	36	629

Table 6. Simulated yearly electric consumption for Venus Station Buildings

Building No.	Electrical consumption[a] $KWh_{(e)}$
G-51	398,191
G-52	207,558
G-53A	82,816
G-53B	371,655
G-56	15,150
G-58	207,543
G-60	110,109
G-62	2,523
G-63	17,398
Total	1,412,943

[a]1979 meter reading is 1,416,480 $KWh_{(e)}$

ORIGINAL PAGE IS
OF POOR QUALITY

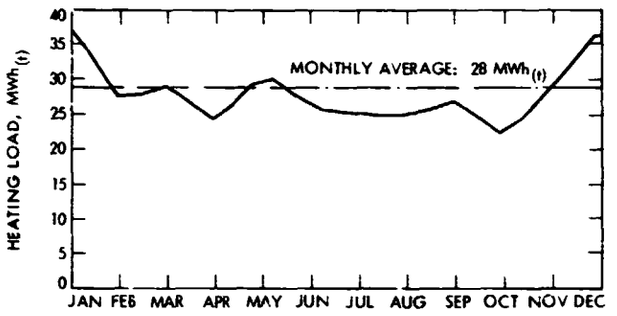

Fig. 1. Monthly heating load of the Venus Station

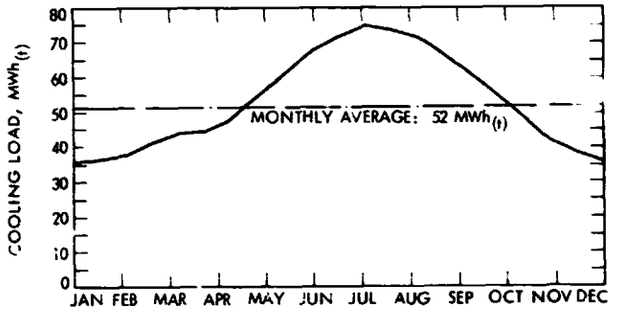

Fig. 2. Monthly cooling load of the Venus Station

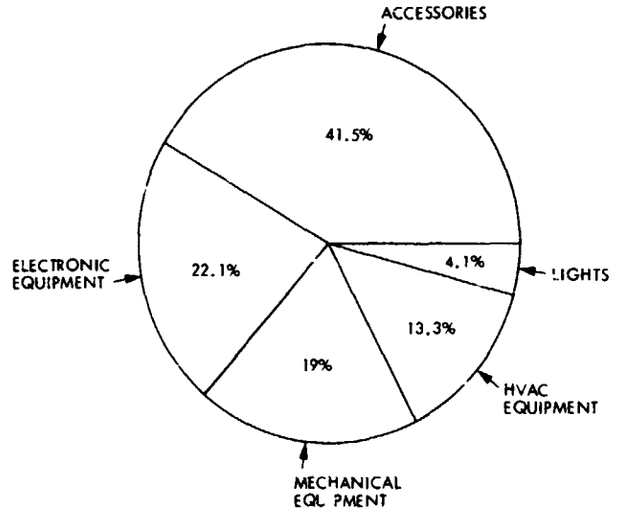

Fig. 3. Itemization of annual electrical consumption, Venus Station

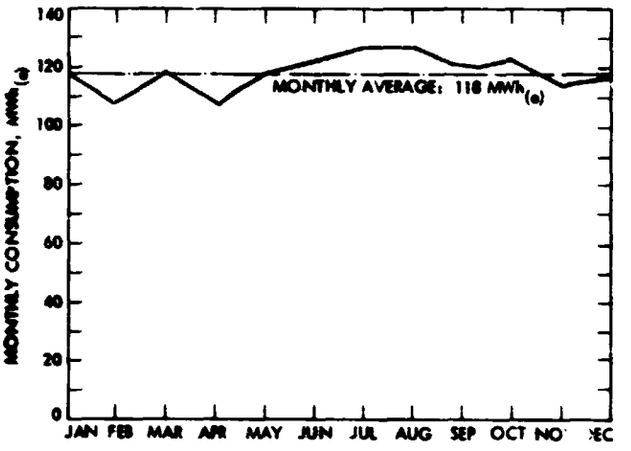

Fig. 4. Electrical consumption on a monthly basis, Venus Station

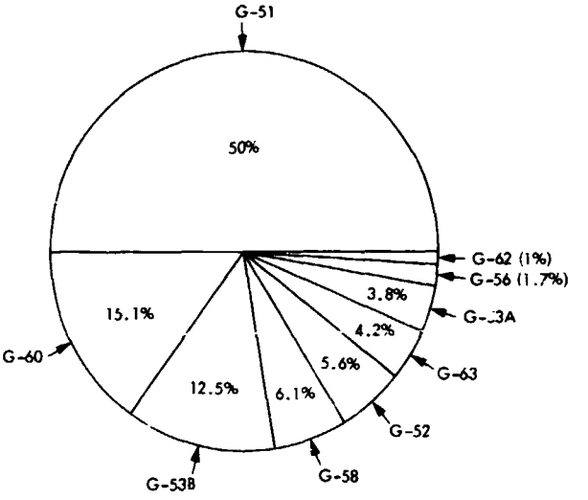

Fig. 5. Electrical consumption of HVAC equipment of major buildings, Venus Station

ORIGINAL PAGE IS
OF POOR QUALITY

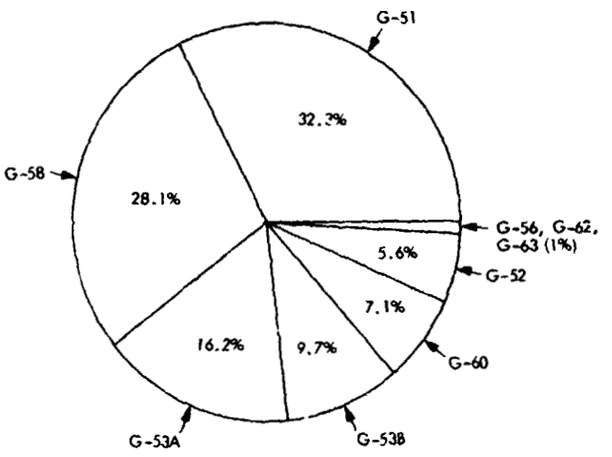

Fig. 6. Electrical/electronics equipment consumption of major buildings, Venus Station

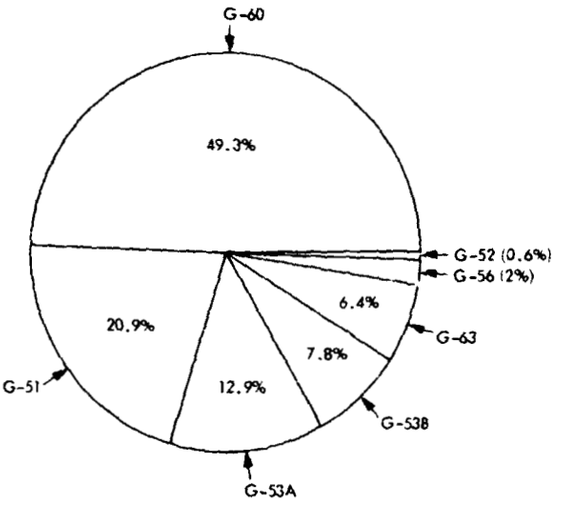

Fig. 8. Lighting consumption of major buildings, Venus Station

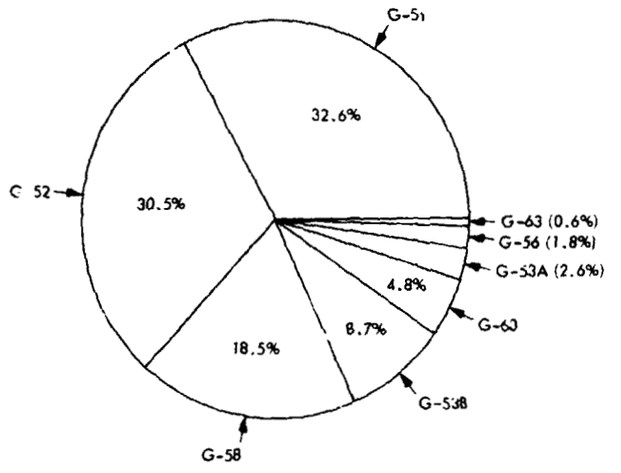

Fig. 7. Accesso... consumption of major buildings, Venus Station

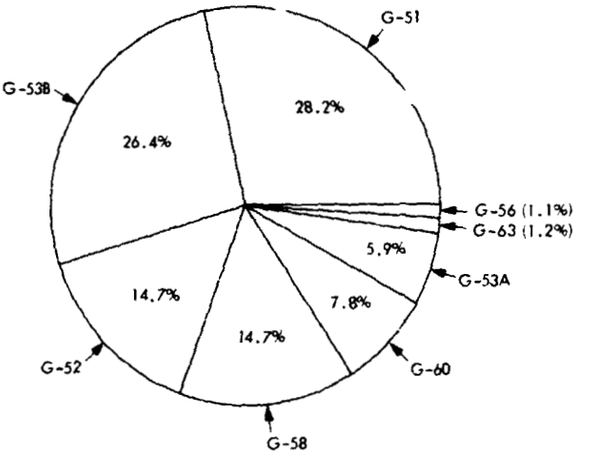

Fig. 9. Yearly electrical consumption of major buildings, Venus Station

ORIGINAL PAGE IS
OF POOR QUALITY

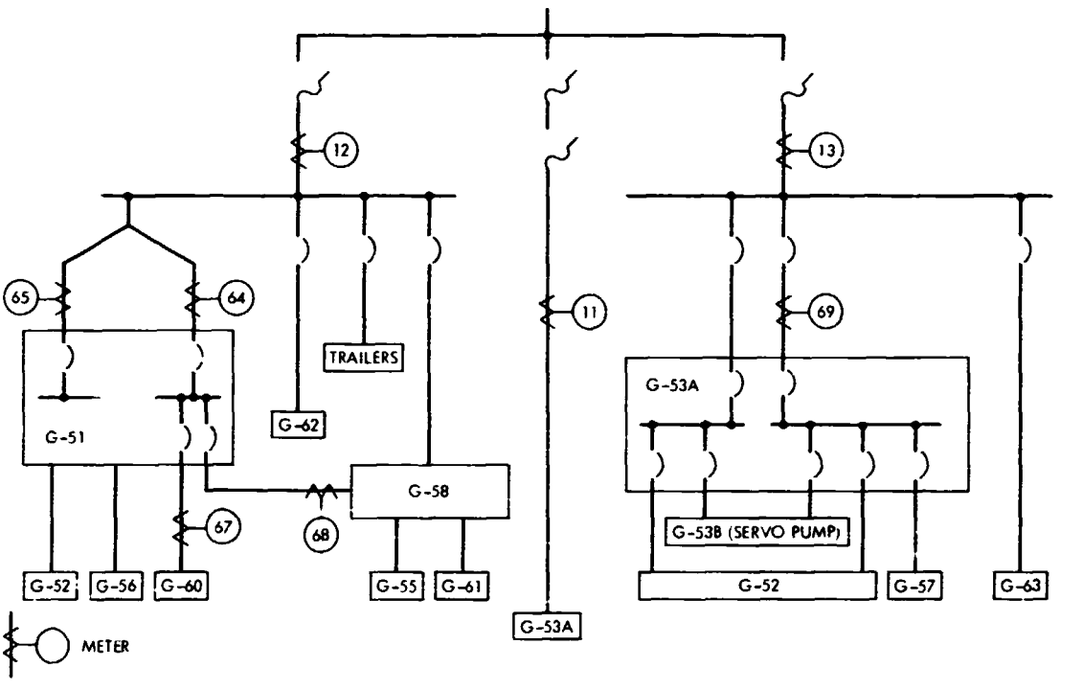

Fig. 10. Layout of watt-hour meters at Venus Station

D13 N84 13414

A Study of the Charged Particle Calibration Requirements for the Deep Space Network

S. A. Townes
Communication Systems Research Section

This report presents a study made of the DSN charged particle calibration requirements. The effects of charged particles on navigation and timing systems were reviewed and it was proposed that a system based upon the Global Positioning System satellites be used to measure the charged particle content of the ionosphere. The system would be required to measure the total electron content of the ionosphere to the order of 10^{16} electrons/meter^2. Two types of systems were suggested as possible candidates for making these measurements.

I. Introduction

This report details the charged particle calibration requirements and reviews systems available for performing the calibration function for the Deep Space Network (DSN). It will be shown that a calibration system based upon the Global Positioning System (GPS) capable of measuring the ionospheric total electron content (TEC) to the order of 10^{16} electrons/meter^2 (el./m^2) (1σ) every 60 seconds will provide the needed accuracy.

It is well known (Refs. 1,2) that radio signals traveling through a region of charged particles, like the earth's ionosphere or interplanetary plasma, can be corrupted by these particles in many ways. The DSN relies upon radio signals traversing these regions not only for data transmission but also for spacecraft orbit determination, and time and frequency synchronization. It is then necessary to determine the charged particle effects upon these signals and adequately calibrate them out to maintain the required accuracy.

Each flight project (Galileo, Voyager, etc.) has its own requirements for navigation accuracy, and time and frequency synchronization. The specifications are usually made in terms of range and velocity (or Doppler) measurement error, and synchronization accuracy requirements. In some cases, requirements for charged particle calibration are explicitly detailed but this is not necessarily a standard practice. Where it is done, the method of specification varies. It would be good practice in the future if each flight project would specify its charged particle calibration requirements. These requirements should be specified in a standard form such as TEC.

The Frequency and Timing System of the DSN currently uses a GPS based system as well as VLBI techniques for maintaining frequency and time synchronization. The GPS system will be used here although the same requirements apply to the VLBI system. The DSN requirements levied upon this system must also be considered since charged particles affect the signals from the GPS satellites.

The requirements detailed here are gleaned from many DSN documents and conversations with people in the navigation, tracking, and frequency and timing areas.

II. Proposed DSN Charged Particle Calibration Requirements

The proposed DSN charged particle calibration requirements have been determined from the navigation, and frequency and timing requirements of the Voyager, Galileo and International Solar Polar Mission (ISPM) projects as well as the requirements on the Frequency and Timing System. The requirements are first stated in these terms and then the required TEC measurements are derived.

The strongest requirement on range accuracy is that of Voyager. It requires 3 m or less (3σ) ranging noise at S-band for a 10 minute integration time at the 64 m dish ("Voyager-Uranus/Interstellar Mission, Support Instrumentation Requirements Document," PD 618-502, JPL internal document). If we ignore the 10 minute integration time, thus making it a tougher specification, the 3 m requirement at 2295 MHz translates to a TEC of 3.9×10^{17} el./m^2 (3σ). This comes from the fact that the effective range change, ΔR, is (Ref. 3).

$$\Delta R = \frac{AI}{f^2} \tag{1}$$

where A = 40.3 in MKS units, I is the TEC in el./m^2 and f is the frequency in Hz.

The ISPM requires the ability to measure velocity, hence Doppler, to 1 mm/s (assumed 3σ) for a 60 s count ("International Solar Polar Mission – Mission Requirements Document," Pub. 628-51, JPL internal document). This is the tightest specification of all of the projects. At 2295 MHz, this radial velocity imparts a frequency shift of approximately

$$f_D = -\frac{\dot{\rho}}{c} f_T = -7.65 \text{ MHz} \tag{2}$$

where $\dot{\rho}$ is the radial velocity, c is the speed of light and f_T is the transmitted frequency. This amount of Doppler at 2295 MHz due to charged particles would be caused by a changing TEC of 5.2×10^{15} el./m^2/s. Here the effective frequency change is related to the TEC by (Ref. 3)

$$\Delta f = \frac{-A}{4\pi^2 fc} \cdot \frac{dI}{dt} \tag{3}$$

Over a 60 s interval this is a total TEC change of 3.1×10^{17} el./m^2 if we assume a constant rate.

The Frequency and Timing System performs time and frequency synchronization functions via the GPS signal at 1575.42 MHz (L_1). The proposed time synchronization accuracy is 10 ns (1σ) ("Deep Space Station [Mark III-77] and Deep Space Communications Complex [Mark IVA] Subsystem Requirements – Frequency and Timing Subsystem [1981-1986]," Pub. 824-13, JPL internal document). A 10 ns delay at the L_1 frequency would be caused by a TEC of 1.85×10^{17} el./m^2. The frequency synchronization is required to be known to $\pm 3 \times 10^{-14}$ $\Delta f/f$. Since this measurement is based upon a number of GPS time measurements the question is whether the 10 ns accuracy on the time measurements is sufficient. It can be shown that for a sufficient number of measurements over a length of time (e.g., 2 measurements a day for 10 days), the 10 ns requirement is good enough assuming that the only error in the measurements is due to charged particles.

In summary then, if the charged particle errors were the only errors measurement accuracy on the order of 10^{17} el./m^2 would be sufficient. Table 1 presents a summary of the individual requirements. Since charged particle errors are not the only ones in the navigation or frequency and timing systems it would be nice to keep these down even lower – say by a factor of ten. This would require the ability to measure TEC to 10^{16} el./m^2 every 60 s. The next section will address the feasibility of making such a measurement.

III. Charged Particle Calibration Systems

A. Introduction

The charged particle calibration system can be integrated into the spacecraft for navigation purposes or it can be independent of it. The charged particle information necessary for the time and frequency functions can be determined from the GPS satellite signals or independently of them. Each of these possibilities has its advantages and disadvantages.

The spacecraft borne systems, their performance and hardware implications are adequately discussed in Refs. 5 and 6. Suffice it to say that an onboard dual frequency ranging transponder is the best for navigation requirements. Spacecraft borne systems have the advantage that the charged particle measurements are made in the direction of the spacecraft so no mapping is required. The measurements also include the effects of all charged particles between the spacecraft and the tracking site. The range error over a pass has been estimated to be 0.5 m using this method (Ref. 6). A primary disadvantage of the type of system is the cost of the additional hardware for the spacecraft and ground systems. The use of such a system as the main charged particle calibration system for the DSN would also require that the ranging function be performed more often than is necessary for navigation purposes alone.

ORIGINAL PAGE IS
OF POOR QUALITY

Since this would require the use of one of the large dish antennas, it could be a severe inconvenience. With regard to the time and frequency measurements via GPS, a mapping would be needed of this charged particle data to the line of sight to the satellites (approximately 5% error).

The best general purpose approach to charged particle calibration then is one that is spacecraft independent. This reduces the necessity for costly hardware onboard the spacecraft and for continuous ranging. There are many methods to perform the calibration function but currently all but one can be ruled out. Ionospheric sounding techniques are not as accurate as needed by the DSN (Ref. 7) and a thorough job of top and bottom sounding as often as needed could be an expensive process. The VHF satellite beacons currently being used for making Faraday rotation measurements are becoming unavailable at the DSN tracking sites through the demise or relocation of the satellites. While this is certainly an accurate technique, there are no replacement satellites being planned for the foreseeable future. This leaves the dual frequency measurement technique as the most likely candidate. It has the capability of providing all of the accuracy required, and the GPS satellites are configured to provide the dual frequency signals exactly for this purpose.

The GPS satellites produce signals at 1575.42 MHz (L_1) and 1227.6 MHz (L_2) that are modulated with identical ranging codes (P-code). The TEC can be determined by measuring the difference in arrival times of these codes at the receiver as can be derived from Eq. (1). Information about the derivative of the TEC can also be determined from the Doppler on the carrier frequencies if needed as can be derived from Eq. (3).

There are two basic types of systems for determining the TEC via the GPS satellites. One requires a knowledge of the P-code and the other does not. There are advantages and disadvantages to each approach.

B. Delay-Lock Loop

The conventional approach requires a knowledge of the ranging code and tracks this code via some form of delay-lock loop (DLL) (Ref. 8). A generalized expression for the variance of the measurement noise in a DLL (in s^2) can be written (Ref. 9):

$$\sigma^2 = \left[\frac{K_1 B_n}{(C/N_0)} + \frac{K_2 B_i B_n}{(C/N_0)^2}\right] \cdot T^2$$

where

C/N_0 = carrier-to-noise density ratio,

B_n = one-sided code tracking loop noise bandwidth,

B_i = IF bandwidth for noncoherent code tracking loops,

K_1, K_2 = loop mechanization constants,

T = bit period.

It should be noted that this system is relatively complex and requires some time for initial acquisition. A coherent DLL is shown in Fig. 1.

C. Delay and Multiply

The second approach uses the standard delay and multiply technique (Ref. 8) for recovering the 10.23 MHz clock signal of the P-code. This is done at the L_1 and L_2 frequencies and the difference in clock phases is used to measure the delay due to the TEC. Note that if the difference is more than one clock cycle (97.75 ns) there is an ambiguity problem but this can usually be resolved in software.

Consider the baseband delay and multiply circuit with non-return to zero pulses, a 1/2 bit delay and a first order Butterworth low pass filter of bandwidth B followed by a phase lock loop of bandwidth B_L centered at 10.23 MHz, as shown in Fig. 2. The variance of the measurement noise (in s^2) is as follows (Ref. 10 and "TOPEX Notes," private communication to B. Crow from B. K. Levitt):

$$\sigma^2 = \frac{N B_L}{P} \cdot \frac{T^2}{4\pi^2}$$

$$P = \frac{2 S^2 \eta^2}{K^2}\left[\frac{K^2 (1-\beta)^4 (2+\beta)^2 + 16\eta^2}{C_1 C_2}\right]$$

$$N = U + V$$

$$U = \frac{2 S N_0 \eta^2}{C_1}\left[1 - \frac{(3-\beta^2)(1-\beta^2)(K^4 + K^2\eta^2 + 6\eta^4)}{2\eta C_1 C_2}\right]$$

$$V = \frac{N_0^2 \eta^3 (1-\beta^2)}{2T C_2}$$

where

$$\eta = 4BT$$

$$\beta = e^{-2BT}$$

$$K = 2\pi$$

$$C_1 = K^2 + \eta^2$$

$$C_2 = K^2 + 4\eta^2$$

The equations presented above are for single measurements but each delay measurement involves measurements at L_1 and L_2. The variance of the delay measurement for equal power at L_1 and L_2 is then

$$\sigma_T^2 = 2\sigma^2$$

A simple comparison can be made between the delay and multiply system and the DLL as discussed. The delay and multiply circuit is shown in Fig. 1 and has an input bandwidth B such that $BT = 1.1$ and the phase-locked loop noise bandwidth is B_L = 1 Hz. The coherent (2Δ) DLL shown in Fig. 2 has a noise bandwidth B_n = 1 Hz also for comparison. Figure 3 presents the standard deviation of the delay measurement, σ_T versus the carrier power-to-noise power density ratio, C/N_0. The important point to notice is that while the performance of the DLL is in general superior to that of the delay and multiply, in the region of interest (σ_T = 0.35 ns) there is about a 5 dB difference in the required C/N_0. Note that for the large enough C/N_0 the performance of the two systems is essentially equivalent.

To put these results in perspective, the GPS P-code signal at L_2 has a received power of -166 dBW (-163 dBW at L_1), and a receiver with a noise temperature of 100 K would produce a C/N_0 of 43 dB-Hz. Reducing the receiver noise enough to meet the C/N_0 requirements for the delay and multiply and DLL would require noise temperatures of 4 K and 12 K respectively. This would require significant and expensive cooling. An alternative to reducing the noise temperature is adding an antenna with gain. The minimum gains required for the DLL and delay and multiply would be 10 dB and 16 dB respectively. The disadvantage of using an antenna with gain is the inherent directivity this implies. Ideally one would want the capability of receiving all visible satellites at one time but this does not appear to be possible. The best compromise would be some sort of electronically steerable array that could sequence through the visible satellites. The logistics of this would have to be considered in terms of how fast this could be accomplished in conjunction with taking the required readings from each satellite signal and locating each satellite in the sky with software. Some compromises must be made while still making most efficient use of the system.

One final point concerning the use of the GPS satellites needs to be considered. The time difference between the L_1 and L_2 P-codes onboard the satellite is specified to be no larger than 1.5 ns. This 1.5 ns translates to 4.3×10^{16} el./m^2 such that the ultimate limitation on TEC measurement may be this figure. It is not known currently what the delays really are for each satellite but this may in fact be something that can be measured and calibrated at a later date.

IV. Currently Available Equipment

The currently available commercial equipment uses the conventional DLL code tracking technology. The delay and multiply technique is used in development systems with the intent of future production.

The major manufacturers of the DLL based systems are Stanford Telecommunications Inc. (STI), Texas Instruments (TI), Magnavox and Rockwell-Collins. Examples of equipment that could perform the ionospheric calibration task are the STI 5010 and the TI-4100. The basic equipment price without any modification that might be required is on the order of $150,000 for each of these units.

The delay and multiply based systems are currently under development at JPL and International SERIES Technology Applications Corp. The JPL versions are the SERIES-X receiver and the Satellite L-Band Ionospheric Calibration (SLIC) system (Ref. 11). Current accurate prices are not known for this equipment but it is conceivable that it could be less expensive than the DLL based receivers.

V. The Ideal System and Minimum Requirements

The ideal charged particle (ionospheric) calibration system based upon the GPS satellites would have the following characteristics:

(1) The ability to monitor all visible satellites simultaneously (continuously).

(2) The ability to measure L_1/L_2 P-code time of arrival differences to 0.350 ns (1σ) at least every 60 s providing a TEC measurement accuracy of 10^{16} el./m^2.

(3) The ability to measure L_1/L_2 Doppler to 1 MHz (equivalent to a changing TEC of 5.16×10^{14} el./m^2/s which in turn is equivalent to 0.1 mm/s velocity at 2295 MHz).

(4) A mapping/modeling capability for determining the line of sight charged particle information from the GPS data.

This may prove expensive since 4 or 5 complete L_1/L_2 single satellite receivers would be needed in addition to four antennas. What then are the minimum requirements?

(1) The ability to monitor at least one of the visible satellites.

(2) The ability to measure the L_1/L_2 P-code (or P-code clock) time of arrival differences to 0.350 ns (1σ) every 60 s providing a TEC measurement on the order of 4×10^{16} el./m^2 or less.

(3) A mapping/modeling capability for determining the line of sight charged particle information from the GPS data.

The technology is currently available for the ideal system as well as the minimum system. Any of the previously discussed available systems could meet these minimum requirements.

VI. Conclusion

The GPS system has been recommended as a viable means of providing charged particle calibration for navigation and timing purposes. It is capable of providing the near earth calibration data needed and at the accuracy required.

The one possible problem with this system is that the Department of Defense controls it and may choose to change the P-code or otherwise degrade the system accuracy. The SLIC system is felt to have an advantage in this area since it does not require knowledge of the P-code. The likelihood of this event arising, however, is felt to be remote and thus should not constitute a major consideration.

The use of a GPS based calibration system should not preclude other systems. In fact, the DSN is encouraged to continue requesting beacons on geostationary satellites for making Faraday rotation measurements. A Faraday rotation system is an inexpensive (ground segment) back up or supplement to the GPS system. Calibration systems aboard deep space probes, etc. can also provide information about interplanetary charged particles that the GPS based system cannot.

The DSN should also make an effort to make its ionospheric/charged-particle measurements available to the radio science community. These data will be of use to those investigating ionospheric phenomena and this in turn will ultimately benefit the DSN. Through a better understanding of the ionosphere, better mapping and modeling can be accomplished thus improving navigational and timing accuracy.

References

1. Lawrence, R. S., Little, C. G., and Chivers, H. J. A., "A Survey of Ionospheric Effects Upon Earth-Space Propagation," *Proceedings of the IEEE*, Vol. 52, no. 1, pp. 4-27, January 1964.

2. Davies, K., *Ionospheric Radio Propagation*, Dover Publications, Inc., New York, 1966.

3. Yip, K. W., and Mulhall, B. D., "A system analysis of error sources in the technique used for ionospheric calibration of deep space probe radio metric data," *JPL Tech. Report 32-1526*, Vol. XVIII, pp. 48, December 15, 1973.

4. Yuen, J. H., Ed., *Deep Space Telecommunications Systems Engineering*, JPL Pub. 82-76, July 1982, p. 60.

5. Mulhall, B. D., "Charged-Particle Calibration System Analysis," *JPL Space Programs Summary 37-64*, Vol. II, pp. 13-21.

6. von Roos, O. H., and Mulhall, B. D., "An Evaluation of Charged Particle Calibration by a Two-Way Dual-Frequency Technique and Alternatives to this Technique," *JPL Technical Report 32-1526* Vol. XI, pp. 42-52, October 15, 1972.

7. Garriott, O. K., da Rosa, A. V., and Ross, W. J., "Electron content obtained from Faraday rotation and phase path length variations," *J. Atmos. and Terr. Physics*, Vol. 32, pp. 705-727, 1970.

8. Spilker, J. J., *Digital Communications by Satellite*, Prentice-Hall, Inc., Englewood Cliffs, N. J., 1977.

9. Martin, E. H., "GPS User Equipment Error Models," *Global Positioning System*, Institute of Navigation, Washington, D. C., 1980, pp. 109-118.

10. McCallister, R. D., and Simon, M. K., "Cross-Spectrum Symbol Synchronization," *ICC Conference Record 1981*, pp. 34.3.1-34.3.6.

11. MacDoran, P. F., Spitzmesser, D. J., and Buennagel, L. A., "SERIES: Satellite Emission Range Infrared Earth Surveying," *Proceedings of the Third International Geodetic Symposium on Satellite Positioning*, Las Cruces, New Mexico, February, 1982.

Table 1. DSN requirements used for determining proposed charged particle calibration requirements

Requirement	Error	TEC equivalent (electron/m^2)
Range[a]	3 m (3σ)	3.9×10^{17}
Velocity[a]	1 mm/s (3σ)	3.1×10^{17} (over 60 s)
Time sync[b]	10 ns (1σ)	1.8×10^{17}
Frequency sync	$\pm 3 \times 10^{-14} \Delta f/f$	–

[a] 2295 MHz
[b] 1575.42 MHz

ORIGINAL PAGE IS
OF POOR QUALITY

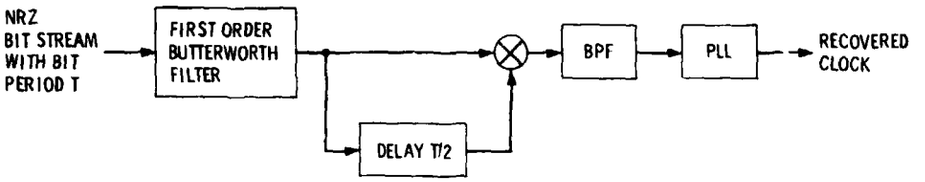

Fig. 1. Baseband delay and multiply circuit

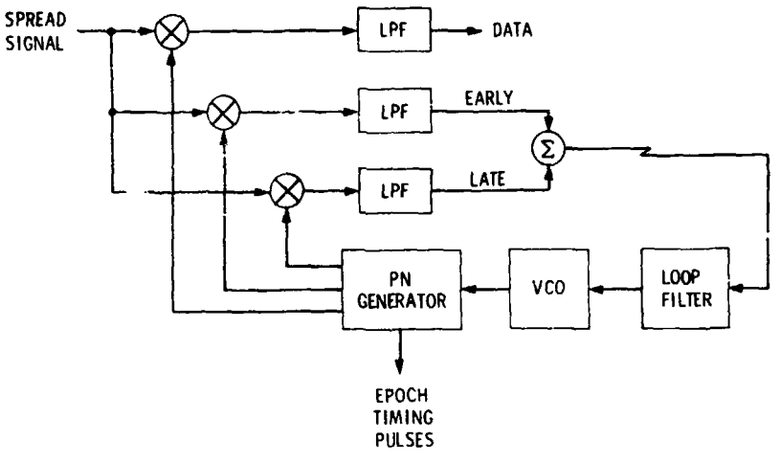

Fig. 2. Coherent delay-lock loop (DLL)

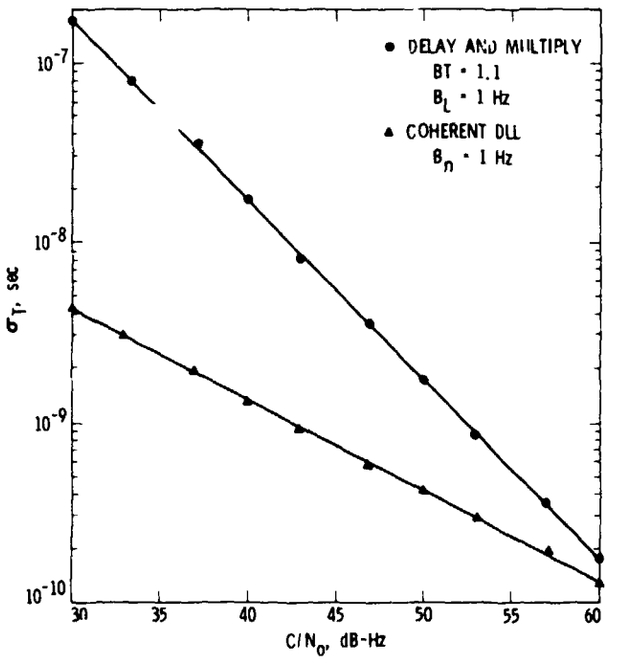

Fig. 3. Comparison of delay-lock loop and delay and multiply circuit

D14

N84 13415

Design Issues in the GCF Mark IV Development

R. A. Crowe
DSN Data Systems Section

This article outlines some of the major design problems facing the computer based GCF Digital Communication System for the Mark IV Network Consolidation Program and discusses the solutions to each as implemented in the software of the GCF Operation Programs.

Ground Communications Facility (GCF)

I. Introduction

The requirements of the Network Consolidation Program (NCP) (Ref. 1) mandate that the Ground Communications Facility (Ref. 2) be extensively upgraded in order to support upcoming projects in the nineteen eighties and beyond. Both hardware and software changes are necessary (Ref. 3).

When the Mark IV changes are complete there will exist three Deep Space Communication Complexes, one at each of the principal sites of the DSN (Fig. 1). The SPC building at each DSCC will house the computers and equipment necessary for tracking support. More than one mission may be simultaneously supported at each complex. Deep Space Stations (DSS) will be configured from a set of equipment within the SPC along with outlying antenna. The Area Routing Assembly (ARA) is the GCF Computer at each SPC responsible for the processing of DSN Data Blocks (Fig. 2). The ARA will perform transmission, reception and routing of data for all DSSs active at the SPC For this purpose the ARA will interface to 2 or 3 digital communication circuits that connect the SPC with the Central Communications Terminal (CCT) at the Jet Propulsion Laboratory (JPL). One circuit will permit full duplex traffic both into and out of the SPC. The ARA will utilize it for low rate data to JPL. The other one or two circuits shall be simplex circuits that will carry outbound traffic only. The ARA will transmit high-rate data blocks on these circuits. Data from all DSSs must share the available circuits.

At JPL the eventual terminuses of all SPC circuits are the five Error Correction and Switch (ECS) computers of the CCT area (Fig. 2). A solid state digital communication switching hardware device shall allow flexibility in the assignment of circuits to individual computers. The ECS computers handle not only the circuits from the ARAs but also digital circuits to Remote Mission Operation Centers (RMOC), Remote Information Centers (RIC) and other remote sites in the DSN. Each of the ECS computers "knows" the circuit assignments of the remaining ECS computers. A network, therefore, has been established here that permits ECS to ECS communication necessary for (remote) site to (remote) site exchange of data using the CCT as a central hub.

The major problems encountered in developing the Mark IV GCF are summarized as follows:

(1) The shared usage among DSSs of the duplex and multiple simplex circuits.

(2) The necessity for "visualizing" the data flow both at the SPC and at JPL.

(3) The difficulty at the CCT of handling both Mark III and Mark IV data blocks for an extended period of time.

(4) Delayed project requirements specifying that the ECS computers route the same data block to two destinations.

(5) The retention by the ECS software of essential routing features currently supported by hardware but scheduled for removal.

Each of these subjects is discussed individually in the following paragraphs.

II. Economy of SPC Circuit Utilization

For the ARA software implementations, the servicing of the duplex circuit to the SPC presents no particular design problems. Low rate (1200-bit) data blocks from each DSS will be multiplexed on a first-come-first-served basis. Error correction of data blocks via retransmission in cooperation with the ECS will be implemented in a manner similar to the method used for Mark III stations. The servicing of two *simplex* circuits to the ECS, however, does present some difficulties. How was the ARA to decide on which simplex channel it should transmit the data blocks for each DSS? The utilization of both circuits equally for transmission would result in blocks arriving out of their original sequence at the ECS. An operator assignment of each DSS to a particular circuit seemed laborious and quite inefficient since typically one circuit might be overloaded while the other sat idle. Operational attention to the load balance between simplex circuits would constantly be demanded.

The solution to this problem was undertaken by utilizing the GCF fields of the data blocks that are normally used for the error correction algorithm. Since error correction is not performed on the simplex circuits, these fields are free for the assignment of an Arrival Sequence Number (ASN) by the ARA when the blocks arrive at the ARA and before transmission to the ECS. The ASN assignment of data blocks permits the ARA to switch them automatically to either simplex circuit as load conditions dictate. Out-of-sequence arrivals at the ECS are handled promptly by means of a short retention queue and a simple resequencing algorithm based on the ASN.

III. Data Flow Visability

A significant problem at the ARA and particularly at the ECS was the tracing of the data block flow through each computer. This capacity is crucial in the verification of the new software and instrumental in diagnosing system problems when the programs are operational. The existing one-dimensional data block dump features of the Mark III programs were inadequate for the following reasons:

(1) The formatting of data blocks was performed within the core storage of the computer and passed immediately to the line printer. Since the Mark IV data rates are measurably enhanced and because the core size of the computers is relatively small (64 K words) the dumping of even a modest contiguous sample of data blocks is precluded

(2) Data blocks could be dumped at only one transition point (e.g. Input/Output interface) of the program. In the case of the ECS, this was too restrictive since any one data block might be delivered to several local or remote sites. It is useful to record the passage of the block through each transition point of the program.

To solve these inadequacies, the Mark IV Programs implemented a dumping facility that utilizes a multifile disc spooling capability (Fig. 3). Disc storage has been partitioned into several spool files. Each file is available for assignment to a particular I/O Interface or other transition point of the program. After I/O handling, data blocks are relayed to the Formatter and Spooler Task where information is extracted, converted to ASCII, and immediately relayed to the spooler disc file that is servicing the I/O Interface. Following this relatively fast operation, the data blocks are released for transit through the remainder of the program. By this mechanism, since the disc files are relatively large (10 K words each), it is possible to capture long contiguous samples of data blocks passing through several I/O Interfaces *simultaneously*.

The Despooler and Printer Task will print one file at a time at the (slow) rate of the line printer. When an end-of-file is detected, the despooler will initiate the printing of another spooler file. Blocks dumped simultaneously but to different spooler files may later be time correlated by comparing dump information from the sequential print-outs.

IV. Transition to Mark IV

The transition of the DSN to a Mark IV configuration was a particularly keen problem in the design of the ECS Program. Facing the development effort were the following known facts:

(1) A network of four ECS computers, one Central Communication Monitor (CMF) computer and three Data Records Generator (DRG) computers, were currently on-line to support Mark III data flow. Operations normally operated each program from the CCM. Each pro-

ram was to be modified for Mark IV. A strict protocol governed data block exchanges among computers

(2) The transition is not abrupt. The phasing over of the DSN to Mark IV will take 10 to 14 months. Therefore, there is an extended period of time where both Mark III and Mark IV data must be handled.

(3) The set of source/destination codes to be used in Mark IV data blocks is different from the set used for Mark III. Newly identified Block Format Codes (BFC) placed in each data block allowed discrimination between Mark III and Mark IV data blocks.

(4) Removal of some CCT hardware as part of the new effort would jeopardize deliveries of Mark III data to two local JPL sites (VLBI/MCC).

The basic question to be answered before design could proceed was whether to retain the existing ECS during the transition phase and create the new ECS to support Mark IV data only, or create the new ECS to support both Mark III and Mark IV data thereby retiring the current ECS. In support of two operational versions of the ECS were the facts that fewer functions would need to be lodged in the new program and that introduction of the new software would be less catastrophic: Mark III support would be assured in any event.

Balancing these considerations were the facts that:

(1) The new software would be forced to abide by existing protocols, operator input formats, etc. thereby placing a severe constraint on the free design of the new program.

(2) Operations would be forced to operate two versions of the ECS at the same time, thereby causing confusion and inevitably leading to procedural errors.

(3) A single program would allow any Mark III/IV mix of communication circuits on the same computer thereby optimizing computer/communication circuit utilization.

(4) The new CCM program would not be able to communicate with the old ECS thereby causing gaps in the monitor information displayed to operations.

For the above reasons, it was decided to incorporate the support of Mark III data flow within the new ECS program and have but one version of the ECS on-line at any given time. A ramification of this decision is that the new software must now prove its capabilities at two different instances; the first will occur when the current software is replaced, well in advance of any Mark IV station, and the second occurs when the first Mark IV station is brought up for operational support and begins the generation of the new data blocks.

V. Multiple Routing

Halfway into the coding of the ECS program came the eleventh hour requirement that some data blocks transmitted from a generating DSS would need to be routed to two different sites in the DSN. This was not an extant ECS capability but it was felt that because the DSN was gravitating toward High Earth Orbit, (HEO) support missions (with multiple users), it would be a wise inclusion in the new software.

The design response to this requirement was to invent dummy destination codes that the originating source would insert into data blocks when multiple routing was desired. The ECS routing construction is such that the destination code from each block is used to index into a 256 word table corresponding to its field width of 8-bits. Normally, the position of the table at this point determines the (one) output path of the data block. For multiple routing destinations, however, two translation destination codes are inserted in the table at this point and flagged as such. The action of the ECS upon detection of a multiple destination code is to overlay the dummy destination code in the block with the first code from the table, and to store the second destination code in a data structure associated with the data block. The block is then passed through the various internal ECS tasks where it is routed as specified by the first destination code. Following this transit, the second destination code is used to overlay the first destination code and the block is released for another circuit through the internal tasks of the ECS.

A noteworthy feature of this capability is that operations may, in the future, invent dummy and associated translation destinations *without* a modification to the program as transferred. Operator inputs will cause alteration of the routing table thereby defining the multiple routing desired and a periodic save of this table to disc storage will permit a restart (Warm Start) of the software to recognize the changes.

VI. Replacement of Hardware Routing Features

The delivery of 4800-bit Mark III data blocks to the Mission Control and Computing Center (MCCC) and to the Very Long Baseline Interferometry (VLBI) processors was implemented by means of a hardware switch in the CCT called the Wideband Distributed Amplifier (WDA) (Fig. 4). Data blocks are tapped-off from each of the six possible circuits and passed to the MCCC and VLBI organizations directly. Because each circuit is driven by but one computer (VLBI or MCCC Telemetry) at the DSS a "pure stream" of data is routed by the WDA. The ECS, in this case, does not route the blocks by destination code but does monitor the circuit and deliver the blocks to the DRG computers for tape records.

In Mark IV the use of the WDS will no longer be possible. The ARA will multiplex data from all DSSs of the SPC on the available circuits. A tap-off by the WDA will no longer produce a "pure stream" of data blocks. Yet because no resources are available to modify the MCCC or VLBI processors to sort through a mixture of data blocks, the ECS was to be burdened with routing to each delivery circuit an unadulterated stream of data blocks generated by one and only one source (DSS)! In the Fig. 5 example, it is assumed that DSSs 12, 14 and 42 are all active and transmitting data to the CCT with the same destination code. The ECS computers are charged with sorting these data by the originating source and placing them in Delivery Lines (DL) 1, 2, or 3, respectively.

In order to solve this organizational problem, it was decided to add a secondary routing table to the ECS software. An operator would cause entries to be made in the secondary table by assigning each DSS to a unique Delivery Line. Internally, the ECS would flag the Common Destination Code so that its detection would cause reference to this table. The secondary table is then scanned for a match on *Source Code* and the block is routed as previously specified by the operator to the proper Delivery Line.

References

1. Yeater, M. L., and Herrman, D. T., "Networks Consolidation Program," *TDA Progress Report 42-65, July and August 1981*, Jet Propulsion Laboratory, Pasadena, Calif., Oct. 15, 1981.

2. Evans, R. H., "DSN Ground Communications Facility," *TDA Progress Report 42-65, July and August 1981*, Jet Propulsion Laboratory, Pasadena, Calif., Oct. 15, 1981.

3. Mortensen, L. O., "GCF Mark IV Development," *TDA Progress Report 42-70, May and June 1982*, Jet Propulsion Laboratory, Pasadena, Calif., Aug. 15, 1982.

ORIGINAL PAGE IS
OF POOR QUALITY

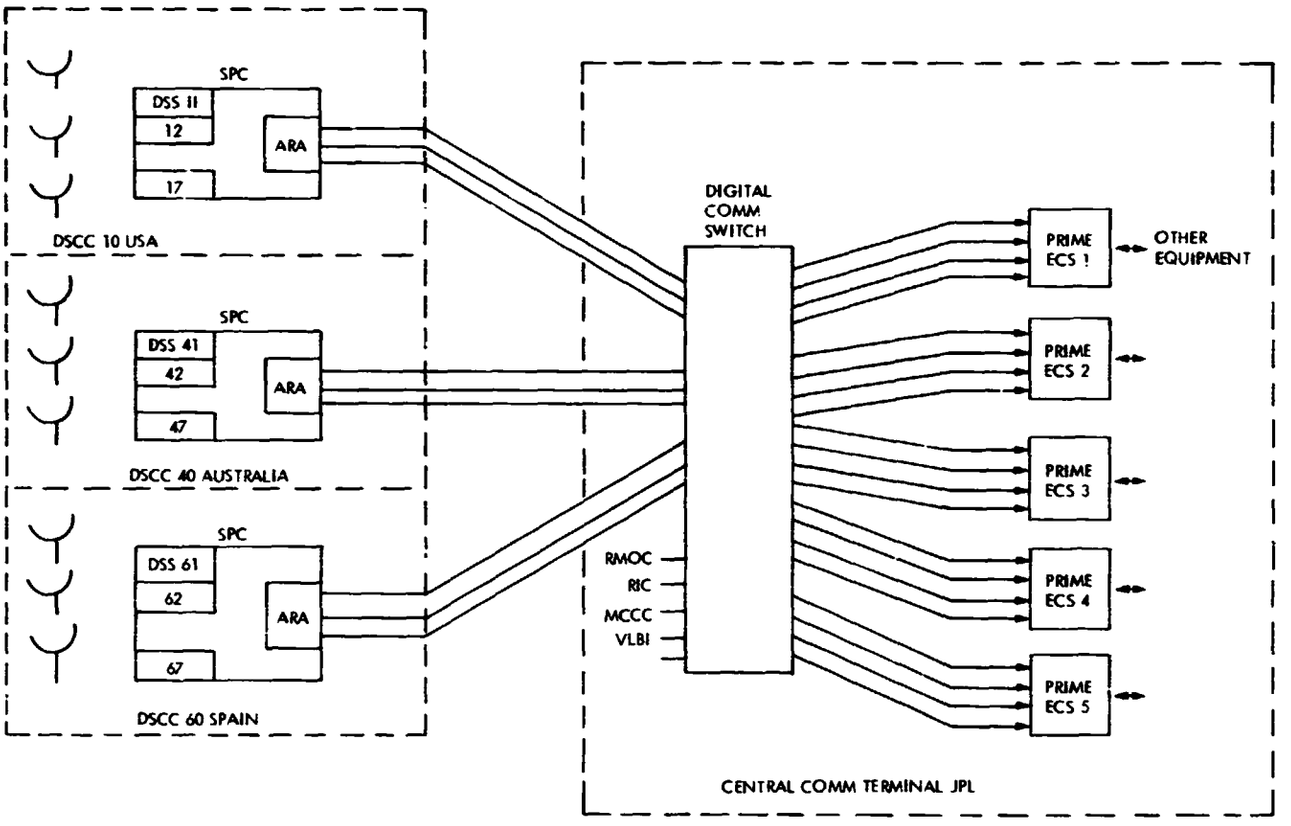

Fig. 1. The Mark IV project

ORIGINAL PAGE IS
OF POOR QUALITY

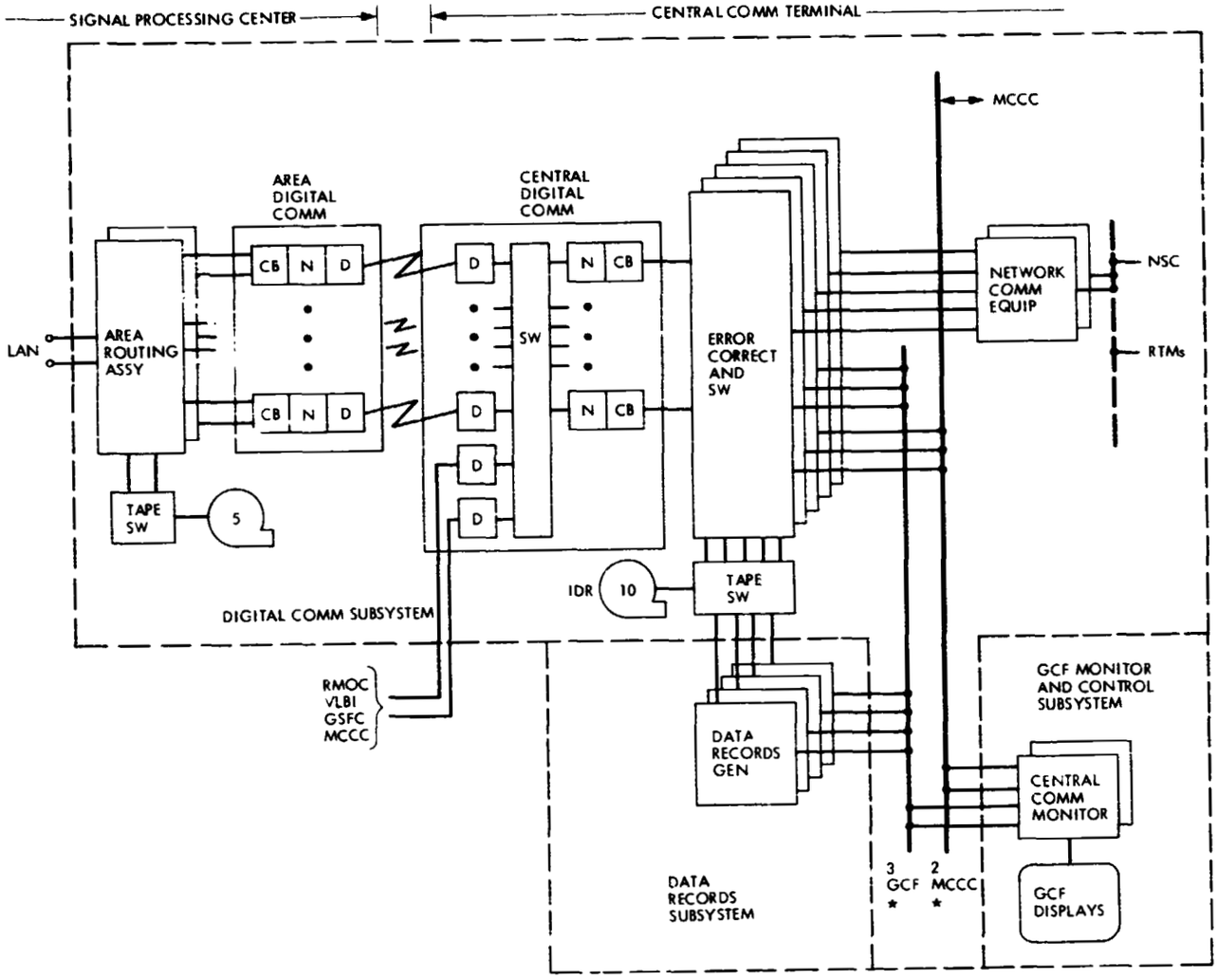

Fig. 2. Digital communications subsystem overview of GCF digital configuration

ORIGINAL PAGE IS
OF POOR QUALITY

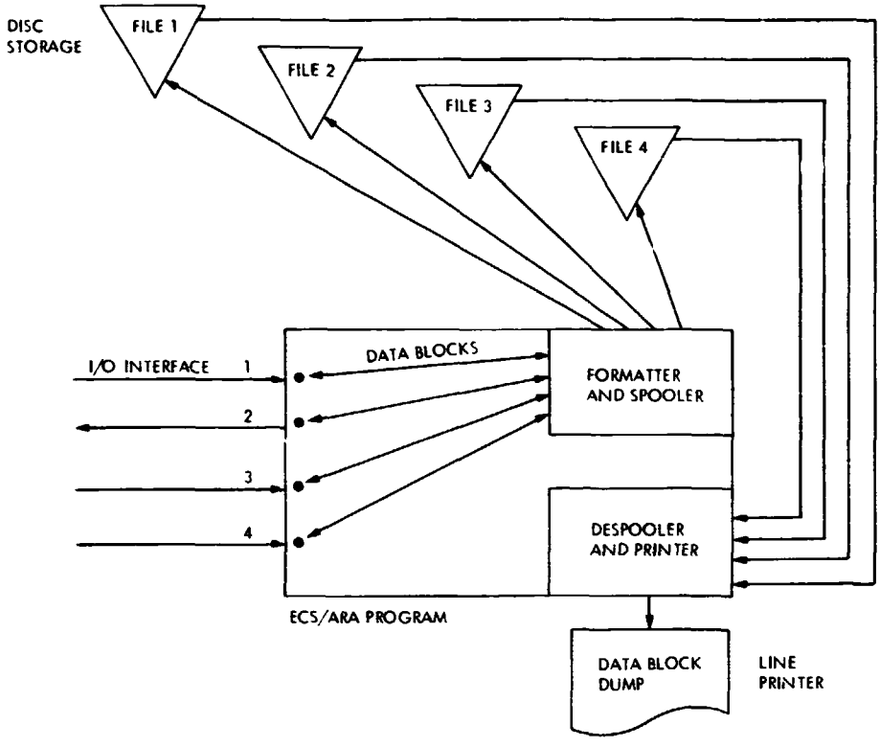

Fig. 3. Data block dump mechanism

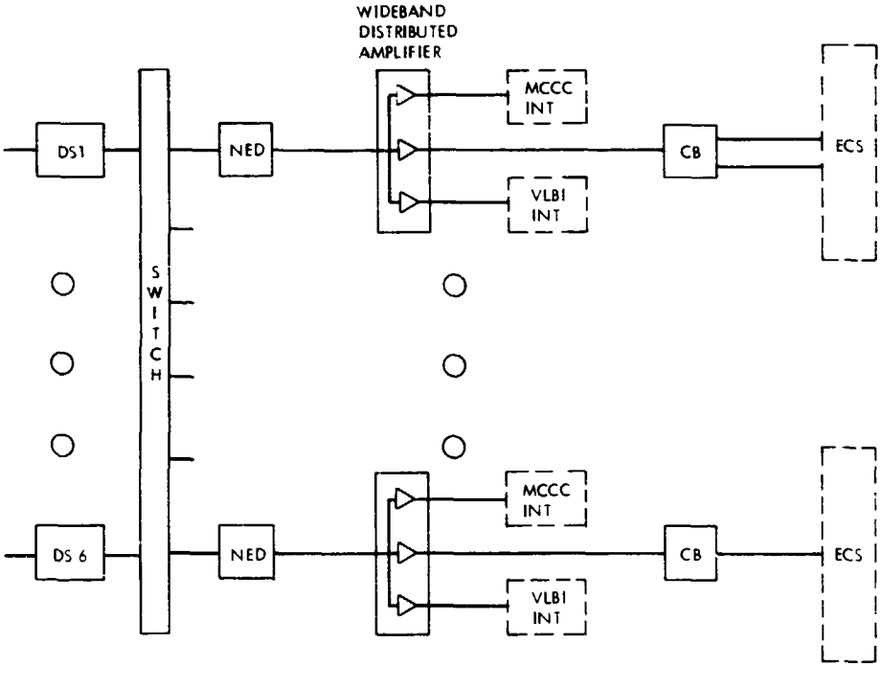

Fig. 4. MCCC/VLBI routing in Mark III

ORIGINAL PAGE IS
OF POOR QUALITY

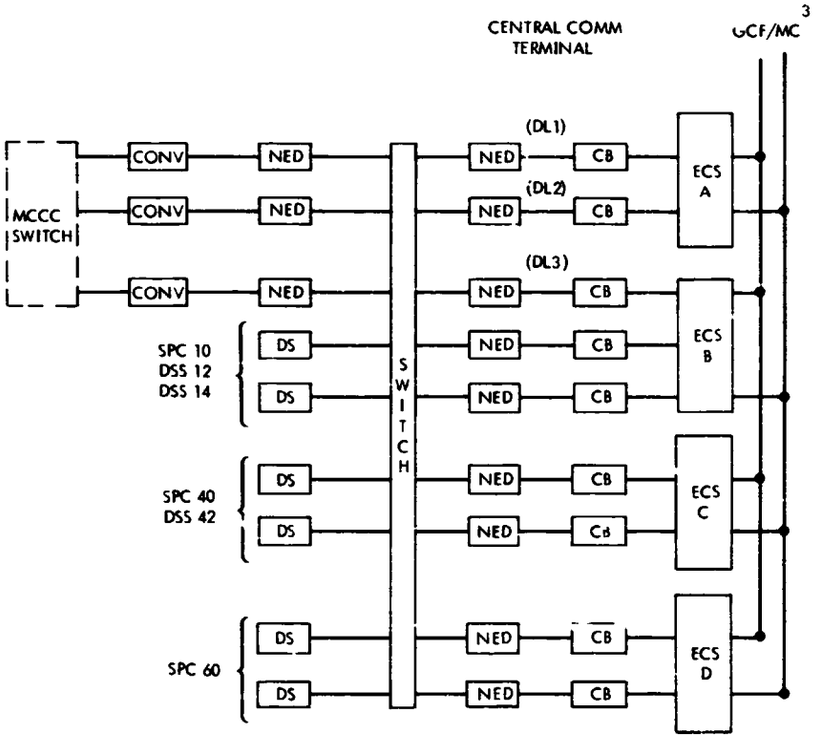

Fig. 5. Mark IV ECS–MCCC wideband data routing example

315

N84 13416

Results of the Australian Geodetic VLBI Experiment

B. R. Harvey and A. Stolz
University of New South Wales, Kensington, Australia

D. L. Jauncey
CSIRO, Epping, Australia

A. Niell, D. Morabito and R. Preston
Tracking Systems and Applications Section

The 250-2500 km baseline vectors between radio telescopes located at Tidbinbilla (DSS43) near Canberra, Parkes, Fleurs (X3) near Sydney, Hobart and Alice Springs were determined from radio interferometric observations of extragalactic sources. The observations were made during two 24-hour sessions on 26 April and 3 May 1982, and one 12-hour night-time session on 28 April 1982. The 275 km Tidbinbilla – Parkes baseline was measured with an accuracy of ±6 cm. The remaining baselines were measured with accuracies ranging from 15 cm to 6 m. The higher accuracies were achieved for the better instrumented sites of Tidbinbilla, Parkes and Fleurs. The data reduction technique and results of the experiment are discussed in this paper.

I. The Australian Geodetic VLBI Experiment

The Australian Geodetic VLBI Experiment described by Stolz *et al.* (Ref. 1) has been completed and results obtained. Briefly, from 20 April to 3 May, 1982, five Australian radio telescopes were operated in synchronism to form a single radiotelescope. The five telescopes are sited at the NASA Deep Space Network (DSN) communications complex at Tidbinbilla near Canberra (DSS 43), the CSIRO Radio Observatory at Parkes, the University of Tasmania's Radio Observatory near Hobart, the University of Sydney's Fleurs Observatory near Sydney (X3), and the LANDSAT tracking station at Alice Springs (Fig. 1). The experiment was designed principally to provide high-resolution maps of distant quasars and galaxies. However, it also provided a means of making accurate geodetic measurements.

The antennas at Fleurs, Hobart and Alice Springs were instrumented at S-band (2.3 GHz) only, while those at Tidbinbilla and Parkes were instrumented at both X- (8.4 GHz) and S-band. Tidbinbilla was equipped with a Hydrogen maser and one was installed at Parkes especially for the experiment. Rubidium frequency standards were available at the other sites except Hobart where one was obtained on loan from the Division of National Mapping. The Mark II recording system was used (Refs. 2 and 3). Tidbinbilla, Parkes and Fleurs were instrumented with bandwidth synthesis (BWS) equipment to improve the accuracy of the VLBI observables. In this system

a spanned bandwidth of 38 MHz is synthesized by sequential switching between two frequency channels. A single 2 MHz frequency channel was recorded at Hobart and Alice Springs.

The geodetic measurements were made during two 24-hour sessions on 26 April and 3 May, and one 12-hour night-time session on 28 April. Tidbinbilla and Parkes observed on 26 April and 3 May at both X- and S-bands, and on 28 April at S-band only. During the nights of 26 April, 28 April and 3 May, Fleurs, Hobart and Alice Springs were to observe at S-band. No observations were successful at Fleurs on 3 May. The Hobart antenna moved too slowly to observe all the scheduled sources, and those observed were spread over less than one half of the sky. On 28 April the Parkes maser failed and was replaced by a Rubidium frequency standard. The maser was back in operation on 3 May.

Twenty-three radio sources were successfully observed. The positions of 17 of these had been determined from intercontinental VLBI measurements using the DSN antennas (Ref. 4). The new sources were located south of -45° declination. Each radio source was observed for 10 minutes when all sites were observing, or 4 minutes when only Tidbinbilla and Parkes were observing. About 40 observations were made during a 12-hour session.

II. Data Reduction Technique

After the experiment the video tapes, on which the data were recorded at each station, were brought together for digital cross-correlation on the Mark II VLBI Processor at the California Institute of Technology. The post-correlation computer tapes, containing the highly compressed data, were then further processed at the Jet Propulsion Laboratory. Essentially, this involved extracting the phase as a function of time (phase tracking) to obtain the delay and delay rate observables. The ambiguities in BWS delays were then removed. The phase tracking and BWS techniques are described by Thomas (Ref. 3).

To obtain the baseline vectors, the model parameters are adjusted by least squares. Initially, the observations were weighted according to system noise and a variance factor of one. However, this produced residuals which were larger than would be expected. The original error estimates were then increased until the weighted RMS of the residuals divided by the number of degrees of freedom in the adjustment approximately equalled one. The models for delay and delay rate comprise principally a geometric delay, instrumental delays, and transmission media delays. Stolz *et al.* (Ref. 1) describe some of the parameters required to model the geometric delay. In this experiment uncertainties in the geometric delay due to errors in the earth orientation parameters are small in comparison with other errors as discussed below. That is, these parameters have been obtained with sufficient accuracy by independent measurements so that they may be treated as known quantities. Therefore, only the components of the baselines and the source positions were regarded as "solve-for" parameters in the geometric delay. The instrumental delay can, in the ideal case, be modelled by a series of constant (clock offset) and linear drift (clock rate difference) terms, but often a more complicated form is necessary to account for frequency oscillator instabilities. We solved for clock terms at all sites except Tidbinbilla. The transmission media (ionosphere and troposphere) delays could not be reliably estimated from the data. On the short baselines they are highly correlated. On the long baselines other errors dominate. We corrected for the effect of the ionosphere by using S- and X-band data where available, and for the troposphere by using models and meteorological data (Ref. 1).

Observations at a single frequency produce baseline lengths which are too long and source positions which are distorted. To avoid this problem we obtained the results in three steps. First we solved for the three components of the Tidbinbilla-Parkes baseline, 11 clock parameters, and 45 source coordinates from 145 delay and 145 delay rate observations obtained on 26 April and 3 May, 1982. The right ascension of radio source 3C273 was held fixed at $12^h\ 26^m\ 33^s.2792$ (epoch 1950.0) to refer the source positions to the dynamical equinox (Ref. 5). We assigned a variance of 0.0009 arcsec^2 to each of the catalogue source positions. The catalogue variances are smaller. Our value represents an accuracy estimate. Covariance terms were not available. Second, we solved for the three coordinates of Fleurs and 18 clock parameters from the 185 delay and 185 delay rate S-band (BWS) observations acquired at Tidbinbilla, Parkes and Fleurs on 26 and 28 April. The coordinates of Parkes, the catalogue source positions, and the positions of the new sources, as obtained above, were held fixed. Third, we solved for the six coordinates of Alice Springs and Hobart and 23 clock parameters from the 217 delay and 217 delay rate S-band (single channel) observations at Tidbinbilla, Parkes, Hobart and Alice Springs on 26 and 28 April and 3 May. The coordinates of Parkes, the catalogue source positions, and the positions of the new sources, as obtained above, were again held fixed. We adopted a cylindrical reference coordinate system with axes parallel to those of the conventional system defined by the geocentre, the CIO pole, and the Greenwich Meridian. The coordinates of Tidbinbilla were held fixed to define the origin of the reference system and to relate our measurements to the global network of VLBI stations (Ref. 4).

III. Results and Discussion

The baseline measurements and their formal errors are summarized in Tables 1 and 2. The distance from Parkes to Tidbin-

billa was measured with a precision of 3 cm (0.1 ppm). The remaining distances are all precise tc better than 0.7 ppm except those to Hobart which are precise to about 4 ppm.

We estimated the accuracy of the results by solving for the baselines, the source positions and clock terms from portions of the data and by covariance analysis. Bounds for subjective aspects of the analysis (e.g. selecting the clock parameters) were also estimated. The estimated errors are summarized in Fig. 2.

The Parkes-Tidbinbilla data were partitioned as follows: (a) 26 April; (b) 3 May; (c) night-time on 26 April and 3 May; and (d) day-time on 26 April and 3 May. The Fleurs data were partitioned into that gathered on 26 April and on 28 April. The Alice Springs and Hobart data were partitioned into that gathered on 26 April and 28 April and that gathered on 28 April and 3 May. The baseline solutions from the partitioned data are summarized in Table 3. The corresponding lengths agree to better than twice their formal error. The site coordinates agree to better than three times their formal error except the Parkes longitude for the day-time solution. Radio source 3C273 could not be observed at day-time and another source was chosen as the origin of right ascension. This accounts for a significant portion of the latter discrepancy.

The results for Tidbinbilla-Parkes should not be significantly affected by incorrect modelling of the ionospheric delay since the measurements were made at both S- and X-bands (Ref. 1). We estimated the effect of the ionosphere on the results for Tidbinbilla-Fleurs and for Parkes-Fleurs by solving for the baseline vector between Tidbinbilla and Parkes from S/X-band night-time observations and from S-band night-time observations and taking the difference. The source positions were held fixed in both cases. Figure 2 shows that the baselines Tidbinbilla-Fleurs and Parkes-Fleurs are about 5 cm too long. The formal errors of the results are also larger than they would be if the ionospheric delay had been correctly modelled.

Errors in surface meteorological measurements and the models for the tropospheric delay sum to about 5 cm at the zenith (Ref. 6). Covariance analysis showed that this 5 cm systematic error produces a 4 mm error in the Tidbinbilla-Parkes baseline length. The effect on the baseline components is significant (Fig. 2). For instance, the height difference between Parkes and Tidbilbilla would be in error by about 10 cm.

The Love numbers h and l, and the tidal phase lag were held fixed at 0.610, 0.085 and 0°.0 respectively, at all sites. Systematic errors of 0.05, 0.03 and 2° in h, l and phase lag produced errors of less than 1 mm in the length and the components of the Tidbinbilla-Parkes baseline.

Errors in polar motion and UT1 do not affect baseline lengths; they do however affect baseline orientation. Errors of 30 cm and 0.001 sec in the adopted BIH values for polar motion and UT1 caused errors of less than 2 cm in baseline components (Fig. 2).

Results for Tidbinbilla-Parkes were also obtained by holding fixed the catalogue values of the source positions, and by assigning the variances given in the catalogue. In both cases the new results differ from those shown in Tables 1 and 2 by less than the corresponding formal errors.

The analyst decides which data points to delete from the solution, which clock parameters to solve for, what *a priori* weights to assign to the catalogue source positions, and what *a priori* variances to assign to the observations. We estimate the magnitude of these subjective errors on the Tidbinbilla-Parkes baseline length and components to be of the order 3–4 cm. The errors are significant. They can be reduced by using more stable clocks which require little or no modelling and increasing the observation rate so that there is greater redundancy, and by obtaining more reliable estimates of the accuracy of the data and the source positions.

IV. Comparison with Ground Survey

In addition to the VLBI measurements reported here, the baselines have also been determined by conventional survey techniques. We show the surveyed baselines in Table 2. They are preliminary results computed from coordinates of the 1983 adjustment of the Australian Geodetic Datum (J.S. Allman, 1983, private communication). Doppler data have not been included in the tabulated values. Table 2 shows that the differences between the VLBI and survey measurements are less than 3 ppm except for the baselines to Hobart. Both the VLBI and ground measurements to Hobart are of low quality. The ground measurements should be much improved when Doppler data are included in the adjustment.

V. Summary and Conclusions

The 275 km Tidbinbilla-Parkes baseline length has been determined with an accuracy of ±6 cm. The baseline components have been determined to better than ±15 cm. The 235 km Tidbinbilla-Fleurs and 250 km Parkes-Fleurs baseline lengths have each been determined with an accuracy of ±14 cm. The baseline components have been determined to ±45 cm. The Tidbinbilla-Alice Springs and Parkes-Alice Springs baseline lengths have been determined with accuracies of ±1.8 m and the components with accuracies of ±2.2 m. The Tidbinbilla-Hobart and Parkes-Hobart baseline lengths and components have been measured with accuracies of ±6.4 m

and ±8 m respectively. The higher accuracies were achieved for the better instrumented sites of Tidbinbilla, Parkes and Fleurs.

The results clearly demonstrate that long baselines in Australia can be measured by VLBI with an accuracy of a few centimeters in a matter of days. These accuracies are largely independent of baseline length. The accuracies can be improved upon by installing more sophisticated equipment such as the Mark III recording system which together with other instrument improvements will allow determinations of baseline measurements potentially accurate to 1 cm with modest size antennas.

Preliminary discussions have taken place to repeat the experiment described in this paper, to utilize the proposed $25 million Australia Telescope for geodetic VLBI measurements and to bring a highly mobile VLBI system to Australia, possibly as soon as 1984-1985. For the future experiments, we recommend

(1) that masers be installed at Fleurs, Hobart and Alice Springs so that measurements can be made at X-band;

(2) that BWS equipment be acquired at both Alice Springs and Hobart for improved delay measurements;

(3) that the slew rate of the Hobart antenna be increased;

(4) that the data acquisition rate be substantially increased; and

(5) that only about 15 well chosen source be observed.

References

1. Stolz, A., Harvey, B., Jauncey, D. L., Niell, A., Morabito, D., Preston, R., Greene, B., Tzioumis, A., Watkinson, A., Royle, G. W. R. and Johnson, D. 1983. Geodetic Surveying with Quasar Radio Interferometry. *Aust. Surv., 31*, 305-314.

2. Rogers, A. E. E., 1970. Very-long-baseline Interferometry with Large Effective Bandwidth for Phase-delay Measurements. *Radio Science, 5*, 1239-1247.

3. Thomas, J. B. 1981. Analysis of Radio Interferometry with the Block-0 System, *JPL Publication 81-49*, Jet Propulsion Laboratory, Pasadena, CA.

4. Thomas, J. B. et al., 1983. "Radio Interferometric Determinations of Source Positions, Intercontinental Baselines, and Earth Orientation with Deep Space Network Antennas – 1971 to 1980." TDA Progress Report *42-73*, 128-155, Jet Propulsion Laboratory, Pasadena, CA.

5. Fricke, W. 1981. Definition and Practical Realization of the Reference Frame in the FK5 – The Role of Planetary Dynamics and Stellar Kinematics in the Definition. In E. M. Gaposhkin & B. Kolaczek (eds.) "Reference Coordinate Systems for Earth Dynamics." *Astrophys. Space Sci. Library*, Vol. *86*, 331-340, D. Reidel Publishing Co., Dordrecht.

6. Moran, J. M. and Rosen, B. R. 1980. The Estimation of the Propagation Delay Through the Troposphere from Microwave Radiometer Data. In "Radio Interferometry – Techniques for Geodesy." *NASA Conference Publication 2115*, 363-376.

ORIGINAL PAGE IS
OF POOR QUALITY

Table 1. Site coordinates

Site	R[a], m		L[b], deg[c]		Z[d], m	
Tidbinbilla (DSS 43)	5205 251.365		148.981 279 10		-3674 748.367	
Parkes	5354 918.85	±0.05	148.263 526 19	±0.02	-345[illegible] 035.80	±0.05
Fleurs (X3)	5302 029.34	±0.19	150.763 759 9	±0.06	-3533 527.69	±0.14
Alice Springs	5841 280.8	±0.8	133.882 357	±0.9	-2554 104.9	±2.0
Hobart	4683 738.3	±1.1	147.512 08	±1.4	-4314 838.7	±4.5

[a]Distance from the Z axis
[b]Longitude from the Greenwich meridian.
[c]The formal precisions of the longitudes are in metres.
[d]Distance from the equatorial plane.

Table 2. Baseline measurements and comparisons with survey

Baseline	VLBI, m		Survey, m	Difference ppm
Tidbinbilla-Parkes	274 751.78	±0.03	274 752.10	-1.2
Tidbinbilla-Fleurs	236 681.19	±0.07	236 681.46	-1.2
Parkes-Fleurs	251 340.46	±0.07	251 341.06	-2.4
Tidbinbilla-Alice Sp.	1938 997.1	±1.3	1938 994.8	1.2
Tidbinbilla-Hobart	835 297.0	±3.6	835 299.8	-3.4
Parkes-Alice Springs	1733 991.1	±1.2	1733 989.3	1.0
Parkes-Hobart	1093 516.8	±3.7	1093 520.3	-3.2
Hobart-Alice Springs	2445 610.4	±3.0	2445 610.9	-0.2
Fleurs-Hobart	1035 709.1	±3.7	1035 712.5	-3.3
Fleurs-Alice Springs	1979 707.5	±1.3	1979 705.5	0.5

Table 3. Repeatability

Baseline	26 April	28 April	3 May	Night-time	Day-time
			Length, m		
Tidbinbilla-Parkes	0.038		-0.049	-[illegible]9	0.009
Tidbinbilla-Fleurs	-0.027	0.035			
Parkes-Fleurs	0.029	-0.058			
	26 and 28 April		28 April and 3 May		
Tidbinbilla-Hobart	+1.1		-4.1		
Tidbinbilla-Alice Springs	0.0		+0.6		
Parkes-Hobart	+1.1		-4.0		
Parkes-Alice Springs	0.0		+0.6		
			Coordinates[a]		
Parkes R	-0.054		-0.095	0.000	-0.137
Parkes L	0.009		-0.017	0.061	-0.092
Parkes Z	0.014		0.001	-0.018	0.078
Fleurs R	0.37	-0.43			
Fleurs L	0.01	-0.02			
Fleurs Z	-0.31	0.38			
	26 and 28 April		28 April and 3 May		
Alice Springs R	+1.0		-0.3		
Alice Springs L	-0.1		-0.4		
Alice Springs Z	-0.8		+0.8		
Hobart R	+1.6		-0.3		
Hobart L	-1.5		+2.0		
Hobart Z	-2.6		+5.1		

[a]See Table 1

ORIGINAL PAGE IS
OF POOR QUALITY

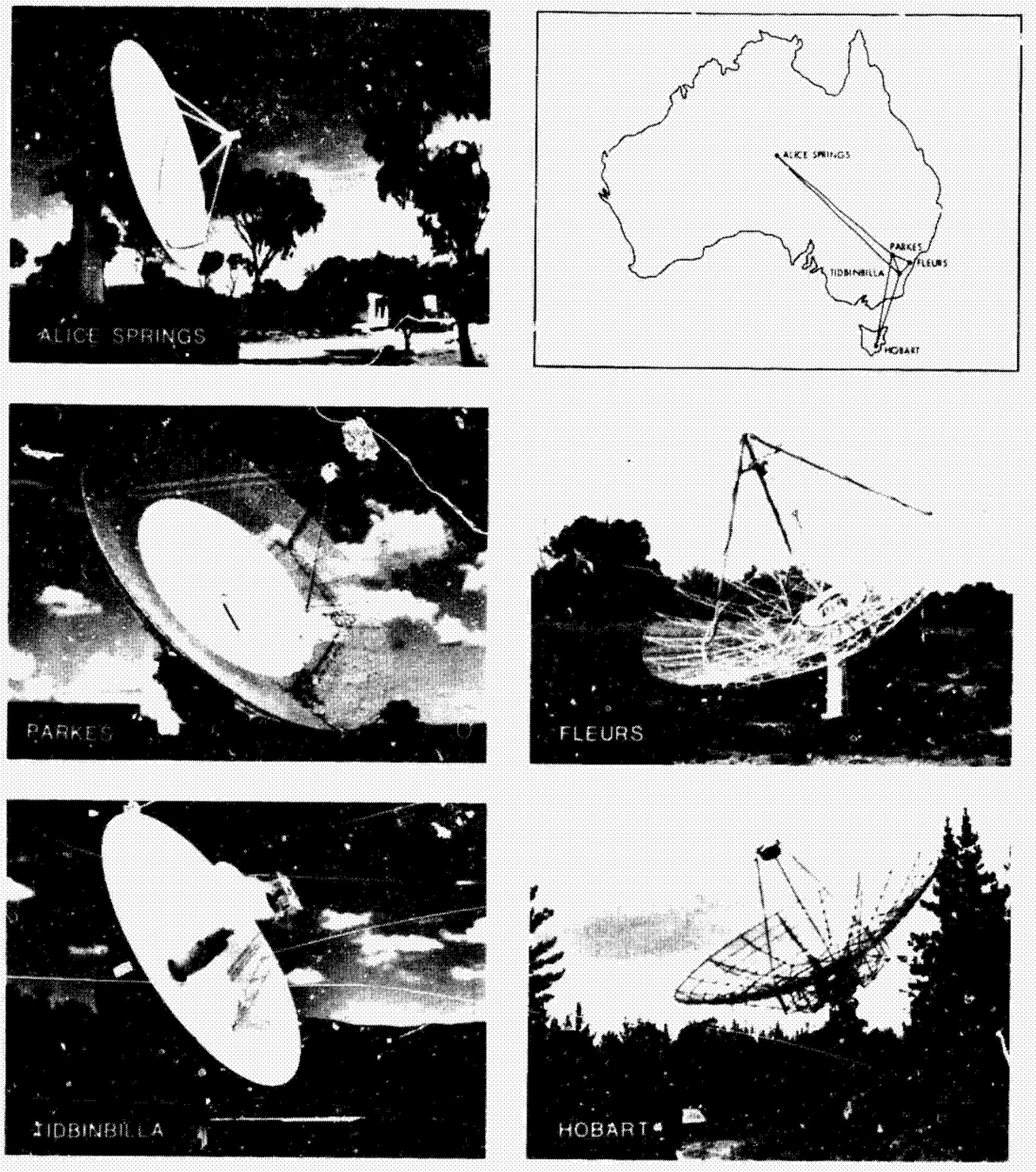

Fig. 1. Australian VLBI geodesy network, 1982

ORIGINAL PAGE IS
OF POOR QUALITY

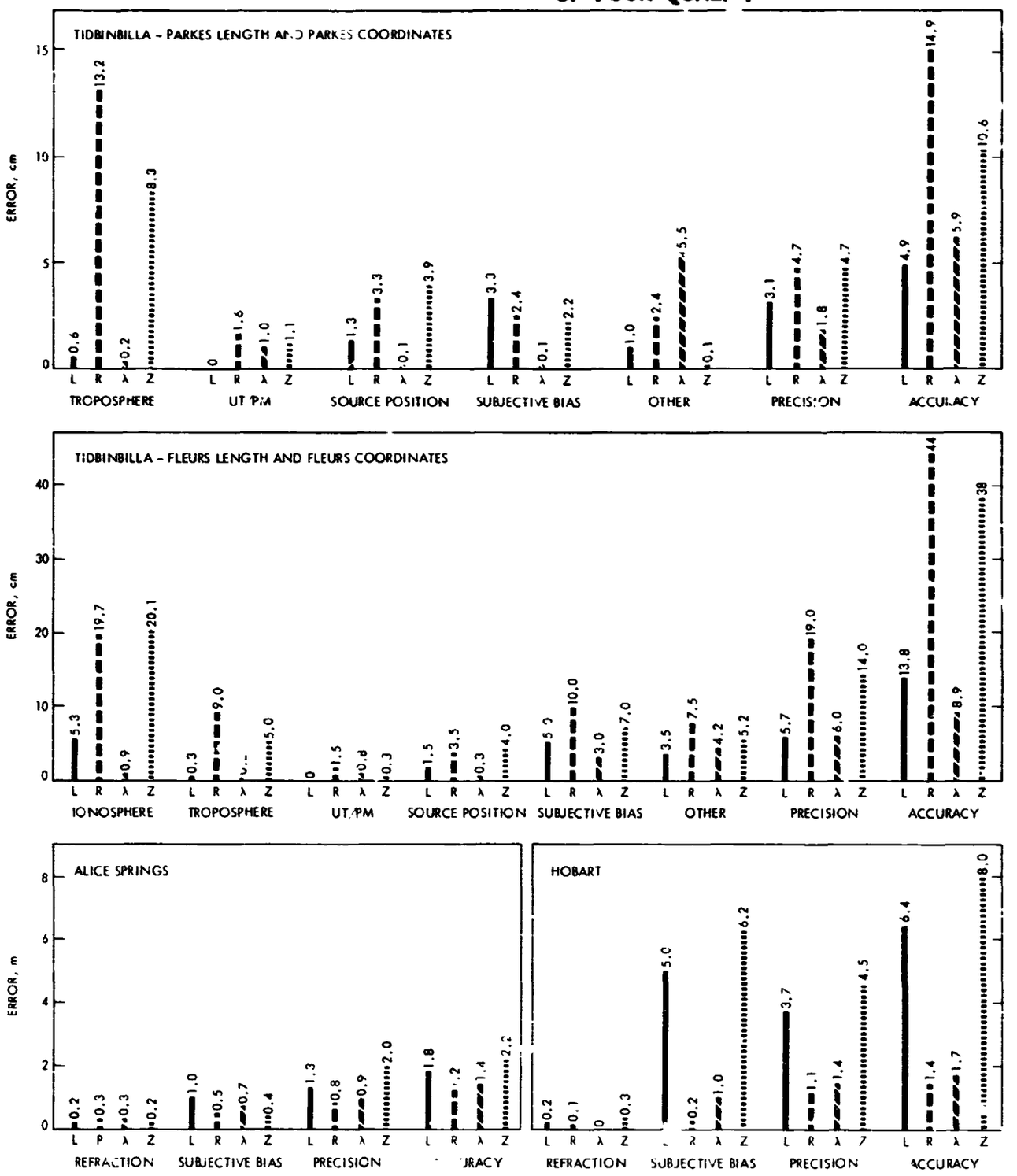

Fig. 2. Error budgets

NASA—JPL—Comi. LA. Calif